GEOLOGY, GEOCHEMISTRY AND PETROGENESIS OF THE MOUNT SIDLEY VOLCANO, MARIE BYRD LAND, ANTARCTICA

by
Kurt S. Panter

Submitted in Partial Fulfillment of the
Requirements of the Degree of
Doctor of Philosophy in Geology
November, 1995

Department of Earth and Environmental Science
New Mexico Institute of Mining and Technology
Socorro, New Mexico, USA

TABLE OF CONTENTS

Table of Contents	i
List of Figures	iii
List of Tables	v
Acknowledgements	vi
Abstract	vii
Introduction	x
References	xv
Part A: Volcanic History	A-1
Volcanic history of Mount Sidley, a major alkaline volcano in Marie Byrd Land, Antarctica	
ABSTRACT	A-1
INTRODUCTION	A-1
GEOLOGICAL BACKGROUND	A-2
Marie Byrd Land	A-2
Executive Committee Range	A-2
Mount Sidley	A-3
FIELD RELATIONSHIPS	A-4
Eruptive environment	A-4
Stratigraphy	A-4
$^{40}Ar/^{39}Ar$ DATING	A-8
Methods	A-8
Results	A-9
DISCUSSION	A-10
Volcanic evolution of Mount Sidley	A-10
Stage I: Sidley activity (5.7-4.8 Ma)	A-11
Stage II: Pirrit activity (4.6-4.5 Ma)	A-12
Stage III: Doumani activity (4.4-4.3 Ma)	A-12
Stage IV: parasitic cones	A-13
Volcanic migration	A-13
CONCLUSIONS	A-14
ACKNOWLEDGEMENTS	A-13
REFERENCES	A-15
Part B: Geochemistry and Magma Genesis	B-1
Petrogenesis of a phonolite-trachyte succession at Mt. Sidley, Marie Byrd Land, Antarctica	
ABSTRACT	B-1
INTRODUCTION	B-3
VOLCANIC GEOLOGY	B-5

PETROGRAPHY AND MINERAL CHEMISTRY B-8
Olivine B-10
Clinopyroxene B-12
Feldspars B-19
Spinel B-24
Amphibole and mica B-25
Feldspathoids and apatite B-28
GEOCHEMISTRY B-29
Methodology B-29
Major Element Chemistry B-34
Trace Element Chemistry B-39
Isotope Geochemistry B-43
Chemical effects of alteration B-46
MAGMA GENESIS B-52
Fractionation modeling B-52
Phonolite Series B-56
Fractional crystallization B-57
Magma mixing B-64
Trachyte Series B-67
Fractionation of alkali basalt B-73
Origin of the *LT*-trachyte suite and assessment of crustal contributions B-76
Fractionation of *LT*-trachyte magmas and development of *HT*-trachyte compositions B-83
MAGMA ORIGIN AND PHYSICAL MODELS OF EVOLUTION B-89
Partial melting and magma ascent B-91
Chemical zonation and eruption of trachyte magmas B-95
CONCLUSIONS B-100
REFERENCES B-103

Part C: Appendices C 1

Appendix C.1: Sample information C-1
Appendix C.2: $^{40}Ar/^{39}Ar$ analyses C-7
Appendix C.3: Mineral analyses C-25
Appendix C.4: Major and trace element analyses C-44
Appendix C.5: Isotopic analyses C-53

LIST OF FIGURES

Part A: Volcanic History

A 1	Regional map of West Antarctica.	A-2
A 2	Simplified map of the Executive Committee Range.	A-3
A 3	U.S. Navy aerial photograph of Mount Sidley.	A-4
A 4	Topographic map of Mount Sidley illustrating simplified distribution of major volcanic rock compositions.	A-5
A 5	Photographs of SE caldera wall.	A-6
A 6	Generalized composite stratigraphic column for Mount Sidley.	A-7
A 7	Photographs of (a) anorthoclase crystals in a tephriphonolite lava; (b) basaltic enclave within commingled trachyte lavas.	A-8
A 8	Representative $^{40}Ar/^{39}Ar$ age spectra for anorthoclase.	A-10
A 9	Schematic sketch map illustrating the geologic evolution of the Mount Sidley edifice.	A-11

Part B: Geochemistry and Magma Genesis

B 1	Topographic map of Mt. Sidley showing simplified distribution of volcanic rock compositions.	B-4
B 2	Generalized composite stratigraphic column for Mt. Sidley.	B-7
B 3	Electron microprobe analyses of clinopyroxene	B-11
B 4	atomic % Ti + Al versus *mg*-number for clinopyroxene from phonolites and trachytes.	B-17
B 5	Electron microprobe analyses of clinopyroxenes and alkali amphibole plotted in terms of atomic % Na + K, Mg, Mn + Fe_t.	B-18
B 6	Clinopyroxene analyses from phonolite lavas of the Sidley volcano plotted in terms of atomic % Ti + Al versus *mg*-number.	B-20
B 7	Composition of feldspars for Mt. Sidley volcanic rocks plotted in terms of molecular % An, Ab, Or.	B-21
B 8	Classification of Mt. Sidley volcanic rocks on a total alkalis versus silica diagram.	B-35
B 9	Variation of selected major elements with silica content.	B-36
B 10	Whole-rock compositions of Mt. Sidley phonolites and trachytes projected onto the normative plane Q-Ne-Ks at 1 atm.	B-38
B 11	Variation of selected trace elements relative to Zr.	B-40
B 12	Chondrite-normalized REE patterns and trace-element spidergrams of representative Mt. Sidley volcanic rocks	B-42
B 13	Age corrected Sr-Nd isotopic variation in Mt. Sidley volcanic rocks.	B-45
B 14	$\delta^{18}O$ versus initial $^{87}Sr/^{86}Sr$.	B-47
B 15	Loss on ignition (LOI) versus $\delta^{18}O$ for whole-rock samples.	B-48
B 16	Variation of selected elements (ppm) and elemental ratios from phonolitic lavas of the stage-I succession.	B62-63

B 17	Th (ppm) versus K/Ta diagram illustrating trachyte subdivisions.	B-68
B 18	Plot of La/Yb versus *mg*-number showing mugearite types, DPM and SFM, relative to basanite and Mt. Waesche basalts.	B-72
B 19	Comparison of chondrite-normalized multi-element patterns for selected Mt. Sidley and Mt. Waesche mugearites and trachytes.	B-75
B 20	Graphical presentation of FC and assimilation–fractional crystallization (AFC) models.	B79-80
B 21	Plot of Nb (ppm) versus K/Ta showing model AFC curves.	B-84
B 22	Plot of Rb (ppm) variations with stratigraphy from the western caldera wall succession.	B-87
B 23	Rb/Ta versus Th (ppm) diagram showing main differentiation trends.	B-90
B 24	Plot of chondrite-normalized Yb versus normalized Ce/Yb for Mt. Sidley and Mt. Waesche basalts and mugearites.	B-93
B 25	Model for the chemical zonation and eruption of trachyte magmas.	B96-97

Part C: Appendicies

C1.1	Sample location map for Mt. Sidley.	C-5
C1.2	Sample location map for Mt. Waesche.	C-6

C2: $^{40}Ar/^{39}Ar$ age spectra

C2.1	sample MB33.3	C-11
C2.2	sample K168	C-12
C2.3	sample K85	C-13
C2.4	sample MB29.4	C-14
C2.5	sample MB35.5	C-15
C2.6	sample MB42.3	C-16
C2.7	sample K105	C-17
C2.8	sample K106	C-18
C2.9	sample K108	C-19
C2.10	sample K137	C-20
C2.11	sample K149	C-21
C2.12	sample K51	C-22
C2.13	sample K55	C-23
C2.14	sample K68	C-24

LIST OF TABLES

Part A: Volcanic History

A 1 Representative $^{40}Ar/^{39}Ar$ age spectra data. A-9

Part B: Geochemistry and Magma Genesis

B 1 Summary of petrographic features for Mt. Sidley volcanic rocks. B-9
B 2 Representative electron microprobe analyses of olivine. B-13
B 3 Representative electron microprobe analyses of clinopyroxene. B-15
B 4 Representative electron microprobe analyses of feldspars. B-22
B 5 Representative electron microprobe analyses of spinel. B-26
B 6 Representative electron microprobe analyses of amphibole. B-27
B 7 Representative analyses of whole-rocks from Mt. Sidley and selected samples from the Mt. Waesche volcano. B30-31
B 8 Sr, Nd and O isotopic determinations on whole-rock and anorthoclase separates. B-33
B 9 Selected mineral/liquid partition coefficients. B-53
B 10 Values of elemental bulk distribution coefficients (D^i) calculated from log-log diagrams. B-55
B 11 Closed system fractional crystallization models for the Phonolite Series. B-58
B 12 Trace element concentrations calculated by Rayleigh fractionation equations and D^i determined by the log-log method. B-59
B 13 Least-squares model for mixing between tephriphonolite and 'evolved' phonolite. B-66
B 14 Least-squares and Rayleigh fractionation for evolution of Mt. Waesche series rocks. B-74

Part C: Appendicies

C1.1 Sample information for Mt. Sidley and Mt. Waesche. C-1
C2.1 $^{40}Ar/^{39}Ar$ age spectra data. C-7
C3.1 Electron microprobe analyses, olivine. C-25
C3.2 Electron microprobe analyses, clinopyroxene. C-29
C3.3 Electron microprobe analyses, feldspars. C-33
C3.4 Electron microprobe analyses, spinel. C-41
C3.5 Electron microprobe analyses, amphibole. C-43
C4.1 Major and trace element analyses, Mt. Sidley. C-44
C4.2 Major and trace element analyses, Mt. Waesche. C-50
C5.1 Sr and Nd isotopic analyses, Mt. Waesche. C-53
C5.2 Lead iotopic analyses for Mt. Sidley and Mt. Wasesche. C-54
C5.3 Oxygen isotopic analyses for Mt. Sidley. C-55

ACKNOWLEDGEMENTS

There are many people that I wish to thank for their direct involvement in this dissertation. First, I would like to gratefully acknowledge Philip Kyle for including me as part of the WAVE project and also for his guidance throughout my dissertation research. I would like to extend a special acknowledgment to Bill McIntosh, John Smellie (British Antarctic Survey) and John Gamble (Victoria University of Wellington) for offering their knowledge of physical volcanology, field skills and friendship during three field seasons in Marie Byrd Land. I would also like to thank Andy Campbell for the use of his stable isotope laboratory. Andy's encouragement and guidance during my M.S. degree helped establish many of my research skills. My special thanks to Bob Pankhurst (British Antarctic Survey) for his knowledge and supervision of radiogenic isotope analysis. Also, Larry Snee and Mick Kunk of the U.S. Geological Survey for guidance and the use of their $^{40}Ar/^{39}Ar$ laboratory facilities. Finally, I wish to thank Richard Wysoczanski, Thom Wilch and Nelia Dunbar for helpful discussion of my work, as well as Chris Beck for his skilled draftsmanship.

I owe an immeasurable debt of gratitude to Ann for her understanding, patience and perseverance throughout my trials as a graduate student. And, to my daughter Sage for putting-up with "daddy spending too much time at work". The pursuit of my degree could not have occurred without the support of family and friends, especially Barbara Panter and Jim and Shirley Beck. Finally, this dissertation is dedicated to the memory of my father, John Panter.

ABSTRACT

The volcanic history and geochemical evolution of the Pliocene Mt. Sidley volcano (4181), Marie Byrd Land, Antarctica, is examined using $^{40}Ar/^{39}Ar$ geochronology, major and trace element geochemistry, and Sr, Nd, O and Pb isotopic data. Over 200 km^3 of alkaline volcanic rocks were erupted from at least four major central vents and are composed primarily of strongly silica-undersaturated sodic lavas, ranging from basanite (> 10% *Ne*-normative) to phonolite and silica-saturated to oversaturated trachytes. Detailed mapping and high-precision $^{40}Ar/^{39}Ar$ ages reveal a complex, polygenetic volcano constructed over 1·5 m.y. from 5·7 to 4·2 Ma. During this period, three major phonolitic centers were constructed and superseded by many smaller vents. Major changes in magma composition coincide with a southward migration of activity, occurring in four main stages. The first stage (I) of activity (5·7–4·8 Ma), produced phonolitic lavas in the northern portion of the edifice. During stage I, three calderas formed and were partially infilled with lavas and volcaniclastic sediments. Trachytic lavas, domes and pyroclastic deposits of stage II (4·6–4·5 Ma) were erupted roughly 5 to 6 km to the south. Stage III activity (4·4–4·3 Ma) began with a highly explosive paroxysmal eruption and catastrophic landslide of the southern flank of the volcano, forming a large breached caldera (5 × 5 km, 1200 m deep). This was followed by eruption of mugearites and benmoreites ~ 9 km south of stage I activity. Then, following the eruption of xenolith-bearing parasitic cones of basanite at ~ 4·2 Ma (stage IV), volcanism migrated to Mt. Waesche (2·0–0·5 Ma). Mt. Sidley volcanic rocks are porphyritic with olivine (Fo_{86-1}), clinopyroxene (Wo_{52-43} En_{49-1} Fs_{53-1}), feldspar (An_{54-2} Ab_{74-44} Or_{48-1}), and spinel (Usp_{77-2}). Apatite and

feldspathoids are present within stage I phonolites and arfvedsonite occurs within some trachytic lavas.

Mt. Sidley rocks have high incompatible element contents and are enriched in light rare earth elements (REE) relative to heavy REE [$(La/Yb)_n = 9–19$]. The basanites have trace element concentrations comparable to ocean island basalts (OIB) and the majority of rocks fall within a narrow range of $^{87}Sr/^{86}Sr_i$ (0·7028–0·7032), $^{143}Nd/^{144}Nd_i$ (0·51285–0·51290) and $\delta^{18}O$ (5·0–6·0‰). Moreover, radiogenic Pb signatures (e.g., $^{206}Pb/^{204}Pb >$ 19) help characterize a high U/Pb (HIMU) OIB-type mantle source. Mugearite compositions of stage III are subdivided into two types: low *mg*-number (20–30) lavas from the southern flank (SFM) and; high *mg*-number (40–50) tephras from Doumani Peak (DPM). SFM lavas have higher incompatible trace element contents and are light REE-enriched relative to DPM tephras, suggesting their formation from two distinct basaltic parents; basanite and alkali basalt (< 8% *Ne*), respectively.

Based on relative stratigraphy and chemical characteristics, phonolites and trachytes cannot be related to a single magma lineage. The phonolites have restricted SiO_2 and relatively uniform trace element contents, whereas trachytes show wide variations and are subdivided into three main types: high Th (> 60 ppm) trachytes (*HT*); low Th (~20 ppm) trachytes (*LT*) and; 'normal' trachytes (*N*). Differentiation of the phonolite series is modeled by fractionation of diopside, olivine, plagioclase, magnetite, nepheline and/or apatite from basanite, producing 35% mugearite, 25% benmoreite and 20% phonolite as residuals. The *N*-trachyte suite formed by fractionation crystallization of alkali basalt. Some trachytes have elevated $^{87}Sr/^{86}Sr_i$ (0·7033–0·7042), low $^{143}Nd/^{144}Nd_i$ (0·51280–

0·51283) and high $\delta^{18}O$ (6·5–8·4 ‰) values, suggesting contamination by crust. The petrogenesis of *LT*-trachytes require assimilation of calc-alkaline granitoids by alkali basalts within the middle crust. Differentiation at high assimilation to crystallization rates (high-*r* AFC) explains Nd and Sr isotopes and the depletion of Ta and Nb relative to K, Rb and light REE. Fractionation of *LT*-trachytes by low-*r* AFC within the upper-crust produced *HT*-trachytes.

The change in parental composition from basanite to alkali basalt reflects a shift to higher degrees of mantle partial melting. Models for non-modal equilibrium batch melting of peridotite produce basanitic magmas at $\leq 2\%$ partial melts, whereas alkali basalts require $\geq 5\%$ melting of the same mantle source. The partial melting cycle reflects the passing influence of a mantle upwelling (plume ?) beneath that portion of the lithosphere. Magmas emplaced within the upper-crust were released by tectonically driven tensional fractures, propagating southward.

INTRODUCTION

The Mt. Sidley volcano is located at the southern edge of the Late Cenozoic Marie Byrd Land alkaline province, west Antarctica. The Marie Byrd Land province is part of a broad region of crustal extension and young (~ 35 Ma to presently active) alkaline volcanism that occurs along the Pacific margin of Antarctica from Ellsworth Land to the northern coast of Victoria Land (~ 3500 km). It comprises one of the world's major continental rift systems (LeMasurier, 1990). In Marie Byrd Land, 18 large composite centers rise above the West Antarctic Ice Sheet, but only a few have adequate ice-free exposures to permit comprehensive study of their eruptive history and petrogenesis. At Mt. Sidley, a large breached caldera has exposed volcanic strata deep within its interior, revealing a long and complex history of eruptive activity. Volcanic rocks range from basanite, mugearite and benmoreite to strongly silica-undersaturated anorthoclase phonolite and silica-saturated to oversaturated trachytes. The broad compositional spectrum of the sample suite and its well constrained eruptive history provide an ideal opportunity to study the genesis of alkaline magmas within a continental setting. This dissertation represents the first detailed petrologic investigation of a Marie Byrd Land volcano and is part of a multinational effort (West Antarctic Volcano Exploration–WAVE) by United States, United Kingdom and New Zealand scientists to study the geology of volcanoes, glacial history and lithospheric composition and structure in Marie Byrd Land (Smellie *et al.*, 1990; Smellie *et al.*, 1993; Wilch *et al.*, 1993; Wysoczanski, 1993; McIntosh & Wilch, 1995).

Alkaline igneous rocks are defined as those with alkali contents in excess of the amount necessary to form feldspars. Excess sodium and potassium partition into minerals such as feldpathoids, sodic pyroxenes and amphiboles. The rocks represent an extremely broad compositional spectrum that owes its diversity (in part) to the large number of mineral species that coexist in equilibrium with silica-poor alkali-rich magmas (Fitton & Upton, 1987). Yet, a common feature of alkaline suites within continental settings is the occurrence of quartz-normative rocks coexisting with nepheline-normative compositions. The processes involved in the formation of magmas representing such strongly divergent liquid lines of descent has been a long-standing enigma for petrologists (e.g., Bowen, 1928; Tilley, 1957; Fudali, 1963; Sørensen, 1974; Wilkinson, 1977; Fitton & Upton, 1987). In recent years it has become generally accepted, primarily due to isotopic evidence, that silica-oversaturated alkaline rocks develop from undersaturated mantle-derived magmas by contamination with felsic crust (e.g., Downes, 1984; Halliday *et al.*, 1988; Foland *et al.*, 1993; Macdonald *et al.*, 1994; 1995).

Bowen (1928), theorized that crystallizing magmas may simultaneously assimilate the surrounding wall-rock. The heat required for assimilation is derived from heat contained within the magma and heat generated during precipitation of minerals. Theoretical models to describe the trace element and isotopic evolution of magmas undergoing concurrent assimilation and fractional crystallization (AFC) are presented in key papers by Allegre & Minster (1978), Taylor (1980) and DePaolo (1981). Adopting the method of DePaolo (1981), and taking into account a reassessment of the limits on the rate of assimilation to fractional crystallization discussed by Reiners *et al.* (1995), models

are developed to describe the geochemical variations of some Mt. Sidley rocks. Furthermore, AFC models help 'fingerprint' a distinct crustal source contaminant within the Marie Byrd Land lithosphere.

Geochemical studies of alkaline rocks erupted within continental settings indicate that magmas belong to two primary lineages; a strongly silica-undersaturated series (e.g., basanite → phonolite) and a more silica-saturated series (e.g., alkali basalt → trachyte) (e.g., Kyle & Rankin, 1976; Baker *et al.*, 1977; Coombs *et al.*, 1986; Downes, 1987). Rarely has the recognition of the two magma lineages been traced through a suite of coexisting rocks from a single volcano, often due to the preponderance of either basaltic or highly evolved compositions and dearth of intermediate rock-types. Because of the common occurrence of coexisting phonolites and trachytes within individual centers, petrological studies often invoke complex open system processes to explain their evolution from a common parent (e.g., Fitton, 1987; Barbieri *et al.*, 1988, Turbeville, 1993). However, other studies appeal to their formation as separate rock series evolving from fundamentally different parental magmas (e.g., Kyle, 1982; Downes, 1984, Price *et al.*, 1985).

The fundamental goal of this project is to determine the petrogenesis and petrogenetic relations between silica-undersaturated and silica-saturated to oversaturated rocks within the Mt. Sidley volcanic succession. First, a coherent volcanic history is established through detailed field investigations coupled with high-precision $^{40}Ar/^{39}Ar$ dating. Then, the magmatic evolution is examined using major and trace elements, Sr, Nd, O, and Pb isotopic data. The volcanic history of Mt. Sidley and aspects of its petrogenesis

are compared with other extension-related Antarctic volcanoes as well as other major alkaline centers worldwide. This study addresses three additional objectives: 1) the characterization of a mantle source; 2) mechanisms for volcanic migration and; 3) affects of surficial alteration on volcanic rocks.

The dissertation is divided in two parts. Part (A) describes the geology of Mt. Sidley and its history of eruption, constrained by high-precision $^{40}Ar/^{39}Ar$ ages. This paper was published in the Bulletin of Volcanology (1994, vol. 56, 361-376). Part (B) describes the mineralogy, petrology and petrogenesis of Mt. Sidley magmas. Part B builds on the first, and the conclusions drawn reflect the integrated knowledge gained from both studies. The manuscript is being prepared for publication and will be submitted to the Journal of Petrology. The two papers are followed by appendices which contain the location of each sample and the analysis performed. Data tables include complete sample sets of $^{40}Ar/^{39}Ar$ incremetal heating results, mineral chemistry, major and trace element analyses of whole-rock samples and isotopic data. Unpublished major, trace and isotopic analyses from the neighboring Mt. Waesche volcano are also included. Aspects of Mt. Waesche magma genesis are discussed in Part B and related to Mt. Sidley petrogenesis.

Both papers include authors other than myself. Bill McIntosh and John Smellie are authors on the Bulletin of Volcanology paper because of their invaluable expertise in the field. In addition, Bill McIntosh acted as coordinator and supervisor for $^{40}Ar/^{39}Ar$ analyses and John Smellie was responsible for mapping, sampling and interpreting a large portion of Mt. Sidley. I was primarily responsible for integrating stratigraphic relationships, laboratory analysis, data interpretation, and the preparation of the

manuscript for publication. On the second paper, Philip Kyle is included because of his active participation in the project and his supervision of INAA analysis. John Smellie is also included because of his continuing involvement with aspects of Mt. Sidley petrogenesis and his efforts as coordinator of major element and radiogenic isotope analysis through the British Antarctic Survey.

REFERENCES

Allègre, C. J., & Minster, J. F., 1978. Quantitative models of trace element behavior in magmatic processes. *Earth Planet. Sci. Lett.* **38**, 1-25.

Baker, B. H.,, G. G., Leeman, W. P., & Lindstrom, M. M., 1977. Geochemistry and petrogenesis of a basalt-benmoreite-trachyte suite from the southern part of the Gregory rift, Kenya. *Contrib. Mineral. Petrol.* **64**, 303-32.

Barbieri, M., Peccerillo, A., Poli, G., & Tolomeo, L., 1988. Major, trace element and Sr isotopic composition of lavas from Vico volcano (central Italy) and their evolution in an open system. *Contr.Miner. Petrol.* **99**, 485-97.

Bowen, N. L., 1928. *The Evolution of Igneous Rocks*. Princeton Univ. Press, 322 pp.

Coombs, D. S., Cas, R. A., Kawachi, Y., Landis, C. A., McDonough, W. F., & Reay, A., 1986. Cenozoic volcanism in north, east and central Otago. In: Smith, I. E. M. (ed.) *Late Cenozoic Volcanism in New Zealand*, The Royal Society of New Zealand, Bulletin 23, 278-312.

DePaolo, D. J., 1981. Trace element and isotopic effects of combined wallrock assimilation and fractional crystallization. *Earth Planet. Sci. Lett.* **53**, 189-202.

Downes, H., 1984. Sr and Nd isotope geochemistry of coexisting alkaline magma series, Cantal, Massif Central, France. *Earth Planet. Sci. Lett.* **69**, 321-34.

Downes, H., 1987. Tertiary and Quaternary volcanism in the Massif Central, France. In: Fitton, J. G., & Upton, B. G. L. (eds.) *Alkaline Igneous Rocks*, Geol. Soc. Spec. Pub. 30, Blackwell, Oxford, 517-30.

Fitton, J. G., 1987. The Cameroon line, west Africa: a comparison between oceanic and continental alkaline volcanism. In: Fitton, J. G., & Upton, B. G. L. (eds.) *Alkaline Igneous Rocks*, Geol. Soc. Spec. Pub. 30, Blackwell, Oxford, 273-91.

Fitton, J. G., & Upton, B. G. J. (eds.), 1987. *Alkaline Igenous Rocks*. Geol. Soc. Spec. Pub. 30, Blackwell, Oxford, 568 pp.

Foland, K. A., Landoll, J. D., Henderson, C. M. B., & Jiangfeng, C., 1993. Formation of cogenetic quartz and nepheline syenites. *Geochim. Cosmochim. Acta* **57**, 697-704.

Fudali, R. F., 1963. Experimental studies bearing on the origin of pseudoleucite and associated problems of alkalic rock systems. *Geol. Soc. Amer. Bull.* **74**, 1101-1126.

Halliday, A. N., Dickin, A. P., Fallick, A. E., & Fitton, J. G., 1988. Mantle dynamics: A Nd, Sr, Pb and O isotopic study of the Cameroon line volcanic chain. *J. Petrology* **29**, 181-211.

Kyle, P. R., 1982. Volcanic geology of The Pleiades, northern Victoria Land, Antarctica. In: Craddock, C. (ed.) *Antarctic Geoscience*. Univ. Wisconsin Press, 747-54.

Kyle, P. R., & Rankin, P. C., 1976. Rare earth elment geochemistry of Late Cenozoic alkaline lavas of the McMurdo Volcanic Group, Antarctica. *Geochem. Cosmochim. Acta* **40**, 1497-1507.

LeMasurier, W. E., 1990. Late Cenozoic volcanism on the Antarctic plate: an overview. In: LeMasurier, W. E., & Thomson, J. W. (eds.) *Volcanoes of the Antarctic Plate and Southern Oceans.* Antarctic Research Series **48**, Am. Geophys. Union, Washington D.C., 1-17.

Macdonald, R., Navarro, J. M., Upton, B. G. J., & Davies, G. R., 1994. Strong compositional zonation in peralkaline magma: Menengai, Kenya Rift Valley. *J. Volcanal. Geotherm. Res.* **60**, 301-25.

Macdonald, R., Davies, G. R., Upton, B. G. J., Dunkley, P. N., Smith, M., & Leat, P. T., 1995. Petrogenesis of Silali volcano, Gregory Rift, Kenya. *J. Geol. Soc. Lond.* **152**, 703-20.

McIntosh, W. C., & Wilch, T. I., 1995. Late Pleistocene (223-125 ka) plinian eruptions in Marie Byrd Land: potential time horizons in west Antarctic ice cores. (*Abst.*) VII International Symposium on Antarctic Earth Sciences, Siena, Italy, 261.

Price, R. C., Johnson, R. W., Gray, C. M., & Frey, F. A., 1985. Geochemistry of phonolites and trachytes from the summit region of Mt. Kenya. *Contrib. Mineral. Petrol.* **89**, 394-409.

Reiners, P. W., Nelson, B. K., & Ghiorso, M. S., 1995. Assimilation of felsic crust by basaltic magma: thermal limits and extents of crustal contamination of mantle-derived magmas. *Geology* **23**, 563-6.

Smellie, J. L., McIntosh, W. C., Gamble, J. A., & Panter, K. S., 1990. Preliminary stratigraphy of volcanoes in the Executive Committee Range, central Marie Byrd Land. *Antarctic Sci.* **2**, 353-4.

Smellie, J. L., McIntosh, W. C., Gamble, J. A., Panter, K. S., Kyle, P. R., & Dunbar, N. W. 1993. Preliminary lithofacies assessment and $^{40}Ar/^{39}Ar$ ages of Cenozoic volcanic sequences in eastern Marie Byrd Land. *Antarctic Sci* **5**: 105-6.

Sørensen, H., 1974. *The Alkaline Rocks.* J. Wiley & Sons, 622 pp.

Taylor, H. P., 1980. The effects of assimilation of country rocks by magmas on $^{18}O/^{16}O$ and $^{87}Sr/^{86}Sr$ systematics in igneous rocks. *Earth Planet. Sci. Lett.* **47**, 243-54.

Tilley, C. E., 1957. Problems of alkali rock genesis. *Quart. J. Geol. Soc. Lond.* **113**, 323-60.

Turbeville, B. N., 1993. Petrology and petrogenesis of the Latera Caldera, central Italy. *J. Petrology* **34**, 77-123.

Wilch, T. I., McIntosh, W. C., Panter, K. S., & Dunbar, N. W., 1993. Preliminary report on field investigations and $^{40}Ar/^{39}Ar$ geochronology of the Crary Mountains volcanoes, Marie Byrd Land, west Antarctica. *Antarctic J. U.S.* **28**, 7-9.

Wilkinson, J. F. G., 1977. Petrogenetic aspects of some alkali volcanic rocks. *Jour. & Proc., R. Soc. New South Wales* **110**, 117-38.

Wysoczanski, R. J., 1993. Lithospheric xenoliths from the Marie Byrd Land volcanic province, west Antarctica. Unpublished Ph.D. thesis, Victoria University of Wellington, New Zealand, 475 pp.

Bull Volcanol (1994) 56:361–376

ORIGINAL PAPER

K. S. Panter · W. C. McIntosh · J. L. Smellie

Volcanic history of Mount Sidley, a major alkaline volcano in Marie Byrd Land, Antarctica

Received 29 November 1993 / Accepted 15 July 1994

Abstract Mount Sidley is a complex, polygenetic stratovolcano composed primarily of phonolitic and trachytic lavas and subordinate pyroclastic lithologies at the southern extremity of the Executive Committee Range, a linear chain of volcanoes in central Marie Byrd Land, Antarctica. Detailed field investigation coupled with 14 high precision $^{40}Ar/^{39}Ar$ age determinations reveal a 1.5 million year life span between 5.7 and 4.2 Ma in which three major phonolitic central vent edifices (Byrd, Weiss and Sidley volcanoes) and their calderas were developed (5.7–4.8 Ma). This was followed (4.6–4.5 Ma) by the eruption of trachytic magmas from multiple vent localities further south, and then by small volume benmoreite-mugearite lavas and tephras around 4.4–4.3 Ma at the southern end of Mount Sidley. The final phase of activity was the eruption of basanite cones at approximately 4.2 Ma. The southward migration of volcanic activity was accompanied by distinct changes in magma composition and is best explained by the sequential release of magmas stored within an intricate system of conduits and chambers in the crust by tectonically driven (magma assisted?) fracture propagation. The style of volcanic migration at Mount Sidley is emulated on a larger scale by other volcanoes in the Executive Committee Range, in which progressive southward displacement of volcanic activity corresponds with significant petrological variations between major centers.

Key words volcanism · stratigraphy · $^{40}Ar/^{39}Ar$ geochronology · migration · Marie Byrd Land

K. S. Panter (✉) · W. C. McIntosh
Department of Geoscience,
NM Institute of Mining and Technology,
Socorro, NM 87801, USA

J. L. Smellie
British Antarctic Survey, NERC, High Cross,
Madingley Road, Cambridge CB3 OET, UK

Introduction

The Late Cenozoic Marie Byrd Land (MBL) volcanic province is located along a 1000 km section of the Pacific coast of West Antarctica (Fig. 1). Because of its often stormy weather, relative inaccessibility and an extensive ice-cap, it is the least studied region in Antarctica. In recent years, detailed and comprehensive snowmobile-supported fieldwork by the West Antarctic Volcano Exploration (WAVE) group (Gamble et al. 1990; Smellie et al. 1990; Smellie et al. 1993b; Wilch et al. 1993) has provided new insights into MBL glacial history (McIntosh et al. 1991), volcanic petrogenesis (Panter et al. 1991; Smellie et al. 1991) and a preliminary understanding of lithospheric composition and structure through crustal and mantle xenolith studies (Wysoczanski and Gamble 1992). During the 1989–90 field season the WAVE project focused on volcanoes in the Executive Committee Range (ECR), one of three Miocene to Recent volcanic mountain chains in MBL (Fig. 2). Mount Sidley (4181 m), situated at the southern end of the ECR, is the largest in the chain and is also the highest volcano in Antarctica (Fig. 3).

Previous studies of individual MBL volcanoes were limited to reconnaissance mapping and sampling (Doumani 1964; González-Ferrán and González-Bonorino 1972; LeMasurier 1972). The relatively poor exposure of most MBL volcanoes, particularly large undissected massifs such as Mount Takahe (McIntosh et al. 1985), have made it difficult to assess their internal structure and stratigraphy. At Mount Sidley, an impressive breached caldera has exposed a large portion of the volcanic interior (Fig. 3), thus allowing comprehensive mapping and systematic sampling for geochemical analysis and radiometric dating. Although K–Ar ages have been determined from one or more samples of most MBL volcanoes (LeMasurier and Wade 1976) and have allowed the recognition of regional trends in volcanism (LeMasurier and Rex 1989), their resolution is insufficient for a quantitative history of any single center. In

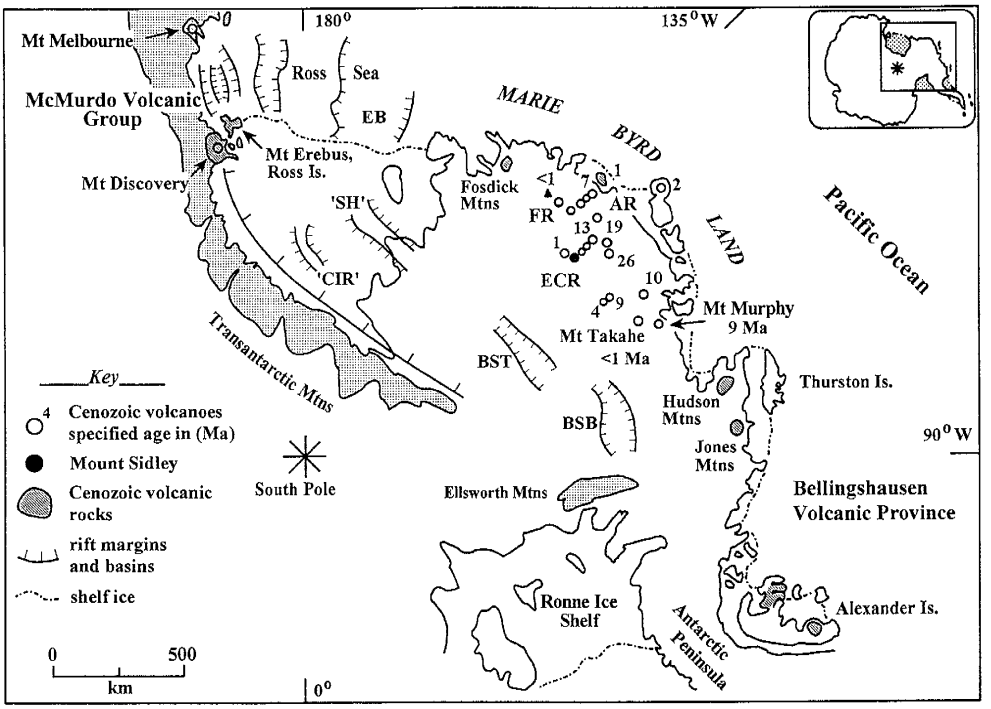

Fig. 1 Regional map of West Antarctica showing Cenozoic volcanism in Marie Byrd Land, western Ross Sea and Bellingshausen province. Included are locations of major volcanic centers within Marie Byrd Land, along with representative ages compiled from $^{40}Ar/^{39}Ar$ (LeMasurier and Rex 1990b; Wilch et al. 1993; Smellie et al. 1993b; and unpublished WAVE analyses) and K–Ar (LeMasurier and Rex 1989) dates. Ages are in millions of years (Ma). Abbreviations of volcanic ranges in Marie Byrd Land are as follows: ECR = Executive Committee Range; FR = Flood Range, including Mt Berlin (▲), which is active; AR = Ames Range. Approximate boundaries of rift basins in the Ross Sea are after Cooper et al. (1987); EB = East Basin. Faulted-bounded features under ice-covered areas are interpreted from Drewry (1983). Abbreviations are as follows: 'CIR' = 'Crary Ice Rise'; 'SH' = 'Steers Head'; BST = Bentley Subglacial Trench; BSB = Byrd Subglacial Basin

this study, dating by the high precision, $^{40}Ar/^{39}Ar$ age method has defined individual stages of Mount Sidley activity which were not apparent with previous, conventional, K–Ar ages. Detailed field investigations and $^{40}Ar/^{39}Ar$ dating provide a coherent volcanic history and support an ongoing study of magmatic evolution of this major phonolite–trachyte center.

Geological background

Marie Byrd Land

The MBL alkaline volcanic province consists of at least 18 major central vent composite volcanoes, in addition to many smaller centers (LeMasurier 1990b). Volcanic rocks in MBL are almost exclusively alkaline (LeMasurier 1990a, 1990b) and range in composition from alkali basalt and basanite to intermediate and evolved types including mugearite, benmoreite, phonolite, comenditic and pantelleritic trachyte and rhyolite (classification based on IUGS criteria: Le Maitre 1989). Felsic (>56 wt.% SiO_2) lavas dominate many volcanoes and parasitic cones of basanite are common. Other volcanic deposits in MBL include mafic hyaloclastites (LeMasurier 1972; McIntosh et al. 1985, 1991), hydrovolcanic tuff cones (Doumani 1964) and pyroclastic fall and flow facies (Smellie et al. 1990).

Voluminous alkali volcanism, fault offsets of pre-volcanic erosion surfaces and deep sub-ice basins (LeMasurier 1990b) indicate that MBL represents an extensional intraplate tectonic environment. This interpretation is supported by the many compositional similarities between MBL volcanism and the McMurdo Volcanic Group in the western Ross Sea (Kyle 1990; LeMasurier 1990a, 1990b). Crustal extension within the Ross Embayment has produced major rift basins (Cooper et al. 1987) and volcanism, including two active alkaline volcanoes, Mount Melbourne and Mount Erebus (Fig. 1). The combination of topographic characteristics and intraplate alkaline volcanism has led to the concept of a West Antarctic rift system (LeMasurier 1990a; Behrendt et al. 1991, and references cited therein). The rift system, which links three volcanic provinces (McMurdo, MBL and Bellingshausen), extends nearly 4000 km from the western Ross Sea to the Antarctic Peninsula (Fig. 1) and is comparable in size and structure with the Basin and Range/Rio Grande Rift provinces of North America.

LeMasurier and Rex (1989) recognized that felsic volcanoes in the linear MBL volcanic chains (Ames, Flood and Executive Committee ranges) become progressively younger towards the perimeter of the MBL province and the youngest volcanoes, including Mount

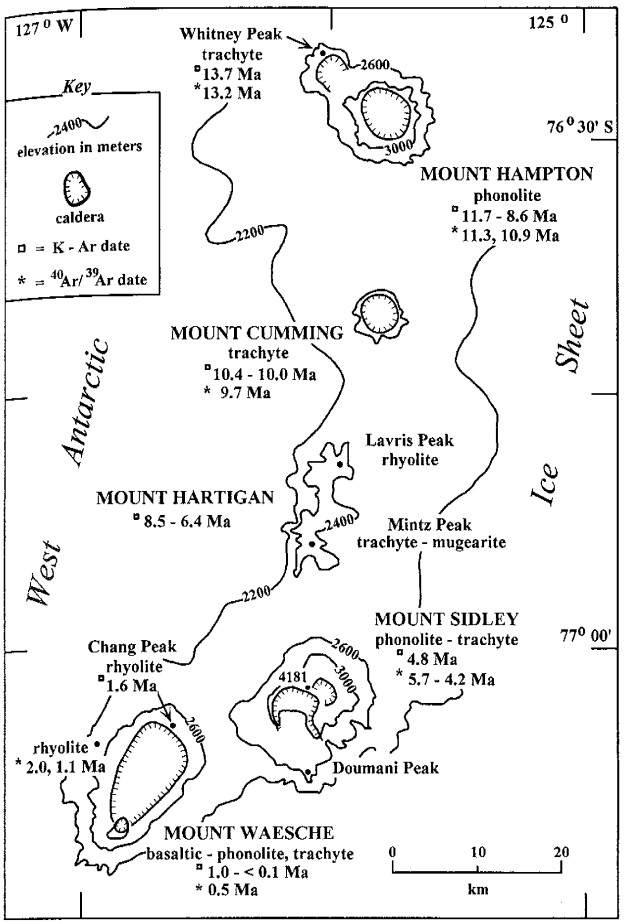

Fig. 2 Simplified map of the Executive Committee Range. $^{40}Ar/^{39}Ar$ analyses from this study and unpublished WAVE data. K–Ar dates from LeMasurier (1990b). Volcanic rock classification follows IUGS criteria (Le Maitre 1989) and is based on major element analyses (LeMasurier 1990b; Smellie et al. 1991; unpublished WAVE data)

Berlin, which is currently active (steam issuing from summit ice towers), are located on the periphery (Fig. 1). In addition, basement elevations (pre-volcanic erosion surfaces) are highest beneath the oldest volcanoes in the center of the region (LeMasurier and Rex 1983). The radial-circular pattern of volcanism cannot be explained by plate motion and studies indicate that the Antarctic plate has remained relatively immobile for the past 80 Ma (Duncan 1981). LeMasurier and Rex (1989) inferred that the dome-like pattern in basement morphology and outward migration of volcanism in MBL were related to a 550–650 km hot-spot on the shoulder of the West Antarctic rift system. In their model, regional doming is attributed to the rise of the asthenosphere/lithosphere boundary, causing systematic extension, thereby reactivating a relict rectilinear fracture pattern in the brittle portion of the crust. Fracture propagation along these pre-existing structures allowed trapped magmas to fractionate and to be released sequentially, thus explaining the systematic migration of felsic volcanism.

More recent papers explaining MBL volcanism propose a thermal mantle plume model (Kyle et al. 1991; LeMasurier and Rex 1991; Behrendt et al. 1992; Hole et al. 1994). Kyle et al. (1991) suggested that the pattern of volcanism is best explained by a single, stationary plume located beneath MBL; underplating of the crust above the plume axis may have channeled plume flow progressively outwards, resulting in the observed linear trends of volcanism along some of the ranges.

Executive Committee Range

The ECR comprises five major alkaline stratovolcanoes, extending 100 km in a north–south direction (Fig. 2). Doumani (1964) recognized a southward migration of volcanism and the consistent spacing between volcanic centers (15–20 km). Based on K–Ar geochronology, volcanic activity migrated from Whitney Peak (13.7 Ma) to Mount Waesche (<0.1 Ma) at an average rate of 0.7 cm/year (LeMasurier and Rex 1989). LeMasurier and Rex (1989) reported a narrow and nearly exclusive compositional range within each volcano and abrupt changes in petrological character between centers. Furthermore, they found little or no evidence for sequential chemical change in any single volcano. As a result of later, more extensive investigation of the ECR by WAVE, it has been shown that two of the volcanoes, Mount Sidley and Mount Waesche, display wide compositional arrays and distinctive evolutionary trends (Smellie et al. 1991).

Mount Sidley

The Mount Sidley massif rises approximately 2200 m above the present West Antarctic Ice Sheet and has an estimated exposed volume of greater than 200 km^3. It is a composite edifice, described by LeMasurier (1990c) as two volcanoes forming a closely coalesced doublet. The smaller (3 km wide), ice-filled caldera related to the older edifice ('Weiss volcano': González-Ferrán and González-Bonorino 1972) is north-east of the summit of Mount Sidley (Fig. 3). The younger volcano ('Sidley volcano': González- Ferrán and González-Bonorino 1972) contains an impressive caldera, 5 km across and >1200 m deep, which is partly filled by ice and breached on the south side (Fig. 3). This younger caldera exposes volcanic strata deep within the core of the volcano, including parts of two older volcanoes, the Weiss volcano and the 'Byrd volcano' (identified in this study) and their calderas. A 600 m high, 6 km long ice-covered plateau extends south from the Weiss Amphitheater (Figs. 3 and 4) and is rimmed by lavas, domes and subordinate pyroclastic deposits. Ice supplied to the plateau originates in the northern headwall of the Weiss Amphitheater and along with rafted caldera wall debris is drained to the south-east by the Parks Glacier. Prominent englacial moraines are developed at the

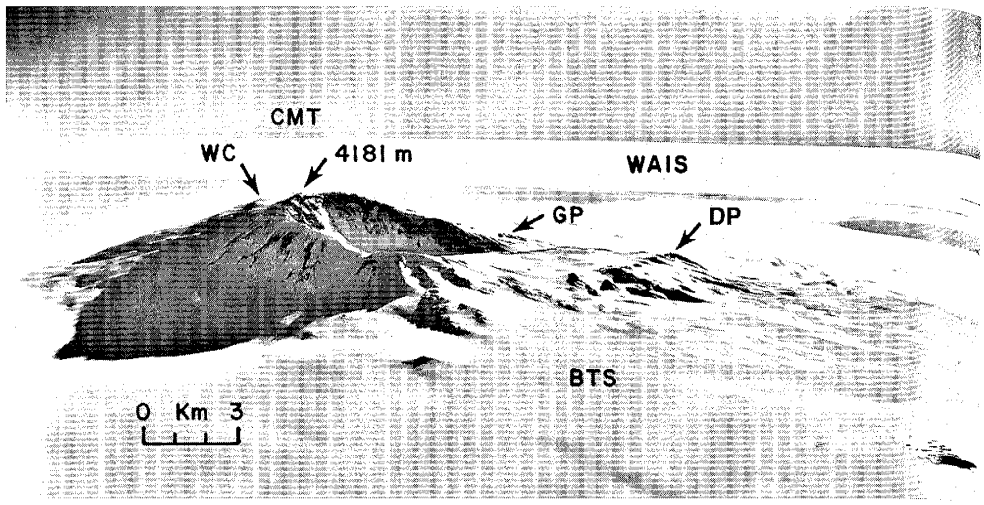

Fig. 3 US Navy aerial photograph (TMA 571 F33 0169) of Mount Sidley looking ENE. Note ice-covered plateau extending south of the main Mount Sidley caldera and the smaller, ice-filled caldera (WC, Weiss caldera) just visible to the left of the summit. Abbreviations are as follows: DP = Doumani Peak; WAIS = West Antarctic Ice Sheet; BTS = Bennett Saddle; 'GP' = 'Gonzáles Peak'. The Crary Mountains (CMT) are visible on the horizon, approximately 200 km away

southern tip of Mount Sidley, where the Parks and the Bennett Saddle glaciers converge and coalesce.

Previously published information on Mount Sidley is based on field observations from two brief visits (Doumani and Ehlers 1962; LeMasurier 1972) and five geochemical analyses (LeMasurier 1990c). Three samples collected from different lava units were dated by the K–Ar method at 4.75 ± 0.40, 4.75 ± 0.30 and 4.75 ± 0.28 Ma (LeMasurier and Wade 1976). Based on this information, LeMasurier (1990c) suggested that the development of Mount Sidley occurred within the analytical uncertainty of K–Ar dating (about 0.7 Ma).

Field relationships

Eruptive environment

Most (>90%) of the exposed rocks on Mount Sidley are lava flows, many of which exhibit brecciated, reddened tops and bases indicative of subaerial eruption and emplacement. Volumetrically minor pyroclastic deposits (flow, fall and surge) were emplaced under essentially 'dry' conditions with the exception of a single, phreatomagmatic tuff cone sequence located at Doumani Peak (Figs. 3 and 4), which is largely comprised of wet base-surge and associated fall deposits. There are also minor occurrences of pillowed and/or hyaloclastic lava bases, hyaloclastite and hyaloclastic sediments, which are interpreted as evidence for a limited interaction between magma and ice or snow in valleys and craters during the development of Mount Sidley.

The predominance of subaerial volcanic rocks in the Mount Sidley succession indicates that a continental ice sheet was not present at the level of the exposures seen today. However, we do not preclude an early, subglacial history for Mount Sidley.

Geophysical studies indicate that the volcanoes of the ECR are constructed on bedrock with an elevation of about 500–1000 m above sea level (Drewry 1983), suggesting a present day ice thickness greater than 1 km. Thus a significant unexposed volume of Mount Sidley (>300 km^3) is obscured beneath the present West Antarctic Ice Sheet. A Late Miocene–Early Pliocene ice sheet in MBL has been suggested by LeMasurier (1972, 1990b; see also LeMasurier and Rex 1983; LeMasurier et al. 1994) and may have interacted with early Mount Sidley volcanism. We postulate that the early development of Mount Sidley could have been subglacial and structurally and lithologically analogous to sequences described in subglacially erupted volcanoes in Antarctica and elsewhere (e.g. Jones 1970; McIntosh et al. 1985, 1991; Smellie et al. 1993a; Smellie et al. 1993b).

Stratigraphy

Based on geological mapping (Fig. 4) and a detailed description of the internal stratigraphy exposed in the caldera wall (Fig. 5), we have compiled a composite volcanic succession shown in Fig. 6. A sequence of three major volcano-building episodes, each culminating in the formation of a summit caldera, are recognized; respectively, the Byrd, Weiss and Sidley volcanoes (Fig. 5a). Effusion from multiple vents on the southern flanks produced volumetrically subordinate but diverse lithologies that overlie the proceeding successions. In the following description, volcanic rock names are based on major element analyses and are classified using the total alkali–silica (TAS) diagram of Le Maitre (1989).

The lowest exposed sequence at Mount Sidley (Byrd volcano) is found at the base of the eastern wall of the Weiss Amphitheater (Fig. 5a) and includes several small exposures on the south-east flank. The sequence consists of thick (ca. 20 m), gray to reddish brown tephriphonolite and phonolite lavas and lava base breccias containing distinctive, euhedral anorthoclase phenocrysts up to 8 cm in length (Fig. 7a). Capping the lava sequence of the Byrd volcano is a sinuous and laterally continuous unconformity (U_1, Fig. 5), draped by interbedded yellow brown epiclastic and hyaloclastic sedi-

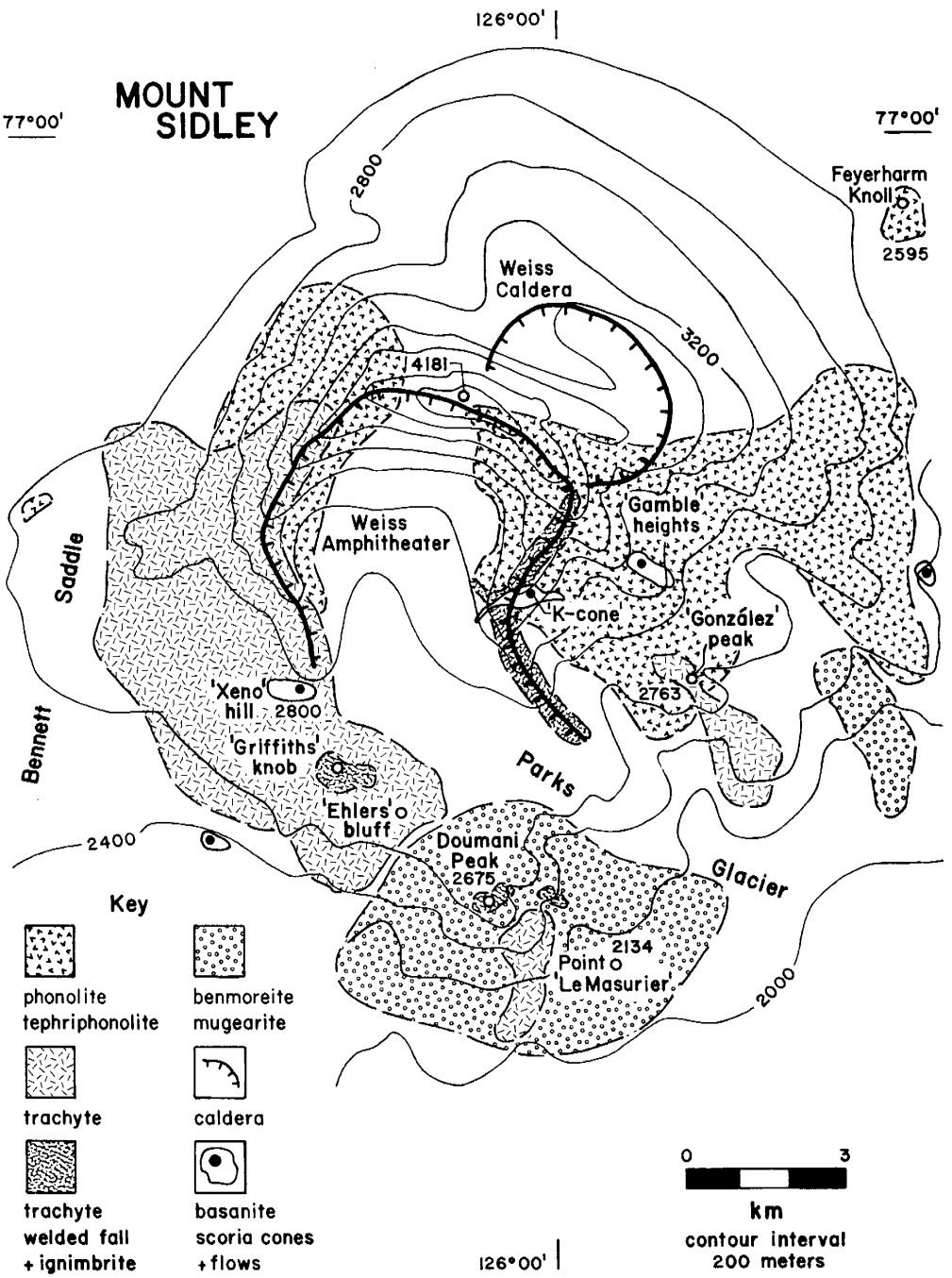

Fig. 4 Topographic map of Mount Sidley illustrating simplified distribution of major volcanic rock compositions. The present Sidley caldera (Weiss Amphitheater) and Weiss Caldera are represented by bold, hatchured curves. Informal place names are designated by single quotation marks (e.g. 'Xeno hill'). All elevations in meters

ments (Fig. 5b). In the eastern wall, the unconformity dips steeply (30–40° NW) and is considered to be the margin of an early caldera (Fig. 5a).

A series of thin (ca. 10 m), gray and relatively crystal-poor phonolite lavas of the Weiss volcano onlap the basal succession. The lava flow sequence is thickest (300 m) where it fills the older Byrd caldera and the flows are interbedded with thin (ca. 5 m) sedimentary units, some of which contain reworked, pumice-rich, pyroclastic material. Deposited against the Byrd caldera margin is a thick (up to 200 m) sequence of hyaloclastite breccias and intercalated bedded sediments. In the upper portion of the section, a striking red and white altered carapace breccia is considered to be the result of a localized hydrothermal system formed during the shallow emplacement of a benmoreite intrusion. The lavas of the Weiss volcano are capped by yellow, thin-bedded pumice-bearing sediments which are deformed and down-faulted along the margin of a younger caldera (U_2; Weiss caldera: see Figs. 3, 4 and 5a, 5b). The Weiss caldera is, in turn, filled by a series of dark gray to black, porphyritic phonolite lavas of the Sidley volcano, which are well exposed in the amphitheater wall below the summit, on the north-west outer slopes, the base of the western caldera wall and along the eastern caldera rim.

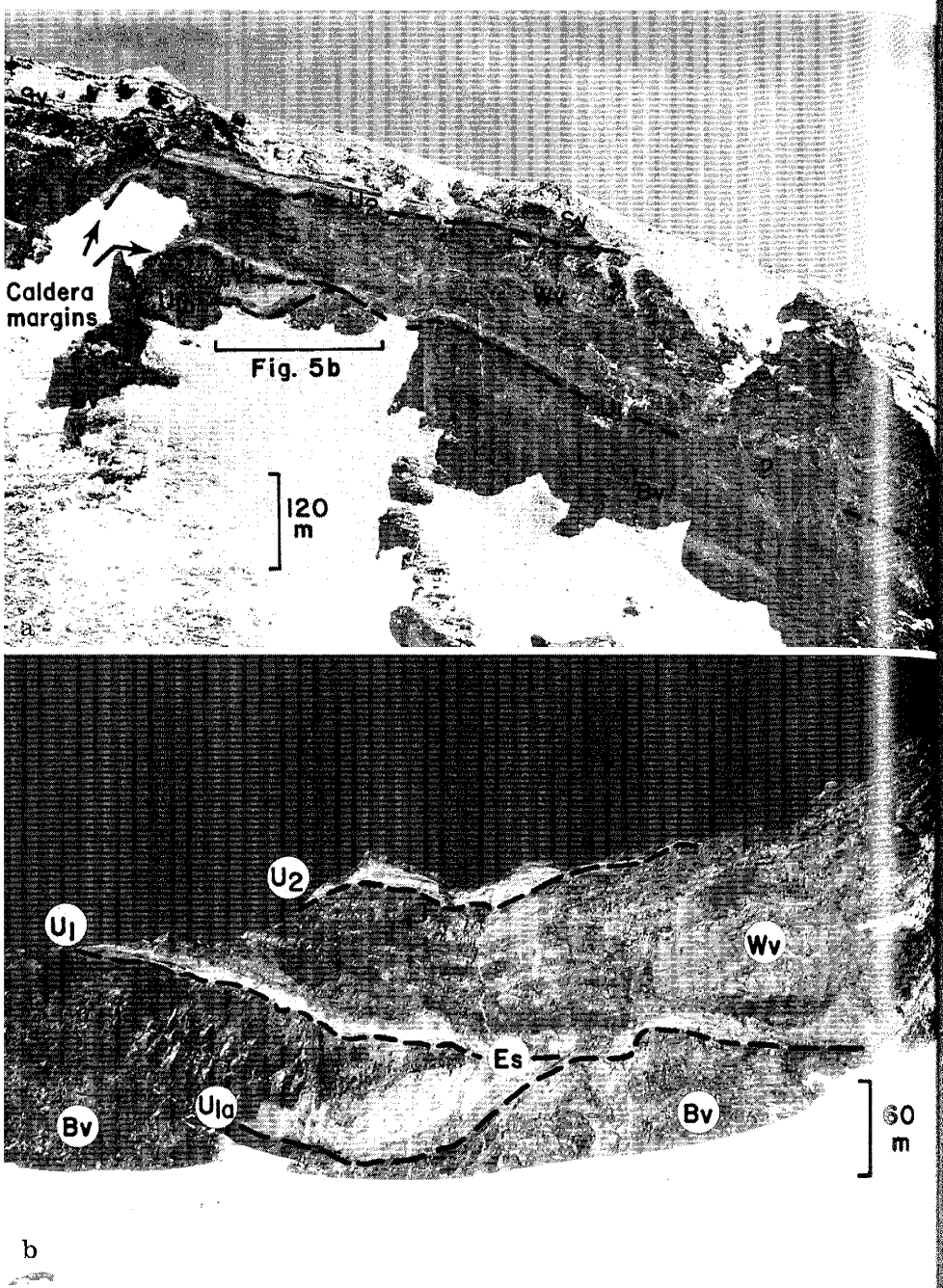

Fig. 5 Photographs of south-east-caldera wall. **a** Unconformities (U_1 and U_2) separating major volcano building episodes (Bv, Byrd volcano; Wv, Weiss volcano; Sv, Sidley volcano). Epiclastic sediments lie on top of unconformities and in places are faulted down and or drape older caldera margins of the Byrd and Weiss volcanoes. U_{1a} represents the surface of an early crater of the Byrd volcano. **b** Photographic detail of lava flows and lava base breccias of the phonolitic Weiss volcanic succession (WV); tephriphonolitic lavas of the Byrd volcano (BV) and bedded epiclastic sediments (Es) deposited upon unconformities; U_2, U_1, and U_{1a}, as in Fig. 5a

In the west amphitheater wall and on the outer western slopes, a widespread, black, poorly welded fall deposit overlies the tephriphonolite–phonolite lava flow successions of the Weiss and Sidley volcanoes, marking a significant petrological transition towards predominately trachyte magmas. The black, monomict fall is compositionally heterogeneous (ranging from phonolite to trachyte) and it is superseded by thick, multiple trachyte flows with a complicated eruptive history. Some of the flows on the south-west slopes are dome-like, with steep-dipping fluidal banding and lithic-rich carapace breccias. Several trachyte domes and flows contain prominent, dark colored basaltic enclaves with vesicular (miarolitic) textures and strongly crenulate margins embayed by the trachyte host (Fig. 7b). The textural relationships are characteristic of magma commingling (Gamble 1979).

The trachyte flows on the west flank are draped by a conspicuous red and black colored, welded pyroclastic fall deposit with abundant lithic clasts. Along the eastern caldera rim (up to 3700 m; Fig. 4) another, lithic-rich (ca. 5%), welded trachyte fall deposit overlies, unconformably, tephriphonolite and phonolite lavas of the Sidley volcano. This khaki colored pyroclastic fall deposit is in sharp, conformable contact with an overlying yellow colored, pumice-rich, unwelded ignimbrite

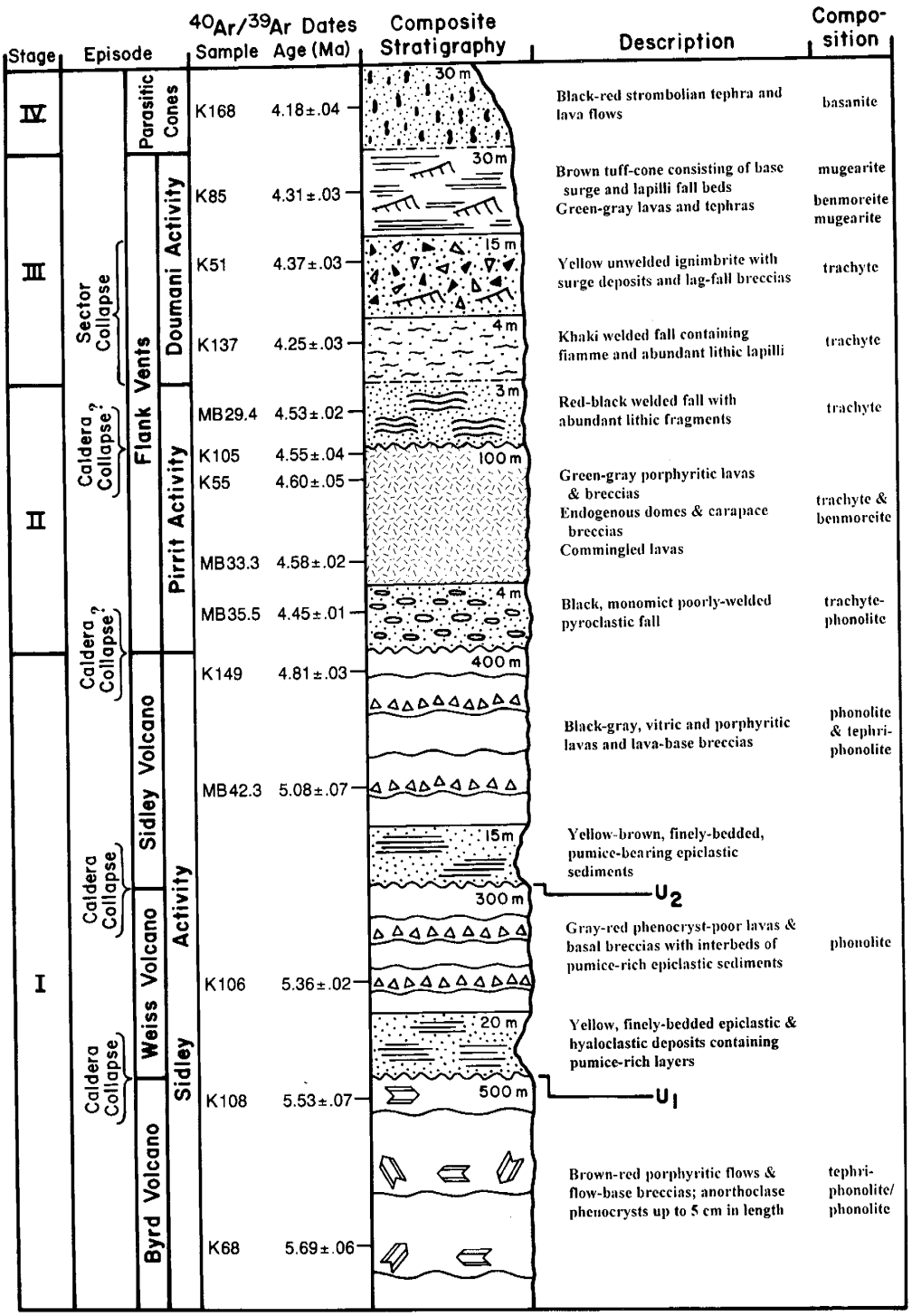

Fig. 6 Generalized, composite stratigraphic column for Mount Sidley, compiled from mapped wall sections and flank exposures. Rock compositions determined from major element analyses and classified using the total alkali versus silica diagram of Le Maitre (1989). Samples dated by the $^{40}Ar/^{39}Ar$ incremental heating technique are arranged in their relative stratigraphic positions. Also shown are major volcano-building episodes and volcanic stages (see discussion)

and associated surge deposits. The trachytic pyroclastic flow varies in thickness from 3 to 15 m and contains pumice fragments as large as 30 cm, together with lithic clasts (volcanic and subvolcanic origin), ranging in size from lapilli to blocks. In the south-eastern wall of the Weiss Amphitheater the ignimbrite is intimately associated with an overlying co-ignimbrite breccia. The co-ignimbrite breccia is extremely coarse and lithic-rich, containing ignimbrite matrix-supported angular blocks (up to 3 m) of volcanic lithologies, including the khaki

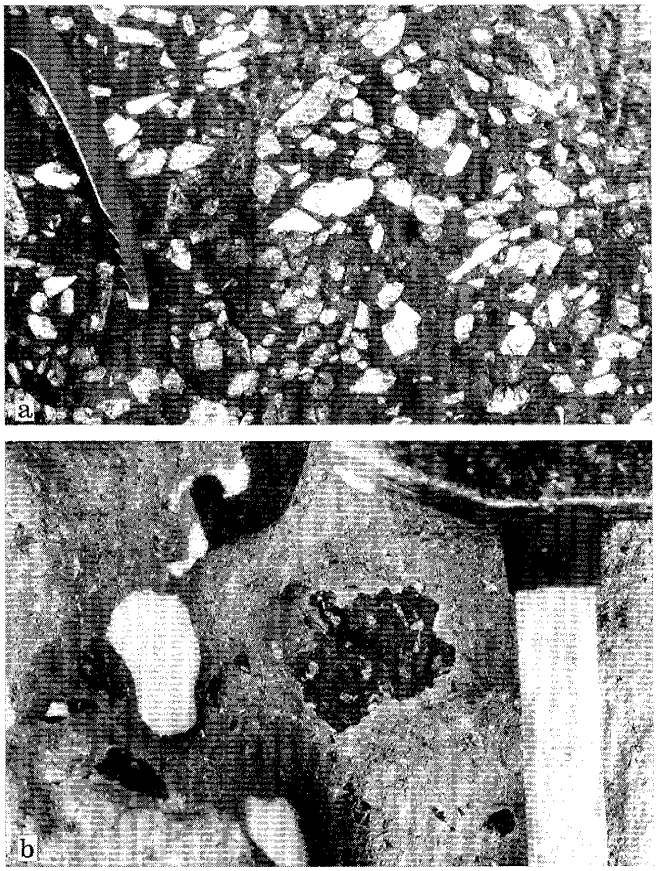

Fig. 7 **a** Anorthoclase crystals in a tephriphonolite lava near the base of the Byrd volcanic succession; larger phenocrysts are approximately 5 cm in length. Macroscopically similar anorthoclase phonolites occur on Mount Erebus in the western Ross Sea and on several other Marie Byrd Land volcanoes. **b** Basaltic enclave (about 10 cm diameter) within trachyte; crenulate margin suggests comingling of the two lavas

colored welded fall. The ignimbrite appears to have flowed within and mantled the southern walls of the breached caldera, but is absent above 3200 m and within the Weiss Amphitheater. Based on their field relationships and distribution, the khaki welded fall and yellow ignimbrite (including co-ignimbrite lithofacies) are considered to be coeval with the early stages of collapse which created the Weiss Amphitheater. Following their eruption, trachyte volcanism ceased. Subsequently, several small volume benmoreite and mugearite flows and domes were erupted on the southern flank of Mount Sidley (Fig. 4). Within this period, a mugearite tuff cone was formed at Doumani Peak, consisting of surge and fall tephra with abundant accretionary and armored lapilli.

The final phase of eruptive activity at Mount Sidley produced small basanite Strombolian cones and associated flows, some of which contain crustal and mantle xenoliths. Lavas from K-cone flowed into the Weiss Amphitheater through a breach in the caldera wall (Fig. 4) and are thus clearly post-caldera in origin.

$^{40}Ar/^{39}Ar$ dating

Methods

A total of 13 anorthoclase separates and one basanite sample from Mount Sidley were dated using the $^{40}Ar/^{39}Ar$ incremental heating technique. The samples encompass nearly the full range of rock compositions and stratigraphic positions within the Mount Sidley succession (Fig. 6). Anorthoclase separates (150–250 μm grain size) were prepared using conventional magnetic and heavy liquid techniques, then hand-picked to >99.9% purity. Anorthoclase separates from pyroclastic deposits (samples MB35.5, MB29.4, K137, K51 and K85) were extracted from pumice-fiamme and bomb material. Basanite matrix was hand-picked to obtain the fine-grained, holocrystalline groundmass devoid of phenocrysts and xenolithic material. Samples of anorthoclase (80–200 mg each) and basanite (360 mg) were sealed in aluminum capsules and packaged in silica vials along with vertically and radially distributed interlaboratory $^{40}Ar/^{39}Ar$ standards, MMhb-1 (McClure Mountain hornblende, 520.4 Ma; Samson and Alexander 1987) and FCT-1 (Fish Canyon Tuff sanidine, 27.83 Ma, Kunk et al. 1985) to monitor neutron flux. Packages were irradiated for 15 hours at 1 MW in the low gradient center line area of the central thimble facility of the TRIGA reactor, United States Geological Survey (USGS) in Denver, Colorado (Dalrymple et al. 1981).

Incremental heating analyses were performed at USGS $^{40}Ar/^{39}Ar$ laboratories in Reston, Virgina and Denver. Extraction procedures involved initial degassing of each sample at 600° C in a low blank resistance furnace. Samples were incrementally heated for 10–15 min intervals in five to ten temperature steps. In Reston, the extraction system blank at furnace temperatures of 1400° C was between 4.0×10^{-15} and 4.5×10^{-14} mol ^{40}Ar. Argon was analyzed using an electron multiplier on a VG-Micromass 1200B spectrometer with a detection limit of 6.6×10^{-17} mol. In Denver, the extraction system blank is 8×10^{-14} mol ^{40}Ar at furnace temperatures of 1250° C. Gas fractions were analyzed using the Faraday cup on a Mass Analyzer Products, 215 series spectrometer with a detection limit of 1×10^{-17} mol argon.

Sample ages were calculated from gas fractions comprising the flat portion of the age spectrum, or plateau as defined by Fleck et al. (1977). Plateaus within age spectra are composed of two or more contiguous gas fractions that make up over 50% of the total ^{39}Ar released and must be indistinguishable at the 95% confidence level based on the critical value test derived by Dalrymple and Lanphere (1969). Plateau ages were calculated by weighting the age of each plateau gas fraction according to the inverse of its analytical variance. The uncertainty of each plateau age was calculated by quadratically combining the ages with the measure

Table 1 Representative $^{40}Ar/^{39}Ar$ age spectra data

Temperature (°C)	$^{40}Ar/^{39}Ar$	$^{37}Ar/^{39}Ar$	$^{36}Ar/^{39}Ar$	^{39}Ar (%)	$^{40}Ar^*$ (%)	^{39}Ar (mol)	K/Ca	Apparent age (Ma) $\pm 1\sigma$
MB33.3 (anorthoclase; $J=0.001849$; wt. = 0.1490 g; RD84; Reston)								
825	1.837	8.72×10^{-3}	1.64×10^{-3}	8.8	73.7	9.50×10^{-14}	59.6	4.51 ± 0.06
900	1.422	8.62×10^{-3}	2.0×10^{-4}	7.5	95.9	8.10×10^{-14}	60.3	4.54 ± 0.08
975	1.388	8.65×10^{-3}	4.0×10^{-5}	10.1	99.2	1.08×10^{-13}	60.1	4.59 ± 0.06
1050	1.390	9.19×10^{-3}	4.0×10^{-5}	14.7	99.1	1.58×10^{-13}	56.6	4.59 ± 0.04
1125	1.400	9.66×10^{-3}	7.0×10^{-5}	23.2	98.5	2.50×10^{-13}	53.8	4.59 ± 0.03
1175	1.379	8.96×10^{-3}	9.0×10^{-5}	26.7	98.1	2.87×10^{-13}	58.0	4.51 ± 0.02
1250	1.405	8.72×10^{-3}	2.0×10^{-5}	7.7	99.5	8.30×10^{-14}	59.6	4.66 ± 0.07
1400	1.456	1.53×10^{-2}	9.0×10^{-5}	1.3	98.1	1.40×10^{-14}	34.0	4.76 ± 0.36
Total gas								4.57
plateau	825–1125			64.3				4.58 ± 0.02
M35.5 (anorthoclase; $J=0.003396$; wt. = 0.3580 g; RD79; Reston)								
925	1.870	3.001×10^{-2}	4.03×10^{-3}	2.1	36.3	2.60×10^{-13}	17.3	4.15 ± 0.10
1000	0.875	2.914×10^{-2}	5.10×10^{-4}	7.8	82.6	9.79×10^{-13}	17.8	4.42 ± 0.03
1060	0.774	2.830×10^{-2}	1.60×10^{-4}	12.0	94.0	1.50×10^{-12}	18.4	4.45 ± 0.02
1110	0.778	2.739×10^{-2}	1.70×10^{-4}	12.2	93.6	1.53×10^{-12}	19.0	4.46 ± 0.02
1160	0.775	2.694×10^{-2}	1.70×10^{-4}	11.2	93.6	1.40×10^{-12}	19.3	4.44 ± 0.01
1245	0.765	2.676×10^{-2}	1.20×10^{-4}	19.3	95.5	2.41×10^{-12}	19.4	4.47 ± 0.01
1350	0.776	2.707×10^{-2}	1.30×10^{-4}	26.2	94.9	3.28×10^{-12}	19.2	4.51 ± 0.01
1525	0.842	2.828×10^{-2}	3.50×10^{-4}	9.3	87.9	1.17×10^{-12}	18.4	4.53 ± 0.02
Total gas								4.47
plateau	1000–1245			62.5				4.45 ± 0.01
K106 (anorthoclase; $J=0.001198$; wt. = 0.0823 g; Denver)								
625	5.150	0.206	8.601×10^{-3}	4.3	50.1	7.23×10^{-14}	2.5	5.58 ± 0.50
750	8.400	6.173×10^{-2}	1.751×10^{-3}	29.3	29.7	4.88×10^{-13}	8.4	5.38 ± 0.02
900	2.716	5.882×10^{-2}	8.172×10^{-4}	36.6	90.6	6.09×10^{-13}	8.8	5.33 ± 0.04
1025	2.691	6.788×10^{-2}	8.236×10^{-4}	19.7	91.0	3.28×10^{-13}	7.7	5.30 ± 0.05
1125	2.915	7.690×10^{-2}	1.193×10^{-3}	6.3	87.4	1.04×10^{-13}	6.8	5.51 ± 0.39
1250	6.160	9.217×10^{-2}	1.176×10^{-2}	2.3	43.3	3.89×10^{-14}	5.6	5.76 ± 0.98
1450	14.797	0.532	4.329×10^{-2}	1.5	13.7	2.45×10^{-14}	1.0	4.38 ± 0.89
Total gas								5.36
plateau	750–1025			85.6				5.36 ± 0.02
K149 (anorthoclase; $J=0.001217$; wt. = 0.1001 g; Denver)								
625	2.891	0.546	2.385×10^{-3}	14.2	75.2	1.48×10^{-13}	1.0	4.78 ± 0.17
750	4.449	0.465	7.931×10^{-3}	21.4	47.2	2.22×10^{-13}	1.1	4.61 ± 0.13
925	2.473	0.444	9.296×10^{-4}	34.3	88.5	3.57×10^{-13}	1.2	4.82 ± 0.03
1100	2.504	0.457	1.353×10^{-3}	14.7	84.5	1.53×10^{-13}	1.1	4.66 ± 0.21
1250	3.342	0.498	3.805×10^{-3}	10.0	55.5	1.04×10^{-13}	1.0	4.81 ± 0.34
1450	3.968	1.818	7.477×10^{-3}	5.3	44.0	5.55×10^{-14}	0.3	3.84 ± 0.30
Total gas								4.69
plateau	625–1250			94.7				4.81 ± 0.03

Explanation: Each data set is preceded by sample number, mineral, irradiation parameter (J), sample weight, irradiation batch number for Reston samples and USGS laboratory. Columns in data sets give temperature of incremental heating steps, ratios of Ar isotopes (^{40}Ar = initial and radiogenic, ^{39}Ar = potassium-derived, ^{37}Ar = calcium-derived, ^{36}Ar = initial), % of total ^{39}Ar in heating steps, radiogenic yield of ^{40}Ar, moles of potassium-derived ^{39}Ar, K/Ca ratio calculated from $^{37}Ar/^{39}Ar$ ratio, sample age and 1σ error. Lines following each data step show total gas K/Ca and age, and plateau temperature range, ^{39}Ar per-cent, age and error (method of Fleck et al. 1977). Results of all Mount Sidley $^{40}Ar/^{39}Ar$ incremental heating analyses are available through K. Panter.

uncertainty in the irradiation parameter J ($\pm 0.25\%$) and uncertainties in isotopes produced by interfering reactions during irradiation (Dalrymple et al. 1981).

Results

Representative $^{40}Ar/^{39}Ar$ incremental heating results for Mount Sidley volcanic rocks are compiled in Table 1 and age spectra are presented in Fig. 8. $^{40}Ar/^{39}Ar$ plateau ages of the lowermost (sample K68, 5.68 ± 0.06 Ma) and the uppermost (sample K168, 4.18 ± 0.04 Ma) volcanic units in the exposed stratigraphic sequence indicate a 1.5 million year life span of Mount Sidley volcanism (Fig. 6). Each of the 14 samples satisfies the plateau age requirements discussed earlier. Most plateaus ($n=10$) contain 70–100% of the total ^{39}Ar released and nearly all weighted-mean pla-

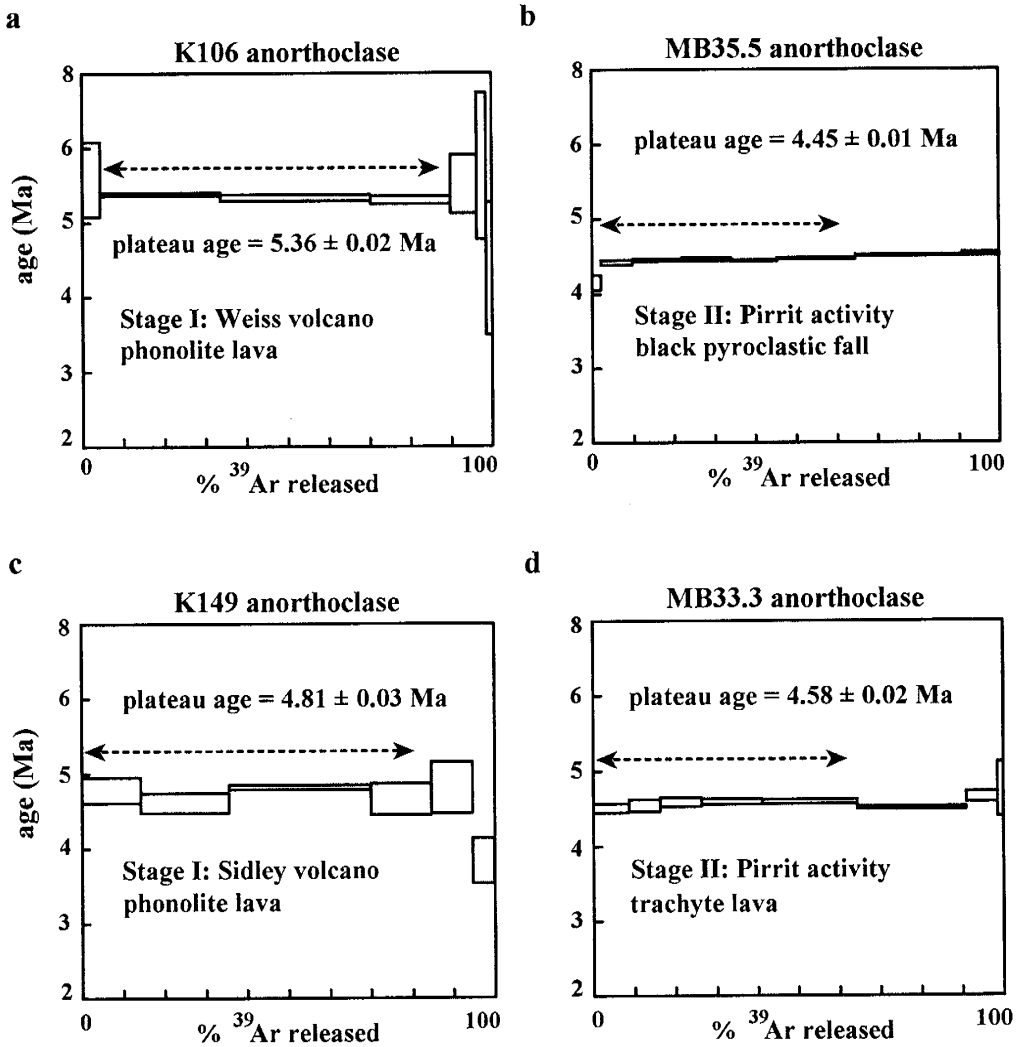

Fig. 8a–d Representative $^{40}Ar/^{39}Ar$ age spectra from Mount Sidley anorthoclase. The width of each incremental heating step is proportional to its analytical uncertainty. The plateau age of MB35.5 (**b**) is young relative to its stratigraphic position (see text), yet the age spectrum is concordant, indicating that the sample has remained thermally undisturbed

teau ages are within 1σ of their mathematically recombined total qcs ages.

Plateau age analysis has been used in this study because many samples show high radiogenic yields ($^{40}Ar^* \geqslant 90\%$) of individual gas fractions, resulting in excessive errors in the slope and intercept on isotope correlation plots. Evaluation of incremental heating results by isochron analysis (for samples with relatively high precision, $<1\%$, and regression line fit parameters equivalent to MSWD $\leqslant 2$) indicate only trapped atmospheric argon. High precision isochron ages agree within analytical uncertainty (1σ) with plateau ages.

The 14 dated samples from Mount Sidley display rather simple $^{40}Ar/^{39}Ar$ age spectra and their interpretation is straightforward. Individual weighted-mean plateau ages show a 1σ precision ranging from $\pm 0.3\%$ to 1.4% (± 0.01–0.07 Ma). In the following discussion, $^{40}Ar/^{39}Ar$ age determinations allow a general resolution of volcanic episodes that approach 100000 years in duration.

Discussion

Volcanic evolution of Mount Sidley

Samples dated by the $^{40}Ar/^{39}Ar$ incremental heating method show an order of magnitude increase in precision over previous conventional K–Ar ages and reveal a minimum time frame of 1.5 million years of volcanic activity, which is significantly longer than the duration proposed by LeMasurier (1990c). Beyond extending the time-interval of Mount Sidley activity, high precision $^{40}Ar/^{39}Ar$ ages provide a quantitative chronology of its volcanic history. In Fig. 6, $^{40}Ar/^{39}Ar$ plateau ages are presented within the generalized stratigraphy. All of the samples except one are consistent within analytical uncertainty (2σ) with the stratigraphy deduced from field relationships. The discordant sample

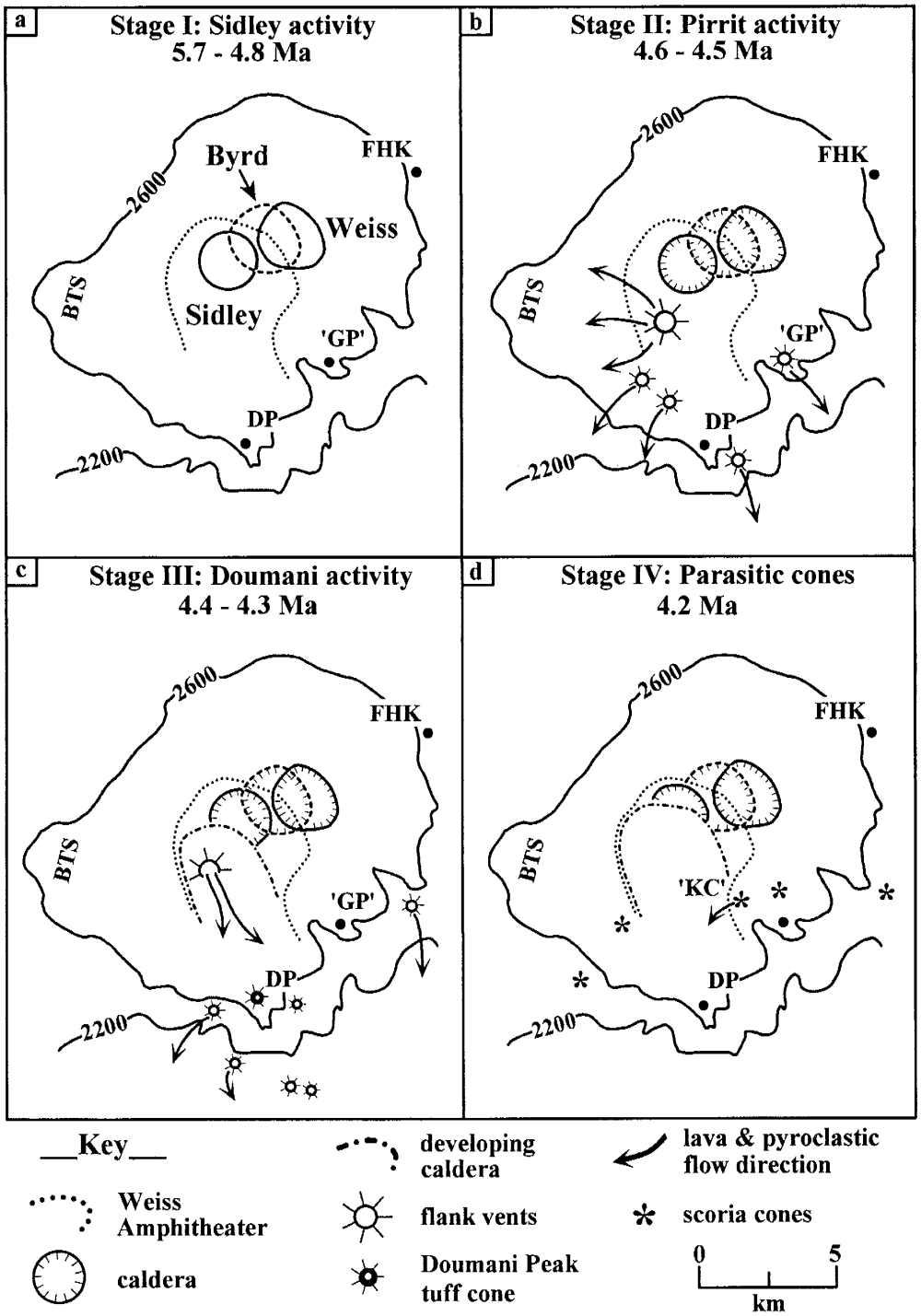

Fig. 9a–d Schematic sketch map illustrating the geological evolution of the Mount Sidley edifice. **a** Stage I: Sidley activity (5.7–4.8 Ma); development of three phonolitic central vent volcanoes; Byrd, Weiss and Sidley, each forming a summit caldera. DP = Doumani Peak; 'GP' = 'González peak'; BTS = Bennett Saddle; FHK = Feyerharm Knoll. **b** Stage II: Pirrit activity (4.6–4.5 Ma); wide dispersion of trachytic activity south of Stage I volcanoes including the construction of a major center on the south-west flank of the Sidley volcano (stage I). The orientation of lava and pyroclastic flow directions suggest a topographic barrier to the north-east, created by the stage I edifice. **c** Stage III: Doumani activity (4.4–4.3 Ma); explosive eruption(s) associated with sector collapse of the southern flank issued an expansive trachytic welded fall (Fig. 7e) and unwelded ignimbrite. This was closely superseded by phreatomagmatic activity at Doumani Peak and multicenter effusion of intermediate lavas and tephras to the south and east. **d** Stage IV: parasitic cones (4.2 Ma); cones of basanite scoria were emplaced in an arcuate pattern around the southern portion of the volcano. Lava from one cone ('KC' = 'K-cone') flowed over the caldera wall and has remained relatively unmodified by erosion. Further enlargement of the breached caldera in the northern headwall was controlled by erosion along older caldera structures

MB35.5 (4.45 ± 0.01 Ma), was collected from a black pyroclastic fall deposit in the west caldera wall where its widespread occurrence and distinctive lithology make it a conspicuous, mappable datum. Two other dated samples, MB42.3 (5.08 ± 0.07 Ma) and MB33.3 (4.58 ± 0.02 Ma), were collected from the same section, below and above MB35.5, confirming its unreasonably young relative age. The anorthoclase has not suffered appreciable ^{40}Ar loss (Fig. 8b) and the age discrepancy is apparently analytical.

Stage I: Sidley activity (5.7–4.8 Ma)

The first stage of Mount Sidley development constitutes the majority of the present Mount Sidley massif and extends over approximately one million years of eruptive activity. In this period three central edifices, the Byrd (≈ 5.7–5.5 Ma), Weiss (≈ 5.4 Ma) and Sidley (≈ 5.1–4.8 Ma) volcanoes, were built concurrently and partly superimposed, showing an overall displacement in activity towards the south-west (Fig. 9a). The con-

struction of each volcano was followed by caldera formation and erosion, signifying substantial periods of inactivity between volcano-building events. All three volcanoes are dominated by subaerially deposited tephriphonolite–phonolite lavas and flow breccias, although occurrences of hydroclastic lithofacies in the lower portion of the Weiss sequence indicate limited glacio-volcanic interaction during its early activity (Fig. 6).

Calderas of the Byrd, Weiss and Sidley volcanoes overlap and are ENE–WSW aligned, passing just south of the present summit of Mount Sidley (Fig. 9a). An ancestral Sidley caldera is predicted and its location has been estimated by the mapped distribution and thickness variations of its erupted products. It is suggested that each caldera formed by small-scale eruptive activity. This is supported by the absence of primary pyroclastic lithologies within stage I, precluding caldera formation by large-scale ignimbrite and Plinian eruptions (e.g. Krakatoa, AD 1883 and Somma-Vesuvius AD 79). Some explosive activity linked to caldera formation is suggested by the presence of pumice-bearing epiclastic facies overlying the Byrd and Weiss successions (upon the U_1 and U_2 surfaces, Fig. 5), but the volume of erupted products is much less than the estimated volumes of the calderas produced and much of the tephra may have been lost to erosion. The volume discrepancy may be explained by the withdrawal of magmas within a crustal fracture system by regional tectonic movement. Caldera collapse in response to magma drainage at depth has been proposed for several volcanic centers, including the Fernandia volcano (Simkin and Howard 1970), Askja volcano (Sigurdsson and Sparks 1978) and the Suswa volcano (Skilling 1993).

We estimate the total volume of magma erupted during this period of Mount Sidley activity to be about 180 km^3 (about 90% of the exposed volume above the 2000 m continental ice level), yielding an average output rate of ca. 0.2 km^3/ka. It should be noted that this average effusion rate does not account for dormant periods and thus the rate of construction for the individual volcanic centers would have been greater.

Stage II: Pirrit activity (4.6–4.5 Ma)

The second stage is distinguished by a significant petrological change to trachyte magmas (Fig. 6), accompanied by a shift of the eruptive centers to the south (Fig. 9b). The eruptive style also changed with the formation of several small, widely distributed centers flanking the large central vent massif. During Pirrit activity, thin flows (5–10 m thick) issued from several small vents south of Doumani Peak and on the south-east flank near González Peak (Fig. 4). Concurrently, complex multiple vent activity between Xeno hill and Ehlers bluff produced thick (>50 m) trachyte lavas and endogenous domes, as well as lavas formed by the comingling of trachyte and basaltic magmas. A substantial outpouring of material on the western flank is related to eruptions from a single monogenetic vent constructed on the southern slopes of the Sidley volcano. The products of this eruptive phase comprise a basal black, phonolitic–trachytic pyroclastic fall deposit that passes up into a thick (ca. 70 m) cogenetic unit of alternating foliated trachyte flows and carapace breccias. Slightly younger (sample MB29.4, 4.53 ± 0.02 Ma) explosive activity, possibly from the same vent, deposited a red and black, lithic-rich welded fall found exclusively in western exposures. This trachyte fall unit is the youngest eruptive phase of the Pirrit period and may represent a caldera-forming event. The Sidley massif was largely undissected and was a major topographic barrier controlling the distribution of stage II volcanic sequences (Fig. 9b).

Age determinations within the second stage of Mount Sidley volcanism are indistinguishable within analytical uncertainty (Fig. 6). Samples obtained from near the base (trachyte lava; MB33.3, 4.58 ± 0.02) and top (red–black welded fall; MB29.4, 4.53 ± 0.02) of the monogenetic sequence allow a rough estimate of < 90 ka for the duration of stage II. An estimated total eruptive volume of 18 km^3 (approximately 9% of the exposed Mount Sidley massif) suggests a minimum construction rate of about 0.2 k^3/ka, similar to the output rate during stage I.

The presence of multiple vents, comingling of lavas and the variability in eruptive style strongly suggest an intricate magma plumbing system during stage II. This model is in sharp contrast with the proceeding eruptive history of Mount Sidley, in which the constituent volcanoes were built by eruptions from major central conduit edifices. Because of the dispersion of stage II vents an accurate measure of the geographical displacement is speculative. Based on the volume and distribution of eruptive products, the bulk of stage II activity was centered in the vicinity of Griffiths knob/Xeno hill (Fig. 4) and thus an empirical 5–6 km southward migration between stages I and II is postulated.

Stage III: Doumani activity (4.4–4.3 Ma)

The beginning of this period was marked by pyroclastic eruptions of trachytic magmas depositing a lithic-rich khaki colored welded fall unit closely followed, conformably, by a yellow unwelded ignimbrite and associated surge tephras and co-ignimbrite breccias (Fig. 6). We speculate that these pyroclastic deposits were erupted during a single episode. The welded fall (K137) and ignimbrite (K51) yield ages of 4.25 ± 0.03 and 4.37 ± 0.03 Ma, respectively, which is reverse of their observed stratigraphic positions (Fig. 6); however, the two ages are indistinguishable at 2 σ uncertainty. A period of inactivity between stage II (4.53 Ma; sample MB29.4, red–black welded fall) and stage III (4.37 Ma; sample K51, yellow ignimbrite) may have lasted 100–200 ka.

Explosive activity at the onset of stage III was probably contemporaneous with the initial collapse of the present day breached Sidley caldera (Weiss Amphitheater). An explosive origin for the caldera was favored by Doumani (1964) and González-Ferrán and González-Bonorino (1972). LeMasurier (1990c) described the broad plateau south of the caldera opening (Fig. 3) as a pyroclastic apron emplaced during a major phreatomagmatic event related to the caldera collapse. In contrast, our detailed mapping has shown that the plateau is composed primarily of lava flows and minor pyroclastic materials, including a small tuff cone at Doumani Peak (Fig. 4).

The Mount Sidley massif shows many morphological similarities with recent volcanoes that have experienced major catastrophic landslide and paroxysmal eruption events such as Mount St Helens (Voight et al. 1981) and the Kamchatka volcanoes, Bezymianny (Gorshkov 1959) and Shiveluch (Gorshkov and Dubik 1970). In each modern event, mass movement and eruption of material excavated large (e.g. 1×4 km, Mount St Helens) horseshoe-shaped amphitheaters and produced substantial quantities (1–3 km^3) of volcaniclastic debris consisting of chaotic mixtures of predominantly non-juvenile (rockslide–avalanche debris) and juvenile (pyroclastic flows and tephra) material. Despite the topographic similarities with other volcanoes, avalanche–landslide deposits are absent at Mount Sidley and tephras associated with the collapse (khaki-welded fall and yellow ignimbrite) can only account for a small portion of material exhumed from the 5×5 km Weiss Amphitheater.

The formation of the present day Weiss Amphitheater is a likely result of both explosive landslide and erosional processes. We envisage an initial explosive episode (khaki-welded fall and yellow ignimbrite) accompanied by a sector collapse on the southern flank of the Sidley volcano around 4.3–4.4 million years ago (Fig. 9c). Volcaniclastic debris associated with the collapse was removed by ice flow on and around the volcano. Further enlargement of the newly formed breached caldera by mass movement processes was hastened by periodic intersection with older structures of the Sidley, Byrd and Weiss volcanoes. Glacial ice within the caldera basin continually carried away rock slide–avalanche debris to the south, probably along the present course of the Parks Glacier (Fig. 4). Erosion of the north-eastern headwall of the Weiss Amphitheater and glacial transport of debris continues to the present.

At Doumani Peak, the yellow ignimbrite (dated sample K51, 4.37 ± 0.03 Ma) is conformably overlain by a mugearitic hydrovolcanic tuff cone sequence dated at 4.31 ± 0.03 Ma (sample K85, Fig. 6). Formation of the tuff cone represents the only known phreatomagmatic activity on Mount Sidley and, together with multiple center activity issuing intermediate composition lavas and tephras to the south and east (Figs. 4 and 9c), represents the last significant magmatic pulse (<1% of the total exposed volume) at the volcano. The conformable relationship of pyroclastic deposits at Doumani Peak (the succession: welded fall→ignimbrite→tuff cone) and the indiscriminate ages within this stage, suggest a brief episode of volcanic activity, well within analytical uncertainty of $^{40}Ar/^{39}Ar$ dating (Fig. 6).

The broad shift in Mount Sidley volcanism towards the south terminates in the Doumani Peak area and shows a total geographical displacement between stage I activity (centred near the present summit of Mount Sidley) and the end of stage III to be approximately 9 km.

Stage IV: parasitic cones

Small basanite scoria cones characterize the final eruptive phase of Mount Sidley volcanism (Fig. 9d). Their crudely arcuate distribution may reflect a structural control by fractures in the subvolcanic basement. Three of the larger cones (Xeno hill, K-cone and Gamble heights; Fig. 4) contain xenoliths of mantle and lower crustal origin, suggesting that the melts ascended rapidly from depth. One xenolith-bearing cone (K-cone) erupted lavas which issued through a breach in the south-east caldera margin and flowed down the caldera wall; this is demonstrably post-caldera in origin (Fig. 9d). A dated whole rock sample from this cone confirms its post-caldera age at 4.18 ± 0.04 Ma and distinguishes this final stage from Doumani activity (Fig. 6).

Volcanic migration

Mount Sidley offers a unique record of spatial, temporal and petrological changes within a single alkaline volcano. Our detailed field observations, coupled with high precision $^{40}Ar/^{39}Ar$ age determinations, reveal a southward migration of volcanism at Mount Sidley at a rate of 0.6 cm/a. Furthermore, each major geographical relocation of volcanic activity (stages I–IV) corresponds with significant changes in magma composition. On a larger scale, the migration of volcanic activity within the ECR emulates that found at Mount Sidley. For example, the rate of migration calculated for ECR volcanism is nearly identical (0.7 cm/a) and abrupt changes in the composition of erupted magmas coincide with major southward displacement between successive centers (e.g. Mount Hampton→Mount Cumming →Mount Hartigan, etc. ...; Fig. 2). Hence a model explaining magmatic plumbing and structural controls affecting volcanism and magmatic evolution on the scale of Mount Sidley may yield information applicable to the entire ECR.

The close geographical proximity of compositionally contrasting volcanic centers at Mount Sidley and their systematic migration to the south are best explained by magmas held within an intricate plexus of conduits and chambers and their subsequent release by dilation of

pre-existing structures during fracture propagation (cf. LeMasurier and Rex 1989).

The long-lived (≈1 Ma) magmatic episode which constructed three major phonolitic–tephriphonolitic centers during stage I (Figs. 6 and 9c) suggests the formation of large and temporally discrete magmatic systems evolving compositionally similar magmas. In this stage, an overall shift in activity towards the south-west is marked by a small (2–3 km) displacement between central vent localities and may reflect the emplacement of discrete magma batches along an advancing fissure system. The tectonically induced fracture migration may have been assisted to some degree by magma injection (e.g. Spence and Turcotte 1985) and evidence for magma mixing and intermingling indicates that the reservoirs were able to communicate at times. For example, the explosive eruptions marking the beginning of Pirrit activity may have been initiated by magma mixing (e.g. Sparks and Sigurdsson 1977), producing the heterogeneous phonolitic–trachytic black-fall unit (Fig. 6). At other times, evidence for magma comingling in some stage II lavas indicates more limited interaction (Fig. 7b). Conversely, some proximal and coeval vents (e.g. stage III) appear to have evolved independently, suggesting the isolation of small systems. During the final stage of Mount Sidley volcanism, the eruption of xenolith-bearing basanite cones and associated lavas indicate a rapid ascent of magma along a pervasive structural trend. This last episode of tensional fracturing differs in its tectonomagmatic style from earlier stages where the periodic dilation of fractures released evolved magmas in pulses.

An overall decrease in volume and duration of activity with each successive stage of Mount Sidley volcanism may indicate fracture migration away from a principle source of magma supply. We suggest that propagating fractures encountered less extensive magma reservoirs within the crust as the tensional event shifted southward. This may coincide with the closure of an abyssal fracture system during regional tectonic movement (related to dome-centered radial tensional stresses which Kyle et al. (1991) attributed to a mantle plume), thereby 'cutting-off' a major source of magma supply to the crust from a deep-seated site of melt generation. Then, approximately two million years later and 15–20 km to the WSW of Mount Sidley, propagating tensional fractures released a new pulse of magma to the surface producing the rhyolitic volcano of Chang Peak (Fig. 2).

Conclusions

Mount Sidley is a complex, multicenter, polygenetic volcano of Early Pliocene age. It comprises at least three major overlapping stratovolcanoes (Byrd, Weiss and Sidley), together with several smaller centers, including minor late-stage monogenetic vents. Volcanic lithologies are dominated by subaerially emplaced lavas, indicating that the present Mount Sidley edifice was constructed above the level of a continental ice sheet. Hyaloclastic lithologies lying on the Byrd volcanic succession suggest local glacio-volcanic interaction within summit calderas and valleys on the volcano. Significant breaks in activity are indicated by the presence of at least two prominent unconformities (U_1 and U_2, Fig. 5) exposed in the present caldera wall suggesting that volcanic construction occurred over an extended period of time as a series of discrete magma pulses. This is confirmed by detailed $^{40}Ar/^{39}Ar$ geochronology, which shows that Mount Sidley was built in successive stages over 1.5 million years (5.7–4.2 Ma).

At Mount Sidley, major changes in the rock composition are coincident with the geographical relocation of volcanic activity southward at a rate of 0.6 cm/a. Variations in erupted magma composition consist of early phonolitic lavas issued in the northern portion of the edifice (stage I: 5.7–4.8 Ma), superseded by the eruption of trachytic domes, lavas and pyroclastic materials roughly 5–6 km to the south (stage II: 4.6–4.5 Ma). The next period of volcanic activity (stage III: 4.4–4.3 Ma) began with the explosive eruption of trachytic tephras and sector collapse of a portion of the southern flank, which ultimately produced the Weiss Amphitheater. This event was followed by eruption of intermediate composition lavas and tephras at the southern end of the present Mount Sidley massif and represents the final pulse of differentiated magmas. The termination of Mount Sidley volcanism produced parasitic cones of basanite during stage IV activity around 4.2 Ma.

The rate and style of volcanic migration at Mount Sidley is mirrored on a larger scale by the ECR, where the southward geographical displacement of volcanic activity corresponds with significant changes in the composition of erupted magmas between major massifs (e.g. Mount Sidley→Mount Waesche) and between centers within a single massif (e.g. Whitney Peak→Mount Hampton and Lavris Peak→Mintz Peak, Fig. 2). We envisage the style of volcanic migration at Mount Sidley to be controlled by the sequential release of magma batches from a complex crustal plumbing system during the southward migration of tensional fractures. The propagation of fractures in response to regional tectonic stresses may have been assisted by magma injection.

Acknowledgements This project was funded by the Division of Polar Programs, NSF Grant #DPP-8816342 with assistance from NSF Grant #OPP-9118806 in manuscript preparation. We are grateful to Mick Kunk (USGS, Reston) and Larry Snee (USGS Denver) for their guidance with $^{40}Ar/^{39}Ar$ analyses; P. Floyd and G. Lees (University of Keele, UK) for X-ray fluorescence analysis. We also thank Philip Kyle and John Gamble for their valuable comments during the preparation of the manuscript; mountaineers Chris Griffiths and Bill Atkinson for their assistance in the field; and USAP and NZAP staff for logistical support. A special acknowledgment is extended to Simon Stevenson (NSF) and the Navy VXE-6 squadron for making the 1989–90 WAVE field season possible. Reviews by John Gamble, Gerhard Wörner, Mauro Rosi and an anonymous contributor improved the manuscript.

References

Behrendt JC, LeMasurier WE, Cooper AK, Tessensohn F, Tréhu AM, Damaske D (1991) The West Antarctic rift system – a review of geophysical investigations. In: Contributions to Antarctic Research II. Antarctic Res Ser 53. AGU, Washington, pp 67–112

Behrendt JC, LeMasurier W, Cooper A (1992) The West Antarctic Rift system – A propagating rift "captured" by a mantle plume? In: Yoshida Y, Kaminuma K, Shiraishi K (eds) Recent progress in Antarctic earth science. Proceedings of the Sixth International Symposium on Antarctic Earth Sciences, Saitama, Japan, 9–13 September 1991, National Polar Research, Japan. Terra Scientific Publishing, Tokyo, pp 315–322

Cooper AK, Davey FJ, Cochrane GR (1987) Structure of extensionally rifted crust beneath the western Ross Sea and Iselin Bank, Antarctica, from sonobouy seismic data. In: Cooper AK, Davey FJ (eds) The Antarctic continental margin; geology and geophysics of the western Ross Sea. Circum-Pacific Council for Energy and Natural Resources. Earth Sci Ser 5b, pp 93–118

Dalrymple GB, Lanphere MA (1969) Potassium–argon dating: principles, techniques, and applications to geochronology. Freeman, San Francisco

Dalrymple GB, Alexander EC, Lanphyre MA (1981) Irradiation of samples for $^{40}Ar/^{39}Ar$ dating using the Geological Survey TRIGA reactor. US Geol Surv Prof Pap 1176:1–55

Doumani GA (1964) Volcanoes of the Executive Committee Range, Byrd Land. In: Adie RJ (ed) Antarctic geology. North Holland, Amsterdam, pp 666–675

Doumani GA, Ehlers EG (1962) Petrography of rocks from mountains in Marie Byrd Land, west Antarctica. Geol Soc Am Bull 73:877–882

Drewry DJ (1983) Antarctica: glaciological and geophysical folio. Scott Polar Research Institute, Cambridge

Duncan RA (1981) Hotspots in the southern oceans – an absolute reference frame for motion of the Gondwana continents. Tectonophysics 74:29–42

Fleck RJ, Sutter JF, Elliot DH (1977) Interpretation of discordant $^{40}Ar/^{39}Ar$ age-spectra of Mesozoic tholeiites from Antarctica. Geochim Cosmochim Acta 41:15–32

Gamble JA (1979) Some relationships between coexisting granitic and basaltic magmas and the genesis of hybrid rocks in the Tertiary central complex of Slieve Gullion, northeast Ireland. J Volcanol Geotherm Res 5:297–316

Gamble JA, Smellie JL, McIntosh WC, Panter KS (1990) West Antarctic Volcano Exploration (WAVE – volcanoes of the Executive Committee Range, west Antarctica. N Z Antarctic Rec 10:16–17

González-Ferrán O, González-Bonorino F (1972) The volcanic ranges of Marie Byrd Land between Long 100° and 140°W. In: Adie RJ (ed) Antarctic geology and geophysics. Universitetsforlaget, Oslo, pp 261–275

Gorshkov GS (1959) Gigantic eruption of the Volcano Bezymianny. Bull Volcanol 20:77–112

Gorshkov GS, Dubik YM (1970) Gigantic directed blast at Shiveluch Volcano (Kamchatka). Bull Volcanol 34:261–276

Hole MJ, Storey BC, LeMasurier WE (1994) Tectonic setting and geochemistry of Miocene alkalic basalts from the Jones Mountains, West Antarctica. Antarctic Sci 6:85–92

Jones JG (1970) Intraglacial volcanoes of the Laugarvatn region, southwest Iceland, II. J Geol 78:127–140

Kunk MJ, Sutter JF (1985) High-precision $^{40}Ar/^{39}Ar$ ages of sanidine, biotite, hornblende, and plagioclase from the Fish Canyon tuff, San Juan volcanic field, south-central Colorado. Geol Soc Am Abstr Progr:636

Kyle PR (1990) McMurdo Volcanic Group western Ross embayment. In: LeMasurier WE, Thomson JW (eds) Volcanoes of the Antarctic plate and southern oceans. Antarctic Res Ser 48. American Geophysical Union, Washington, pp 19–25

Kyle PR, McIntosh WC, Panter KS, Smellie JL (1991) Is volcanism in Marie Byrd Land related to a mantle plume? In: Abstracts. Sixth International Symposium on Antarctic Earth Sciences, Saitama, Japan, 9–13 September 1991, National Institute of Polar Research, Japan, p 337

Le Maitre RW (1989) A classification of igneous rocks and glossary of terms: recommendations of the International Union of Geological Sciences subcommision on the systematics of igneous rocks. Blackwell, London

LeMasurier WE (1972) Volcanic record of Cenozoic glacial history of Marie Byrd Land. In: Adie RJ (ed) Antarctic geology and geophysics. Universitetsforlaget, Oslo, pp 251–259

LeMasurier WE (1990a) Late Cenozoic volcanism on the Antarctic plate: an overview. In: LeMasurier WE, Thomson JW (eds) Volcanoes of the Antarctic plate and southern oceans. Antarctic Res Ser 48. American Geophysical Union, Cambridge University Press, New York, pp 531–532

LeMasurier WE (1990b) Marie Byrd Land: summary. In: LeMasurier WE, Thomson JW (eds) Volcanoes of the Antarctic plate and southern oceans. Antarctic Res Ser 48. American Geophysical Union, Washington, pp 147–163

LeMasurier WE (1990c) Mount Sidley: a report. In: LeMasurier WE, Thomson JW (eds) Volcanoes of the Antarctic plate and southern oceans. Antarctic Res Ser 48. American Geophysical Union, Washington, pp 203–207

LeMasurier WE, Rex DC (1983) Rates of uplift and the scale of ice level instabilities recorded by volcanic rocks in Marie Byrd Land, west Antarctica. In: Oliver RL, James PR, Jago JB (eds) Antarctic earth sciences. Cambridge University Press, New York, pp 663–670

LeMasurier WE, Rex DC (1989) Evolution of linear volcanic ranges in Marie Byrd Land, west Antarctica. J Geophys Res 94:7223–7236

LeMasurier WE, Rex DC (1991) The Marie Byrd Land volcanic province and its relation to the Cainozoic west Antarctic rift system. In: Tingey RJ (ed) Geology of Antarctica. Oxford Monogr Geol Geophys 17. Clarendon Press, Oxford, pp 249–284

LeMasurier WE, Wade FA (1976) Volcanic history in Marie Byrd Land: implications with regard to southern hemisphere tectonic reconstructions. In: González-Ferran O (ed) Proceedings of the symposium on Andean and Antarctic Volcanology Problems (Santiago, Chile). IAVCEI, Rome, pp 398–424

LeMasurier WE, Harwood DM, Rex DC (1994) Geology of Mount Murphy volcano: an 8-m.y. history of interaction between a rift volcano and the West Antarctic ice sheet. Geol Soc Am Bull 106:256–280

McIntosh WC, LeMasurier WE, Ellerman PJ, Dunbar NW (1985) A re-interpretation of glaciovolcanic interaction at Mount Takahe and Mount Murphy, Marie Byrd Land, Antarctica. Antarctic J US 20:57–59

McIntosh WC, Smellie JL, Panters KS (1991) Glaciovolcanic interactions in eastern Marie Byrd Land, Antarctica. In: Abstracts. Sixth International Symposium on Antarctic Earth Sciences, Saitama, Japan, 9–13 September 1991. National Institute of Polar Research, Japan, p 402

Panter KS, McIntosh WC, Smellie JL, Gamble JA (1991) Volcanic history of Mount Sidley, Marie Byrd Land, Antarctica. In: Abstracts. Sixth International Symposium on Antarctic Earth Sciences, Saitama, Japan, 9–13 September 1991. National Institute of Polar Research, Japan, p 476

Samson SD, Alexander EC (1987) Calibration of the interlaboratory $^{40}Ar–^{39}Ar$ dating standard, MMhb-1. Chem Geol 66:27–34

Sigurdsson H, Sparks SRJ (1978) Lateral magma flow within rifted Icelandic crust. Nature 274:126–130

Simkin T, Howard KA (1970) Caldera collapse in the Galapagos Islands, 1968. Science 169:429–437

Skilling IP (1993) Incremental caldera collapse of Suswa volcano, Gregory rift valley, Kenya. J Geol Soc London 150:885–869

Smellie JL, McIntosh WC, Gamble JA, Panter KS (1990) Preliminary stratigraphy of volcanoes in the Executive Committee Range, central Marie Byrd Land. Antarctic Sci 2:353–354

Smellie JL, Panter KS, McIntosh WC, Kyle PR (1991) Geochemical evolution of volcanoes in the Executive Committee Range, central Marie Byrd Land, west Antarctica. In: Abstracts. Sixth International Symposium on Antarctic Earth Sciences, Saitama, Japan, 9–13 September 1991. National Institute of Polar Research, Japan, p 536

Smellie JL, Hole MJ, Nell PR (1993a) Products and processes in subglacial eruptions: 1. Late Miocene valley-confined subglacial volcanism in northern Alexander Island, Antarctic Peninsula. Bull Volcanol 55:273–288

Smellie JL, McIntosh WC, Gamble JA, Panter KS, Kyle PR, Dunbar NW (1993b) Preliminary lithofacies assessment and $^{40}Ar/^{39}Ar$ ages of Cenozoic volcanic sequences in eastern Marie Byrd Land. Antarctic Sci 5:105–106

Sparks RSJ, Sigurdsson H (1977) Magma mixing: a mechanism for triggering acid explosive eruptions. Nature 267:315–318

Spence DA, Turcotte DL (1985) Magma-driven propagation of cracks. J Geophys Res 90:575–580

Voight B, Glicken H, Janda RJ, Douglass PM (1981) Catastrophic rockslide avalanche of May 18. In: Lipman PW, Mullineaux DR (eds) The 1980 Eruptions of Mount St Helens, Washington. US Geol Surv Prof Pap 1250:347–377

Wilch TI, McIntosh WC, Panter KS, Dunbar NW (1993) Preliminary report on field investigations and $^{40}Ar/^{39}Ar$ geochronology of the Crary Mountains volcanoes, Marie Byrd Land, West Antarctica. Antarctic J US 28:7–9

Wysoczanski RJ, Gamble JA (1992) Xenoliths from the volcanic province of west Antarctica and implications for lithospheric structure and processes. In: Yoshida Y, Kaminuma K, Shiraishi K (eds) Recent progress in Antarctic earth science. Proceedings of the Sixth International Symposium on Antarctic Earth Sciences, Saitama, Japan, 9–13 September 1991, National Polar Research, Japan. Terra Scientific Publishing, Tokyo, pp 273–277

Editorial responsibility: M. Rosi

Petrogenesis of a phonolite–trachyte succession at Mt. Sidley, Marie Byrd Land, Antarctica

K. S. Panter[1], P. R. Kyle[1] and J. L. Smellie[2]
[1] Department of Earth and Environmental Science, New Mexico Institute of Mining and Technology, Socorro, NM 87801, USA
[2] British Antarctic Survey, NERC, High Cross, Madingley Road, Cambridge CB3 OET, UK

ABSTRACT

The 1·5 Ma evolution of the Pliocene (5·7 to 4·2 Ma) Mt. Sidley volcano, Marie Byrd Land, is examined using major and trace elements, Sr, Nd, O and Pb isotopic data. Over 200 km^3 of alkaline volcanic rocks were erupted from at least four major vents and range in composition from basanite (> 10% *Ne*-normative) and mugearite to phonolite and trachyte. Major changes in magma composition coincide with a southward migration of activity which occurred in four main stages (I, 5·7–4·8; II, 4·6–4·5; III, 4·4–4·3; and IV, 4·2 Ma). The volcanic rocks are porphyritic with olivine (Fo_{86-1}), clinopyroxene (Wo_{52-43} En_{49-1} Fs_{53-1}), feldspar (An_{54-2} Ab_{74-44} Or_{48-1}), and spinel (Usp_{77-2}). Apatite and feldspathoids are present in stage I phonolites and arfvedsonite occurs within some trachytes.

Mt. Sidley volcanic rocks have high incompatible element contents and are light rare earth element (REE) enriched relative to heavy REE [$(La/Yb)_n$ = 9–19]. The basanites have trace element contents comparable to ocean island basalts (OIB) and the majority of volcanic rocks fall within a narrow range of $^{87}Sr/^{86}Sr_i$ (0·7028-0·7032), $^{143}Nd/^{144}Nd_i$ (0·51285-0·51290) and $\delta^{18}O$ (5·0-6·0‰). Moreover, radiogenic Pb signatures (e.g., $^{206}Pb/^{204}Pb$ > 19) help characterize a high U/Pb (HIMU), OIB-type mantle source. The

mugearites are subdivided into two types: low *mg*-number (20–30) southern flank mugearite (SFM) and; high *mg*-number (40–50) Doumani Peak mugearite (DPM). SFM lavas have higher abundances of incompatible trace elements and are light REE-enriched relative to DPM tephras, suggesting their evolution from two distinct basaltic parents; basanite and alkali basalt (< 8% *Ne*), respectively.

Based on stratigraphy and geochemical relationships, phonolites and trachytes cannot be related to a single differentiation trend. The phonolites have restricted SiO_2 and relatively uniform trace element contents, whereas trachytes show wide ranges in major and trace elements and are subdivided into three main types: high Th (> 60 ppm) trachyte (*HT*); low Th (~ 20 ppm) trachyte (*LT*) and; 'normal' trachyte (*N*). The differentiation of the phonolite series is modeled by fractionation of diopside, olivine, plagioclase, magnetite, nepheline and/or apatite. Fractionation of this assemblage from a basanite produces 35% mugearite, 25% benmoreite and 20% phonolitic liquids. The *N*-trachyte suite is modeled by fractional crystallization of alkali basalt. Some trachytes have elevated $^{87}Sr/^{86}Sr_i$ (0·7033–0·7042), low $^{143}Nd/^{144}Nd_i$ (0·51280–0·51283) and high $\delta^{18}O$ (6·5–8·4 ‰), suggesting contributions from the crust. The petrogenesis of *LT*-trachytes require assimilation of calc-alkaline granitoids by alkali basalts in the middle crust. Differentiation at high assimilation to crystallization rates (high-*r* AFC) can explain Nd and Sr isotopes and strong depletions in Ta and Nb relative to K, Rb and light REE. Fractionation of *LT*-trachytes at low-*r* AFC in the upper-crust produced the *HT*-trachytes.

The change in parent magmas from basanite to alkali basalt reflects a shift to higher degrees of partial melting in the upper mantle. Non-modal equilibrium batch melting of

mantle peridotite produces basanitic magmas at ≤ 2% partial melting, whereas more silica-saturated alkali basalts require ≥ 5% melting of the same source.

INTRODUCTION

Mt. Sidley is an Early Pliocene composite volcano located at the south end of the Executive Committee Range, a 100-km chain of volcanoes within the Marie Byrd Land province of west Antarctica. The Marie Byrd Land province is part of a broad region of crustal extension and young (~ 35 Ma to presently active) alkaline volcanism that occurs along the Pacific margin of Antarctica from Ellsworth Land to the northern coast of Victoria Land (~ 3500 km). It comprises one of the world's major continental rift systems (LeMasurier & Thomson, 1990). In Marie Byrd Land, 18 large composite centers rise above the West Antarctic Ice Sheet, but only a few have adequate ice-free exposures to permit comprehensive study of their eruptive history and petrogenesis. At Mt. Sidley, a large breached caldera has exposed volcanic strata deep within its interior (Fig. 1), revealing a long and complex history of eruption (Panter *et al.*, 1994).

Volcanic rocks in the Marie Byrd Land province show a wide range in composition from alkali basalt and basanite to intermediate and evolved alkaline types including hawaiite, mugearite, benmoreite, phonolite and, comenditic and pantelleritic trachyte and rhyolite. Geochemical studies of similar continental alkaline suites, including those within the Kenya alkaline province (Wright, 1963; Baker *et al.*, 1977), the Otago province of New Zealand (Coombs & Wilkinson, 1969; Coombs *et al.*, 1986) and the Massif Central of France (Downes, 1987), have shown that alkaline rocks evolve along two main magma

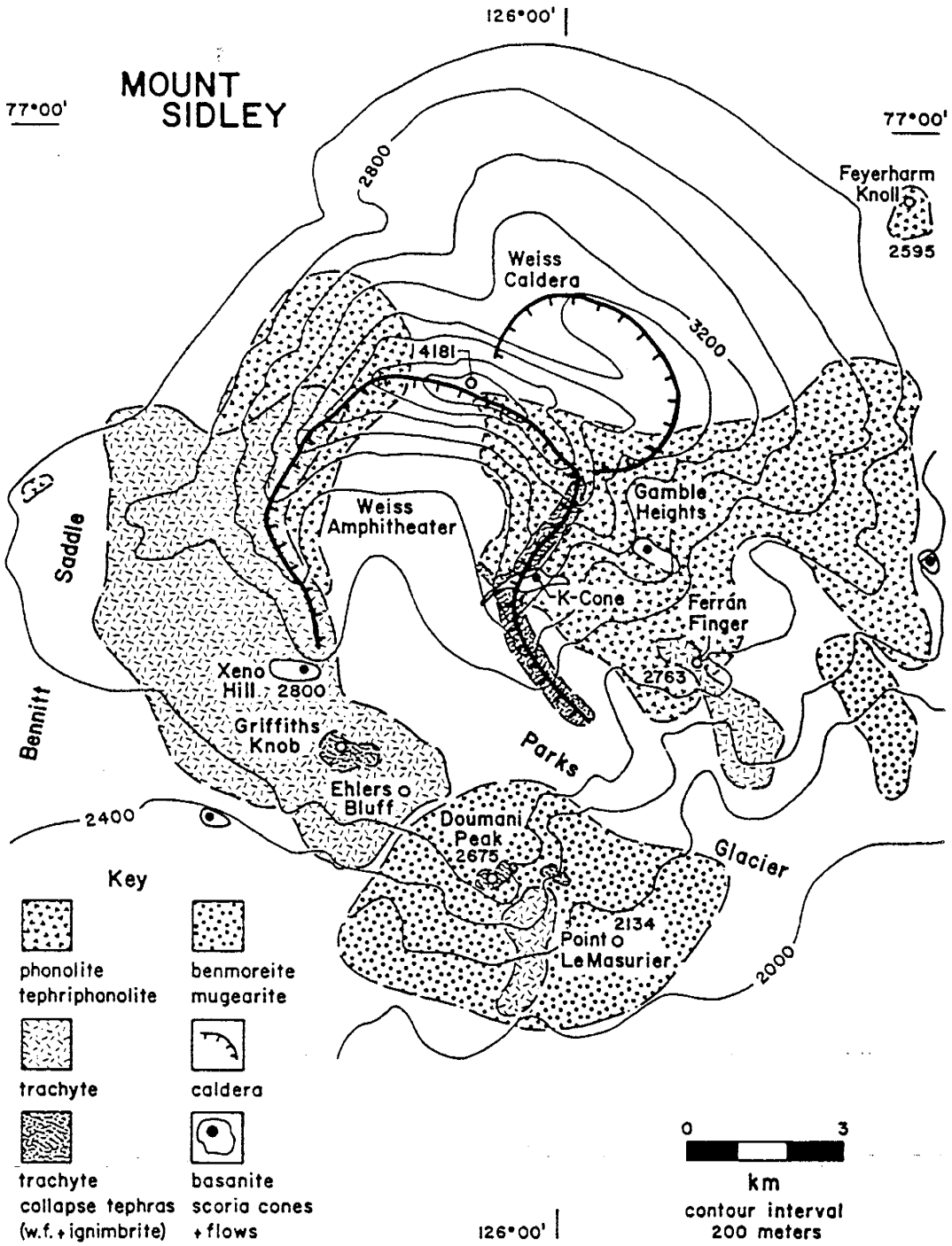

Figure 1. Topographic map of Mt. Sidley showing simplified distribution of volcanic rock compositions. Bold hatchured curves represent caldera margins. Informal place names are designated by single quotation marks and all elevations are in meters.

lineages; a strongly silica-undersaturated series (e.g., basanite → phonolite) and a more silica-saturated series (e.g., alkali basalt → trachyte). Rarely has the recognition of the two lineages been traced through a suite of coexisting rocks from a single volcano, often due to the preponderance of either basaltic or highly evolved compositions (e.g., phonolites or trachytes) and dearth of intermediate rock-types. Petrogenetic studies of closely associated silica-undersaturated and silica-oversaturated rock suites often invoke complex open system processes to explain their origin from a common parental magma (e.g., Barbieri *et al.*, 1988; Turbeville, 1993; Freundt & Schmincke, 1995) and specifically, the assimilation of crust by mantle derived silica-undersaturated melts to produce oversaturated alkaline magmas (e.g., Halliday *et al.*, 1988; Foland *et al.*, 1993; Macdonald *et al.*, 1995).

In this paper we present elemental and isotopic data for the Mt. Sidley suite with attention focused on the origin and evolution of phonolitic and trachytic magmas. Our objective is to determine the genetic relations between silica-undersaturated and silica-saturated to oversaturated rocks within the volcanic succession. Theoretical modeling of geochemical variations address both open and closed system processes and reveal a complex magmatic history, involving variable degrees of mantle partial melting, crystal fractionation, magma mixing and assimilation of crust.

VOLCANIC GEOLOGY

Mt. Sidley (4181m) is a large (> 200 km^3) alkaline volcanic center composed primarily of phonolitic and trachytic lavas and subordinate pyroclastic deposits (Fig. 2).

Detailed mapping, stratigraphy and 14 high-precision $^{40}Ar/^{39}Ar$ age determinations reveal a complex, polygenetic volcano constructed in successive stages over a 1·5 m.y. life-span during the Early Pliocene, from 5·7 to 4·2 Ma (Panter *et al.*, 1994).

Mt. Sidley comprises at least three major phonolitic centers, the Byrd, Weiss and Sidley volcanoes, and many smaller vents. Major changes in magma composition coincide with a southward migration of volcanic activity (0·6 cm/a). The migration occurred in four main stages (Fig. 2). The first stage (I) of activity between 5·7 and 4·8 Ma produced phonolitic lavas which issued in the northern portion of the volcano. During stage I, three calderas formed and were partially infilled with lavas and volcaniclastic sediments. Trachytic lavas, domes and pyroclastic materials of stage II (4·6–4·5 Ma) were erupted roughly 5 to 6 km to the south of the stage I vents. Stage III activity (4·4–4·3 Ma) began with a highly explosive paroxysmal eruption of trachytes and catastrophic landslide of the southern flank of the volcano, forming a large breached caldera (Weiss Amphitheater). The 5 × 5 km, 1200 m deep, Weiss Amphitheater dominates the present-day morphology of Mt. Sidley (Fig. 1). The caldera forming event was followed by eruption of mugearite and benmoreite lavas and tephras from vents approximately 9 km south of stage I activity. These represent a final pulse of differentiated magmas. Volcanism ceased at around 4·2 Ma (stage IV) following the eruption of xenolith-bearing (crustal and mantle) basanite parasitic cones.

During stage I, large quantities (~ 180 km^3) of phonolitic lavas were erupted. The period was relatively long-lived (~ 1 Ma), reflecting a stable magmatic system. It is apparent, however, that the magma reservoirs were able to communicate at times and

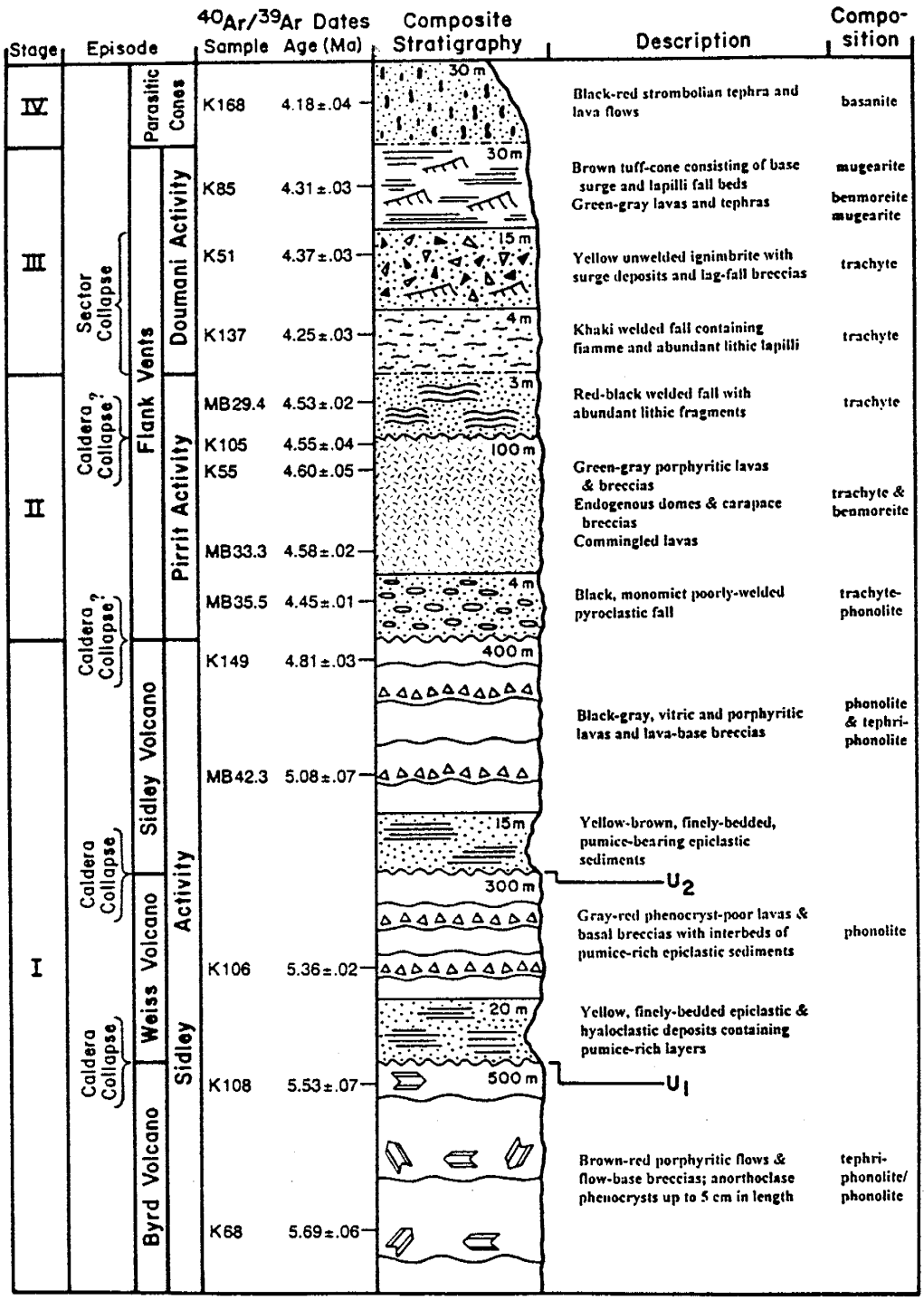

Figure 2. Generalized composite stratigraphic column for Mt. Sidley. Samples dated by the $^{40}Ar/^{39}Ar$ method are arranged in their relative stratigraphic positions. $^{40}Ar/^{39}Ar$ plateau ages (Ma) with 1σ errors. U_1 and U_2 represent major unconformities exposed in the eastern caldera wall. Also shown are major volcano-building episodes and stages of activity (refer to Panter *et al.*, 1994).

mixing played an important role in the petrogenesis of magmas. Several deposits are considered to be a direct result of magma mixing. They include a compositionally heterogeneous (phonolite and trachyte) black-colored fall deposit marking the beginning of stage II activity (Fig. 2) and several trachyte flows containing partially resorbed 'mafic' enclaves (Panter *et al.*, 1994, Fig. 7b). Further evidence for magma mixing and intermingling within the Sidley succession as well as chemical indications for the assimilation of crust suggest that magmatic evolution involved both open and closed system processes.

PETROGRAPHY AND MINERAL CHEMISTRY

Mt. Sidley volcanic rocks are strongly porphyritic and general petrographic features are summarized in Table 1. Alkali feldspar, clinopyroxene, olivine and magnetite are ubiquitous phenocryst phases. In rocks of stage I, the groundmass is often glassy. In contrast, trachytic and intermediate lavas of stages II and III have coarse, holocrystalline groundmasses. Plagioclase feldspar phenocrysts occur in basaltic and tephriphonolite rocks and as microphenocrysts in phonolites and intermediate compositions. Feldspathoids and apatite are restricted to benmoreite and phonolitic rocks within stage I. Hydrous minerals are rare and limited to dark, bluish-green amphibole within comingled and trachytic lavas (stage II) and microphenocrysts of brownish-red mica in several mafic and intermediate lavas (stage III).

Minerals were analyzed on an automated JEOL-733 electron microprobe at Victoria University of Wellington, New Zealand, using 15 kV accelerating potential, 12–13 nA

Table 1. Summary of petrographic features for Mt. Sidley rocks. Samples grouped by stage and episode of volcanic activity (refer to Fig. 2).

	episode	rock type	major minerals (≥ 5%)	minor minerals	accessory	phenocryst %	texture
IV	Parasitic Cones	basanite	Plag + Ol + Cpx	–	Ox	5 - 30	p → fp, t
III	Doumani Activity	trachyte tephras: welded fall	Akf	Cpx + Ol	Ox	10 - 15	w, vtph
		ignimbrite (pumice)	–	Akf + Cpx	–	≤ 1	vtph
		benmoreite	Akf	Ol » Cpx » mica	Ox	30	fp, t
		phonotephrite	Ol	Plag > mica	Ox	10	fp → mp
		mugearite	Plag > Ol	mica + Cpx	Ox	40	p
II	Pirrit Activity	trachyte	Akf + Cpx	Ol + Plag » Amp	Ox	5 - 30	gp → p, t
		comingled lavas: trachytic	Akf	Cpx + Ol + Amp	Ox	10 - 25	cp → p
I	Sidley Volcano	phonolite	Akf	Cpx + Ol + Fspth	Ox + Ap	5 - 45	cp → fp, amg, vtph
	Weiss Volcano	phonolite	Akf	Fspth + Plag + Cpx + Ol	Ox + Ap	1-10	fp → mp, t, amg
		intrusives: phonolite	Akf	Ol » Cpx	Ox > Ap	25	vtph
		benmoreite	Akf > Fspth > Cpx	Ol	Ox > Ap	–	so
	Byrd Volcano	tephriphonolite - phonolite	Akf + Fspth	Plag + Ol + Cpx	Ox + Ap	30-60	cp, t, amg

abbreviations: *minerals* Akf = alkali feldspar; Fspth = Feldspathoid; Cpx = clinopyroxene; Ol = olivine; Plag = plagioclase; Ox = Fe-Ti oxides; Ap = apatite; Amp = alkali-amphibole; mica = brownish-red mica (phlogopite-biotite).

textures cp = coarsely porphyritic (> 1cm); p = porphyritic (> 5mm); fp = finely porphyritic (< 5mm); mp = microporphyritic (< 2mm); gp = glomeroporphyritic; amg = amygdaloidal; t = trachytic; w = welded; vtph = vitrophyric; so = subophitic.

sample current, 1–10 μm electron beam and correction factors of Bence & Albee (1968). Natural mineral standards were measured between sample runs to check calibration, accuracy, and precision (approximately ± 1% for element oxides with abundances of > 10 wt.% and ± 5 to 10% for elements with lower abundances).

Olivine

Olivine phenocrysts occur in rocks of all compositions, ranging from 10% (modal) in mafic and intermediate lavas to ≤ 2 % in phonolites and trace amounts in trachytes. Olivine ranges from forsterite (Fo_{86}) in mafic enclaves of comingled lavas to fayalite (Fo_1) in trachytes (Fig. 3; Table 2; Appendix C3.1). Colorless, euhedral olivine crystals predominate in basanite ($Fo_{\sim 74}$) and mugearite (Fo_{41-43}) but show variable alteration and oxidation effects in more evolved rock types. Light greenish yellow olivine (Fo_{37-38}) is mantled by Fe-Ti oxides in many benmoreite and tephriphonolite lavas. In phonolites (Fo_{32-37}) and trachytes (Fo_{1-15}) olivine phenocrysts are often subhedral to skeletal, and some are pseudomorphed by hematite.

The CaO content of olivine cores varies from 0·1–0·2 wt.% in basanite, 0·3–0·4 wt.% in mugearite and 0·5–0·8 wt.% in phonolite. Geobarometric studies reveal that calcium solubility in olivine decreases systematically with pressure (e.g., Köhler & Brey, 1990), thus, the corresponding increase in CaO with sample differentiation may reflect equilibrium crystallization at lower pressures (cf. Simkin & Smith, 1970; Stromer, 1973). MnO concentration in olivine varies from ≤ 1·0 wt.% in mafic rocks to ~ 2·0 wt.% in phonolites and up to 5·0 wt.% in trachytes. Watson (1977) demonstrated that Mn is more

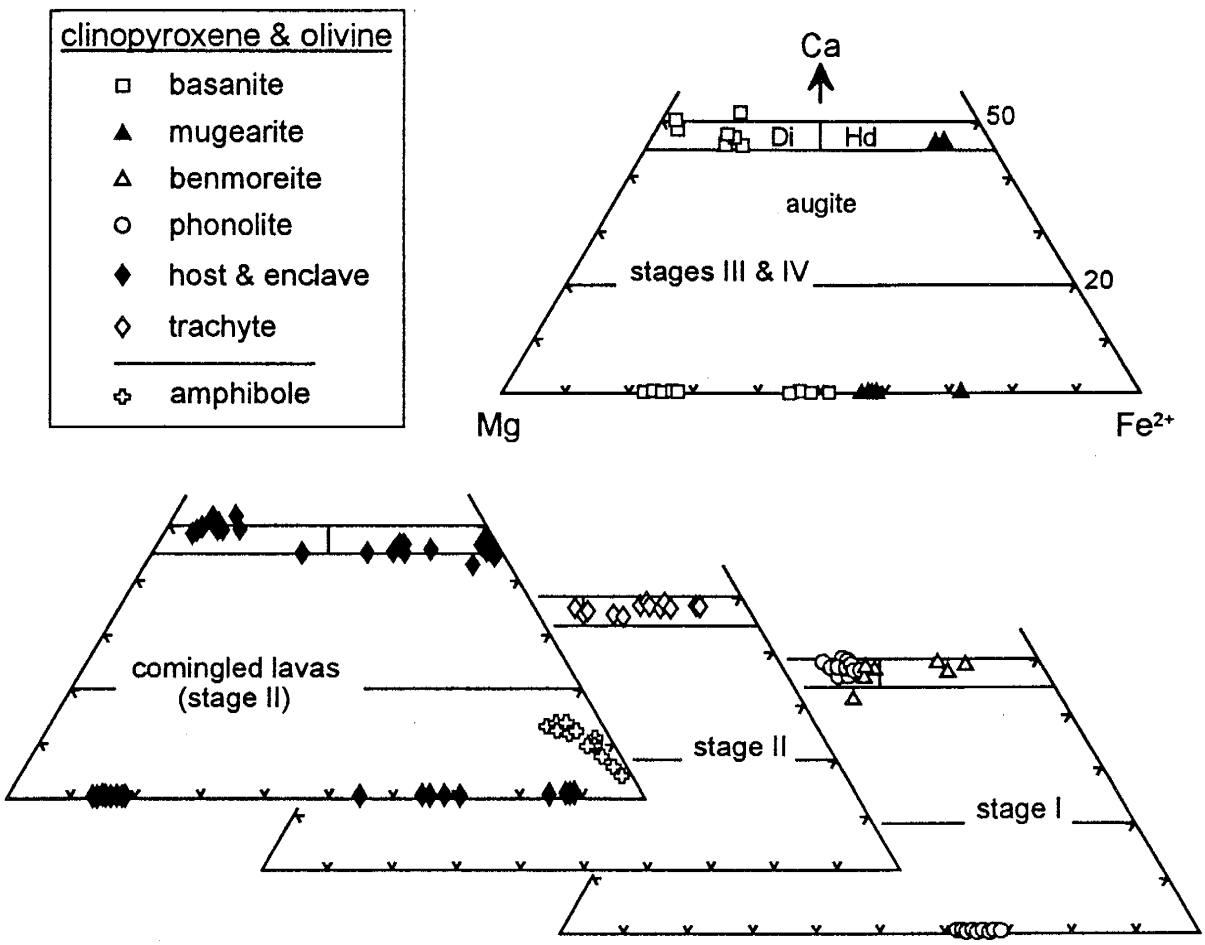

Figure 3. Electron microprobe analyses of clinopyroxene, olivine and amphibole (open crosses) from Mt. Sidley plotted in terms of atomic % Ca, Mg, Fe^{2+}. Composition of olivines plot along the Mg- Fe^{2+} join and clinopyroxenes are shown relative to fields for diopside (Di), hedenbergite (Hd) and augite (Morimoto *et al.*, 1988). Analyses of amphibole, clinopyroxene and olivine (filled diamonds) from mafic enclaves and their trachytic hosts (comingled lavas) are presented together. Composition of clinopyroxenes in benmoreite (open triangles) are from a single intrusion emplaced during stage I activity.

strongly partitioned into olivine at lower temperatures and with increasing SiO_2 content of the coexisting melt.

Zoned olivine phenocrysts normally display homogeneous cores mantled by more fayalitic rims. Conversely, reverse zoning occurs in olivine in several of the uppermost phonolite lavas of the Sidley volcano (stage I, Fig. 2) and within comingled trachyte lavas (stage II). The outermost rims of reversely zoned olivines in phonolites reveal enrichment in MgO and CaO (up to 0·6 wt.% and 0·1 wt.%, respectively) with depletions in FeO (≤ 1·0 wt.%) and MnO (≤ 0·2 wt.%) relative to their cores. This type of zoning suggests an abrupt compositional change in the coexisting melt during olivine crystallization.

Clinopyroxene

Pyroxene is ubiquitous in Mt. Sidley volcanic rocks and is here classified according to Morimoto *et al.* (1988). Euhedral phenocrysts (up to 3 mm) of pale, green-yellow diopside occur in phonolites and subhedral to anhedral microphenocrysts (< 1 mm) of dark, grass-green hedenbergite are abundant in trachytes. Diopside also occurs as light, brownish yellow subhedral microphenocrysts in basanite and as rare anhedral grains within intermediate lavas.

The pyroxenes plot mostly in the Ca-Mg-Fe quadrilateral (Fig. 3), although a few samples lie above the CaMg–$CaFe^{2+}$ join. Diopside in basanite are subsilicic (< 1·75 Si atoms per formula unit, henceforth abbreviated a.f.u.) aluminian, calcian (Ca > 0·9 a.f.u.) and magnesian (Mg > 0·9 a.f.u.). Diopside and calcian diopside occur in phonolites and ferroan (Fe^{2+} > 0·5 a.f.u.) hedenbergite within trachytes and mugearites (Fig. 3; Table 3;

Table 2. Representative electron microprobe analyses of olivine phenocrysts.

sample no.	K168	K93	K108	K120	K144	K144	K66	K63	K63	K63
rock	bas	mug	tphn	phn	phn	phn	trac	CL-encl.	CL-encl.	CL-host
position	core	core	core	core	core-	rim	core	core-	rim	core
	wt.% oxide									
SiO_2	38.26	33.83	33.17	33.31	33.02	32.56	30.36	39.50	32.78	29.76
FeO*	23.23	45.78	47.77	49.52	50.79	49.80	64.50	14.45	52.41	67.40
MnO	0.31	0.94	1.93	2.04	2.39	2.20	5.14	0.21	1.96	2.76
MgO	38.27	19.23	16.53	15.44	13.65	14.23	0.81	46.03	12.86	0.49
CaO	0.14	0.33	0.56	0.57	0.65	0.73	0.22	0.25	0.37	0.36
sum	100.21	100.11	99.96	100.88	100.50	99.52	101.03	100.44	100.38	100.77
	formula based on 4 oxygens									
Si	0.998	0.997	0.996	0.999	1.004	0.997	1.008	0.987	1.004	0.997
Fe^{2+}	0.507	1.128	1.200	1.242	1.291	1.275	1.791	0.302	1.342	1.889
Mn	0.007	0.023	0.049	0.052	0.062	0.057	0.145	0.004	0.051	0.078
Mg	1.487	0.844	0.740	0.690	0.618	0.649	0.040	1.714	0.587	0.024
Ca	0.004	0.010	0.018	0.018	0.021	0.024	0.008	0.007	0.012	0.013
total	3.003	3.002	3.003	3.001	2.996	3.002	2.992	3.014	2.996	3.001
mg-number	75	43	38	36	32	34	2	85	30	1

* Total Fe as FeO. *mg*-number = atomic % ($Mg/Mg + Fe^{2+}$)

Abbreviations: bas = basanite; mug = mugearite; tphn = tephriphonolite; phn = phonolite; trac = trachyte comingled lavas (CL), consisting of mafic enclaves (encl) and trachytic host compositions.

Appendix C3.2). Clinopyroxenes in comingled lavas show a large compositional range (Fig. 3) from subsilicic aluminium diopside and magnesian diopside in mafic enclaves to ferroan hedenbergite within the felsic host. Estimates of non-quadrilateral components [based on coupled substitutions in the standard chemical formula $M2M1T_2O_6$, method of Cameron & Papike (1981)] show that hedenbergites in trachytes contain up to 16% nonquadrilateral aegirine ($NaFe^{3+}SiO_6$) or as much as 6% of the NATAL ($NaTiAlSiO_6$) components. Diopside in phonolitic lavas have up to 14% calcium ferrian Tschermak's molecule ($CaFe^{3+}AlSiO_6$) and ≤ 11% NATAL or aegirine components. In contrast, diopside in basanite and mafic enclaves within comingled lavas contain as much as 33% of the $CaMg_{0.5}\ Ti^{4+}_{0.5}\ AlSiO_6$ molecule.

With sample differentiation, Ti and Al concentrations in clinopyroxene decrease with increasing Fe content, comparable to pyroxenes within the alkaline Shiant Isles Sill, Scotland (Gibb, 1972) and those within weakly understaturated volcanic rocks from The Pleiades, Antarctica (Kyle, 1986). Clinopyroxene in Mt. Sidley phonolites have higher Al and higher average Ti contents than those in trachytes yet both show decreasing Ti and Al contents with increasing silica. A negative correlation of Si versus Ti + Al demonstrates that increasing silica activity in the coexisting melt decreases Al and Ti solubility in pyroxenes (Gibb, 1972; Gupta *et al.*, 1973).

A further distinction between pyroxenes in phonolites and those in trachytes is presented on a *mg*-number versus Al + Ti plot (Fig. 4). The vertical variation shown by diopsides in phonolites is controlled, predominately, by Al activity in the liquid, a result of

Table 3: Representative electron microprobe analyses of clinopyroxene phenocrysts.

sample no.	K168	K166	K166	K122	K144	K144	K144	K55	K100	JG025	JG025
rock	bas	ben	ben	phn	phn	phn	phn	trac	trac	CL-host	CL-host
position	core	core-	rim	core	core-	rim-a	rim-b	core	core	core-	rim
	wt.% oxide										
SiO_2	54.15	51.13	49.72	51.00	51.15	50.95	51.48	50.83	49.10	48.07	49.24
TiO_2	0.30	0.55	0.60	0.79	0.53	0.77	0.61	0.51	0.49	0.45	0.35
Al_2O_3	0.67	1.15	1.01	1.85	1.55	2.19	1.67	1.28	0.70	0.38	0.40
FeO*	2.73	15.27	21.78	13.06	14.07	13.50	13.27	17.69	24.42	28.06	24.62
MnO	0.16	0.46	0.73	0.64	0.64	0.51	0.52	0.77	0.93	0.84	0.92
MgO	17.16	8.95	4.45	10.09	9.19	9.80	10.13	8.40	3.40	0.86	3.48
CaO	24.25	22.22	19.44	21.98	21.65	22.49	22.65	21.09	20.79	20.20	20.08
Na_2O	0.26	0.67	1.74	0.84	0.84	0.71	0.72	0.51	0.44	0.54	0.64
sum	99.68	100.40	99.47	100.25	99.62	100.92	101.05	101.08	100.27	99.40	99.73
Fe_2O_3	0.81	1.81	3.82	2.28	1.21	2.19	2.34	1.76	1.05	1.08	1.38
FeO	2.00	13.64	18.35	11.01	12.98	11.53	11.17	16.10	23.47	27.09	23.38
total	99.76	100.58	99.86	100.48	99.74	101.14	101.29	101.25	100.37	99.51	99.87
	formula based on 6 oxygens										
Si	1.975	1.957	1.969	1.934	1.963	1.924	1.939	1.950	1.970	1.982	1.984
Ti	0.008	0.016	0.018	0.023	0.015	0.022	0.017	0.015	0.015	0.014	0.011
Al	0.029	0.052	0.047	0.083	0.070	0.098	0.074	0.058	0.033	0.018	0.019
Fe^{3+}	0.022	0.052	0.114	0.065	0.035	0.062	0.066	0.051	0.032	0.033	0.042
Fe^{2+}	0.061	0.437	0.607	0.349	0.417	0.364	0.352	0.517	0.788	0.934	0.788
Mn	0.005	0.015	0.024	0.021	0.021	0.016	0.017	0.025	0.032	0.029	0.031
Mg	0.933	0.511	0.263	0.570	0.526	0.552	0.569	0.480	0.203	0.053	0.209
Ca	0.948	0.911	0.825	0.893	0.890	0.910	0.914	0.867	0.894	0.893	0.867
Na	0.018	0.050	0.134	0.062	0.063	0.052	0.053	0.038	0.034	0.043	0.050
sum	3.999	4.001	4.001	4.000	4.000	4.000	4.001	4.001	4.001	3.999	4.001
mg-number	94	54	30	62	56	60	62	48	20	5	21

* Total Fe as FeO. *mg*-number = atomic % ($Mg/Mg + Fe^{2+}$).

Fe_2O_3 and FeO partitioned using the charge balance equation of Papike et al. (1974).

Abbreviations: ben = benmoreite; other rock names as in Table 2.

olivine → clinopyroxene → plagioclase fractionation, whereas, compositional variations displayed by hedenbergite in trachytes can be explained by changes in Fe activity.

Sodium and potassium in Mt. Sidley clinopyroxenes are low (< 1·0 wt.%) and are only enriched in pyroxenes from a benmoreite intrusion (Fig. 5). These clinopyroxenes show increasing substitution by the aegirine component ($NaFe^{3+}Si_2O_6$) between diopside (7–9%), ferroan hedenberite (~ 14%) and aegirine-augite (23%). In addition, the Fe^{3+}/Fe_t ratio increases from < 0·1 to ~ 0·3 with increasing Na_2O (0·7 to 3·0 wt.%). Na in pyroxene is controlled by the activity of Fe^{3+} in the melt and is thus a function of oxygen fugacity (Nash & Wilkinson, 1970; Gibb, 1972). This suggests that increasing $Na\text{-}Fe^{3+}$ substitution in benmoreite clinopyroxene may be related to increasing fO_2 during crystallization of the intrusion. In other instances, fO_2 may play a role in establishing the chemical distinction between pyroxenes in phonolites and those in trachytes. Higher Fe^{3+}/Fe_t ratios and the high Na and $Ca\text{-}Fe^{3+}$-Tschermak's content of diopsides in phonolites relative to trachytes may be a result of higher fO_2 conditions (Onuma *et al.*, 1981; Dobosi, 1989).

Chemically zoned clinopyroxenes provide insight into changes in magma composition and crystallization environments. Pyroxene phenocrysts within mafic enclaves of comingled lavas have Fe-rich rims relative to cores (Δ = 14 wt.% FeO), whereas, pyroxene in the felsic host are reversely zoned with MgO content increasing (~ 1 to 4 wt.%) and FeO decreasing (~ 28 to 25 wt.%) from cores to rims. Such changes in mineral chemistry can be expected if crystallization and magma mingling were coincident (e.g., Downes, 1989). Pyroxene in uppermost phonolitic lavas of the

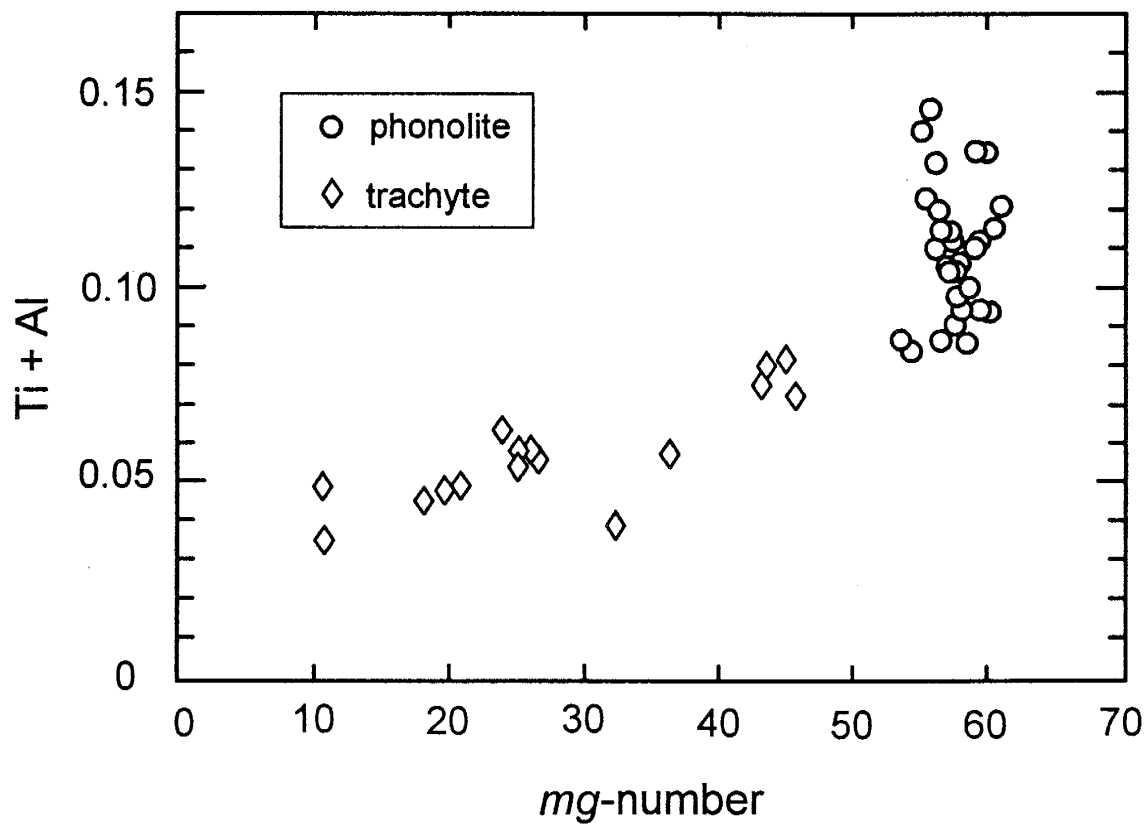

Figure 4. Composition of clinopyroxene from phonolites and trachytes plotted on a atomic % Ti + Al versus *mg*-number (atomic % = Mg/Mg + Fe^{2+}) diagram.

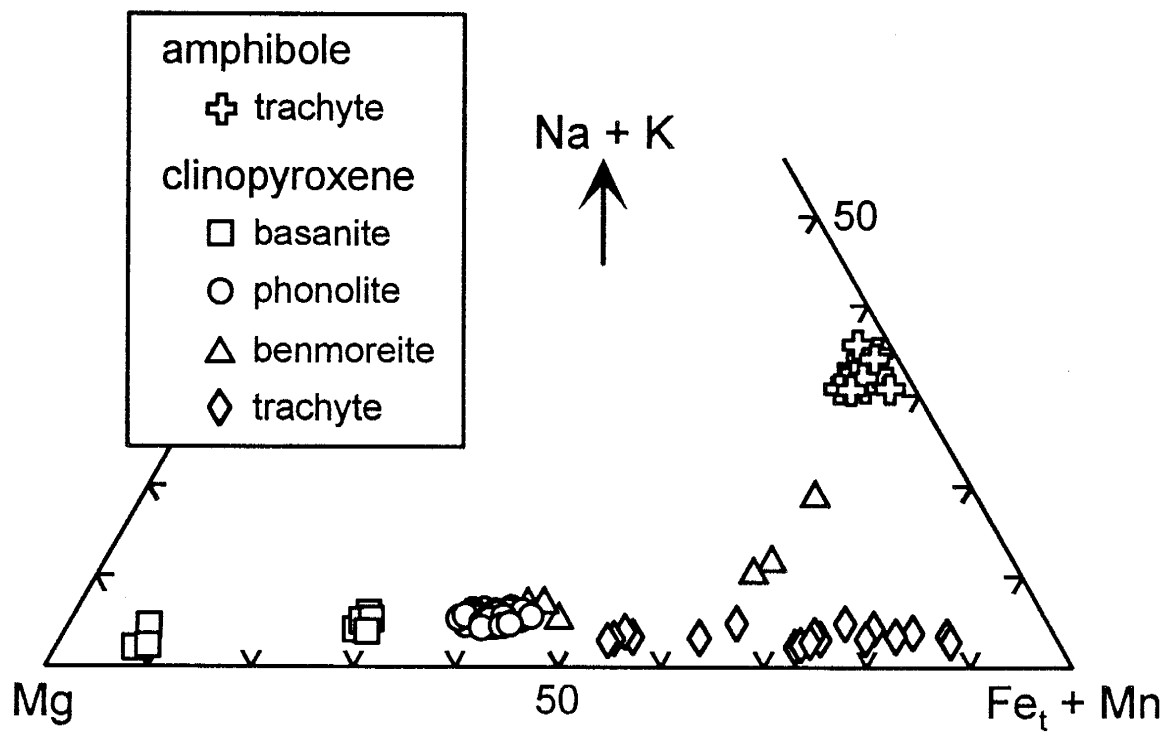

Figure 5. Electron microprobe analyses of clinopyroxenes and alkali amphibole plotted in terms of atomic % Na + K, Mg, Mn + Fe_t ($Fe_t = Fe^{2+} + Fe^{3+}$). Composition of clinopyroxenes from a stage-I benmoreite intrusion (open triangles) show elevated concentration of alkalis.

Sidley volcano are chemically zoned and microprobe analyses of several phenocrysts in a single flow reveal variable core compositions and significant chemical changes between cores and rims (Fig. 6). Rims show consistently higher *mg*-numbers and variable Ti + Al contents relative to cores, indicating disequilibrium conditions during crystal growth.

Feldspars

Feldspar phenocrysts are ubiquitous and typically are >10% of the mode. Anorthoclase is the dominant phenocryst phase in trachytes and phonolites, and within several tephriphonolite lavas, crystals up to 7 cm in length may comprise 50% of the rock. Anorthoclase-bearing phonolites exist at several alkaline volcanoes in Antarctica including Mt. Erebus (Kyle *et al.*, 1992) and other Marie Byrd Land volcanoes, Mt. Frakes (Boudette & Ford, 1966; LeMasurier *et al.*, 1990) and Mt. Hampton (Smellie *et al.*, 1993). Mt. Sidley anorthoclase contains inclusions of pyroxene, olivine, Fe-Ti oxides and apatite, sometimes as clots within phenocryst cores, which may have provided nuclei for anorthoclase growth. In several vitrophyric phonolites, resorbed anorthoclase crystals are embayed and display sieve textures.

Compositions range from labradorite (e.g., An_{54} Ab_{44} Or_2) in basanites and mugearites to sodic sanidine (e.g., Or_{44} Ab_{54} An_2) in tephriphonolites and trachytes (Fig. 7; Table 4; Appendix C3.3). Phenocrysts of feldspar show a progressive variation from two feldspars (oligoclase and sanidine) in tephriphonolites converging towards anorthoclase in phonolites. Furthermore, anorthoclase phenocrysts in phonolites show a progressive trend towards lower albite content with increasing stratigraphic height. The slightly higher

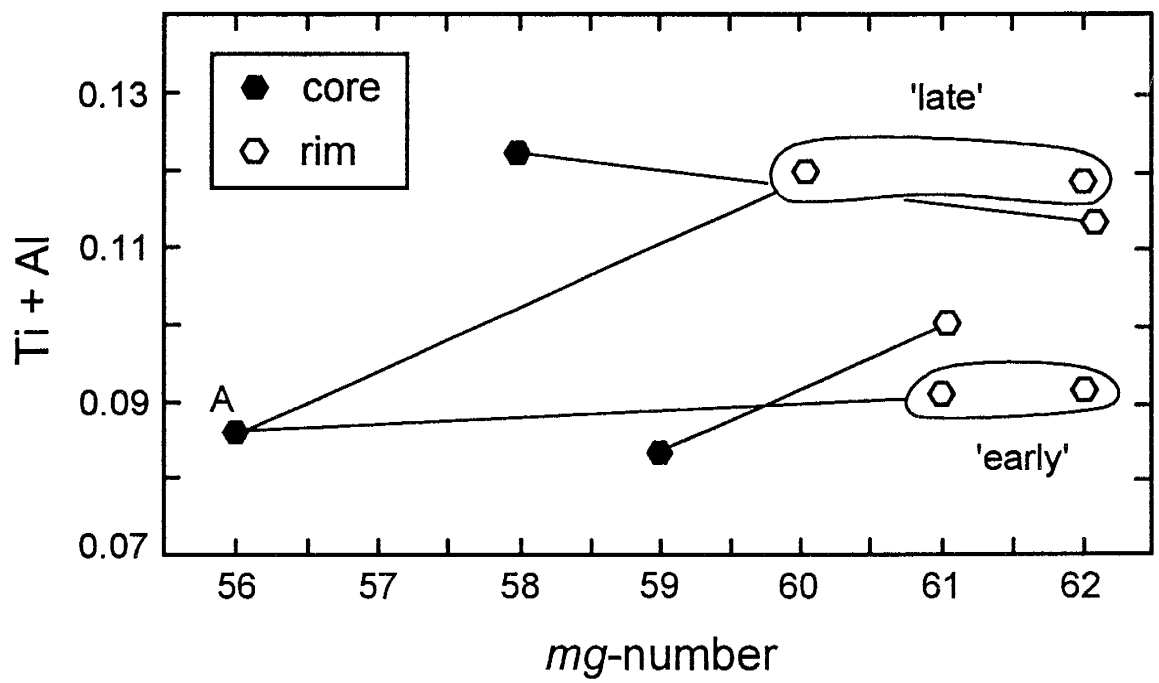

Figure 6. Clinopyroxene analyses from phonolite lavas of the Sidley volcano (stage I) plotted in terms of atomic % Ti + Al versus *mg*-number illustrating compositional variation for zoned phenocrysts. Tie-lines connect core and rim compositions of individual phenocrysts. Chemical variations within a single phenocryst (A) from sample K144, reflect 'early' and 'late' periods of crystallization shown by growth banding.

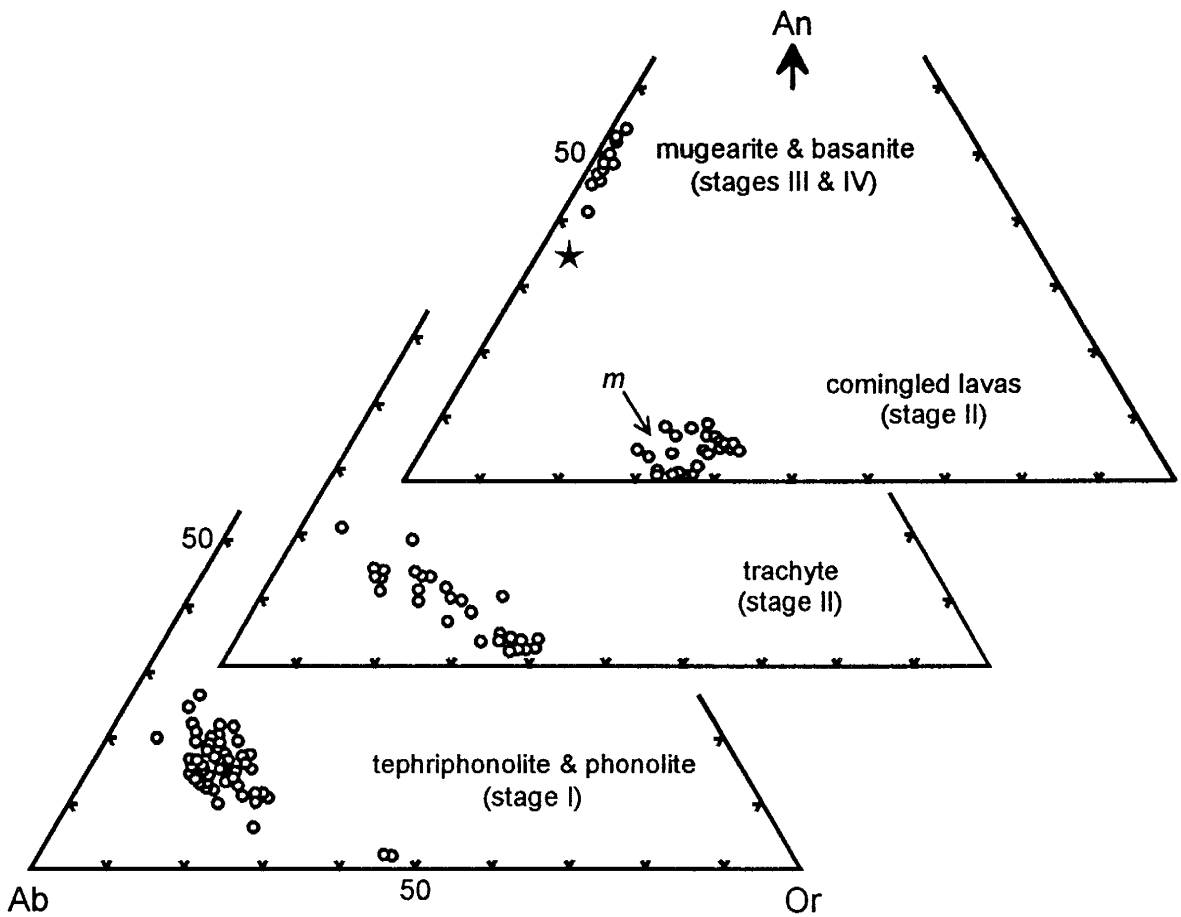

Figure 7. Composition of feldspars in Mt. Sidley volcanic rocks plotted in terms of molecular % An, Ab, Or. Plagioclase in the groundmass of a mafic enclave sample (comingled lavas) is designated by a solid star. The thermal minimum of the system Ab-Or is labeled *m*.

Table 4: Representative electron microprobe analyses of feldspars.

sample no	K168	K093	K166	K166	K114	K114	K141	K55	K066	K063
rock	bas	mug	ben	ben	tphn-phn	tphn-phn	phn	trac	trac	CL-host
position	core	core	core-	rim	core	core	core	core	core	core
	wt.% oxide									
SiO_2	53.79	56.19	64.95	66.78	62.65	65.97	64.41	63.73	66.47	67.76
TiO_2	0.10	-	-	-	-	-	-	-	-	-
Al_2O_3	29.73	27.13	20.73	18.52	22.34	18.91	21.44	21.30	18.82	18.90
FeO*	0.16	0.30	-	0.13	0.23	0.18	0.17	0.28	0.17	0.27
CaO	11.20	9.51	1.80	0.15	4.01	0.43	3.13	2.67	0.42	0.19
Na_2O	6.06	5.82	7.60	5.64	7.59	6.22	7.89	8.02	6.81	7.29
K_2O	0.20	0.35	4.23	8.31	2.70	7.47	2.85	3.50	6.72	5.97
sum	101.24	99.30	99.31	99.53	99.52	99.18	99.89	99.50	99.41	100.38
	formula based on 8 oxygens									
Si	2.412	2.545	2.910	3.012	2.810	2.985	2.867	2.861	2.992	3.007
Ti	0.003	-	-	-	-	-	-	-	-	-
Al	1.571	1.448	1.095	0.985	1.181	1.009	1.125	1.127	0.999	0.989
Fe^{2+}	0.006	0.011	-	0.005	0.009	0.007	0.006	0.011	0.006	0.010
Ca	0.538	0.461	0.086	0.007	0.193	0.021	0.149	0.128	0.020	0.009
Na	0.527	0.511	0.660	0.493	0.660	0.546	0.681	0.698	0.594	0.627
K	0.011	0.020	0.242	0.478	0.155	0.431	0.162	0.200	0.386	0.338
total	5.068	4.996	4.993	4.980	5.008	4.999	4.990	5.025	4.997	4.981
An %	50.00	46.47	8.70	0.72	19.15	2.10	15.02	12.48	2.00	0.92
Ab %	48.98	51.51	66.80	50.41	65.48	54.71	68.65	68.03	59.40	64.37
Or %	1.02	2.02	24.49	48.88	15.38	43.19	16.33	19.49	38.60	34.70

* Total Fe as FeO. Abbreviations as in previous tables.
Dashes mean not determined or not detected.

average albite content of feldspar in lavas of the Byrd volcano (Ab_{71}) relative to the uppermost lavas of the Sidley volcano (Ab_{64}) may be explained by depression of the ternary feldspar solvus at lower temperatures; a possible consequence of a higher water content in pre-eruptive magmas (Brown, 1993).

Potassic anorthoclase in both mafic and felsic components of comingled lavas show a relatively restricted compositional range (Fig. 7). Plagioclase (e.g., An_{35} Ab_{61} Or_4) is found as a groundmass phase only in mafic enclaves. Anorthoclase in comingled lavas approach the thermal minimum of the binary system An–Or (*m*; Fig. 7), suggesting hypersolvus precipitation of one feldspar during late-stage crystallization of highly fractionated liquids (Tuttle & Bowen, 1958; Brown, 1993). Abundant disequilibrium textures such as rounding and embayment of alkali feldspar phenocrysts, which are commonly rimmed or replaced by fine-grained intergrowths of groundmass phases (Fe-Mg silicates and Fe-Ti oxides), imply strong interaction between mafic and felsic components (e.g., Stimac & Pearce, 1992). Indeed, the presence of anorthoclase phenocrysts within mafic enclaves indicates mechanical transfer between lithologies (Gourgaud, 1991). Although alkali feldspars show strong reaction textures, the absence of more Ca-rich overgrowths would suggest that mingling of magmas occurred shortly before eruption.

Feldspars in trachytes display a wide compositional array from sodic sanidine (An_2 Ab_{60} Or_{38}) to oligoclase and calcic anorthoclase (An_{20} Ab_{74} Or_6 –An_{12} Ab_{67} Or_{21}); average $KAlSi_3O_8$ contents are higher (Or_{30}) than those in phonolites (Or_{16}). In trachytic lavas, feldspars are normally-zoned towards more potassic rims, enriched in $KAlSi_3O_8$ (up to 18%). Pronounced, oscillatory normal-zoning of anorthoclase in a benmoreite stock

reveals a pronounced increase in the Or molecule between cores and rims (sample K166; Table 4). Feldspars in phonolitic lavas from the upper portion of the Sidley succession (stage I) display discontinuously zoned rims enriched in the $CaAl_2Si_2O_8$ molecule by as much as 6% (~ 1·0 wt.% CaO). The occurrence of reversely zoned feldspars in these lavas is consistent with compositional changes in coexisting clinopyroxenes and olivines (discussed above), to the extent that the cores of each mineral are mantled by their higher temperature phase.

Spinel

Phenocrysts of spinel are present in all Mt. Sidley lavas. In the phonolites, euhedral crystals are associated with Fe-Mg silicates and apatite as glomerocrysts. Trachytic lavas contain higher modal abundances of microphenocrysts and groundmass phase oxides relative to other compositions. In trachytes, magnetite-maghemite fill interstices between coarse groundmass feldspars, indicating their precipitation as the last major liquidus phase.

Titanomagnetites are intermediate in solid solution between endmembers; ulvöspinel ($2FeO{\cdot}TiO_2$) and magnetite (Fe_3O_4) and range in concentration from 16 to 53 wt.% FeO, 7 to 29 wt.% Fe_2O_3 and 1 to 27 wt.% TiO_2 (Table 5; Appendix C3.4). Ulvöspinel contents range from 77% in mugearite to 58 to 75% in phonolites and 57% in trachytes. Spinels in basanite, are high in $MgAl_2O_4$ component and low in ulvöspinel (~ 2%).

Early crystal fractionation of olivine and pyroxene in basaltic magmas increases Fe_2O_3 relative to FeO, thus raising the oxygen content of the residual liquid (Morse, 1980). Elevated oxygen fugacity will cause magnetite to crystallize. However, the

dissolution of olivine with increasing SiO_2 concentration adds FeO back into the liquid, suppressing Fe_2O_3/FeO enrichment and reducing fO_2. This may cause magnetite saturation to occur later in the crystallization history (Juster *et al.,* 1989) and may explain late-stage precipitation of titanomagnetite in olivine-poor trachytes at Mt. Sidley.

Amphibole and mica

Alkali amphibole occurs within comingled lavas and as trace amounts within some trachytes. Brownish-red mica occurs within several mafic to intermediate lavas (stage III, Table 1) located south of Doumani Peak (Fig. 1). Optically identified, groundmass phase and microphenocrystic (≤ 0·2 mm) micas (phlogopite/biotite), occur as tabular or prismatic crystals with pseudohexagonal outlines and are often associated with olivine and magnetite glomerocrysts. Micas in benmoreite lavas are less abundant and darker-red in color than those within mugearite and phonotephrite lavas. Alkali amphibole within comingled lavas is strongly pleochroic (brownish-green, blue) and occurs as small (≤ 0·3 mm) euhedral crystals in both mafic and felsic lithologies, which are more abundant along mafic-felsic contacts. The crenulate interface between the two lithologies contains miarolitic cavities rimmed by feldspar and amphibole crystals. Amphibole becomes increasingly rare in the mafic component within several millimeters of the contact (unless vesicles are present) but persists several times further into the felsic host. In some instances, clinopyroxenes are mantled and partially replaced by alkali amphibole.

Microprobe analyses of amphibole compositions are present in Table 6 and Appendix C3.5. Stoichiometric amphiboles are arfvedsonite [$Na_3 Fe^{2+}_4 Fe^{3+} Si_8 O_{22} (OH)_2$]

Table 5: Representative electron microprobe analyses of spinel phenocrysts.

sample no	K168	K168	K93	K108	K122	K115	K144	K63
rock	bas	bas	mug	tphn	phn	phn	phn	CL-host
position	core	core	core	core	core	core	core	core
	wt.% oxide							
SiO_2	0.15	0.10	0.16	0.14	0.24	0.13	0.17	0.18
TiO_2	0.79	1.04	26.61	26.35	24.83	22.89	22.10	20.10
Al_2O_3	58.54	57.80	1.67	1.72	1.92	2.03	2.12	0.15
FeO*	22.43	22.66	66.79	67.76	68.81	69.81	71.19	75.32
MnO	0.39	0.21	0.72	1.09	1.32	1.29	1.37	0.88
MgO	16.86	16.63	1.54	1.77	1.53	1.43	1.56	-
CaO	-	-	-	-	-	-	0.07	0.09
sum	99.15	98.44	97.49	98.83	98.65	97.58	98.58	96.72
Fe_2O_3	7.28	7.17	15.44	17.10	19.48	22.79	25.05	29.38
FeO	15.88	16.21	52.90	52.37	51.28	49.30	48.65	48.89
total	99.88	99.16	99.04	100.54	100.60	99.86	101.09	99.67
	formula based on 4 oxygens							
Si	0.004	0.003	0.006	0.005	0.009	0.005	0.006	0.007
Ti	0.016	0.021	0.742	0.723	0.682	0.635	0.605	0.572
Al	1.817	1.810	0.073	0.074	0.083	0.088	0.091	0.007
Fe^{3+}	0.144	0.143	0.431	0.470	0.536	0.633	0.686	0.836
Fe^{2+}	0.350	0.360	1.640	1.598	1.567	1.521	1.482	1.547
Mn	0.009	0.005	0.023	0.034	0.041	0.040	0.042	0.028
Mg	0.661	0.658	0.085	0.096	0.083	0.079	0.085	-
Ca	-	-	-	-	-	-	0.003	0.003
total	3.000	3.000	3.000	3.000	3.001	3.001	3.000	3.000
Usp %	2	2	77	74	71	65	62	57

* Total Fe as FeO.

Cation proportions of Fe^{2+} and Fe^{3+} estimated using the procedures of Stromer (1983).
Percent ulvospinel (Usp) calculated using the model of Carmicaheal (1976).

Table 6: Representative electron microprobe analyses of amphibole.

sample	K063	K063	K063	K063	K063	K100
rock	CL-host	CL-host	CL-host	CL-host	CL-host	trac
	wt. % oxide					
SiO_2	50.20	49.98	48.67	49.10	49.49	52.01
Al_2O_3	0.23	0.23	0.60	0.62	0.60	0.11
TiO_2	0.01	0.18	2.99	3.91	3.46	-
MgO	0.30	0.54	1.31	1.34	1.36	0.17
FeO*	35.31	34.86	33.72	31.64	31.55	31.17
MnO	1.40	1.19	0.92	0.95	0.74	1.18
CaO	1.07	1.92	3.97	3.73	4.23	2.85
Na_2O	8.07	6.25	6.33	6.70	6.35	10.77
K_2O	1.04	1.35	1.25	1.33	1.30	0.01
sum	97.63	96.50	99.76	99.32	99.08	98.27
FeO	28.55	26.85				
Fe_2O_3	7.51	8.91				
total	98.38	97.39				

Sum of recalculated cations partitioned into Z- and Y-sites set to 13.

Si	7.993	7.987
Al $^{(IV)}$	0.007	0.013
sum Z	8.000	8.000
Al $^{(VI)}$	0.037	0.030
Ti	0.001	0.022
Mg	0.071	0.129
Fe^{3+}	0.900	1.071
Fe^{2+}	3.802	3.587
Mn	0.189	0.161
sum Y	5.000	5.000
Ca (M_4)	0.183	0.329
Na (M_4)	1.817	1.671
Na (A)	0.674	0.265
K (A)	0.211	0.275
sum X	2.885	2.540
X+Y+Z	15.885	15.540

Recalculation is nonstoichiometric. All Ca partitioned into the A-site.

Si	7.719	7.747	7.807	8.248
Al	0.112	0.115	0.112	0.021
Ti	0.357	0.464	0.410	-
Mg	0.310	0.315	0.320	0.040
Fe^{2+}	4.473	4.175	4.162	4.134
Mn	0.124	0.127	0.099	0.159
Ca	0.675	0.631	0.715	0.484
Na	1.947	2.050	1.942	3.312
K	0.253	0.268	0.262	0.002
total	15.970	15.892	15.829	16.400

* Total Fe as FeO.

Amphibole structural formulae based on 23 oxygens and 2 OH groups and follows the procedure of Spear & Kimball (1984).

consistent with International Mineralogical Association nomenclature (Leake, 1978; Mogessie *et al.*, 1990).

Arfvedsonite is a product of magmatic-subsolidus processes, principally found in differentiated alkaline magmas (Ernst, 1962; Wolff & Toney, 1993). Compositional trends towards alkali-enrichment and Ca + Mg depletion (Figs. 3 and 5) are similar to the observed amphibole trends within the alkaline Ilímaussaq complex (Larsen, 1976) and the Kungnat Field (Stephenson & Upton, 1982), south Greenland. Such changes in amphibole chemistry can be partly explained by the coupled substitution of (Na, K) + Si for Ca + Al, occurring when residual liquids become peralkaline.

It is clear from textural evidence that alkali amphibole within comingled lavas may have, in part, crystallized from a vapor phase as a direct result of degassing and volatile transfer between contrasting magma types while mingling (cf. Gamble, 1979). In addition, the occurrence of trace amounts of microphenocrystic alkali amphibole within trachyte lavas suggests crystallization of a late-stage liquidus phase.

Feldspathoids and apatite

Feldspathoids are found exclusively in strongly undersaturated rocks (up to 26% normative *Ne*) within the stage I succession (Table 1). Minor nepheline microphenocrysts occur in phonolite compositions. Optically identified leucite is present in the groundmasses of some phonolitic lavas and filling interstices between feldspar laths within a benmoreite stock.

Microphenocrysts of apatite are common as an accessory phase in stage I rocks (Table 1). Apatite, along with olivine, pyroxene and magnetite, forms glomeroporphyritic clusters in tephriphonolite lavas.

GEOCHEMISTRY

Methodology

One hundred and seven representative whole-rock samples from Mt. Sidley and 48 samples from the neighboring and younger (< 2 Ma) Mt. Waesche volcano (Appendix C4.1) were analyzed for major, trace and rare earth elements by X-ray fluorescence (XRF) and instrumental neutron activation analysis (INAA) (Jacobs *et al.*, 1977; Lindstrom & Korotev, 1982). XRF analyses were made at the University of Keele, U.K., on an ARL8420 spectrometer. Major element data used in plots are recalculated on a 100% volatile free basis with total Fe as FeO. Representative major and trace element analyses for Mt. Sidley and Mt. Waesche are presented in Table 7 along with *mg*-number [atomic % = $(Mg/Mg + Fe^{2+})$]. The INAA analyses made at New Mexico Tech used two 20% efficient high-purity Ge detectors (Hallett & Kyle, 1993). Rock powders packed in high purity silica vials were irradiated at the 10 MW University of Missouri Research Reactor for 30 to 40 hours at a thermal neutron flux of $2{\cdot}4 \times 10^{13}$ n.cm^{-2} sec^{-1}. Based on repeat analysis of rock standards, BCR-1 and G-2, estimated analytical precision is < 1% for Sc, Fe, Co, La, Sm; < 3% for Ce, Eu, Hf, Ta, Th, Lu; < 5% for Na, Rb, Ba, Tb; and < 10% for Cr, Sb, Nd, Cs and U.

Table 7: Representative analyses of whole-rocks from Mt. Sidley and selected samples from the Mt. Waesche volcano.

	Mt. Sidley rocks																		
sample	K109	MB27.5	K133	K095	MB32.11	K093	K099	K166	K097	K108	K114	K144	K131	K132	MB35.2	K055	MB32.4	K082	MB33.2
rock type	bas	bas	bas	bas	mug	mug	mug	ben	ben	tphn	tphn-phn	phn	tphn	phn	phn	trac	trac	trac	trac
group	stage IV	stage IV	stage IV	stage IV	DPM	SFM	SFM	stage I	stage IV	Bv	Bv	Sv	Bv	Sv	Sv	*LT*	*N*	*N*	*LT*
SiO_2	44.67	44.71	45.88	47.73	50.62	51.31	51.38	55.17	55.75	55.90	56.03	56.12	56.20	56.31	57.02	61.94	62.51	62.81	63.17
TiO_2	3.03	3.15	3.05	2.48	1.75	1.57	1.54	0.96	0.95	1.26	0.77	0.61	0.83	0.30	0.25	0.47	0.32	0.27	0.65
Al_2O_3	15.03	15.68	16.11	17.36	16.71	16.92	16.91	17.62	17.41	16.62	19.52	19.75	19.75	19.76	19.17	17.87	15.63	16.37	15.50
Fe_2O_3	13.30	13.65	13.65	12.53	10.24	13.70	14.08	8.67	11.20	10.07	6.49	6.78	6.47	6.38	7.17	5.51	5.98	5.50	6.77
MnO	0.17	0.18	0.21	0.19	0.17	0.24	0.25	0.23	0.25	0.31	0.18	0.20	0.17	0.21	0.25	0.16	0.16	0.15	0.19
MgO	8.35	7.44	5.84	5.18	4.48	2.49	2.30	1.23	1.13	1.03	0.72	0.63	0.91	0.24	0.04	0.29	-	0.03	0.34
CaO	9.33	9.11	7.95	7.30	7.11	5.22	5.17	3.44	3.71	2.87	2.71	2.11	3.14	1.16	1.43	2.04	1.05	1.45	2.31
Na_2O	4.42	4.65	5.40	5.16	4.79	5.94	6.21	5.71	6.54	7.86	7.57	8.77	8.30	9.51	9.06	6.81	7.22	6.88	5.68
K_2O	1.45	1.43	1.96	1.63	2.13	2.27	2.25	4.76	2.92	4.12	4.46	5.19	4.13	5.69	5.19	4.82	5.01	5.50	4.64
P_2O_5	0.58	0.76	0.86	0.61	0.47	1.13	1.27	0.35	0.58	0.46	0.27	0.21	0.31	0.08	0.15	0.11	0.11	0.05	0.24
LOI	0	0	0	0	1.13	0	0	1.74	0	0	1.52	0	0	0.18	0.41	0.08	2.06	1.34	0.68
total	100.33	100.76	100.91	100.17	99.60	100.79	101.36	99.88	100.44	100.50	100.24	100.37	100.21	99.82	100.14	100.10	100.05	100.35	100.17
mg-number	55	52	46	45	46	26	24	22	17	17	18	16	22	7	1	9	-	1	9
Sc	21.8	20.6	17.3	15.0	16.7	6.5	5.5	5.3	6.1	6.4	3.3	2.7	3.5	1.4	1.1	3.2	1.1	0.7	5.5
V	193	191	137	143	113	11	4	3	9	6	-	-	2	1	-	1	-	-	2
Cr	145	68	43	-	60	-	-	-	-	-	-	-	-	-	-	-	-	-	-
Ni	136	111	54	31	40	11	9	4	6	5	4	4	4	5	6	4	5	3	6
Cu	80	93	49	47	48	39	42	16	25	16	16	17	17	9	15	13	12	9	16
Zn	87	85	92	81	86	91	97	109	88	169	103	110	98	168	185	90	149	143	127
Ga	22	19	20	20	23	24	20	29	26	36	31	31	33	44	44	31	35	33	31
Rb	35	32	55	44	40	56	56	176	87	105	140	227	141	256	249	214	203	199	165
Sr	752	877	950	715	492	734	756	199	562	210	322	165	371	16	49	220	6	1	133
Y	25	25	34	30	30	40	41	79	41	82	58	68	63	107	107	64	76	75	63
Zr	254	241	334	307	268	433	443	1258	584	995	962	1478	1147	1962	1869	923	1052	935	680
Nb	60	59	96	71	58	93	97	215	117	199	214	263	211	343	341	146	179	160	114
As	1.0	1.2	1.0	-	2.0	-	1.3	-	2.1	3.3	-	6.9	3.1	5.7	8.9	7.7	4.7	3.7	3.3
Sb	-	-	-	-	0.1	0.1	0.1	0.1	0.2	0.2	0.2	0.5	0.3	0.6	0.5	0.3	0.3	0.2	0.2
Cs	0.58	0.42	0.59	0.55	0.50	0.52	0.44	5.84	0.91	1.06	1.94	6.46	1.83	4.65	4.99	4.18	5.49	5.95	7.93
Ba	344	419	666	404	500	662	645	583	891	717	663	350	618	-	105	566	29	-	823
La	40.70	42.9	68.80	52.50	42.50	80.60	83.00	131.70	101.10	112.60	98.90	117.70	94.50	162.50	172.65	109.40	117.80	112.60	87.00
Ce	82.8	84.6	134.0	99.2	82.8	153.9	160.9	238.9	187.1	214.6	201.7	211.5	176.9	300.1	312.0	199.1	225.2	214.1	169.8
Nd	32.0	36	51.0	39.0	32.5	62.0	60.0	82.0	67.0	83.0	60.0	64.0	62.0	97.0	105.0	66.0	96.0	75.0	70.0
Sm	7.60	7.88	11.27	7.80	7.23	11.42	12.00	15.33	11.31	16.80	12.56	12.60	11.99	17.80	19.41	13.65	15.58	15.70	12.50
Eu	2.43	2.57	3.20	2.39	2.26	3.31	3.51	3.41	3.11	4.79	3.36	2.41	3.55	1.78	1.77	2.20	0.63	0.67	2.36
Tb	0.96	0.93	1.24	1.00	0.94	1.31	1.33	2.15	1.28	2.37	1.77	1.85	1.71	2.74	2.95	1.91	2.20	2.18	1.74
Yb	1.84	1.71	2.63	2.47	2.65	3.39	3.48	8.02	3.80	7.82	6.30	8.02	6.61	11.70	11.26	6.84	7.87	7.28	5.80
Lu	0.28	0.25	0.33	0.34	0.39	0.52	0.50	1.19	0.54	1.12	0.94	1.14	0.96	1.74	1.59	1.02	1.15	1.07	0.80
Hf	6.00	5.83	8.12	6.70	5.85	9.20	9.50	24.90	12.81	20.60	21.50	27.90	22.40	39.30	36.95	19.70	22.50	20.30	15.37
Ta	4.30	3.87	6.57	5.20	3.51	6.30	6.50	15.00	8.15	12.80	13.70	17.20	13.60	22.20	21.75	10.30	11.80	10.90	7.84
Pb	7	8	11	6	4	7	9	20	15	7	5	20	8	25	27	25	19	22	23
Th	5.1	5	7.9	7.5	5.9	8.9	8.7	31.6	12.9	17.8	21.0	41.0	22.9	44.9	42.8	28.2	27.3	23.2	21.4
U	1.5	1.5	2.5	2.2	7.1	2.9	1.7	3.2	3.5	4.5	1.7	12.0	6.3	12.6	12.7	8.6	7.3	6.3	5.3

Table 7 (continued)

	Mt. Sidley hybrids							*Mt. Waesche rocks*									
sample	MB33.8	MB33.3	K063A	K063B	MB35.5	MB33.11	MB35.1	MB4.1	K19	K31	MB21.1	K01	MB11.2	MB9.1	MB15.1	MB45.7	MB8.1
rock type	trac	trac	trac	ben	phn	trac	trac	akb	akb	haw	mug	phntph	tphn	phn	trac	trac	rhy
group	*HT*	*HT*	CL-host	CL-encl	bf	bf	bf										
SiO_2	67.57	68.30	65.88	57.22	56.71	59.73	61.98	45.62	45.84	46.12	50.39	51.59	55.97	56.35	59.71	60.41	73.88
TiO_2	0.21	0.26	0.38	1.12	0.19	0.75	0.27	2.03	2.55	2.58	1.77	1.66	1.02	0.56	0.60	0.43	0.27
Al_2O_3	13.58	13.17	14.88	15.84	19.49	17.62	15.77	16.54	15.03	16.56	18.42	17.41	17.38	19.46	17.84	16.23	10.03
Fe_2O_3	5.92	5.84	5.46	7.86	7.15	7.36	7.02	12.38	12.87	12.62	10.55	11.47	8.87	6.26	7.53	9.03	5.21
MnO	0.16	0.15	0.12	0.12	0.25	0.19	0.20	0.18	0.19	0.18	0.18	0.27	0.23	0.17	0.23	0.28	0.10
MgO	-	-	0.35	3.31	-	0.46	0.13	7.63	9.26	7.17	3.01	2.00	1.35	0.83	0.29	0.01	-
CaO	0.80	0.70	1.20	4.43	1.20	2.28	1.30	10.92	9.68	9.92	8.53	5.79	3.54	2.43	2.27	1.81	0.29
Na_2O	5.98	6.07	6.48	5.61	9.41	5.19	7.45	3.31	3.55	4.05	5.35	7.06	7.90	8.97	7.88	7.79	4.93
K_2O	4.91	4.98	5.08	4.03	5.39	5.71	5.13	0.58	1.17	1.05	1.53	2.25	3.71	4.63	3.61	3.83	4.64
P_2O_5	0.09	0.08	0.01	0.13	0.12	0.21	0.11	0.48	0.59	0.55	0.53	0.56	0.37	0.19	0.19	0.15	0.09
LOI	0.32	0.21	0	0.05	0.24	0.95	0.41	0.40	0	0	0	0	0	0.50	0.10	0.30	0.30
total	99.54	99.76	99.84	99.72	100.15	100.45	99.77	100.07	100.73	100.80	100.26	100.06	100.34	100.35	100.25	100.27	99.74
mg-number	-	-	11	45	-	11	4	55	59	53	36	26	23	21	7	< 1	-
Sc	0.3	0.4	2.5	12.7	0.8	4.9	1.0	26.0	25.0	24.0	16.0	8.0	6.0	4.0	2.0	1.0	-
V	13	1	3	78	-	-	3	223	202	211	88	2	22	19	1	-	-
Cr	-	-	15	93	-	-	-	158	412	170	10	-	-	1	-	-	-
Ni	10	9	8	48	7	7	8	80	180	99	20	5	12	12	5	7	8
Cu	22	14	9	57	14	26	17	73	84	73	59	32	26	21	15	16	8
Zn	271	212	130	107	186	133	213	84	91	86	88	11	126	108	129	151	317
Ga	48	46	34	24	44	33	41	23	19	21	23	22	29	33	31	32	37
Rb	672	593	244	96	275	395	350	11	25	19	31	51	90	128	80	86	329
Sr	-	-	23	176	1	76	8	494	581	573	513	589	201	115	221	71	9
Y	210	190	82	40	109	93	123	22	27	27	34	47	62	61	63	69	216
Zr	2291	2260	963	308	2018	1981	1850	135	253	222	269	364	674	818	673	689	1978
Nb	516	405	154	59	369	355	309	27	52	42	59	102	132	165	124	133	247
As	13.3	-	1.7	3.1	8.7	5.0	9.4	0.4	-	1.3	1.1	1.5	2.4	4.0	3.8	1.3	4.1
Sb	1.1	0.6	0.2	0.1	0.6	0.5	0.6	-	-	-	-	0.1	0.2	0.1	-	0.1	0.3
Cs	34.10	10.69	5.84	4.15	6.27	18.45	8.40	0.20	0.50	0.20	0.40	0.60	1.20	2.10	1.70	1.50	7.60
Ba	-	-	-	264	-	450	-	199	250	224	457	703	668	263	1023	1254	67
La	331.00	270.80	122.50	48.20	176.80	181.85	199.50	20.20	39.00	32.10	43.00	70.00	85.80	87.00	81.50	88.80	239.00
Ce	600.0	494.0	235.6	94.6	325.0	344.0	367.0	44.8	80.9	67.5	87.5	135.5	166.0	166.3	161.3	177.1	460.0
Nd	175.0	181.0	77.5	40.0	112.0	106.0	134.0	21.0	34.0	25.0	32.0	53.0	57.0	58.0	63.0	62.0	173.0
Sm	32.75	34.20	16.81	8.16	19.88	18.81	24.50	5.03	7.29	6.99	7.46	11.37	13.30	10.64	12.43	13.98	36.70
Eu	0.67	0.49	0.58	1.51	1.27	2.32	1.09	1.81	2.30	2.24	2.69	3.64	2.82	1.36	3.54	3.79	2.34
Tb	5.64	5.30	2.39	1.12	2.91	2.72	3.46	0.73	0.94	0.98	1.09	1.51	1.90	1.47	1.83	2.09	6.10
Yb	20.50	18.50	8.01	3.41	11.90	11.12	11.95	1.78	2.05	2.22	2.96	4.23	5.80	6.34	6.10	6.69	19.80
Lu	2.83	2.53	1.18	0.51	1.76	1.62	1.78	0.26	0.28	0.31	0.39	0.59	0.85	0.92	0.88	0.97	2.79
Hf	57.15	52.50	23.30	7.36	40.45	41.20	39.00	3.60	5.91	5.24	6.17	8.07	14.29	17.06	14.72	15.00	49.40
Ta	34.80	27.30	11.05	4.36	24.20	23.90	20.80	1.58	3.48	2.80	3.64	6.54	8.34	10.65	8.01	8.35	16.80
Pb	95	29	32	30	26	42	48	4	7	9	6	4	9	8	4	6	80
Th	110.4	86.8	29.5	8.1	47.7	100.3	53.8	1.7	4.1	2.8	4.5	7.5	11.9	16.5	11.3	12.1	50.8
U	33.4	23.7	8.7	4.2	14.5	10.7	10.9	0.5	1.1	1.2	1.2	2.1	2.8	4.4	3.1	3.7	11.4

Major elements are given in wt. %, trace elements in ppm. LOI, loss on ignition; mg-number = atomic % $Mg/(Mg+Fe^{2+})$, where Fe^{2+} is calculated using $FeO = 0.9(Fe_2O_3)$.

Abbreviations for rock types include, bf = black pyroclastic fall; akb = alkali basalt; haw = hawalite; phntph = phonotephrite; rhy = rhyolite;

Other abbreviations are defined in previous tables. Sample group refers to rock subdivisions based on stratigraphy and chemical characteristics (see text).

Neodymium isotopic analyses for 16 whole-rock samples from Mt. Sidley (Table 8) and 10 from Mt. Waesche (Table 8; Appendix C5.1) were made on a 5-collector VG Isotopes 354 mass spectrometer at the NERC Isotope Geosciences Laboratory, Keyworth, U.K. Nd data were normalised to a $^{144}Nd/^{146}Nd$ of 0·7219. The J&M in-house standard was used to correct data to an equivalent value of 0·511850 for the La Jolla standard. Analyses of BCR-1 gave a $^{143}Nd/^{144}Nd$ ratio of 0·512628 ±10 (n=3) and for JB-1 0·512780 ±41(n=6). Nd and Sm concentrations were determined by isotope dilution and gave Sm/Nd ratios averaging 0·2279 for BCR-1 and 0·1933 for JB-1. Strontium isotopic analyses for 22 whole-rock and 4 anorthoclase separates from Mt. Sidley (Table 8) and 16 whole-rock samples from Mt. Waesche (Table 8; Appendix C5.1) were made on a Finnegan MAT 262 instrument using static multiple collection. Long term drift (due to cup efficiency changes) is monitored by running NBS987 in each magazine loading and correcting to a preferred value of 0·710230. During the present work, BCR-1 gave a $^{87}Sr/^{86}Sr$ of 0·704991 ±14 (n=2) and JB-1 gave 0·704111 ±32 (n=5). These results unfortunately suggest that JB-1 is not a homogeneous standard. Rb and Sr concentrations determined by isotope dilution and XRF agree within 10%.

Lead isotopes were measured for 3 rock samples (Appendix C5.2) using a multicollector VG Sector TIMS at the University of Michigan (Mukasa *et al.*, 1987; 1991). A procedural blank run with the samples had 0·2 ng of Pb, a small amount (< 0·5%) of the total Pb in each sample. Within-run precisions for the measured Pb ratios were better than 0·05% at the 95% confidence level, although replicate analyses of NIST standard NBS-981 required applying a fractionation factor of 0·102 per a.m.u.

Table 8: Isotopic analyses of Mt. Sidley volcanic rocks and selected samples from Mt. Waesche.

sample	type / stage	age[a]	Sm[b]	Nd[b]	$^{147}Sm/^{144}Nd$	$^{143}Nd/^{144}Nd_m$	$^{143}Nd/^{144}Nd_I$	1σ	εNd	Rb[c]	Sr	$^{87}Rb/^{86}Sr$	$^{87}Sr/^{86}Sr_m$	$^{87}Sr/^{86}Sr_I$	1σ	$\delta^{18}O$[d]
Mt. Sidley																
MB27.5	bas / IV	4.2	7.66	39.08	0.1185	0.512901	0.512898	6	5.1	32	877	0.1055	0.702994	0.702988	7	5.2
	duplicate	4.2	7.74	39.49	0.1185	0.512899	0.512896	3	5.1	32	877	0.1055	0.703000	0.702994	7	–
K168	bas / IV	4.18	7.76	39.80	0.1179	0.512896	0.512893	9	5.0	36	877	0.1187	0.703038	0.703031	10	5.7
MB32.11	DPM / III	4.3	7.44	38.13	0.1179	0.512851	0.512848	4	4.2	40	492	0.2351	0.703165	0.703151	9	1.8
K99	SFM / III	4.3	–	–	–	–	–	–	–	56	756	0.2142	0.703055	0.703042	7	6.2
K134	ben / III	4.3	–	–	–	–	–	–	–	74.70	483.46	0.4468	0.703078	0.703051	7	6.2
K97	ben / III	4.3	11.19	69.14	0.0979	0.512866	0.512863	8	4.5	76.10	490.71	0.4485	0.703016	0.702989	6	5.7
K54	*N*-trac(ui) / III	4.37	–	–	–	–	–	–	–	–	–	–	–	–	–	-1.0
K137	*N*-trac(wf) / III	4.25	–	–	–	–	–	–	–	218.40	3.81	166.1717	0.714708	0.704879	76	5.3
MB29.4	*LT*-trac / II	4.53	12.53	66.43	0.1140	0.512879	0.512876	7	4.7	163.04	7.23	65.2317	0.709201	0.705005	21	5.8
K105	*LT*-trac / II	4.55	–	–	–	–	–	–	–	291.99	36.88	22.9018	0.704768	0.703288	18	4.1
K55	*LT*-trac / II	4.6	13.78	76.08	0.1095	0.512835	0.512832	8	3.9	191.76	195.54	2.8360	0.703337	0.703152	7	5.8
K66	*LT*-trac / II	4.6	10.23	53.12	0.1164	0.512824	0.512820	6	3.6	124.32	78.30	4.5917	0.704119	0.703819	7	7.6
K63A	*LT*- (host) / II	4.6	16.91	90.60	0.1128	0.512810	0.512807	6	3.4	231.16	20.62	32.4200	0.705202	0.703084	20	5.4
K63B	*LT*- (encl) / II	4.6	7.89	40.37	0.1182	0.512833	0.512829	8	3.8	88.10	163.46	1.5586	0.703201	0.703099	7	5.8
MB33.3	*HT*-trac / II	4.58	33.01	183.18	0.1089	0.512813	0.512810	7	3.4	–	–	–	–	–	–	5.4
MB33.8	*HT*-trac / II	4.6	34.51	189.94	0.1098	0.512806	0.512803	3	3.3	–	–	–	–	–	–	5.1
MB35.5	phn (bf) / II	4.7	–	–	–	–	–	–	–	252.80	4.20	174.2270	0.715455	0.703826	94	5.3
MB38.3	tphn (bf) / II	4.7	15.23	84.42	0.1090	0.512816	0.512813	8	3.5	266.95	41.84	18.4542	0.705332	0.704100	12	–
MB33.11	trac (bf) / II	4.7	–	–	–	–	–	–	–	372.02	72.99	14.7405	0.704083	0.703099	11	–
MB42.3	phn / I (Sv)	5.08	13.09	74.46	0.1063	0.512859	0.512855	6	4.3	192.48	245.03	2.2716	0.703124	0.702960	8	2.4
K144	phn / I (Sv)	5.0	12.62	70.72	0.1078	0.512882	0.512879	9	4.8	207.92	150.87	3.9853	0.703140	0.702868	8	5.7
K115	phn / I (Sv)	5.0	–	–	–	–	–	–	–	205.71	153.94	3.8644	0.703107	0.702833	7	6.2
MB35.2	phn / I (Sv)	5.0	18.71	102.75	0.1101	0.512863	0.512859	4	4.4	234.65	47.96	14.1505	0.704044	0.703039	11	5.2
K108	tphn / I (Bv)	5.53	17.06	89.40	0.1154	0.512886	0.512882	7	4.9	98.83	194.77	1.4673	0.703052	0.702937	7	3.1
K122	tphn / I (Bv)	5.6	–	–	–	–	–	–	–	105.89	279.99	1.0936	0.703019	0.702932	7	3.8
K137an	anorthoclase	4.25				–				90.71	9.80	26.7780	0.705248	0.703632	15	7.8
MB29.4an	anorthoclase	4.53				–				69.35	12.86	15.5967	0.705210	0.704207	15	8.4
MB35.5an	anorthoclase	4.7				–				100.08	11.10	26.0831	0.705020	0.703279	15	6.5
MB42.3an	anorthoclase	5.08				–				21.89	788.33	0.0803	0.702948	0.702942	7	6.1
K105an	anorthoclase	4.55				–				–	–	–	–	–	–	5.1
MB33.3an	anorthoclase	4.58				–				–	–	–	–	–	–	6.6
K54an	anorthoclase	4.37				–				–	–	–	–	–	–	6.0
Mt. Waesche																
MB.4.1	akb	0.1	–	–	–	–	–	–	–	11	494	0.0644	0.702681	0.702681	7	–
K19	akb	0.5	7.33	37.49	0.1182	0.512877	0.512876	9	4.6	25	581	0.1244	0.702732	0.702731	6	–
K01	phntph	0.1	11.18	59.48	0.1137	0.512886	0.512885	8	4.8	51	589	0.2504	0.702697	0.702697	7	–
MB.11.2	tphn	0.5	13.05	68.61	0.1150	0.512890	0.512890	9	4.9	90	201	1.2948	0.702728	0.702719	7	–
MB.15.1	trac	0.5	–	–	–	–	–	–	–	80	221	1.0468	0.702760	0.702753	7	–

abbreviations: akb = alkali basalt; bas = basanite; phntph = phonotephrite; ben = benmoreite; tphn = tephriphonolite; phn = phonolite; trac = trachyte; DPM and SFM = Doumani Peak and south flank mugearites, respectively. ui = unwelded ignimbrite pumice; wf = welded fall; bf = black fall; Sv = Sidley volcano; Bv = Byrd volcano; K63A and B = comingled lava host and enclave samples. See *Trachyte Series* for definition of *N*-, *LT*- and *HT*-trachyte subdivisions.

[a] in millions of years (Ma); Mt. Sidley $^{40}Ar/^{39}Ar$ determinations from Panter *et. al.* (1994), single decimal values indicate interpolated ages.

[b] Sm and Nd concentrations (ppm) determined by isotope dilution.

[c] Rb and Sr concentrations (ppm) determined by XRF and isotope dilution (2 significant figures).

[d] $\delta^{18}O$ values in per mil (‰).

Oxygen isotopes were measured for 32 whole-rock and 7 anorthoclase separates (Table 8; Appendix C5.3) at New Mexico Tech using a Finnigan MAT delta-E mass spectrometer. Oxygen was liberated from samples by reacting them with ClF_3 at temperatures in excess of 450°C for 6-8 hours within a stainless steel, high-vacuum extraction system. $\delta^{18}O$ values are reported in the ‰ notation relative to Standard Mean Ocean Water (SMOW; Craig, 1961). Based on analyses of quartz standard NBS-28 and an in-house basalt standard (Parido-1; Hallett, 1994) the estimated analytical precision is ± 0·2 ‰.

Major Element Chemistry

Alkaline magmas erupted at Mt. Sidley are dominated by strongly silica-undersaturated sodic lavas, ranging from basanite to anorthoclase phonolite and comenditic trachyte (Fig. 8). Trachytic lavas and tephra range from silica-undersaturated through silica-oversaturated compositions and both phonolites and trachytes encompass evolved peralkaline types (molecular $Na_2O + K_2O/Al_2O_3 \leq 1{\cdot}2$). Several siliceous trachytes contain nearly 70 wt.% SiO_2 and up to 15% normative quartz (*Qz*-trachytes) but modal quartz is absent. In Fig. 9, major element variations are evaluated using SiO_2 content as a broad index of differentiation. Samples display a decrease in FeO_t, MgO, CaO and P_2O_5, with increasing silica concentration (Fig. 9). The phonolites and trachytes differ in their relative SiO_2 contents; phonolites have restricted values between 56 and 58 wt.%, whereas trachytes display a wide range in SiO_2 from 60 to 70 wt.%. Nevertheless, phonolitic samples display nearly as much variation with respect to other element oxides as do the trachytes. The distinction between these two suites is illustrated by their relative

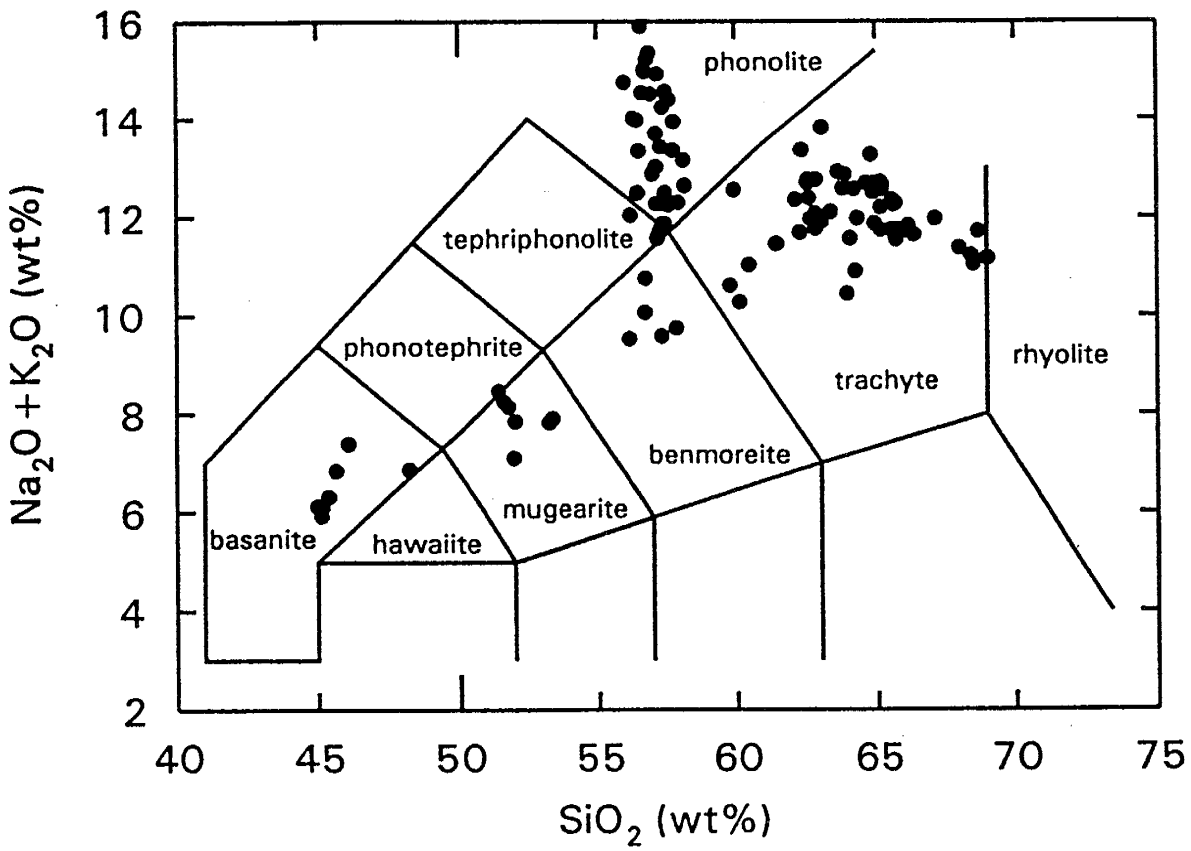

Figure 8. Classification of Mt. Sidley volcanic rocks on a total alkalis versus silica diagram (Le Bas *et al.*, 1986). Data plotted is normalized to 100% anhydrous.

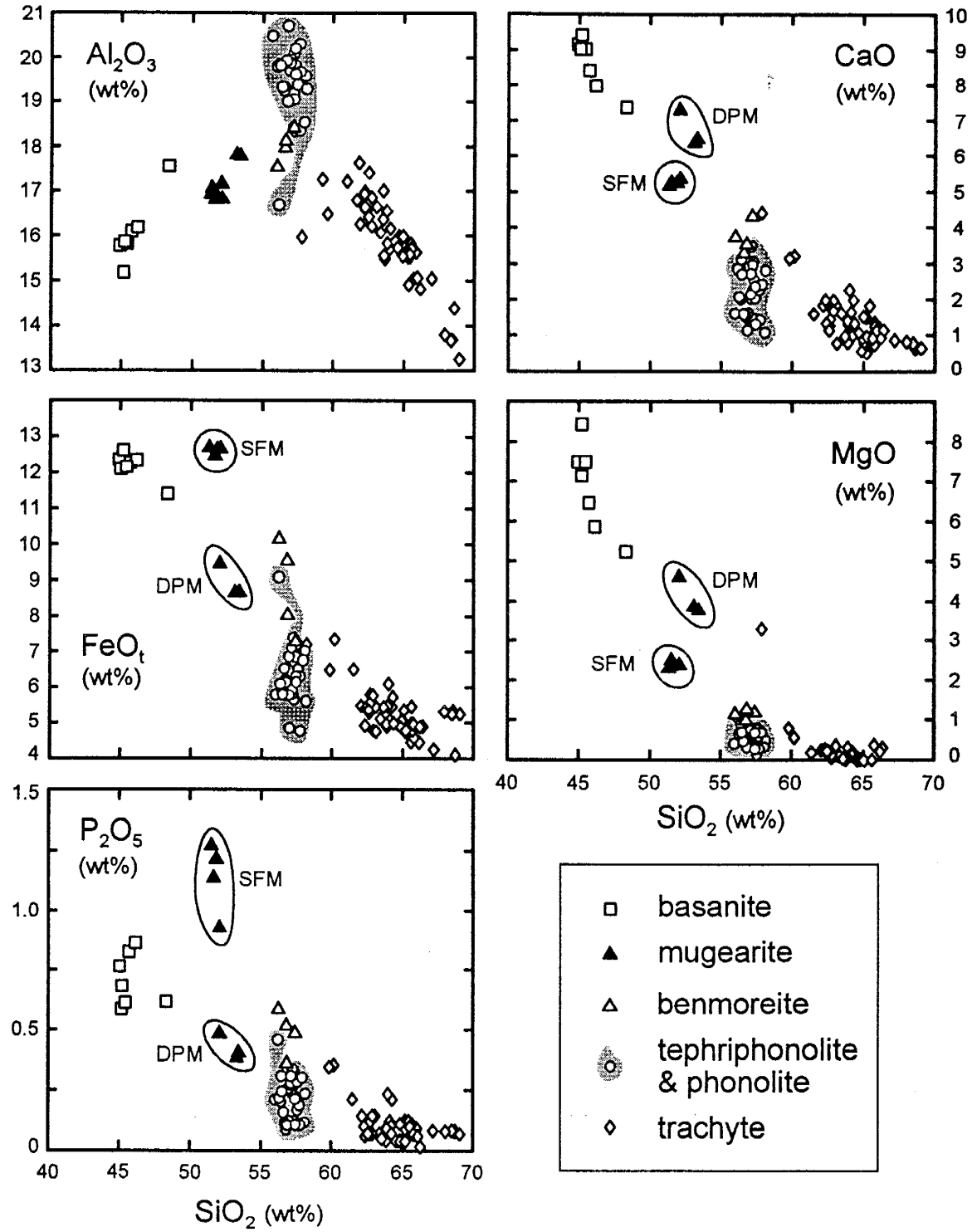

Figure 9. Variation of selected major elements with silica content. Note that phonolitic and trachytic analyses are set apart by their relative SiO_2 and Al_2O_3 contents. Mugearites are subdivided into two types: low MgO, high FeO_t & P_2O_5 lavas located on Mt. Sidley's southern flank (SFM); and higher MgO & CaO tephra from Doumani Peak (DPM).

Al_2O_3 contents (Fig. 9). For trachytes, the trend towards lower Al_2O_3 (18 to 13 wt.%) with higher SiO_2 concentration is best explained by fractionation dominated by feldspar. However, Al_2O_3 enrichment in phonolites (18 to 21 wt.%) would suggest extensive fractionation of Fe-Mg silicates with little feldspar loss. A similar trend for anorthoclase phonolites is observed at Mt. Erebus (The Erebus lineage of Kyle *et al.*, 1992).

Projected onto petrogeny's residua system (*Qz*- SiO_2, *Ne*- $NaAlSiO_4$, *Ks*- $KAlSiO_4$; Bowen, 1937) normative analyses of phonolites and trachytes fall into separate fields (Fig.10). Phonolites plot below the Ab–Or join and cluster around the 1 atm peritectic near the system's thermal minimum (*m*; Fudali, 1963). Trachytes, on the other hand, tend to straddle the Ab–Or join and project into the field of stability for silica-oversaturated compositions.

None of the samples are primary mantle melts according to criteria outlined by Frey *et al.* (1978) (*mg*-number ≥ 68, Ni ≥ 320 ppm, olivine = Fo_{88-90}). The most primitive basanites, have *mg*-numbers < 56, Ni and Cr contents < 150 ppm (Table 7), and olivine of $Fo_{\sim 74}$. Taken together with the range in major element concentrations (Fig. 9), the basanites have clearly fractionated mafic phases. Using mineral chemistry and the value for K_d [Fe/Mg)/(ol/liq)] = 0·30 at 1bar (Roeder & Emslie, 1970; Ulmer, 1989), only cores of olivine phenocrysts ($Fo_{\sim 86}$) within mafic enclaves of comingled lavas approach equilibrium with primary partial melts from upper mantle peridotites (calculated *mg*-number ~ 65 for the coexisting liquid). Yet, enclave samples are unsuitable for forward modeling as parental material because of their evolved bulk chemistry (e.g., sample K63b, Table 9); this coupled with field and petrographic observations and results from mineral

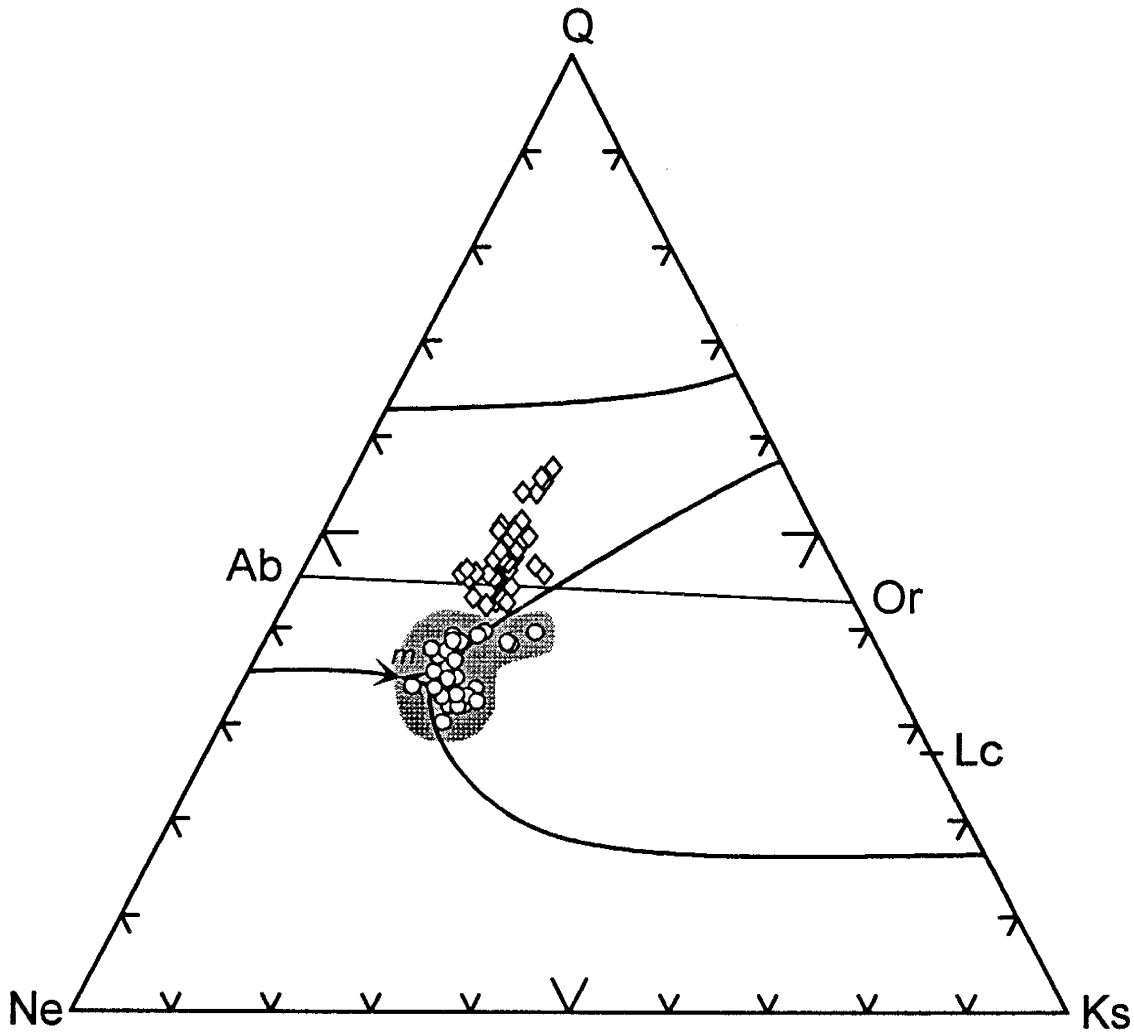

Figure 10. Whole-rock compositions of Mt. Sidley phonolites and trachytes plotted in the system Q-Ne-Ks at 1 atm (Fudali, 1963). Letter *m* approximates the liquidus minimum of the system. Symbols are the same as in Fig. 9.

analyses discussed above, clearly reveal that the dark-colored mafic enclaves are the product of physical mingling and strong chemical diffusion between basaltic liquids and trachyte magmas.

The mugearites can be subdivided into two types; lavas with low *mg*-numbers (20 to 30) and high P_2O_5 concentrations (> 0·9 wt.%) restricted to the southern flanks of Mt. Sidley (SFM), and mugearitic tephras with higher *mg*-number (40 to 50) and moderate P_2O_5 contents (~ 0·4 wt.%) found at Doumani Peak (DPM) (Fig. 9). Chemical distinctions between these two types are small but are important for understanding the petrogenetic differences between the trachyte and phonolite suites.

Trace Element Chemistry

Mt. Sidley volcanic rocks have high concentrations of incompatible elements and are light rare earth element (LREE) enriched with respect to heavy heavy rare earth elements (HREE) [$(La/Yb)_n$ = 9–19, chondrite normalized according to Sun & McDonough, 1989], a feature of intraplate alkaline magmas worldwide. Samples display coherent trace element trends with differentiation (Fig. 11). In general, phonolitic lavas have lower LILE (large-ion lithophile elements)/Zr and LREE/Zr ratios and higher HFSE (high-field strength elements)/Zr ratios relative to trachytic samples. Several *Qz*-normative trachytes deviate from the main trend (Fig. 11), exhibiting extreme incompatible element enrichment (e.g., MB33.8, Table 7; Zr/Rb = 3·5, Zr/Th = 20·0, Zr/La = 7·1 and Zr/Ce = 3·8). The enriched LILE and LREE contents of these comenditic trachytes are among the highest measured from Marie Byrd Land (LeMasurier & Thomson, 1990).

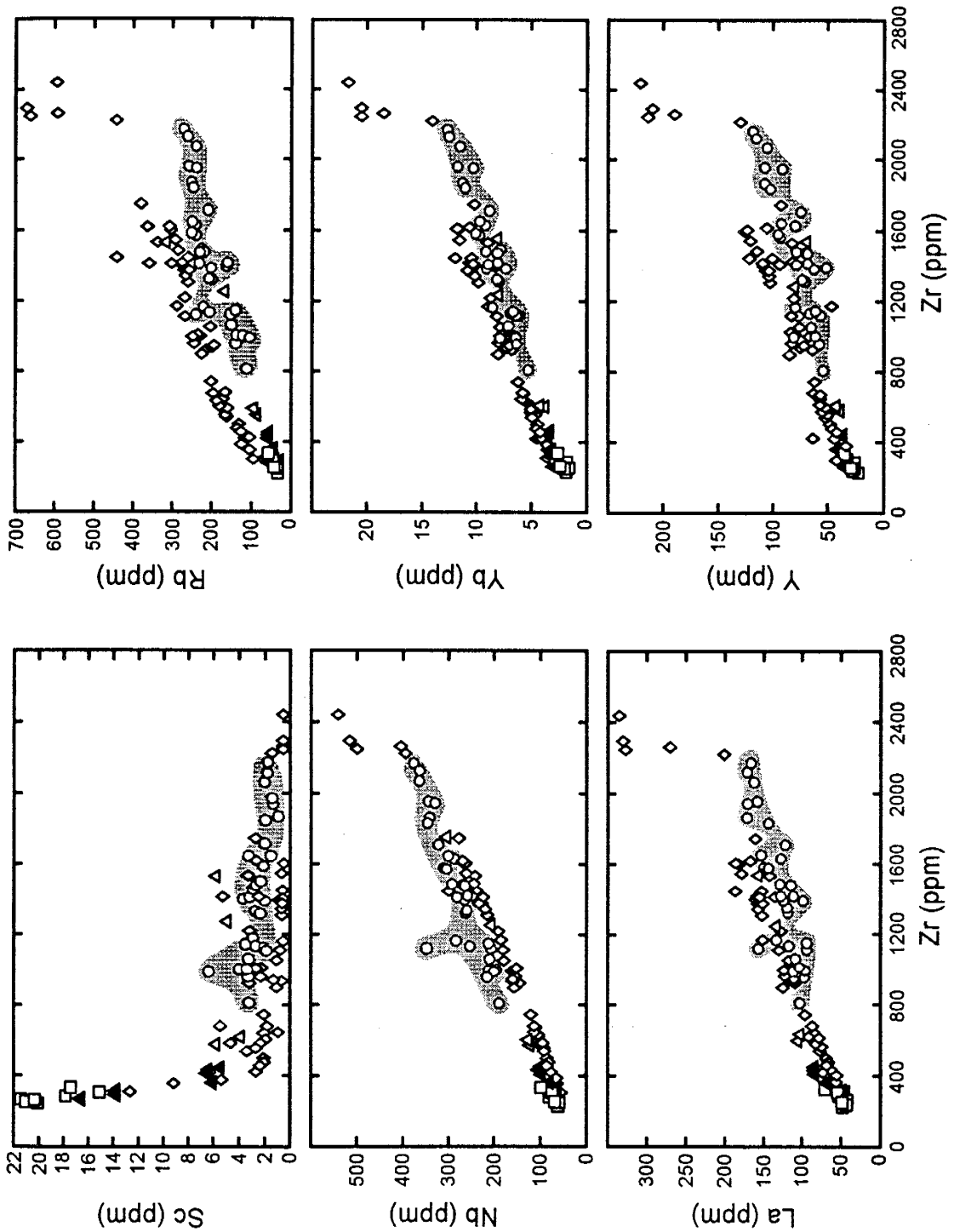

Figure 11. Variation of selected trace elements relative to Zr. Symbols are as in Fig. 9.

The phonolite lavas have remarkably constant trace element compositions (Fig. 12, a and b), considering they were erupted during a ~ 1 m.y. time-interval from three separate, overlapping, centers (Fig. 2) (Panter *et al.*, 1994). The tephriphonolites have similar concentration levels but are less depleted in Ba, K, Sr, P and Ti (Fig. 12b) and they lack significant negative Eu anomalies (Fig. 12a; Eu/Eu* ~ 0·95, Eu* calculated by interpolating between Sm and Tb on chondrite normalized REE plots). The trachytes, in contrast, show a large range of trace element concentrations (Fig. 12, a and b), including highly variable depletions in Sr, Eu and Ba (Ba contents are below detection limit in many samples).

Based on the subdivision of OIB's by Weaver (1991), the least evolved basanites have trace element abundances similar to HIMU (high U/Pb ratios) -type OIB. Mt. Sidley basanites have lower LILE/HFSE and LREE/HFSE ratios (e.g., sample 109, Table 7; La/Nb = 0·68, Ba/Nb = 5·7, Ba/Th = 68, Th/Nb = 0·085) compared with average EM-type OIB (La/Nb = 0·95, Ba/Nb = 12·8, Ba/Th = 101, Th/Nb = 0·123; Weaver, 1991) and strong positive Ta and Nb anomalies, relative to LILE and LREE, on primordial-mantle normalized trace element plots (Wood *et al.*, 1981), characteristic of HIMU OIB.

The mugearites are discriminated by higher elemental abundances in the SFM lavas compared with DPM tephras (Fig. 12, c and d). In addition, SFM are more LREE-enriched, $(La/Yb)_n$ = 15·5–17, relative to DPM compositions, $(La/Yb)_n$ = 11·5–13. Apart from their higher HREE (Yb and Lu) contents, DPM tephras have REE concentrations that are practically identical to less evolved basanites, whereas, SFM lavas have REE levels slightly higher than the more evolved basanites (Fig. 12c). Alkaline magmas are

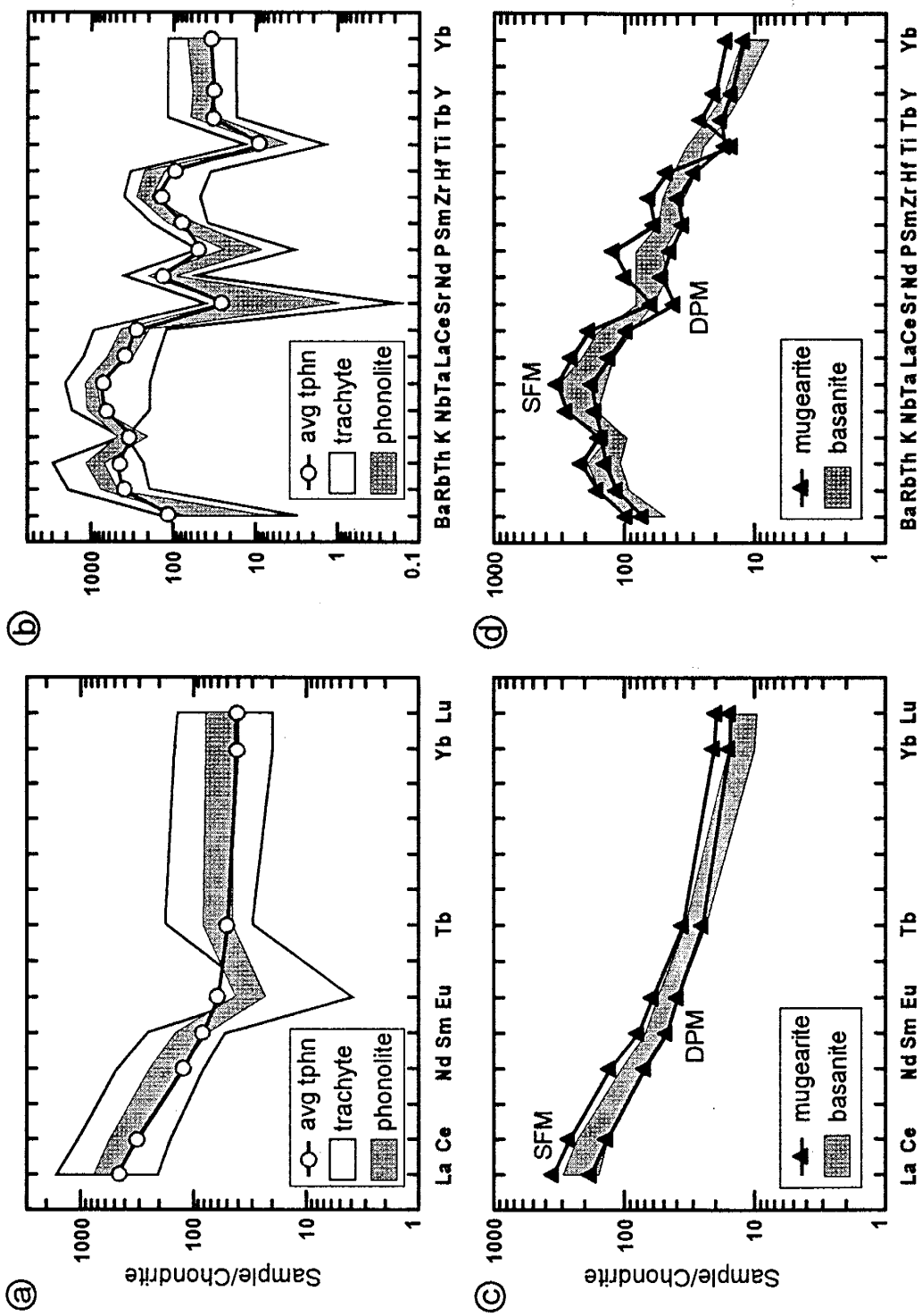

Figure 12. Chondrite-normalized REE patterns and trace element spidergrams of representative Mt. Sidley volcanic rocks, using normalizing values of Sun & McDonough (1989) and Thompson *et al.* (1984), respectively.

typically depleted in K relative to Th and Nb on chondrite normalized diagrams yet DPM tephras display flat patterns (Fig. 12d) and several trachytes show small positive anomalies (Fig. 12b).

Isotope Geochemistry

Radiogenic and stable isotope analyses are listed in Table 8. Initial isotopic ratios have been calculated using $^{40}Ar/^{39}Ar$ age determinations of individual volcanic units or interpolated ages based on relative stratigraphic position (Fig. 2). Age corrections for Nd isotopic ratios are small and well constrained using $^{40}Ar/^{39}Ar$ dates, however, many trachytes and phonolites show high $^{87}Rb/^{86}Sr$ ratios (>10) and the correction for in situ ^{87}Rb decay is important (Table 8). The 1σ errors in initial $^{87}Sr/^{86}Sr$ ratios (Table 8) were calculated by combining the measured uncertainty in $^{87}Sr/^{86}Sr$ (1σ within ± 0·002%) and $^{87}Rb/^{86}Sr$ ratios (± about 1% for XRF and 0·35% for isotope dilution) with uncertainties of individual $^{40}Ar/^{39}Ar$ plateau ages (1σ = ± 0·3–1·4%). The analytical uncertainty for samples with interpolated ages were determined using the mean of 1σ errors on dated samples (Xσ = ± 0·78%). Tephra samples MB35.5 and K137 have high errors on $^{87}Sr/^{86}Sr_i$ values; a consequence of extremely high $^{87}Rb/^{86}Sr$ ratios (Table 8). An order of magnitude increase in the resolution of $^{87}Sr/^{86}Sr_i$ values for several of these Sr-poor compositions was obtained using anorthoclase separates due to their lower Rb/Sr ratios.

Most samples display a narrow range in $^{87}Sr/^{86}Sr_i$ (0·7028–0·7032), $^{143}Nd/^{144}Nd_i$ (0·51285–0·51290) and $\delta^{18}O$ (5·0–6·0‰), indicating their derivation from primitive mantle, broadly similar to OIB. Two basaltic samples, MB32.11 and MB27.5, have

average Pb ratio values of $^{206}Pb/^{204}Pb = 19{\cdot}5$, $^{207}Pb/^{204}Pb = 15{\cdot}7$ and $^{208}Pb/^{204}Pb = 39{\cdot}1$, indicating a significant HIMU mantle source component (Zindler & Hart, 1986), thus supporting the interpretations based on trace elements. A large HIMU-OIB isotopic component ($^{87}Sr/^{86}Sr \leq 0{\cdot}703$ and $^{206}Pb/^{204}Pb \geq 19{\cdot}5$) is ubiquitous in Late Cenozoic volcanic rocks throughout west Antarctica (Kyle *et al.*, 1992; Hart & Kyle, 1994; Kyle *et al.*, 1994) and suggests a common mantle reservoir for west Antarctic rift volcanism (Hart *et al.*, 1994; Hole & LeMasurier, 1994; Weaver *et al.*, 1994).

Linear variation of $^{143}Nd/^{144}Nd_i$ with $^{87}Sr/^{86}Sr_i$ (Fig. 13) for Mt. Sidley samples may be explained by interaction of a HIMU-OIB source with crust. For the majority of samples, as Nd becomes more radiogenic (from ~0·51290 to 0·51280), $\delta^{18}O$ remains relatively constant (between 5·5 and 6·5‰) and $^{87}Sr/^{86}Sr_i$ features only minor variation (from ~0·7028 to 0·7032). This may indicate a 'contaminant' characterized by a relatively low time-integrated Rb/Sr signature. The increase in radiogenic Nd broadly correlates with sample differentiation as expressed by decreasing *mg*-numbers and increasing LREE, HFSE and Rb/Sr ratios from basanite (e.g., sample MB27.5, 0·512898) through trachyte (e.g., sample MB33.8, 0·512803) compositions. A notable exception is mugearite sample MB32.11 (DPM tephra) which contains similar trace element abundances as primitive basanite (Fig. 12) but possess a lower $^{143}Nd/^{144}Nd_i$ value (0·512848).

Several highly differentiated samples (mainly trachytes) reveal high $^{87}Sr/^{86}Sr_i$ (0·7033–0·7042) and low $^{143}Nd/^{144}Nd_i$ (0·51281–0·51283) values. Anorthoclase separated from several tephras (samples MB35.5, MB29.4 and K137) and bulk lava sample K66, show elevated $\delta^{18}O$ values relative to whole-rock values ranging from 6·5 to

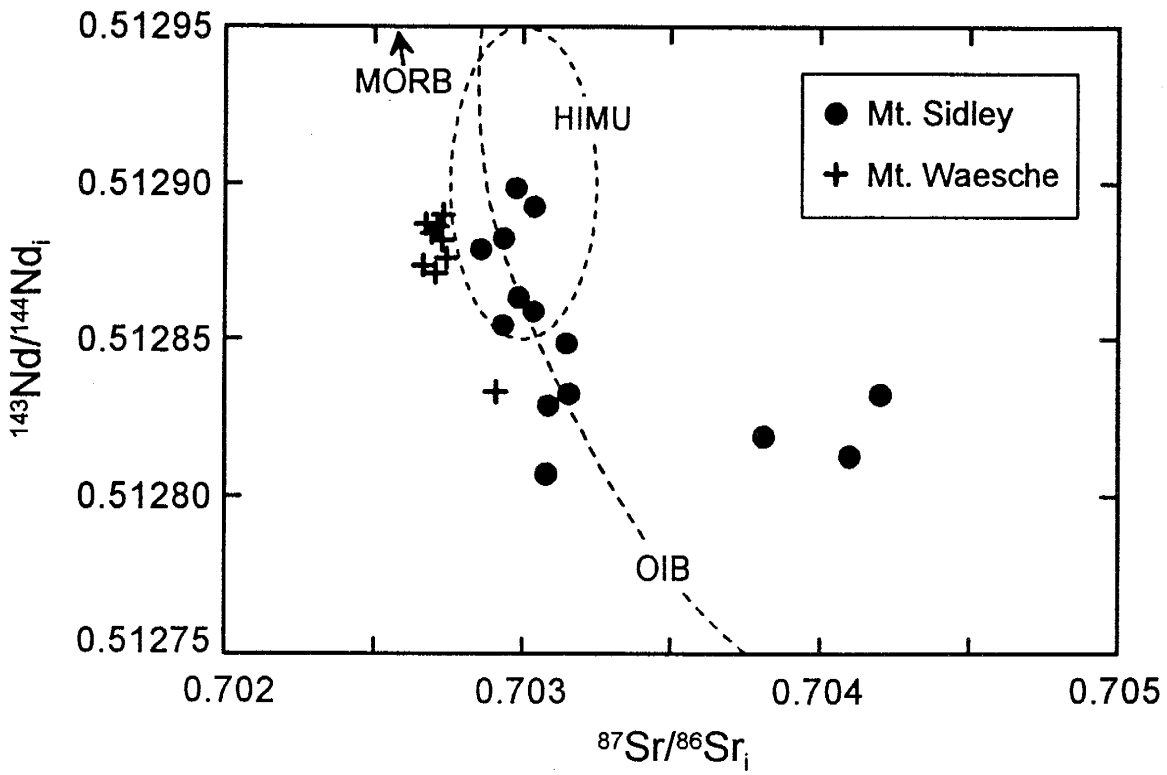

Figure 13. Age corrected Sr-Nd isotopic variation in Mt. Sidley volcanic rocks. Samples from the neighboring and younger (< 2 Ma) Mt. Waesche volcano as well as fields for OIB and HIMU basalts (Zindler & Hart, 1986) are plotted for comparison.

8·4 ‰ (Table 8). A positive correlation of increasing $\delta^{18}O$ with $^{87}Sr/^{86}Sr_i$ (Fig. 14), strongly supports assimilation of crustal material during magma genesis (cf. James, 1981). The large differences in isotopic values between whole rock and anorthoclase pairs (Fig. 14) can be explained by secondary processes. Surficial alteration by ^{18}O depleted meteoric waters (discussed below) can account for the vertical displacement of whole-rocks towards lower $\delta^{18}O$ values. The displacement of three whole-rock tephra samples towards higher $^{87}Sr/^{86}Sr_i$ values relative to anorthoclase (Fig. 14, inset) is explained by the physical entrainment of high time-integrated Rb/Sr and ^{18}O-enriched crustal material within ascending magmas during eruption. Bulk analysis containing accidental xenolithic and/or xenocrystic material could produce misleading isotopic signatures; in this case, elevating $^{87}Sr/^{86}Sr_i$ and $\delta^{18}O$ values above those inherited, prior to eruption, by the assimilation of crust. Subsequent alteration of glass by meteoric waters shifted the whole-rock $\delta^{18}O$ to lower values.

Chemical effects of alteration

Twelve of 32 samples analyzed for oxygen isotopes display $\delta^{18}O$ values of $\leq 4{\cdot}0$ ‰. Such low $\delta^{18}O$ analyses are not restricted to specific rock compositions or lithologies, but, the extent of ^{18}O depletion correlates with measured loss on ignition (LOI) (Fig. 15). Furthermore, there is a broad correlation between high-LOI, low-$\delta^{18}O$ values and incipient alteration featuring palagonitised glass and amygdaloidal zeolites and calcite. As an example, phonolite lava K165 (Appendix C5.3), which has the lowest measured $\delta^{18}O$ (-1·4 ‰) and high LOI (2·4 wt.%), contains up to 20% vesicles with thin alteration halos, partly

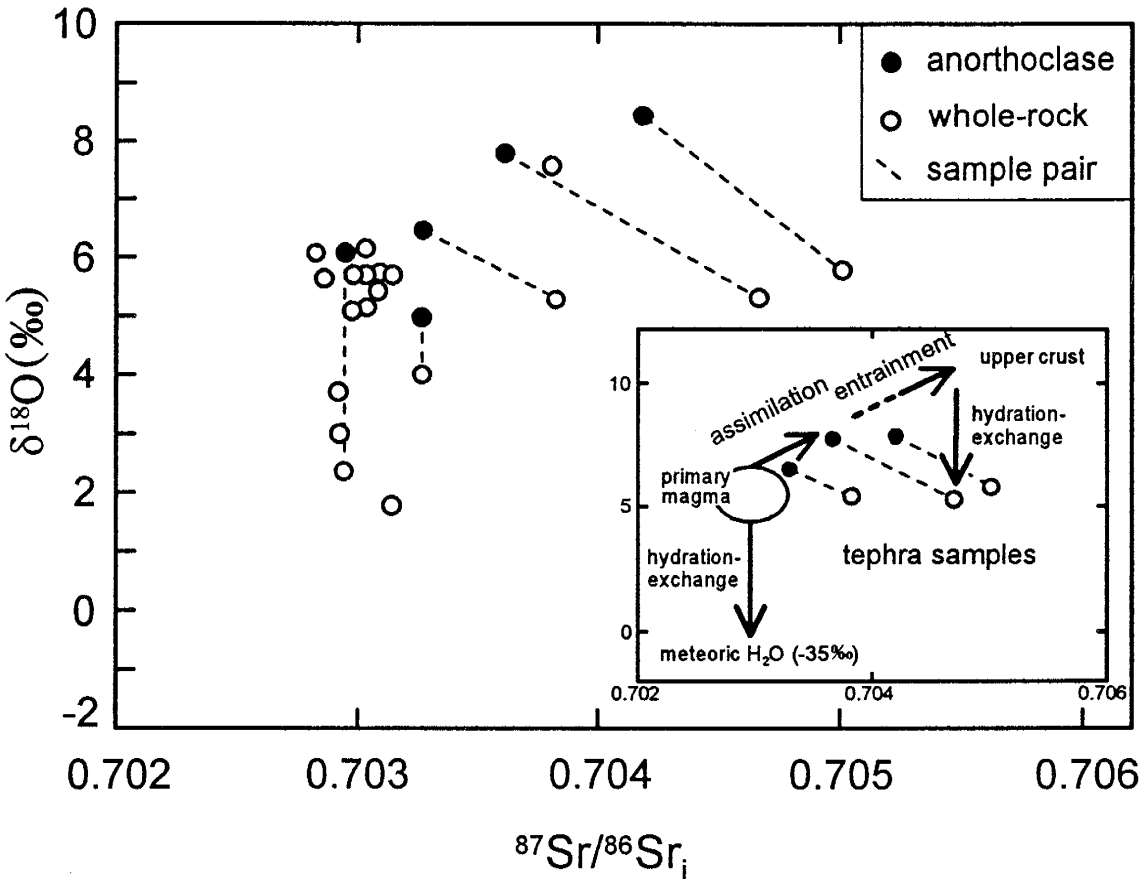

Figure 14. $\delta^{18}O$ versus initial $^{87}Sr/^{86}Sr$. Dashed lines connect rock-mineral sample pairs. Positive correlation between O and Sr isotopes reflect assimilation of crust by magmas. Low $\delta^{18}O$ values (< 5‰) reflect hydration-exchange between volcanic glass and Antarctic meteoric waters (-35‰). Inset describes the isotopic variation of rock-mineral pairs from three tephra deposits. A three stage process is envisaged: 1) magmatic assimilation of crust producing the isotopic signature of anorthoclase (solid circles); 2) physical entrainment of crust during eruption which increases $^{87}Sr/^{86}Sr$ and $\delta^{18}O$ contents of bulk samples (pumice + matrix + lithics) above magmatic values and; 3) alteration of lithic-rich pyroclastic deposits by meteroric water producing the isotopic signature of bulk analyses (open circles).

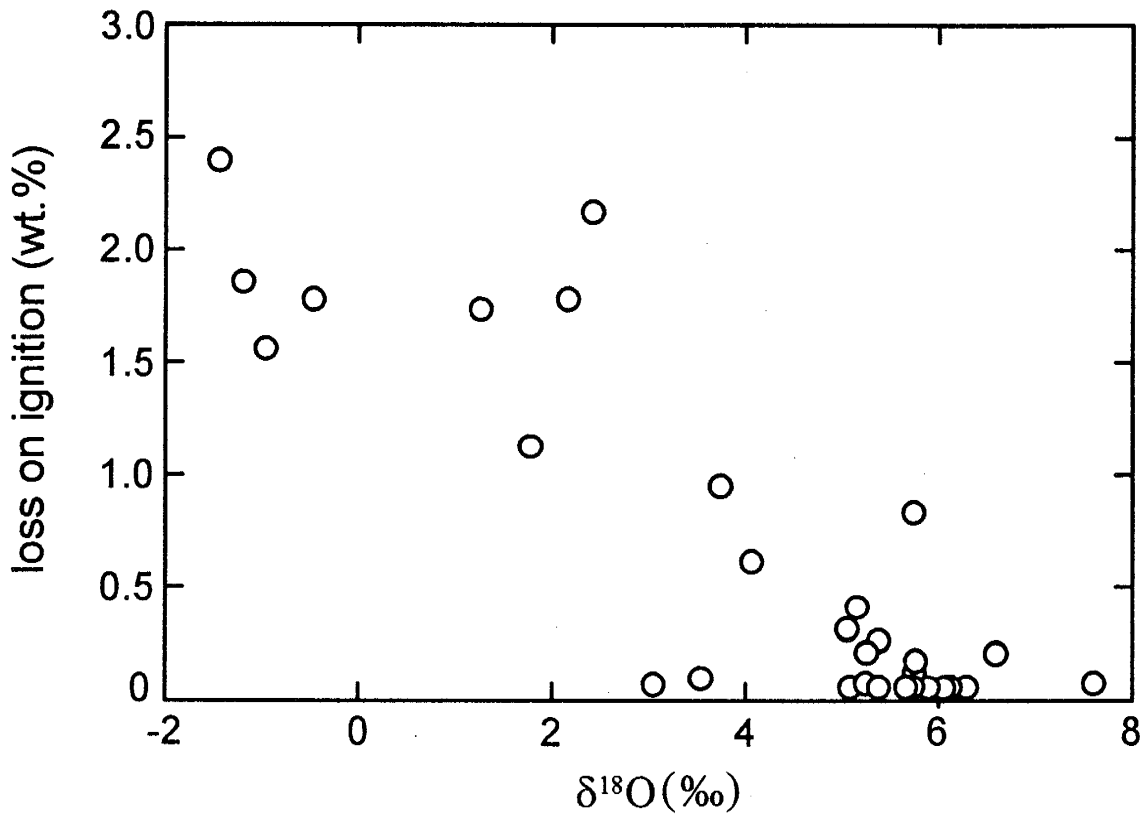

Figure 15. Loss on ignition (LOI) versus $\delta^{18}O$ for whole-rock samples, showing a general depletion of ^{18}O with increasing LOI content.

or completely filled by radiating zeolite crystals. However, several measured samples are visually devoid of secondary mineralization and have low LOI values (≤ 0·09 wt.%) yet show significant ^{18}O depletion ($\delta^{18}O < 4$ ‰).

The low $\delta^{18}O$ samples are considered to be the result of low temperature hydration and exchange with extremely light ($\delta^{18}O < -30$ ‰) Antarctic meteoric waters. Water–rock interaction is restricted to the alteration of available glass and secondary mineralization by solution-precipitation within vesicles, voids and fractures. Anorthoclase phenocrysts appear to be unaffected by alteration-exchange and contain consistently higher, magmatic, $\delta^{18}O$ values relative to whole-rock values (Table 8; Fig. 14).

The extent of ^{18}O depletion cannot be explained by simple, single-stage fractionation of oxygen isotopes between observed secondary minerals and Antarctic waters even at elevated temperatures (> 200°C) and unreasonably high fluid to rock ratios (≥ 1). To effectively deplete bulk sample ^{18}O from magmatic values towards local meteoric signatures with minimal water–rock interaction requires the addition of phases with extremely low $\delta^{18}O$ values. Using simple mass balance calculations, zeolites within lava sample K165 (estimated at 20 vol. %) should have $\delta^{18}O$ values near -30 ‰ to account for the low measured $\delta^{18}O$ whole-rock signature of -1·4 ‰. This is conceivable, since isotopic exchange between zeolite oxygen (oxygen within the aluminosilicate structure and from water within open framework channels) and external waters is extensive and rapid even at low temperatures (Karlsson & Clayton, 1990; Feng & Savin, 1993). Low $\delta^{18}O$ values of zeolitized Mt. Sidley volcanic rocks must reflect contributions from both zeolite framework and channel water oxygen; a result of bulk dehydration during liberation of O_2

in Ni reaction vessels at > 450°C. This may be of consequence since Karlsson & Clayton (1990) discovered that for several zeolite species isotopic signatures of channel water oxygen are related to ambient meteoric waters at their collection site. They found the $\delta^{18}O_{cw}$ of analcime was consistently lower by ~ 5‰ relative to regional precipitation values. As Mt. Sidley is situated at 77° S latitude and 2200–4200 meters elevation, zeolite channel water oxygen undergoing equilibrium exchange with local meteoric waters could be exceptionally ^{18}O-depleted.

Subaerial alteration of peralkaline glass, formation of secondary minerals, and oxygen isotope exchange should be accompanied by element modifications, in particular, alkali loss (Jezek & Noble, 1978; Cerling *et al.*, 1985). Phonolitic lavas show a general correlation between decreasing Na content (and to a lesser extent K and Rb) with increasing LOI and decreasing $\delta^{18}O$. No such correlation occurs in the trachytes; in fact, widely distributed pumice blocks collected from a single unwelded-ignimbrite reveal little change in alkali content between unaltered and altered samples (zones of palagonitization extending into the glass from vesicles), the latter having high LOI values (up to 4 wt.%) and low $\delta^{18}O$ signatures (-0·5 to -1·2 ‰). This may be attributable to the fact that secondary phases were precipitated within a few millimeters of altering glass, effectively masking any net elemental gains or losses in analyses of bulk pumice samples. Apart from minor leaching of alkali metals in some phonolitic lavas, other elements, including Ba, appear to be unaffected by surficial alteration at Mt. Sidley. This is also the case for low-temperature alteration of peralkaline glass from East Africa in which Cerling *et al.* (1985)

concluded that significant hydrogen ion exchange for alkali cations (up to 40%) can occur with little change in the original composition of glass.

We envisage meteoric water infiltrating Mt. Sidley tephra and lavas shortly after their emplacement, probably while the deposits were still cooling. Recent diagenetic alteration seems unlikely, considering the current climatic conditions (precipitation less than 200 mm/yr, Bromwich, 1990; and mean annual temperatures « 0°C) which do not favor penetration of external waters to promote hydration reactions; although warmer periods of deglaciation in Marie Byrd Land are postulated for Early Pliocene time (Moriwaki *et al.*, 1992; LeMasurier *et al.*, 1994). We propose an alteration scheme for zeolitized deposits (e.g., sample K165) in which volcanic rocks coming into contact with water (ice, snow or damp surfaces) allowed fluids to permeate and fill rock cavities. The trapped pore waters, at elevated temperatures, reacted rapidly with available glass. This early palagonization of alkali-rich glass caused pH conditions of the exchanging fluids to rise, thus mobilizing Si and Al to form zeolites at temperatures below 250°C (cf. Höller *et al.*, 1974; Tschernich, 1992; Hernandez *et al.*, 1993). Following deposition, zeolite channel waters were left to equilibrate with residual fluids and/or ambient water vapor, which may have proceeded to the present. This model may explain how small degrees of chemically cryptic alteration could produce low $\delta^{18}O$ whole-rock signatures in Mt. Sidley volcanic rocks.

MAGMA GENESIS

Fractionation Modeling

The origin and differentiation of trachytic and phonolitic suites at Mt. Sidley are discussed separately. On the basis of geological mapping and a well established volcanic stratigraphy (Panter *et al.*, 1994), the phonolites and trachytes cannot be related to an overall compositional progression within a simple, stratified magma system. Furthermore, the major and trace element data and mineral chemistry strongly suggest separate petrogenetic evolutions for trachytes and phonolites.

Forward modeling of magma genesis by fractional crystallization is evaluated using least-squares mass balance methods for major elements (Bryan *et al.*, 1969). In the models, microprobe analyses of phenocrysts from typical Mt. Sidley samples are supplemented by analyses of nepheline (Deer *et al.*, 1966) and apatite (Kyle, 1986). Geologically and mineralogically reasonable models with sums of squares of residuals (ΣR^2) < 0·1 are considered meaningful. Mass balance models are further tested through trace element approximations using published mineral/liquid partition coefficients (K_d) determined for alkaline assemblages (Table 9) and the Rayleigh fractionation equation (Arth, 1976). It is important to emphasize that basanites and mugearites are younger than phonolites and most trachytes (Fig. 2) but are assumed to be representative of parental magmas. In addition, rock compositions from the neighboring and younger (≤ 2 Ma) Mt. Waesche volcano (LeMasurier, 1990; Smellie, *et al.*, 1991) are used to model some aspects of Mt. Sidley petrogenesis.

Table 9: Published mineral/melt partition coefficient (K_d) values.

	~An_{65} Plagioclase		~An_{40}		Clinopyroxene			Olivine	Magnetite		Alkali feldspar		Amphibole	Nepheline	Apatite	
	MA-6	HPP	MA-10	HPP	MA-2	MA-4	HPP	MA-3	MA-7	MA-5	MA-12	HPP	MA-11	GIP	MA-8	HPP
Sc	0.02	-	0.03	-	2.39	2.65	-	0.20	5.04	1.39	0.22	-	7.58	-	0.41	-
Rb	0.03	-	0.20	-	0.10	0.04	-	0.08	0.23	0.08	0.42	-	0.15	0.44	0.56	-
Sr	2.12	1.36	4.41	4.62	0.33	0.16	1.51	-	0.23	0.16	4.11	5.57	1.01	0.24	1.67	0.83
Ba	0.24	0.15	1.08 - 4.65	1.47	0.07	0.04	0.321	0.04	0.14	0.14	3.02	5.04	0.61	0.09	0.95	0.014
La	0.12	0.023	0.46	0.28	0.22	0.10	0.10	0.02	0.53	0.20	0.46	0.219	0.56	0.01	5.16	15.20
Ce	0.14	0.023	0.36	0.215	0.34	0.20	0.18	-	0.56	0.20	0.36	0.173	0.87	0.011	6.34	16.60
Nd	0.07	0.023	0.31	0.170	0.68	0.60	0.38	-	0.55	0.20	0.31	0.152	1.82	0.013	6.60	21.00
Sm	0.12	0.024	0.27	0.135	0.66	0.60	0.56	-	0.55	0.20	0.27	0.139	2.40	0.012	6.30	20.70
Eu	0.22	0.232	1.78	1.10	0.65	0.57	0.58	0.03	0.15	0.06	1.78	1.72	2.08	0.043	3.77	14.5
Tb	0.03	0.018	0.23	0.111	0.77	0.70	0.73	0.04	0.55	0.19	0.23	0.130	2.88	0.014	5.79	19.8
Yb	0.11	0.030	0.18	0.062	0.73	0.70	0.61	-	0.75	0.20	0.18	0.116	1.77	0.016	3.24	9.4
Lu	0.18	-	0.11	-	0.73	0.70	-	-	0.75	0.20	0.11	-	1.77	-	3.40	-
Hf	0.01	-	0.15	-	0.69	0.43	-	0.05	1.77	0.24	0.13	-	0.80	0.008	0.64	-
Ta	0.01	-	0.08	-	0.14	0.04	-	0.03	3.86	0.39	0.12	-	0.89	-	0.09	-
Th	0.02	-	0.16	-	0.13	0.03	-	0.04	0.53	0.18	0.13	-	0.09	0.014	0.95	-

Sources of K_d data: MA, Mururoa Atoll (Caroff *et al.*, 1993); HPP, Hut Point Peninsula (Kyle, 1981); GIP, Gardar Igneous Province (Larsen, 1979).

Trace element modeling based on mass balance calculations is highly dependent on the selection of suitable mineral/liquid K_d values. As magmas evolve through a broad compositional spectrum, substantial changes in trace element behavior are controlled, primarily, by progressive crystallization and dissolution of minerals (or vapor phases) including chemical variations by solid-solution. As a result, trace element bulk distribution coefficients [$D^i = (\Sigma\ K_d i \bullet X)$; where X is the weight fraction of each phase], as well as individual mineral/liquid K_d values, may vary considerably between compositions within a given suite (Villement *et al.*, 1981; Wörner *et al.*, 1983; Lemarchand *et al.*, 1987). Because of this, 'case specific' partition coefficients taken from the literature may seriously limit modeling of multi-step evolutionary sequences.

An alternative technique for estimating bulk distribution coefficients is based on the regression of trace element data on log C^{Th} versus log C^i diagrams (method of Allégre *et al.*, 1977; after Treuil & Joron, 1975), where Th is used as a reference incompatible element ($D^{Th} \ll 1$). Analyses for any element (C^i) that fit a straight line with a slope ≤ 1 ($P = 1 - D^i$) approximate the bulk distribution coefficient for one step of differentiation by closed system fractional crystallization (FC). Because the technique is defined by Rayleigh's law, other models, except for simple mixing, should not produce linear trends. When $P > 1$, the sample set does not adhere to FC and additional processes are likely. The main constraint, of course, is that samples delineate geologically and petrologically reasonable rock series.

Determinations of bulk distribution coefficients from logarithmic diagrams for several crystallization sequences at Mt. Sidley are presented in Table 10. The results

Table 10: Bulk distribution coefficients (D^i) calculated from log–log diagrams.

	basanite	R^2	tephriphonolite	R^2	*N*-trachyte	R^2
Sc	1.66	0.78	$P > 1$	0.64	3.64	0.66
Rb	0.03	0.87	–	–	0.27	0.92
Sr	–	–	1.92	0.88	3.74	0.68
Ba	0.29	0.43	–	–	–	–
La	0.12	0.84	0.79	0.93	0.15	0.94
Ce	0.18	0.78	1.30	0.97	0.09	0.95
Nd	0.31	0.69	0.67	–	0.25	0.83
Sm	0.49	0.47	0.54	0.92	0.24	0.84
Eu	0.74	–	0.73	0.47	2.14	0.39
Tb	0.36	0.90	0.45	0.84	0.15	0.84
Yb	0.19	0.93	0.03	0.99	0.12	0.97
Lu	0.34	0.81	0.19	0.92	0.19	0.93
Hf	0.45	0.80	0.74	0.50	0.02	0.98
Ta	0.12	0.87	–	–	0.08	0.96
Y	0.44	0.83	0.08	0.96	0.09	0.93
Zr	0.37	0.96	0.47	0.63	0.01	0.94
Nb	0.17	0.80	0.83	0.74	0.06	0.96
K	0.55	0.70	1.22	0.42	–	–

Based on Rayleigh's law, closed system fractional crystallization (FC) assumes a constant D^i for each step of differentiation. Assuming that Th behaves as a highly incompatible element ($D^{Th} \ll 1$), then Rayleigh's law can be expressed in logarithmic form:

$$\log C^i = \log C_o^i + (D^i - 1) \cdot \log (C_o^{Th}) + (1 - D^i) \cdot \log C^{Th}$$

where C^i and C^{Th} is the concentration of any element *i* and Th in the liquid and C_o is the concentration in the initial liquid (Allègre *et al.*, 1977). A graph of $\log C^{Th}$ vs. $\log C^i$ is a straight line with a slope $P = (1 - D^i)$ for samples related by FC. Dashes indicate uncorrelatable data.

indicate that D^i for many elements change markedly with composition due largely to changes in minerals and mode fractionated. In general, data regressed for Ba, Sr, Eu and K show low correlation coefficients (Table 10) and the scatter on log–log plots may reflect changes in feldspar stoichiometry. In addition, poor correlation of data on log–log diagrams for several rock suites do not allow D^i to be calculated. This is the case for phonolitic lavas of the Sidley volcano (stage I, Fig. 2). In another case, regression of data for a trachytic rock suite fit a straight line ($R^2 > 0{\cdot}9$) but with a slope greater than one. The inconsistency of some rock series with FC models requires additional processes affecting their petrogenesis.

Phonolite Series

The phonolite series is composed of strongly silica-undersaturated rocks (between 5% and 26% normative *Ne*) ranging from basanites through intermediate compositions (SFM and benmoreite) to tephriphonolite and phonolite lavas.

Basanite lava, K109 (Table 7) is the most primitive sample analyzed and has been selected as being representative of the parental magma of the phonolite series. The basanites, however, are evolved (discussed earlier) and their chemistry is not representative of primary upper mantle melts. Spinel lherzoites are found as inclusions in basanite at one locality (lava sample K168, Appendix C4.1) and lower crustal xenoliths (pyroxenites and granulites) occur in other scoria cones. Wysoczanski (1993) described xenoliths as being angular in form and devoid of decompressive melting textures, attesting to their rapid entrainment and ascent to the surface. This would suggest that the basanitic

melts differentiated within the upper mantle or near the base of the crust (~ 30–35 km; Wysoczanski, 1993).

Fractional crystallization

Two main fractionation schemes are predicted from FC models for compositions within the series and are presented in Tables 11 and 12. They are: a high alkali trend evolving tephriphonolites and phonolites (Phonolitic sequence, Tables 11 and 12, models A–E); and an intermediate sequence producing mugearite and benmoreite liquids (models F–H). The differentiation of the phonolite series is modeled by extensive fractionation of diopside, olivine, plagioclase, titanomagnetite, nepheline and/or apatite. Modeled fractionation of this assemblage from a basanitic melt (sample K109) produces ~ 35% mugearite (models F–G), 25% benmoreite (models F–H), and nearly 20% tephriphonolite and phonolite liquids (models A–C). Small residual sums (5 to 12% liquid remaining) for production of phonolites are obtained in solutions evolving through intermediate compositions and require significant removal of alkali feldspar.

Trace element concentrations predicted by Rayleigh fractionation generally support the mass balance models, with the exceptions of Sc, Th, Rb and Ba (Table 12). Estimated Ba concentrations calculated using bulk distribution coefficients determined from log–log diagrams (Table 10), also depart from measured values (Table 12, models A and D). Published feldspar K_d values for Ba, Sr and, to a lesser extent Rb, show wide ranges (Table 9) and can vary substantially in rocks of similar composition (e.g., Long, 1978; Wörner *et al.*, 1983; Villemant, 1988). Mahood & Stimac (1990) suggest that the

Table 11: Least-squares mass balance solutions for *Phonolite Series* rocks.

	SiO_2	TiO_2	Al_2O_3	FeO	MnO	MgO	CaO	Na_2O	K_2O	P_2O_5	ΣR^2
Phonolitic sequence											
A	*basanite (K109) → 'evolved' basanite (K133)*										
K109 = 0.609(K133) + 0.114Cpx (En_{48}) + 0.061Ol (Fo_{86}) + 0.132 Pl (An_{63}) + 0.048 Mt (Usp_{65}) + 0.036 Ne											
meas	45.12	3.06	15.18	12.09	0.17	8.43	9.42	4.46	1.46	0.59	
calc	45.22	3.04	15.11	12.09	0.22	8.42	9.40	4.48	1.36	0.53	0.032
B	*evolved basanite (K133) → phonolite (K149)*										
K133 = 0.326(K149) + 0.125 Cpx (En_{48}) + 0.072 Ol (Fo_{86}) + 0.268 Pl (An_{47}) + 0.129 Mt (Usp_{58}) + 0.02 Ap + 0.06 Ne											
meas	46.09	3.06	16.18	12.34	0.21	5.87	7.99	5.42	1.97	0.86	
calc	46.15	3.11	16.12	12.32	0.27	5.86	7.97	5.45	1.91	0.88	0.019
C	*evolved basanite (K133) → tphn-phn (K114)*										
K133 = 0.329(K114) + 0.132 Cpx (En_{48}) + 0.067 Ol (Fo_{86}) + 0.237 Pl (An_{47}) + 0.13 Mt (Usp_{58}) + 0.02 Ap + 0.085 Ne											
meas	46.09	3.06	16.18	12.34	0.21	5.87	7.99	5.42	1.97	0.86	
calc	46.17	3.15	16.09	12.31	0.27	5.86	7.96	5.45	1.89	0.89	0.036
D	*tephriphonolite (K122) → 'evolved' tephriphonolite (K121)*										
K122 = 0.933(K121) + 0.057 Akf (Or_{20}) + 0.001 Ap + 0.009 Ne											
meas	57.92	0.79	18.55	6.78	0.23	0.67	2.45	7.63	4.66	0.30	
calc	57.91	0.79	18.62	6.77	0.24	0.73	2.44	7.61	4.67	0.32	0.010
E	*tphn-phn (K114) → phonolite (MB35.2)*										
K114 = 0.478(MB35.2) + 0.02 Ol (Fo_{65}) + 0.223 Pl (An_{35}) + 0.199 Akf (Or_{48}) + 0.03 Mt (Usp_{65}) + 0.01 Ap + 0.04 Ne											
meas	57.13	0.79	19.90	5.95	0.18	0.73	2.76	7.72	4.55	0.28	
calc	57.20	0.80	19.92	5.95	0.17	0.72	2.67	7.70	4.46	0.38	0.032
Intermediate sequence											
F	*basanite (K109) → evolved basanite (K95)*										
K109 = 0.629(K95) + 0.188 Cpx (En_{50}) + 0.055 Ol (Fo_{86}) + 0.019 Pl (An_{54}) + 0.044 Mt (Usp_{65}) + 0.005 Ap + 0.06 Ne											
meas	45.12	3.06	15.18	12.09	0.17	8.43	9.42	4.46	1.46	0.59	
calc	45.21	3.07	15.09	12.08	0.23	8.42	9.41	4.52	1.26	0.60	0.064
G	*evolved basanite (K95) → mugearite (SFM, K93)*										
K95 = 0.558(K93) + 0.070 Cpx (En_{48}) + 0.057 Ol (Fo_{86}) + 0.226 Pl (An_{54}) + 0.050 Mt (Usp_{65}) + 0.039 Ne											
meas	48.25	2.51	17.55	11.40	0.19	5.24	7.38	5.22	1.65	0.62	
calc	48.23	2.44	17.53	11.43	0.20	5.23	7.39	5.27	1.49	0.63	0.035
H	*mugearite (SFM, K93) → benmoreite (K134)*										
K93 = 0.758(K134) + 0.019 Cpx (En_{45}) + 0.051 Ol (Fo_{65}) + 0.110 Pl (An_{54}) + 0.046 Mt (Usp_{58}) + 0.016 Ap											
meas	51.58	1.58	17.01	12.45	0.24	2.50	5.25	5.97	2.28	1.14	
calc	51.57	1.61	17.01	12.44	0.29	2.51	5.25	5.96	2.33	1.13	0.006

Abbreviations: Cpx = clinopyroxene; Ol = olivine; Pl = plagioclase; Mt = titanomagnetite; Ap = apatite; Ne = nepheline; Akf = alkali feldspar.

Table 12: Elemental concentrations for FC models (Table 11) calculated using published K_d's (Table 9) and D^i values from log-log plots (Table 10).

Phonolitic sequence

	A bas → bas K109 to (0.609)K133			**B** bas → phn K133 to (0.326)K149		**C** bas → tphn K133 to (0.329)K114		**D** tphn → tphn K122 to (0.933)K121		
	meas. 109	calc.	D^i bas	meas. 133	calc.	meas. 133	calc.	meas. 122	calc.	D^i tphn
Sc	21.8	20.6	24.00	17.3	4.47	17.3	5.69	3.2	3.12	–
Rb	35	35.55	34.17	55	75.60	55	52.63	111	144.19	–
Sr	752	782.93	–	950	954.48	950	925.81	313	317.46	283.47
Ba	344	432.28	467.98	666	679.20	666	757.62	732	748.03	–
La	40.7	45.58	44.36	68.8	82.48	68.8	67.02	103.5	106.49	108.83
Ce	82.8	91.01	89.18	134.0	153.59	134.0	139.76	244.0	216.23	229.90
Nd	32.0	35.86	36.22	51.0	60.01	51.0	50.22	70.0	63.22	–
Sm	7.60	7.96	8.75	11.27	11.03	11.27	10.28	13.74	14.28	14.48
Eu	2.43	2.25	–	3.20	3.53	3.20	4.01	4.22	4.35	4.10
Tb	0.96	0.88	0.90	1.24	1.53	1.24	1.42	1.85	1.90	1.92
Yb	1.84	1.90	1.76	2.63	4.58	2.63	3.61	5.24	6.66	6.57
Lu	0.28	0.24	0.24	0.33	0.54	0.33	0.44	0.81	1.01	1.01
Hf	6.00	6.12	6.18	8.12	10.99	8.12	9.44	18.70	20.13	21.02
Ta	4.3	5.18	4.25	6.6	6.45	6.6	5.27	12.6	12.68	13.44
Y	25	–	25.76	34	–	34	–	55	–	61.92
Zr	254	–	244.50	334	–	334	–	815	–	1025.46
K	12035	–	13014.0	16464	–	16464	–	38180	–	39280.8
Th	5.1	5.09	ref	7.9	13.77	7.9	8.16	11.7	14.27	ref

Intermediate sequence

	E tphn → phn K114 to (0.478)MB35.2		**F** bas → bas K109 to (0.629)K95		**G** bas → mug K95 to (0.558)K93		**H** mug → ben K93 to (0.758)K134	
	meas. 114	calc.	meas. 109	calc.	meas. 95	calc.	meas. 93	calc.
Sc	3.3	0.68	21.8	22.25	15.0	6.42	6.5	3.47
Rb	140	141.05	35	29.95	44	33.32	56	67.35
Sr	322	338.92	752	742.02	715	649.37	734	768.14
Ba	663	528.74	344	289.34	404	405.54	662	783.72
La	98.9	110.06	40.7	39.57	52.5	49.38	80.6	91.28
Ce	201.7	191.68	82.8	77.59	99.2	95.94	153.9	159.46
Nd	60.0	63.09	32.0	33.78	39.0	39.11	62.0	62.06
Sm	12.56	11.32	7.60	6.72	7.80	7.29	11.42	10.79
Eu	3.36	2.08	2.43	1.99	2.39	2.12	3.31	3.18
Tb	1.77	1.68	0.96	0.88	1.00	0.83	1.31	1.19
Yb	6.30	6.15	1.84	2.04	2.47	2.20	3.39	3.65
Lu	0.94	0.89	0.28	0.27	0.34	0.34	0.52	0.52
Hf	21.50	19.88	6.00	5.51	6.70	6.19	9.20	11.05
Ta	13.7	12.60	4.3	4.20	5.2	4.62	6.3	6.77
Th	21.0	20.43	5.1	4.72	7.5	5.26	8.9	10.45

abbreviations: bas = basanite; mug = mugearite; ben = benmoreite; tphn = tephriphonolite; phn = phonolite.

variability in feldspar partition coefficients for these elements may be a consequence of analyses on un-equilibrated feldspar(s)-matrix pairs. Predicted Sc concentrations are lower than measured values (Table 12); a possible reflection of low Sc K_d values from selected clinopyroxenes (Table 9). Clinopyroxene partition coefficients for Sc increase with Fe content and higher values would be expected for progressive differentiation by FC. Indeed, partition coefficients reported for Fe-rich species (e.g., salite and hedenbergite) in phonolites and trachytes can range from 10 to > 100 (Wörner *et al.*, 1983; Villemant, 1988; Mahood & Stimac, 1990). Apatite appears to be the chief phase controlling Th abundance, and is present throughout the phonolitic sequence (stage I, Table 1). The deviation of calculated model Th contents from measured values may be explained by uncertainties in published partition coefficients. For instance, Michael (1988) and Mahood & Stimac (1990) revealed several cases where Th K_d values have been overestimated due to analyses of mafic phases and feldspars 'contaminated' with accessory minerals and glass inclusions. A further uncertainty lies in the poorly known behavior of Th in apatite during the differentiation of alkaline magmas.

The composition of phonolitic lavas within the high alkali trend (Phonolitic sequence) are distinct for each stage I volcano (oldest to youngest: Byrd → Weiss → Sidley volcanoes; Fig. 2), yet together they form a compositional continuum demonstrated on a plot of Ba versus Ta shown in Fig. 16a. Although the order is inconsistent with the observed stratigraphy, the trend emulates progressive differentiation of Byrd magmas through Sidley compositions to Weiss phonolites. Evolution towards higher incompatible trace element concentrations coincides with a general increase in peralkalinity. If a

common lineage is assumed, strong depletions in Ba must reflect substantial loss of alkali feldspar (Fig. 16), which is underscored by an overall decrease in its average modal abundance between Byrd (33%), Sidley (13%) and Weiss (5%) lavas (Table 1). Mass balance and Rayleigh fractionation approximations (Tables 11 and 12, model E) offer reasonable estimates for the crystallization of tephriphonolite (sample K114) to phonolite (sample MB35.2) but give poor solutions for predicting chemical changes among phonolite lavas of the Sidley volcano (Fig. 16). For example, fractionation of high-Ba phonolites to produce low-Ba phonolites of the Sidley volcano consistently underestimate the degree of Al_2O_3 and Sr depletion (best fit FC models predict fractionation of up to 17% plagioclase and 25% alkali feldspar) and overestimate LREE, Hf and Ta enrichment. It is considered unlikely that the compositional variations in phonolites of the Sidley volcano reflect a simple liquid line of descent.

Despite strong evidence for substantial feldspar fractionation, Al_2O_3 concentrations in the phonolites display an elevated range ($\geq$ 18 wt.%, Fig. 9). Selective mineral fractionation by gravity-induced crystal settling (Wager & Brown, 1968; Cox & Bell, 1972; Cox & Mitchell, 1988) may promote high residual Al contents by disproportionate loss of heavy mafic phases relative to feldspars, albeit experimental studies confine this process to low-viscosity basaltic magmas (Sparks *et al.*, 1993). Nevertheless, the feldspar phyric character of the rocks themselves (crystals up to 3 cm and 40 vol.%) suggest cumulus enrichment and analyses of highly porphyritic lavas may deviate from normal liquid lines of descent (Cox *et al.*, 1979). Phonolites plotting above the FC curve in Fig. 16, are enriched in elements compatible with feldspar addition (K, Ba, Sr, and Eu) yet also

Figure 16. Variation of selected trace elements (ppm) and elemental ratios from phonolitic lavas of the stage-I succession (Byrd → Weiss → Sidley volcanoes). Solid stars indicate samples that show prominent disequilibrium textures (e.g., reversely zoned phenocrysts and embayed crystal forms). (a) Variation of Ta with Ba. Ba content decreases due to alkali feldspar fractionation while Ta (strongly incompatible) increases with more evolved compositions. (b) Ba versus K/Rb showing closed system fractional crystallization (FC) of sample K114. Model curve calculated using D^{K} = 0·8, D^{Rb} = 0·2 and D^{Ba} = 3·5 estimated from data correlation on log-log diagrams and mass balance models (Table 11; model E, using K_d's from Table 9). Numbered tick marks indicate the % magma remaining. (c) variation of Ba with Th. FC model curve calculated as in (b) with D^{Th} = 0·1. Magma mixing curve (straight line) calculated using endmembers K108 and the composition derived from 70% crystallization of sample K114. (d) Ba/Rb versus K/Rb (compare with b) showing a linear mixing trend (cf. Langmuir *et al.*, 1978) for data plotted above the FC curve (inclusive of hybrid samples). Fractional crystallization of K114 calculated using the bulk distribution coefficients in (b). Solid cross marks 30% liquid remaining.

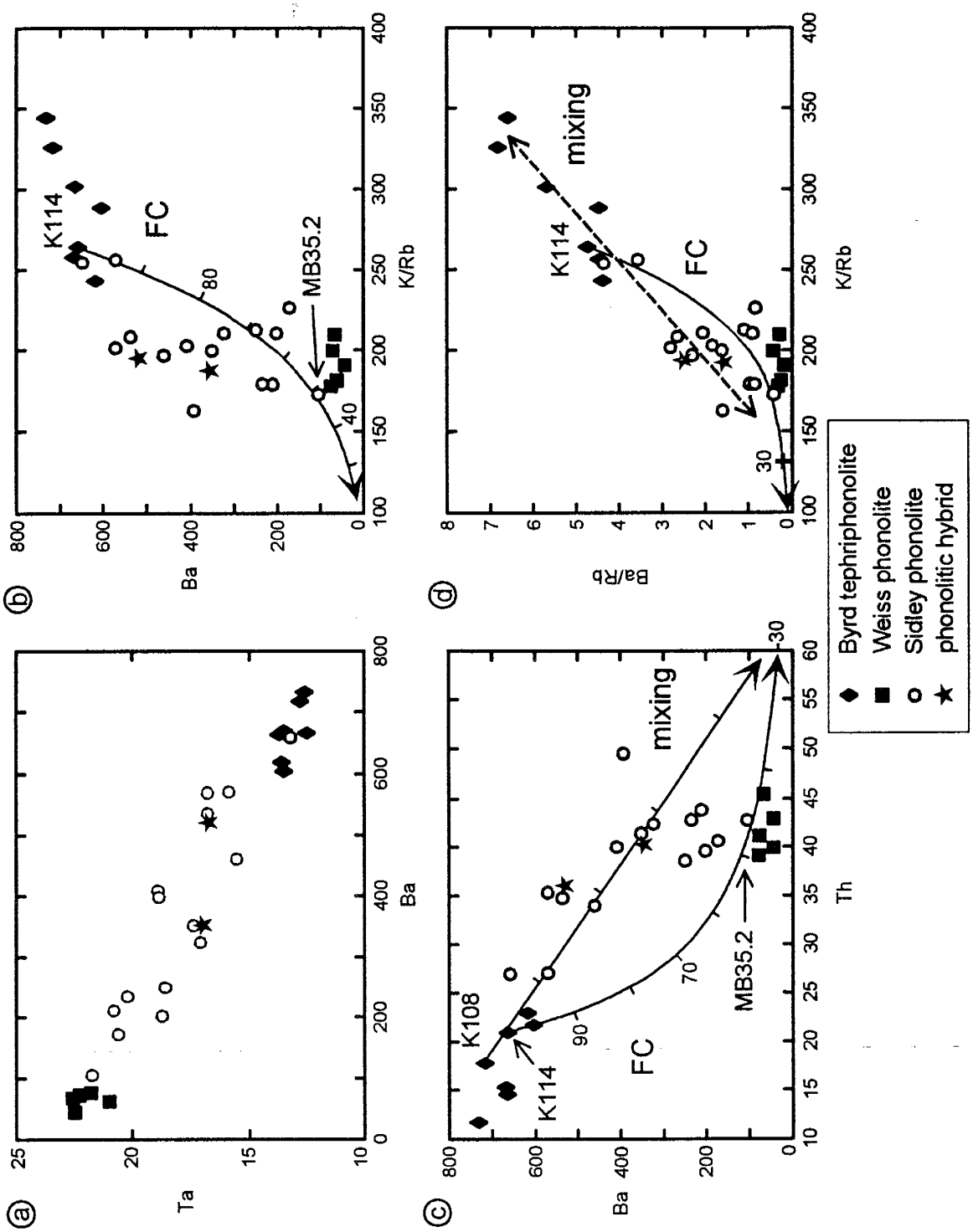
ⓐ
Ta
Ba
ⓑ
Ba
K/Rb
K114
FC
MB35.2
ⓒ
Ba
Th
K108
K114
FC
mixing
MB35.2
ⓓ
Ba/Rb
K/Rb
K114
mixing
FC
Byrd tephriphonolite
Weiss phonolite
Sidley phonolite
phonolitic hybrid

show elevated values for several incompatible elements (Ta, Hf, and Th) relative to model FC liquids (Fig. 16c). This may reflect chemical enhancement by glass and mineral inclusions (apatite, magnetite) observed in large alkali feldspar phenocrysts.

However, any attempt to explain the chemical diversity of the Sidley volcano phonolites by FC processes requires extreme modification of element compatibility involving major changes in the fractionating assemblage and/or selective addition of mineral cumulates through complex fluid dynamical phenomena. The assessment of either mechanism is problematical particularly for closed systems. Theoretical models for crystal-liquid separation within compositionally stratified magma chambers (e.g., Sparks *et al.*, 1984; Baker & McBirney, 1985) have been called upon to explain apparent chemical ambiguities in some erupted sequences (e.g., Bishop tuff; Hildreth, 1979, 1981) including the seemingly excessive amounts of fractional crystallization required to produce the elemental variations observed. Yet, no systematic mineral or chemical progression occurs within the phonolite lava sequence of the Sidley volcano and compositional variations are not likely to be attributable to complex liquid-crystal separation mechanisms within a zoned chamber.

Magma mixing

We interpret the chemical departure of phonolites from FC model liquids to be a consequence of mixing between genetically related compositions of the phonolite series. The presence of reverse zoning in olivine, clinopyroxene (Fig. 6) and feldspar phenocrysts

along with other crystal-liquid disequilibrium features (embayed crystal forms and sieve-textured feldspars) offers compelling evidence that many lavas within the stage I Sidley sequence represent magmatic hybrids. Similar disequilibrium textures are found within one other unit, the comingled lavas of stage II, where strong interaction between basaltic liquids and trachyte host magmas is explicit (see above and Panter *et al.*, 1994). However, unlike comingled lavas which contain coexisting alkali feldspar (anorthoclase) and forsterite (Fo_{86-82}), hybrid phonolites possess a phenocryst assemblage that is considered to be in equilibrium with a limited range of melt compositions. Furthermore, calculated compositions of liquids in chemical equilibrium with olivine cores and rims show small, yet statistically significant, compositional differences (*mg*-number increases from core to rim), suggesting that mixing between endmembers of the phonolitic spectrum is reasonable.

Two lavas featuring pronounced disequilibrium textures, K144 and K149, plot along with other phonolites off the FC model curve in Fig.16. On a plot of K/Rb versus Ba/Rb (Fig. 16d) these samples form a broad linear correlation with tephriphonolites of the Byrd volcano. The scatter of data about a straight line of mixing may be attributable to crystal fractionation following hybridization and/or multiple mixing events allowing for slight variations in endmember compositions. Still, it must be made clear that lavas of the Byrd volcano, which were deposited more than 100 ky before Sidley activity (Panter *et al.*, 1994) may only approximate mafic endmember liquids in hybridization models. Phonolite lava sample K149 (*mg*-number = 17, La/Sc = 44·2) can be modeled as a mixture of

Table 13: Comparison of phonolite lava sample K149 with a hybrid composition calculated by mixing tephriphonolite sample K131 with phonolite sample K132.

	measured phonolite - K149 -	calculated hybrid
SiO_2	56.49	56.48
TiO_2	0.65	0.69
Al_2O_3	19.84	19.84
FeO*	5.82	5.82
MnO	0.20	0.18
MgO	0.67	0.73
CaO	2.74	2.61
Na_2O	8.48	8.67
K_2O	4.86	4.58
P_2O_5	0.24	0.25
ΣR^2		0.137
Sc	2.7	2.9
Rb	205	173
Sr	272	274
Y	73	75
Zr	1330	1370
Nb	259	247
Ba	519	449
La	119.4	113.1
Ce	217.4	210.7
Nd	71	72
Sm	13.5	13.6
Eu	2.73	3.07
Tb	1.92	1.99
Yb	8.03	8.00
Lu	1.17	1.17
Hf	25.2	27.0
Ta	16.9	16.0
Th	35.7	28.9

* Total Fe as FeO.

Major elements are given in wt. %, trace elements in ppm.

Trace element concentrations in the hybrid were calculated using the major element solution: 72.6 % of sample K131 + 27.4 % of sample K132.

tephriphonolite (sample K131: *mg*-number = 22, La/Sc = 27·0) and 'evolved' phonolite (sample K132: *mg*-number = 7, La/Sc = 116·1) presented in Table 13.

The density relationship between different magma compositions is important in that it may provide insight into mechanisms of mixing. Calculated densities (Bottinga *et al.*, 1982) range from 2·29 to 2·31 g/cm^3 for Byrd tephriphonolites and from 2·26 to 2·29 g/cm^3 for Sidley phonolites. The calculated values do not account for density gradients due to volatile, suspended crystal or temperature contrasts. The small density difference indicates that efficient mixing is possible yet discourages mixing by catastrophic overturn within a stratified system (e.g., Huppert *et al.*, 1982, 1984) simply because the transition between phonolite and tephriphonolite liquids would likely be in the form of a gradual downward progression rather than a sharp interface typically invoked in double-diffusive convection models (e.g., Sparks *et al.*, 1984). We propose that mixing was initiated by injection of tephriphonolite liquids into fractionating phonolite magmas. Convective mixing caused minor resorption of phonolite phenocrysts followed by further crystal growth within hybridized magmas prior to eruption.

Trachyte Series

Mt. Sidley trachytes are subdivided into three main types (Fig. 17) based on stratigraphy and differences in chemical and lithologic character. With increasing stratigraphic height they are: (1) High-Th (*HT*)-trachyte, lavas and domes distinguished by Th contents greater than 60 ppm (Ta ~ 25 and Zr ~ 1900 ppm) and low K/Ta ratios (≤ 3000); (2) Low-Th (*LT*) -trachyte, tephras and lavas, including comingled units, which are

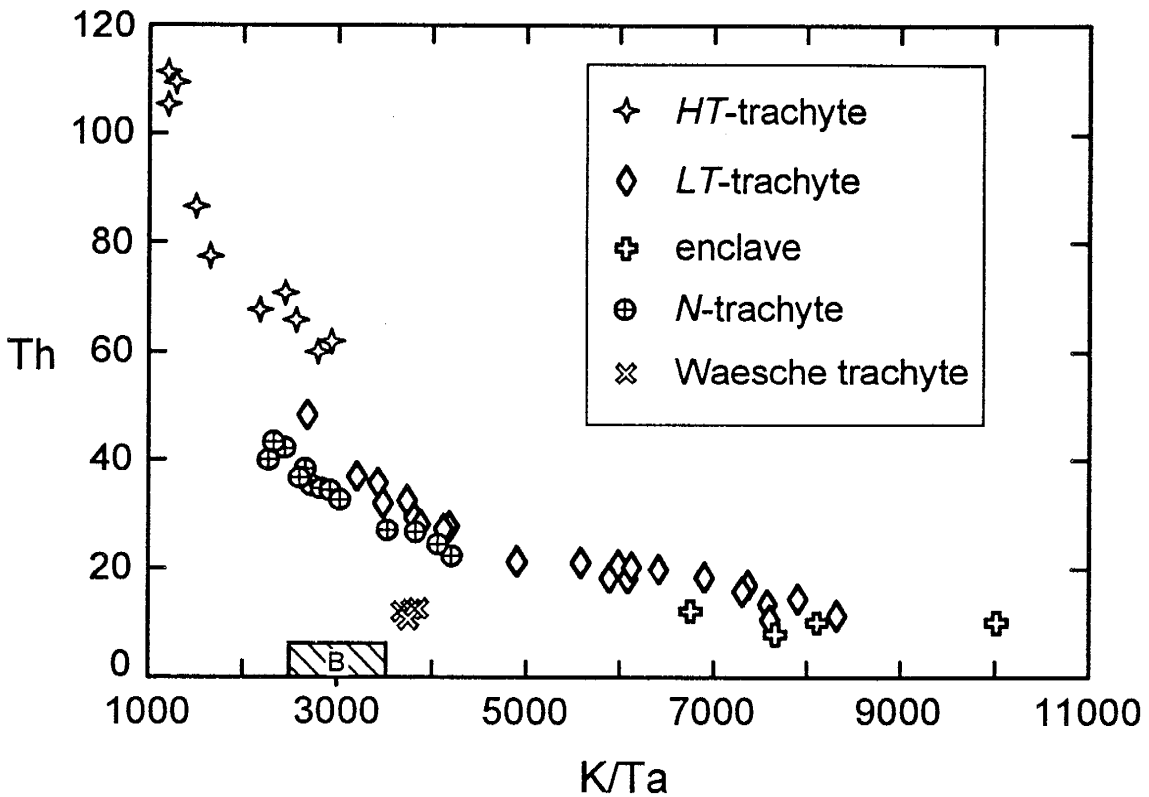

Figure 17. Th (ppm) versus K/Ta diagram illustrating trachyte subdivisions: *HT*-trachyte (High Th contents and low K/Ta ratios); *LT*-trachyte (Low Th and high K/Ta) and; *N*-trachyte ('Normal' Th and K/Ta values that are consistent with those determined by FC modeling). Enclave samples (open crosses) are hosted by *LT*-trachyte lavas. Also shown are trachyte samples from Mt. Waesche. Shaded box includes a range of basaltic samples (B = Mt. Sidley basanite + alkali basalt from Mt. Waesche).

characterized by lower average incompatible element abundances (Th ~ 21, Ta ~ 8 and Zr ~ 725 ppm) and a wide range in K/Ta ratios encompassing the highest values (> 8000) and; (3) 'Normal' (*N*) -trachyte, which are tephras having intermediate concentrations (Th ~ 34, Ta ~ 15 and Zr ~ 1300 ppm) consistent with those determined by FC modeling. All three trachyte types include *Ne*- and *Qz*-normative compositions.

In contrast to the derivation of phonolitic magmas by progressive crystallization of basanitic liquids, the extremely broad and chemically incongruent range of the trachyte series necessitates an interplay of several additional processes. Other mechanisms include: mixing of diverse magma types explicit in comingled lava deposits; and assimilation of crust recorded by elevated $\delta^{18}O$ and $^{87}Sr/^{86}Sr_i$ values (Table 8; Fig. 14). Moreover, isotopic characteristics coupled with trace element data help fingerprint a distinct crustal source contaminant within the Marie Byrd Land lithosphere.

The assimilation of crust by mantle derived melts is often invoked to explain the genesis of silica-oversaturated trachytic magmas (Fitton, 1987; Kyle *et al.*, 1992; Foland *et al.*, 1993; Nono *et al.*, 1994; Macdonald *et al.*, 1995). Using neodymium and strontium isotopes, Macdonald *et al.* (1994) suggested that minor wall rock assimilation accompanied crystal fractionation in the development of silica-oversaturated peralkaline trachytes at the Menengai volcano, Kenya. They argued against differentiation by "liquid state" processes as originally proposed by Leat *et al.* (1984). Turbeville (1993), considered *Qz*- and *Ne*-trachytes and phonolites erupted from the Latera Caldera (central Italy) to have evolved as a single magmatic lineage, transgressing the thermal barrier between silica-undersaturated and -oversaturated compositions by addition of skarn

generated CO_2-rich fluids. Using phase equilibria relationships and isotope data, Foland *et al.* (1993) concluded that cogenetic nepheline and quartz syenites were derived from a common silica-undersaturated parent that became oversaturated by assimilation of granitic crust. The evolution of silica-oversaturated magmas, however, may be possible without contributions from the crust. For example, Caroff *et al.* (1993) suggested that oversaturated comenditic trachytes at the Mururoa atoll in French Polynesia are the result of extensive crystal fractionation within a periodically replenished system. Another mechanism discussed by several workers (e.g., Cawthorn *et al.*, 1973; Villemant *et al.*,1981; Fitton, 1987; Cox *et al.*, 1993) involves the removal of silica-poor phases (amphibole or spinel) to promote oversaturation of residual liquids. Although minor amounts of arfvedsonite exist within Mt. Sidley trachytes (Tables 1 and 6) the fractionation of such silica-rich (up to 52 wt.% SiO_2), *hy*-normative (~ 57%) amphiboles would not lead to silica-oversaturation of the residua.

For evolved alkaline systems, an understanding of the processes involved in the formation of closely associated rocks representing strongly divergent liquid lines of descent is often bound by the assumption that the suite differentiated from common parent. At Mt. Sidley, parental melts evolving trachytic and phonolitic magmas may be distinct, providing a fundamental basis for their diverging petrogenesis. The feasibility of generating trachyte series rocks by fractionation of basanite liquids was evaluated by least-squares major element modeling and Rayleigh trace element approximations and produced unsatisfactory results. The inconsistencies with FC models do not, however, unequivocally preclude a basanite parent but may reflect overprinting by open system

processes. Still, the temporal and spatial separation of trachytic and phonolitic activity (Panter *et al.*, 1994) suggests that they developed within discrete systems, supporting the petrologic investigation of alternative parental source compositions.

The strong geochemical dissimilarity between mugearite types DPM and SFM (Figs. 9 and 12) require the existence of at least two separate basaltic parental compositions. At Mt. Sidley, only basanites (> 10% *Ne*-norm) are exposed. Alkali basalts (< 8% *Ne*-norm) from Mt. Waesche are plotted for comparison along with other mafic compositions in Fig. 18. Values of La/Yb for SFM lavas fall within the range of Sidley basanites but they have significantly lower *mg*-numbers (Fig. 18). Progressive fractionation of olivine, clinopyroxene, plagioclase, magnetite and nepheline from a basanite magma in the proportions predicted by FC models (e.g., Tables 11 and 12, model G) can explain this relationship. On the other hand, DPM samples are not a result of basanite fractionation since incompatible element concentrations in the former are similar or lower (Table 7; Fig. 12). Crystal fractionation of Mt. Waesche alkali basalts can produce hawaiite and more evolved magmas broadly similar to several Mt. Sidley compositions (discussed below). The relationship between alkali basalt and basanite shown in Fig. 18 cannot be explained by fractional crystallization, but may reflect separate source compositions, an interpretation supported by their distinctive isotopic characteristics (Fig. 13). The geochemical signature of DPM rocks allows us to infer that parent liquids, akin to alkali basalts found at Mt. Waesche, were involved in Mt. Sidley magma genesis.

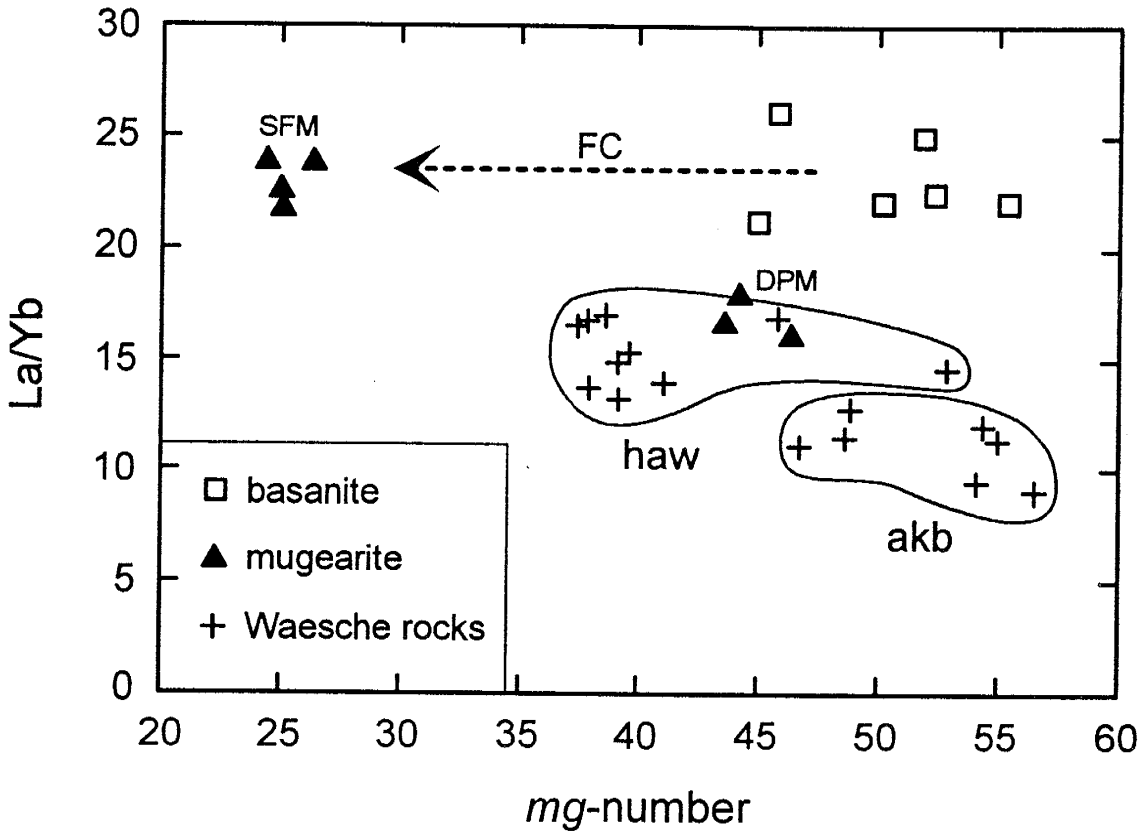

Figure 18. Plot of La/Yb versus *mg*-number (atomic % = Mg/Mg + Fe^{2+}) showing mugearite types, DPM and SFM, relative to basanite and Mt. Waesche basalts (akb). Dashed arrow represents the general trend for fractional crystallization of Mt. Sidley basanite as modeled by least squares mass balance and Rayleigh fractionation equations. Fractional crystallization models also predict the evolution of alkali basalt (akb) to hawaiite (haw) for the Mt. Waesche suite.

Fractional crystallization of alkali basalt

We propose that DPM-type mugearites and *N*-trachytes represent magmas derived by fractional crystallization of 'Waesche-type' alkali basalts. To test this hypothesis, we must first evaluate the factors controlling differentiation of the Mt. Waesche suite to be able to compare its evolved rock-types with those from Mt. Sidley. Incompatible trace elements (e.g., Nb, Zr, Rb and La) for Mt. Waesche rocks (excluding rhyolite compositions, Table 7) show extremely good linear correlations ($R^2 \geq 0{\cdot}95$) on log C^{Th} versus log C^i diagrams strongly suggesting that the suite can be related by FC processes. Discontinuities on logarithmic plots are restricted to elements compatible with feldspars and only appear in evolved compositions. For example, phonolite and trachyte analyses form a sharp break in slope on log Th versus log Sr and log Eu diagrams due to substantial plagioclase removal (increasing value of D^{Sr} and D^{Eu}). Also, concentrations of K and Ba are low in Mt. Waesche phonolites signifying the loss of alkali feldspar.

A two step model describes the genesis of Waesche trachytes from alkali basalts by fractionation of clinopyroxene, olivine, plagioclase, magnetite and apatite (Table 14). In Table 14, the calculated bulk distribution coefficients decrease slightly with differentiation for all elements except Sr and Eu. The compatible behavior of Sr and Eu corresponds with a 14% increase in the modal proportion of plagioclase subtracted for mass balance calculations. Between major steps of differentiation, FC models show a general consistency in the mineral assemblage fractionated (apart from proportional variations and minor compositional changes) and resultant D^i values (excluding Sr and Eu) and thus quantify many of the interpretations based on log–log diagrams.

Table 14: Least-squares mass balance and Rayleigh fractionation for Mt. Waesche rocks.

	SiO_2	TiO_2	Al_2O_3	FeO	MnO	MgO	CaO	Na_2O	K_2O	P_2O_5	ΣR^2
alkali basalt (MB4.1)→ mugearite (MB21.1)											
MB4.1 = 0.31(MB21.1) + 0.14 Cpx (En_{48}) + 0.09 Ol (Fo_{86}) + 0.37 Pl (An_{61}) + 0.08 Mt (Usp_{49}) + 0.01 Ap											
meas	46.35	2.06	16.80	11.32	0.18	7.75	11.09	3.36	0.59	0.49	
calc	46.53	2.03	16.74	11.32	0.23	7.73	11.05	3.24	0.52	0.54	0.06
mugearite (MB21.1) → trachyte (MB15.1)											
MB21.1 = 0.36(MB15.1) + 0.11 Cpx (En_{48}) + 0.02 Ol (Fo_{86}) + 0.4 Pl (An_{51}) + 0.10 Mt (Usp_{49}) + 0.01 Ap											
meas	50.79	1.78	18.57	9.57	0.18	3.03	8.60	5.39	1.54	0.53	
calc	50.69	1.73	18.66	9.59	0.23	3.04	8.62	5.37	1.67	0.51	0.07

Trace element solutions:

	Rb	Sr	Ba	La	Ce	Nd	Sm	Eu	Tb	Yb	Lu	Hf	Ta	Th
MB4.1														
meas	11	494	199	20.2	44.8	21	5.03	1.81	0.73	1.78	0.26	3.60	1.58	1.7
calc	12	420	170	25.1	49.8	21	4.61	1.39	0.67	1.53	0.18	3.20	2.07	1.7
D^i	0.17	0.83	0.16	0.54	0.52	0.62	0.59	0.44	0.59	0.44	0.34	0.44	0.52	0.19
MB21.1														
meas	31	513	457	43.0	87.5	32	7.46	2.69	1.09	2.96	0.39	6.17	3.64	4.5
calc	34	560	443	46.0	88.3	36	6.80	3.61	0.98	3.05	0.42	6.57	3.23	4.7
D^i	0.16	1.91	0.18	0.44	0.41	0.44	0.41	0.89	0.39	0.32	0.27	0.21	0.11	0.15

Bulk distribution coefficients (D^i) for each step of differentiation calculated using published K_d 's (Table 9). Abbreviations: Cpx = clinopyroxene; Ol = olivine; Pl = plagioclase; Mt = magnetite; Ap = apatite.

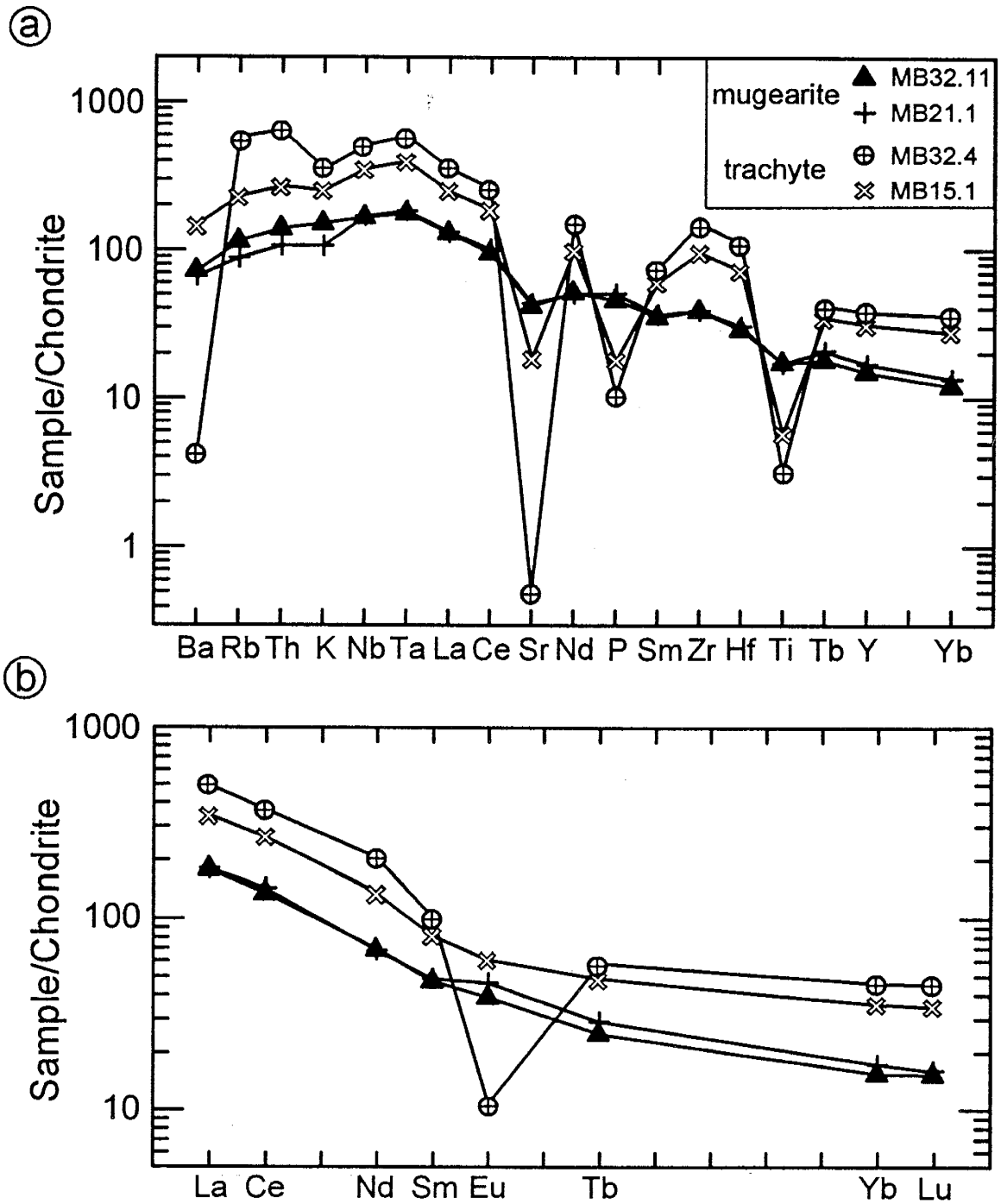

Figure 19. Comparison of chondrite-normalized multi-element patterns for selected Mt. Sidley and Mt. Waesche mugearites and trachytes. Symbols are as in Figs. 17 & 18. (a) Elemental abundances [normalizing values of Thompson *et al.*, 1984] in Mt. Sidley mugearite (DPM sample MB32·11) and mugearite from Mt. Waesche (sample MB21·1) are nearly identical. Patterns for *N*-trachyte (sample MB32·4) and Mt. Waesche trachyte (sample MB15·1) are similar yet do not overlap. The higher incompatible element and lower Sr and Ba concentrations in *N*-trachyte is, primarily, the result of alkali feldspar fractionation (see discussion). (b) Rare earth elements normalized to C1-chondrite of Sun & McDonough (1989).

A comparison can now be made between evolved compositions of the Waesche suite and similar lithologies at Mt. Sidley in order to assess the role of alkali basalt in the genesis of the trachyte series. On chondrite-normalized variation diagrams (Fig. 19) element concentrations of Mt. Waesche mugearite and trachyte (refer to Table 14) are compared with *N*-trachyte and DPM compositions. For mugearites, element abundances are nearly identical with small differences in Rb, Th and K (higher in DPM) and Tb, Y and Yb (lower in DPM). And, although the Sidley trachyte has higher concentrations and more pronounced depletion of Eu, Ba, K, Sr, P and Ti relative to Waesche trachyte, the two "spidergram" patterns are similar. Low concentrations for Ba (< 30 ppm), K, Eu and Sr in *N*-trachytes (Fig. 19) are attributed to alkali feldspar fractionation, a process that did not affect Waesche trachyte genesis (ca. Ba = 1108 ppm). In both comparisons, the relative abundances of Rb and Th (along with K in mugearites) are slightly irregular with values for Sidley analyses being higher than expected considering crystal fractionation as the sole process operative in the system. Anomalous LILE concentrations in DPM and *N*-trachytes may reflect assimilation of crust by magmas evolving from alkali basalt.

Origin of the LT-trachyte suite and assessment of crustal contributions

The lithologic and chemical diversity of *LT*-trachytes can be modeled by a combination of fractional crystallization, crustal assimilation and magma mixing processes. Examined individually, each mechanism fails to account for the wide range of *LT*-trachyte compositions illustrated in Fig. 17. In addition to their distinctive K/Ta values, the majority of *LT*-trachytes have higher K/Nb, Rb/Nb and Rb/Ta ratios compared to other

trachytes including those from Mt. Waesche. The incompatible behavior of Rb, Ta and Nb (Tables 10 and 14; Fig. 11) and variable partitioning of K (positive anomalies in Fig. 12b) perdicted for trachyte genesis make it difficult to explain the depletion of Nb and Ta relative to K and Rb by closed system processes. The fractionation of sphene has been proposed by Wolff (1984) to account for Nb and Ta depletions and systematic variations of Nb/Ta in phonolitic pumice at Tenerife, Canary Islands; and sphene may also be responsible, in part, for the high LILE/HFSE ratios (e.g., K/Ta > 30,000) in phonolites and trachytes at the Latera caldera, Italy (Turbeville, 1993). However, sphene is not present within Mt. Sidley samples and Nb/Ta ratios of the trachyte series are remarkably uniform (between 13·5 and 15·5) precluding progressive fractionation of a Nb- and Ta-rich phase.

The depletion in HFSE relative to LREE and LILE is a prominent chemical feature of magmas generated within subduction zones (Thirlwall *et al.*, 1994). Hence, contamination of alkaline magmas by calc-alkaline compositions may perturb 'normal' OIB-type trace element signatures. A potential arc-related 'contaminant' is the Ford Granodiorite (~350 to 380 Ma; Adams, 1987); a biotite-rich, hornblende bearing granodiorite-monzogranite suite exposed approximately 450 km to the west of Mt. Sidley in the Ford Ranges. Devonian-Carboniferous I-type granitoids in western Marie Byrd Land (also represented in northern Victoria Land, Tasmania and southeast Australia) are related to regional subduction and cordilleran-type magmatism that occurred along the paleo-Pacific margin of Gondwana (Laird, 1991; Weaver *et al.*, 1991; Luyendyk, *et al.*, 1992). Unfortunately, calc-alkaline granites (or any other pre-Cenozoic 'basement'

lithology) do not cropout within the Executive Committee Range, yet we anticipate their presence at depth based partly on the striking compositional similarity (major and trace elements, Ba, Rb, Nb, Sr, Zr and Y) between Ford Granodiorites (Weaver *et al.*, 1991) and several granitoid xenoliths collected at Mt. Sidley (Wysoczanski, 1993).

In the following discussion we explain the geochemical variations of the *LT*-trachytes by magma-crust interaction using Ford Granodiorite as a model assimilant (Weaver *et al.*,1992). Ford Granodiorite $^{87}Sr/^{86}Sr$ and $^{143}Nd/^{144}Nd$ ratios, recalculated to 5 Ma, range from 0·7105 to 0·7361 and 0·51227 to 0·51233, respectively, and are more radiogenic than Mt. Sidley volcanic rocks (Table 8) and lower crustal xenoliths (pyroxenites and granulites; Wysoczanski, 1993). Variations in Sr and Nd isotopic compositions and selected trace elements are modeled by FC and assimilation and fractional crystallization (AFC) processes (DePaolo, 1981) in Fig. 20. The bulk distribution coefficients used in the graphical FC and AFC models were estimated from least-squares mass balance calculations and log C^{Th} versus log C^{i} correlation diagrams, and are considered to be petrologically reasonable.

The majority of Mt. Sidley samples with elevated $^{87}Sr/^{86}Sr_i$ (Fig. 20a) and low $^{143}Nd/^{144}Nd_i$ (Fig. 20b) lie along AFC trends calculated using a Ford Granodiorite contaminant and model magma compositions derived by 80% fractional crystallization of Sidley basanite and Waesche alkali basalt. Sr, Nd and Nb concentrations predicted by FC curves at 20% magma remaining ($F = 0{\cdot}2$; Fig. 20) are comparable to measured values of phonolitic and trachytic compositions. During Mt. Sidley magma genesis Sr is compatible, due to plagioclase fractionation. D^{Sr} values increase from 1·7 to 4·0 in model

Figure 20. Graphical presentation of FC and assimilation–fractional crystallization (AFC) models. (a) Plot of initial $^{87}Sr/^{86}Sr$ versus Sr (ppm). Horizontal FC trends from basanite (squares) and Mt. Waesche alkali basalt (solid crosses) are calculated using a bulk distribution coefficient for Sr of 1·7 (the strong compatibility of Sr denotes plagioclase fractionation). Model AFC curves calculated after DePaolo (1981) use Ford Granodiorite (FG) from coastal MBL (Weaver *et al.*, 1992) as an assimilant (sample R7460; $^{87}Sr/^{86}Sr_{(5)} = 0{\cdot}71174$, $^{143}Nd/^{144}Nd_{(5)} = 0{\cdot}512279$, Sr = 306, Nd = 33·4 and Nb = 15 ppm) and model magma compositions derived by 80% FC of Mt. Sidley basanite and Mt. Waesche alkali basalt (samples MB27.5 and K19, respectively; Tables 7 and 8) at low mass assimilation to mass crystallization rates ($r \leq 0{\cdot}1$) and $D^{Sr} = 4{\cdot}0$. The increase in D^{Sr} marks the onset of alkali feldspar fractionation. Inset shows FG compositions relative to volcanic samples. (b) Plot of initial $^{143}Nd/^{144}Nd$ versus Nb (ppm). Generated FC and AFC trends use the same crustal contaminant and modeled magma compositions as in (a), with $D^{Nd} = 0{\cdot}5$ and $D^{Nb} = 0{\cdot}2$. Note that steep AFC curves for basalt show little change with increasing value of r (> 0·3). In (a) and (b), numbered tick-marks along FC and AFC curves refer to percent magma remaining. Samples from a mixed phonolite-trachyte pyroclastic fall deposit (black fall) are denoted by an asterisk. *HT* and *LT* refer to trachyte types presented in Fig. 17. Other symbols are the same as in previous figures.

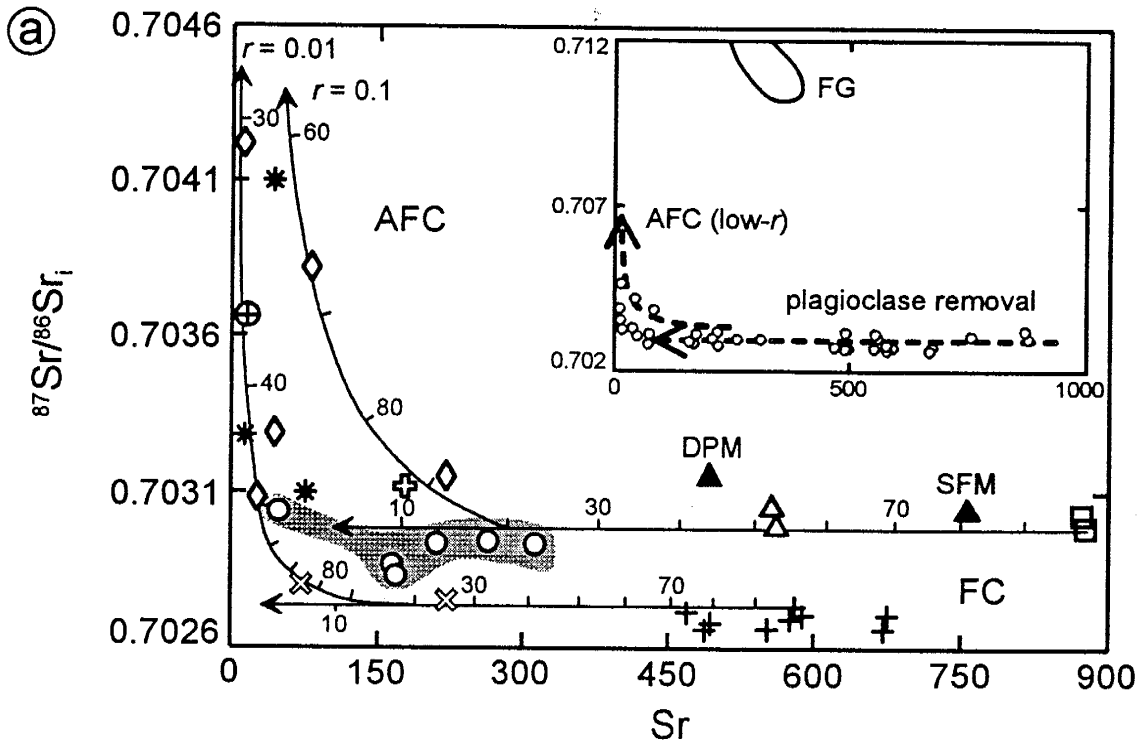
ⓐ
0.7046
0.7041
0.7036
0.7031
0.7026
$^{87}Sr/^{86}Sr_i$
r = 0.01
r = 0.1
AFC
DPM
SFM
FC
0
150
300
450
600
750
900
Sr
0.712
0.707
0.702
FG
AFC (low-r)
plagioclase removal
0
500
1000

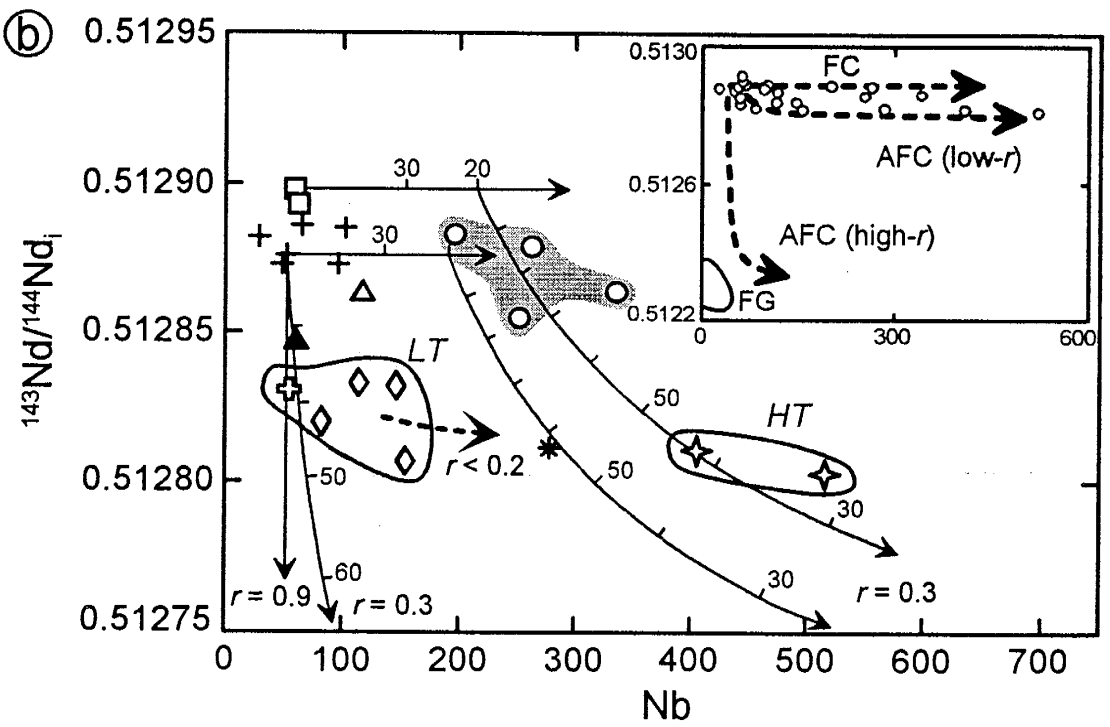
ⓑ
0.51295
0.51290
0.51285
0.51280
0.51275
$^{143}Nd/^{144}Nd_i$
LT
HT
r < 0.2
r = 0.9
r = 0.3
r = 0.3
0
100
200
300
400
500
600
700
Nb
0.5130
0.5126
0.5122
FC
AFC (low-r)
AFC (high-r)
FG
0
300
600

differentiation trends (Fig. 20a) marking the onset of alkali feldspar fractionation predicted for evolved liquids. Assimilation of granodiorite by highly differentiated magmas at low mass assimilation to mass crystallization rates (r = 0·01 to 0·3) and moderate to high F values (≥ 0·3 on AFC curves) can explain the genesis of radiogenic Mt. Sidley samples having low Sr (< 150 ppm) and high Nb (> 200 ppm) contents.

Yet this scenario fails to account for the low Nb concentrations (< 200 ppm) of the *LT*-trachytes. For instance in Fig. 20b, an AFC evolutionary path cannot extend below the Nb content of the initial magma, assuming that D^{Nb} is « 1. Thus, assimilation by differentiated magmas will produce compositions that evolve away from the *LT*-trachyte field. This suggests that low Nb – low $^{143}Nd/^{144}Nd_i$ samples are best explained by AFC involving less fractionated magmas. To illustrate, basaltic magmas incorporating granodiorite at elevated assimilation rates ($r \geq 0{\cdot}3$) can account for low $^{143}Nd/^{144}Nd_i$ analyses having Nb concentrations below 100 ppm (Fig. 20b). The apparent discrepancy between this explanation and the previous model for low Sr – high $^{87}Sr/^{86}Sr_i$ samples in Fig. 20a (many of which are *LT*-trachytes) can be reconciled by understanding trace element and isotopic effects of AFC. Initially, basaltic magmas are buffered against significant changes in Sr isotopic composition because of the high Sr abundance in the initial magmas relative to the assimilant. Because $D^{Sr} > 1$, as fractionation proceeds Sr concentrations decrease and the resultant magmas become more sensitive to contamination. This effect is clearly demonstrated by the analyses in Fig. 20a, where high $^{87}Sr/^{86}Sr$ values are limited to low Sr samples (< 150 ppm). In contrast, Nd behaves incompatibly with differentiation and its abundance in basaltic compositions is roughly

equivalent to that of the contaminant. Hence in AFC model calculations basaltic magmas are displaced towards the Nd isotopic composition of the wallrock much more efficiently than highly evolved magmas. For example, holding variables D^{Nd} and r constant the difference between $^{143}Nd/^{144}Nd$ of the initial magma and compositions at any given value of F along AFC curves is about 40% greater for magmas originating from basanite (e.g., sample MB27.5) than from model phonolite (80% FC of MB27.5). Therefore on a graph of $^{143}Nd/^{144}Nd$ versus a highly incompatible element (e.g., Nb and Ta), whose concentration will increase considerably as magmas fractionate, AFC curves will be steeper for less evolved magmas and flatten out for more evolved compositions. This effect is accentuated with changes in the rate of assimilation to crystal fractionation (r). High-r values are suggested for basaltic AFC trends while low-r paths fit more evolved compositions (Fig. 20b, inset). This may be explained by differentiation of basaltic magmas at deep levels in the crust where high ambient wallrock temperatures and hot basic magmas would facilitate higher rates of assimilation (Davidson & Wilson, 1989; Shaw *et al.*, 1993; Reiners *et al.*, 1995).

To further test and refine our ideas concerning initial magma compositions and the role of granodiorite contaminants in Mt. Sidley magma genesis, model differentiation trends are used to predict high LILE/HFSE ratios shown by the *LT*-trachyte suite. Figure 21 clearly demonstrates that AFC models can adequately explain the shift towards higher K/Ta ratios exhibited by the *LT*-trachyte and DPM samples. The convolute trends emanating from basalt towards Ford Granodiorite compositions bend at a point ($F \cong 0{\cdot}8$ to $0{\cdot}7$) where the relative enrichment of Ta exceeds that of K (e.g., as F becomes small, ~

0·7 → 0, Ta concentrations are enriched by a factor twice that of K). Several interdependent variables control the relative abundance of an element in a magma experiencing AFC (DePaolo, 1981; eqn. 6a) and hence the shape and position of inflection in Fig. 21. Our calculations require high values of r (0·9), low Nb contents in both the assimilant and the initial magma ($C_a \cong$ Ford Granodiorite and $C°_m \cong$ Waesche alkali basalt, respectively, $C_a/C°_m \sim 1$) and low bulk distribution coefficients ($D^K < 1$) in order to best fit high K/Ta – low Nb data. The model curve from sample K19 (Fig. 21) offers a hypothetical magma history linking alkali basalt to DPM and *LT*-trachyte enclave samples, and is broadly consistent with the 'mafic' fractionation trends presented in Fig. 20b.

Fractionation of LT-trachyte magmas and development of HT-trachyte compositions

At some stage during the evolution of the *LT*-trachytes, the effects of assimilation become subordinate to crystallization as alkali feldspar begins to dominate the fractionating assemblage. This is revealed by the progressive depletion of K and Ba relative to Rb, Th, Nb, and Ta on chondrite normalized diagrams and necessitates $D^K \geq 1$. Mass balance calculations involving the fractionation of alkali feldspar and lesser amounts of plagioclase, clinopyroxene, titanomagnetite and alkali amphibole from high K/Ta magmas can explain some 'evolved' (low K/Ta) *LT*-trachyte compositions. The alkali amphibole, arfvedsonite, recorded as a rare groundmass phase in silica-saturated and -oversaturated trachytes elsewhere (e.g., Price, *et al.*, 1985; Bardintzeff, *et al.*, 1986; Nono *et al.*, 1994) is found as a minor phase exclusively within *LT*-trachytes (Tables 1 and 6; Figs 3 and 5) and may reflect late-stage crystallization of volatile-rich alkaline liquids

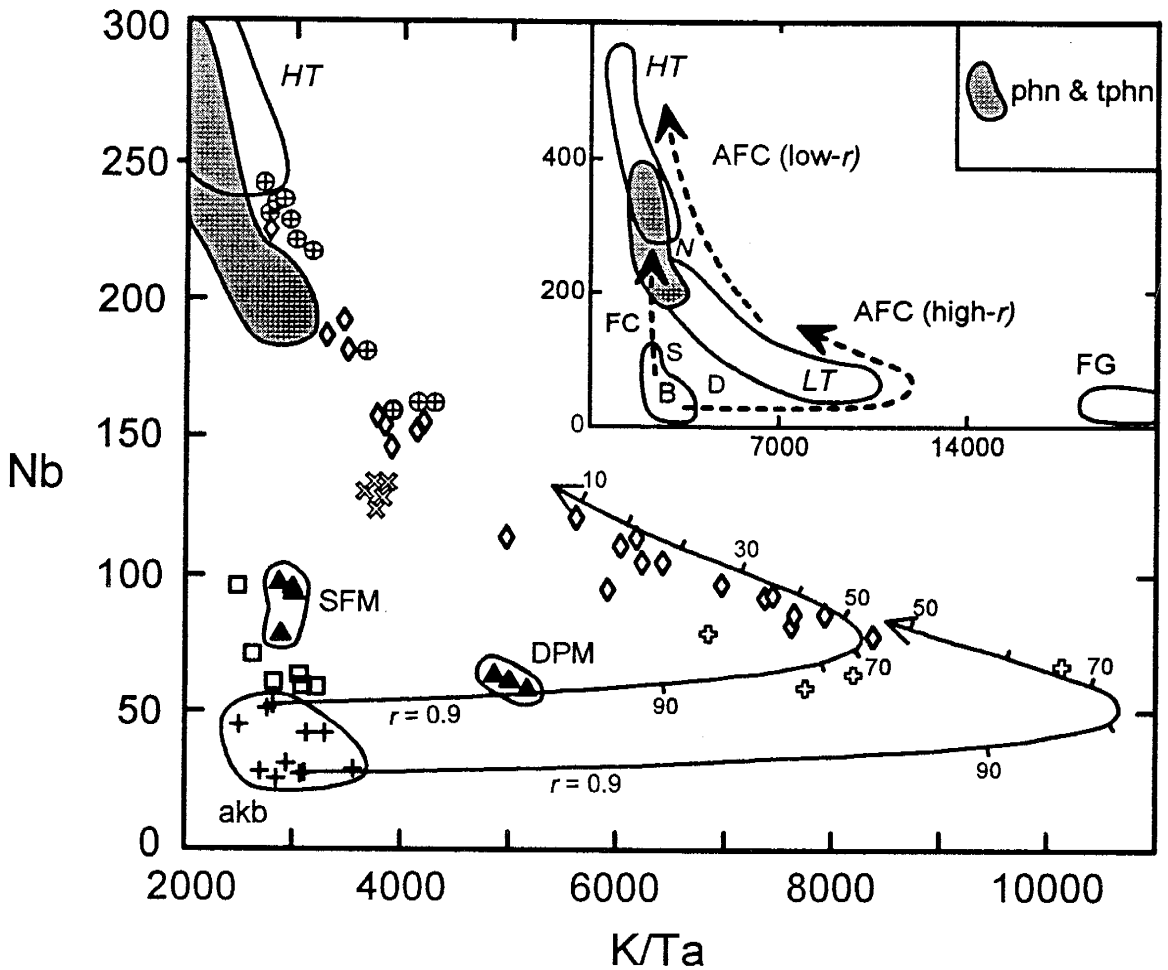

Figure 21. Plot of Nb (ppm) versus K/Ta showing model AFC curves. The two convolute trends describe the contamination of alkali basalts by Ford granodiorite and bend at a point where the relative enrichment of Ta exceeds that of K (60-80% residual liquid). Model calculations use: alkali basalt samples MB4.1 (lower curve) and K19 (upper curve); granodiorite sample R7460 as in Fig. 20; $r = 0{\cdot}9$; bulk distribution coefficients of $D^{K} = 0{\cdot}5$, $D^{Ta} = 0{\cdot}2$ and $D^{Nb} = 0{\cdot}2$. Inset shows Ford Granodiorite (FG) relative to volcanic rocks and general FC and AFC trends. Abbreviations: B = alkali basalt & basanite; D = DPM; S = SFM; phn & tphn = phonolite and tephriphonolite, respectively; *N*, *HT* & *LT* = trachyte types as in Fig. 17.

(Larsen & Sørensen, 1987; Wolff & Toney, 1993). Although it may be reasonable to suggest that crystal fractionation controls the enrichment of incompatible elements as *LT*-trachytes evolve, compelling evidence for open system processes such as intrusion and mixing of basaltic magmas (e.g., comingled lava units) and further assimilation of wallrock (e.g., high $^{87}Sr/^{86}Sr_i$ samples described by low-*r* AFC trends in Fig. 20a) argue against late-stage differentiation purely by FC mechanisms (see Fig. 21, inset).

The progressive fractionation of the *LT*-trachyte magmas may explain high incompatible trace element concentrations in the *HT*-trachyte rocks. Yet, due to the chemical diversity of *LT*-trachytes and the complexity posed by multiple open system processes, models describing the genesis of *HT*-trachytes cannot be suitably constrained. Nevertheless, support for our hypothesis comes from field observations (discussed below) and some broad geochemical comparisons. For example, chondrite normalized REE patterns for the most evolved *LT*-trachyte samples closely match patterns of the least evolved *HT*-trachytes (those with Th < 70 ppm; Fig. 17). Furthermore, the overall range in Eu/Eu* ratios of *LT*-trachytes (0·9 to 0·1) relative to *HT*-trachytes (0·5 to 0·05) favors their association by progressive fractionation (assuming that D^{Eu} remains ≥ 1). In contrast, patterns for *N*-trachytes display large negative Eu-anomalies (Eu/Eu* ranging from 0·2 to 0·03) equivalent to the most evolved *HT*-trachytes yet are lower in overall REE content. This and the fact that *HT*-trachytes were erupted more than 100 ka before the *N*-trachyte tephras (deposited during stages II and III, respectively; Panter *et al.*, 1994) suggests that the two suites evolved separately. Irrespective of their origin, the low $^{143}Nd/^{144}Nd_i$ (Fig. 20b) and high $\delta^{18}O$ (6·6‰ for anorthoclase sample MB33.3an; Table 8) values from

measured *HT*-trachytes indicate contributions from the crust. We propose that further assimilation of felsic country rocks by evolving *LT*-trachytes at low values of r (< 0·2; refer to the generalized AFC trend shown in Fig. 20b) produced the low Nd ratios and high incompatible trace element contents of *HT*-trachytes.

The *HT*-trachyte lavas represent the onset of trachytic activity exposed at Mt. Sidley and underlie the *LT*-trachyte suite in the western caldera wall (Weiss Amphitheater, Fig. 1). Several lines of evidence indicate that the trachyte succession may reflect eruptions from a compositionally stratified system. $^{40}Ar/^{39}Ar$ age determinations from both compositional types are indistinguishable within analytical uncertainty (Fig. 22), and based on field relations we believe the *HT*- and *LT*-trachytes to be cogenetic (Smellie *et al.*, 1990), extruded during a single phase of activity on the southern slopes of the stage I Sidley volcano (Panter *et al.*, 1994). The trachyte succession reveals an overall compositional progression towards lower incompatible element contents (e.g., Rb, Th, La, Nb and Ta) of erupted magmas with time: initially from a black-colored monomict fall deposit that gradually passes up into foliated, incompatible element 'enriched' *HT*-trachyte lavas; then to incompatible element 'depleted' *LT*-trachytes (Fig. 22). The overall depletion of highly incompatible elements with increasing stratigraphic height is broadly consistent with well documented pyroclastic sequences erupted from small (< 10 km^3), strongly zoned alkaline systems (e.g., Wörner & Schmincke, 1984; Wolff *et al.*, 1990; Turbeville, *et al.*, 1993). In Fig. 22, three of the *LT*-trachyte samples (MB39.6, MB30.6 and MB30.3) represent 'host' lavas collected from comingled units. Consequently, abrupt compositional changes may reflect chemical heterogeneities caused by non-homogeneous

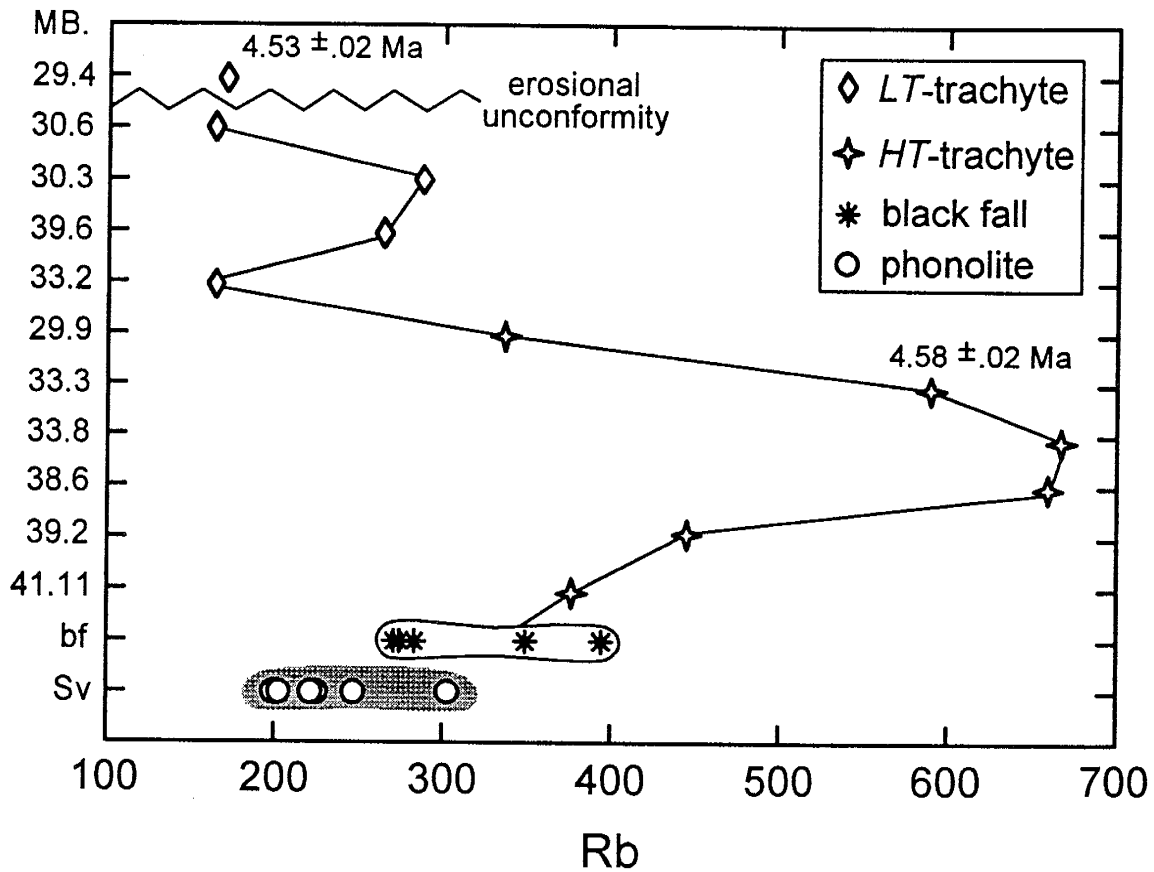

Figure 22. Plot of Rb (ppm) variations with stratigraphy (sample numbers arranged in their relative stratigraphic positions on y-axis) from the western caldera wall succession. Phonolite lavas of the Sidley volcano (Sv) are overlain by a compositionally heterogeneous (phonolite-trachyte) pyroclastic fall deposit (bf = black fall). The black fall is conformably overlain by *HT*-trachyte and then by *LT*-trachyte lavas which include comingled units. *LT*-trachyte sample, MB29.4, is a red-colored pyroclastic fall deposit that caps the caldera wall sequence. $^{40}Ar/^{39}Ar$ plateau ages show 1σ errors.

magma mixing/mingling (i.e. variable intensity of resorption and hybridization of enclaves), or, it may be possible that concentration gradients in the chamber were re-established between eruptive periods.

The relative position of the black pyroclastic fall deposit (a 10–15 m thick, bomb-bearing lapilli tuff) within the western caldera wall succession defines a petrological shift in erupted magmas from phonolites of the Sidley volcano to compositions of the trachyte series (Panter *et al.*, 1994). Moreover, the apparent physical gradation upward into the basal section of the *HT*-trachyte suite (dark-gray unwelded cindery scoria → fiamme-like flattened scoria → light-gray strongly welded tuff → cream-colored thinly foliated flows of trachyte) suggests a genetic link between the black fall and the trachyte series. Although lacking definitive field or petrographic evidence for mixing, the strong chemical variations in clasts in the black fall deposit (Fig. 22) reflect interaction between contrasting magma types. The major element compositions of clasts in the deposit range widely from *Ne*-phonolites (up to 23% *Ne* and 16 wt.% total alkali) to silica-saturated trachytes (up to 1% *Qz* and 11 wt.% total alkali); and trace elements Ba and Sr vary from 450 and 80 ppm, respectively, to concentration levels below detection. In addition, Th contents are elevated and range from 47 ppm to as high as 100 ppm, exceeding measured abundances in *N*- and *LT*-trachytes, yet, are comparable to *HT*-trachytes and some phonolites. The high Sr and low Nd isotopic ratios of black fall sample MB38.3 (Table 8; Fig. 20a) indicate contamination by crust; a signature inherited from component magmas. $^{87}Sr/^{86}Sr_i$ ratios of several other samples are lower and overall the black fall deposit shows a considerable range of values (0·7031–0·7041; Table 8). Attempts to model the clasts as

mixtures of phonolitic compositions immediately beneath the black fall deposit with overlying *HT*-trachytes (Fig. 22) are insufficient to describe the marked chemical heterogeneity of the black fall deposit (Fig. 23) and we infer a more dynamic mixing process involving rapid exchange between two distinct magma reservoirs and simultaneous mixing and eruptive withdrawal of the upper portion of a zoned trachyte system.

MAGMA ORIGIN AND PHYSICAL MODELS OF EVOLUTION

The complex geochemical variations of Mt. Sidley volcanic rocks can be explained by magmatic differentiation along three major lineages: 1) fractional crystallization of basanite ($Ne > 10\%$) to produce the phonolite series; 2) fractional crystallization of alkali basalt ($Ne < 8\%$) to produce the *N*-trachyte suite and; 3) assimilation of crust by alkali basalt and concurrent crystal fractionation evolving *LT*- and *HT*-trachyte compositions (Fig. 23). Magma mixing and the assimilation of wallrock in upper crustal chambers may account for some enigmatic variations within each series, however, these effects are secondary in terms of controlling the main trends of differentiation. The apparent change in parental magma composition from basanite to alkali basalt reflects a shift towards higher degrees of partial melting of mantle peridotite. Different degrees of partial melting may be the fundamental basis for the divergent petrogeneses of Mt. Sidley magmas.

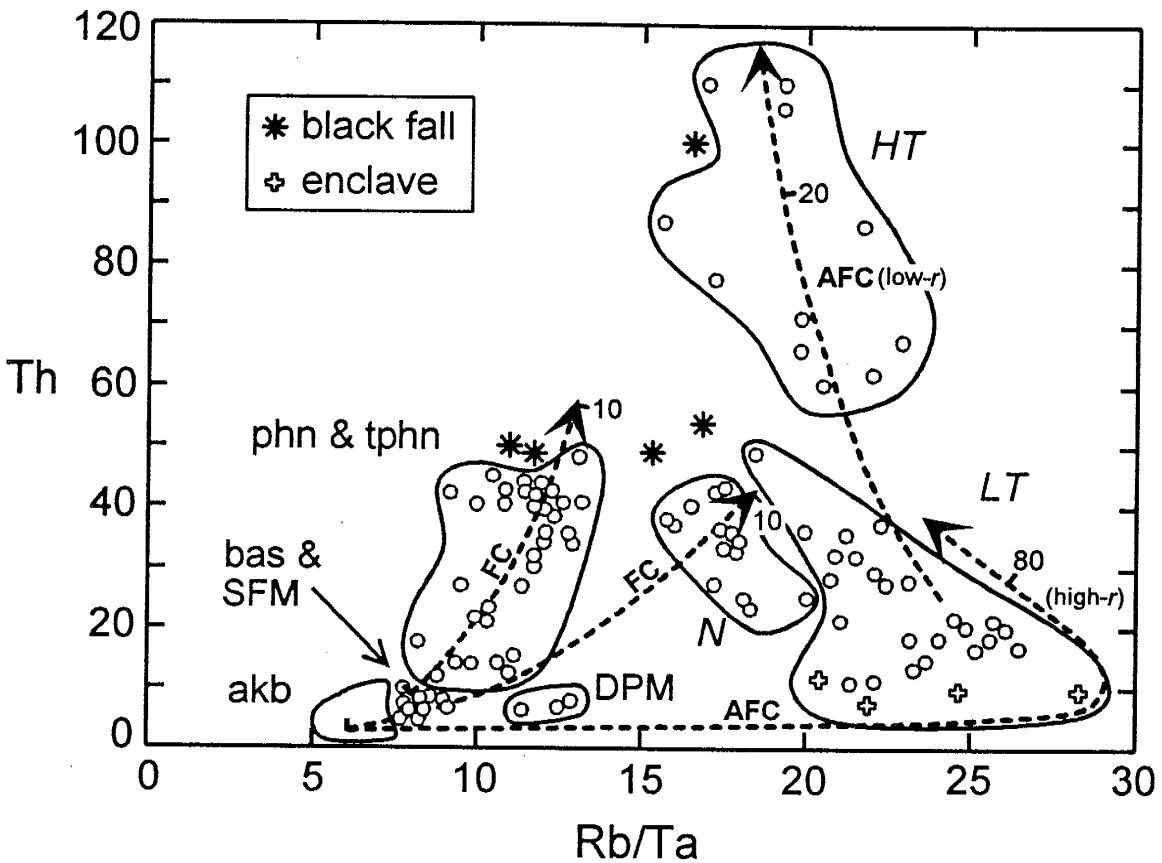

Figure 23. Th (ppm) versus Rb/Ta diagram showing main differentiation trends for Mt. Sidley volcanic rocks. Field for alkali basalts (akb) are Mt. Waesche samples. The black fall (asterisk) is interpreted to be a mixture of multiple endmember compositions. *N*, *HT* and *LT* fields define trachyte subdivisions and SFM and DPM refer to mugearite types. The field of phonolitic compositions include tephriphonolites (tphn) and phonolites (phn). Numbered tick-marks along fractionation trends refer to the percent magma remaining. FC model curves approximate D^{Rb} and $D^{Th} \leq 0{\cdot}1$ and D^{Ta} of 0·4. AFC trends calculated at $D^{Th} = 0{\cdot}1$ and $D^{Ta} = 0{\cdot}2$ with D^{Rb} varying between 1·3 for the high-*r* (~ 1) curve and 0·3 for the low-*r* ($\leq 0{\cdot}1$) curve. The compatibility of Rb during the high-*r* phase of AFC suggests crystal fractionation of biotite and/or amphibole. AFC curves use the same Ford granodiorite contaminant as in Figs. 20 and 21.

Partial melting and magma ascent

The magmatic evolution of Mt. Sidley began with a significant phase (~ 1 m.y.) of mantle-derived basanitic melt which differentiated to form ~ 180 km^3 of exposed lavas comprising the phonolite series. From experimental studies, Green (1973) concluded that basanite can be generated by 6% partial melting of a garnet lherzolite with 0·2–0·4% H_2O at pressures between 25 and 30 kbar. Eggler (1978) investigated the effect of CO_2 in addition to H_2O on melting of peridotite. He concluded that small degrees of melting of a mantle containing high CO_2/H_2O volatile compositions could produce CO_2-saturated basanitic magmas at pressures of 20–30 kbar. Low degrees of melting (< 2%) of a hydrous garnet lherzolite source has also been suggested based on the REE contents of naturally occurring basanitic lavas (Kay & Gast, 1973; Kyle & Rankin, 1976). Frey & Roden (1987) found that melting < 1% of a 'depleted' peridotite could explain REE of basanites from the Massif Central (France), arguing against higher degrees of melting (10–15%) of an 'enriched' source (elevated LREE contents relative to HREE) as originally proposed by Chauvel & Jahn (1984). Hasse & Devey (1994) reached a similar conclusion for the generation of basanites from the Vesteris Seamount, Greenland Basin, estimating partial melts as low as 0·5% from a depleted source. Mt. Sidley basanites are similar to "evolved" basanites from the Vesteris Seamount and Massif Central compositions and our approach to obtain constraints on the degree of partial melting is comparable with that of Frey & Roden (1987) and Hasse & Devey (1994).

In Fig. 24, liquid lines are calculated by non-modal equilibrium batch melting of mantle peridotite. Mt. Waesche alkali basalts have low concentrations of Ni (< 200 ppm)

and low *mg*-numbers (< 60) thus, as with Mt. Sidley basanites, they do not represent primary melts in equilibrium with peridotite. Primary compositions for basanites and alkali basalts can be roughly estimated by extrapolating back along major trends of differentiation towards lower Yb_n values. Liquids calculated using a spinel lherzolite from the Executive Committee Range (sample 40E; Wysoczanski, 1993) show that 2% melting with a clinopyroxene/garnet ratio of between 12/3 and 13·5/1·5 in the residual will approximate primary basanite compositions (Fig. 24). The production of Mt. Waesche alkali basalt from a spinel lherzolite source involves higher degrees of partial melting (≥ 5) leaving a clinopyroxene/garnet ratio of between 10/5 and 13/2.

Small-degree volatile-charged alkaline melts that rise rapidly to the surface, facilitated by magma- and volatile-induced crack propagation (Spera, 1984; Nicolas, 1986), will undergo minimal fractionation and interaction with the lithosphere. Mt. Sidley basanites, although slightly evolved, are not contaminated and the presence of angular inclusions of peridotite and pyroxenite would suggest a rapid ascent through the crust. A low pressure environment for phonolite differentiation is inferred from normative mineralogy (Fig. 10) and its long-term residence within upper crustal chambers would likely facilitate magma-wallrock interaction, however, the isotopic and trace element signatures of phonolitic lavas reveal little if any contamination by crust (Table 8 and Figs. 20 and 21). This may reflect the low assimilation potential of magmas surrounded by 'cold' country-rock in shallow reservoirs. In this case, a large magma–wallrock thermal contrast would promote rapid heat loss by conduction and decrease the rate ratio *r* in AFC models (Reiners *et al.*, 1995). Another explanation could be the lack of a strong

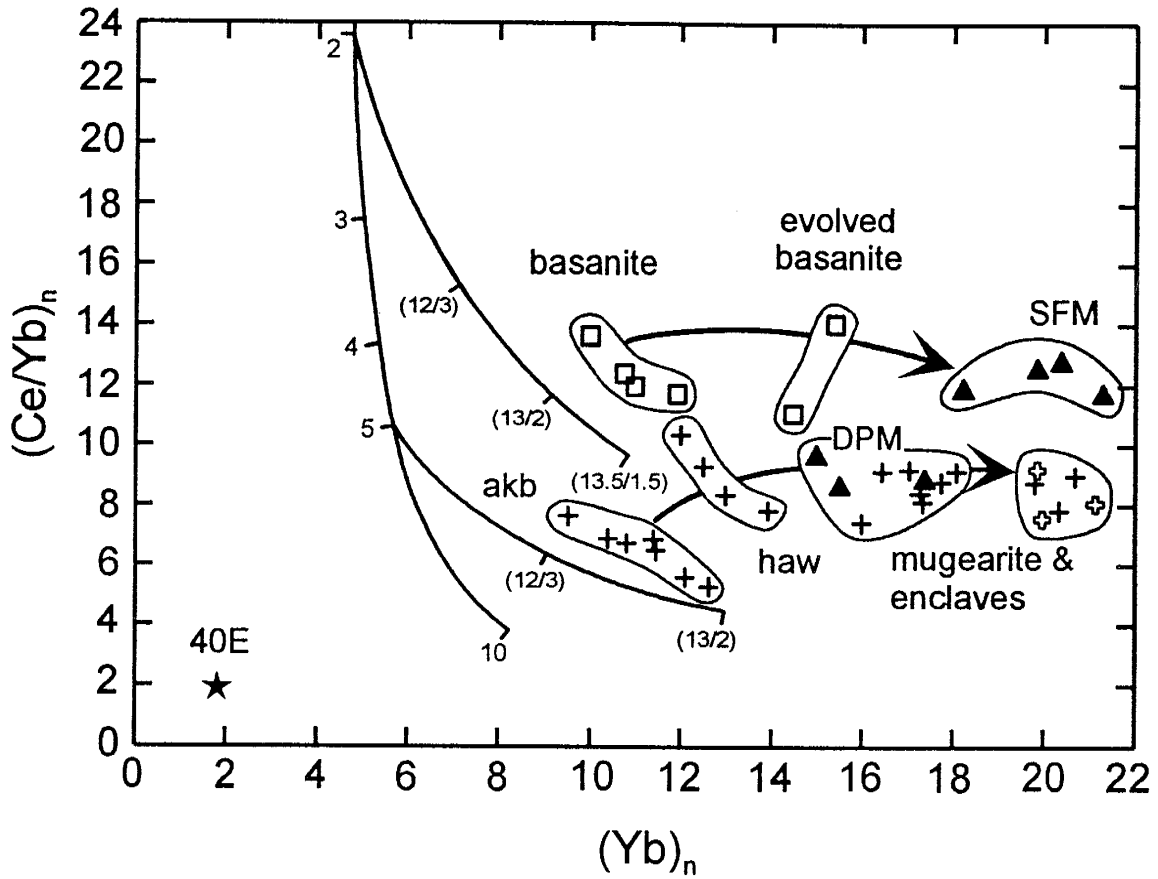

Figure 24. Plot of chondrite-normalized Yb versus normalized Ce/Yb for Mt. Sidley and Mt. Waesche basalts and mugearites. Arrows linking compositional fields illustrate two major magmatic lineages; a strongly silica-undersaturated series (basanite → SFM) and a more saturated series (alkali basalt → DPM). Solid lines represent non-modal equilibrium batch melting (Shaw, 1970) of a spinel lherzolite from the ECR (sample 40E; Wysoczanski, 1993). Partial melting lines are calculated using mineral/liquid partition coefficients from Johnson *et al.* (1990), a melting mode of 5% ol, 5% opx, 50% cpx, 40% gt, and a residual mineralogy of 65% ol, 20% opx, 10% cpx, 5% gt. Secondary curves that branch to the right are for higher residual cpx/gt ratios (12/3, 13/2, 13·5/1·5) calculated at a constant percent of partial melting (denoted by numbered tick marks along the primary curve). Open crosses represent 'mafic' enclaves sampled from comingled trachytic lavas at Mt. Sidley.

compositional dissimilarity between magma and wallrock; a situation that would most likely occur within the rift-related alkaline rocks of the uppermost Marie Byrd Land crust. Magma storage near the surface may be facilitated by horizons of neutral buoyancy within a volcanic pile (Ryan, 1987). Ryan (1987) suggested that magma stored in equilibrium with ambient density must also be in mechanical equilibrium with its surroundings, thus, providing long-term stability to the system. Such a mechanism may explain the ~ 1 m.y. eruptive history of Mt. Sidley phonolites and the prolonged phonolitic activity at Mt. Erebus (~ 235 ka; Esser *et al.*, 1995), including a persistent lava lake in its summit crater (Kyle *et al.*, 1982; 1992).

Higher degrees of melting will produce more silica-saturated volatile-poor melts (Green, 1971). A more saturated melt may rise more slowly to the surface than a strongly undersaturated melt, providing a greater opportunity for magmas to interact with the lithosphere (cf. Hoernle & Schmincke, 1993). Mt. Waesche alkali basalts, which represent higher degrees of partial melting (up to 10% from a spinal lherzolite; Fig. 24), contain abundant upper crustal xenoliths yet inclusions of lowermost crust or mantle are notably absent (Wysoczanski, 1993). This suggests that these magmas may have fractionated at mid-crustal levels en route to the surface. It is interesting to note that within the Executive Committee Range peridotite xenoliths occur only in parasitic cones composed of basanite, arguing for their faster ascent from depth. Mantle-derived melts that pool at deeper levels in the crust where ambient temperatures are higher will likely experience AFC, suffering significant elemental and isotopic changes only if the assimilant is

geochemically distinct from the magma. Such a scenario could explain the origin of the *LT*-trachyte rocks.

Chemical zonation and eruption of trachyte magmas

We have previously discussed the association of the *LT*- and *HT*-trachyte suites based on stratigraphic relationships and fractionation schemes (Figs. 20b and 23), and proposed an eruption model to explain their overall chemical variations with time (Fig. 22). The sequence of events leading to the deposition of the lava sequence sampled on the west caldera wall from a chemically stratified system is summarized in Fig. 25.

The ascent of alkali basalts through the lithosphere was arrested at a level where reaction with crust could occur at high assimilation to fractional crystallization rates (r = 0·9). Based on isenthalpic (energy balanced) AFC calculations, Reiners *et al.* (1995), determined that high r values (≥ 1) can result during early stages of basalt contamination when initial countryrock temperatures are between 400° and 800°C. Such conditions are unlikely to occur at shallow levels in continental crust (< 10 km), even within a rift environment (Chapman, 1986). Pressure-temperature estimates from meta-sediments which pass upward into Ford Granodiorite in the Fosdick Metamorphic Complex, coastal Marie Byrd Land, indicate rapid exhumation from mid-crustal depths (5–6 kbar) during Gondwana rifting (Smith, 1992; Luyendyk *et al.*, 1992). Yet even at mid-crustal depths temperatures greater than 400°C require elevated heat flow. A high geothermal gradient within the Marie Byrd Land crust may be inferred by the presence of young volcanic centers (Palais *et al.*, 1988; LeMasurier & Thomson, 1990; McIntosh & Wilch, 1995),

Figure 25. Model for the chemical zonation and eruption of trachyte magmas. (a) Phonolitic magma-reservoir (Phn) situated within the volcanic edifice at the end of stage-I activity (4.8 Ma). Basanitic melts (bas), parental to stage-I phonolites, are superseded by primary alkali basalt (akb) as a result of an increase in the degree of mantle partial melting. Rising to mid-crustal levels, alkali basalt reacted with granodiorite at high assimilation/fractional crystallization rates (high-*r*) to form *LT*-trachytes. Emplacement of *LT*-trachyte magmas into an upper crustal chamber allowed further differentiation through crystal fractionation and assimilation of wallrock at low-*r*. Chemical stratification of chamber magmas by roofward enrichment in incompatible elements produced *HT*-trachyte compositions. (b) Upper portion of zoned trachytic chamber intrudes a separate body of phonolite causing vigorous convection and vesiculation of the magmas. Chamber overpressure due to the volume increase fractured countryrock and allowed magma to escape to the surface where explosive eruption of mixed magmas (phonolite + trachyte) produced the black pyroclastic fall deposit (bf). (c) As the pressure in the system decreased and mixing abated, lower discharge rates were driven by volatile exsolution in reservoir magmas, erupting lavas of *HT*-followed by *LT*-trachyte compositions (4.6 Ma). At some stage, basalt was injected into the base of the chamber and was rapidly cooled against the overlying magmas. Vesiculation lowered the density of the basalt making the interfacial layer gravitationally unstable. (d) Plumes of vesiculated basalt rose from the layer of instability and mixed with overlying *LT*-trachyte magmas and were erupted as comingled lavas (CL).

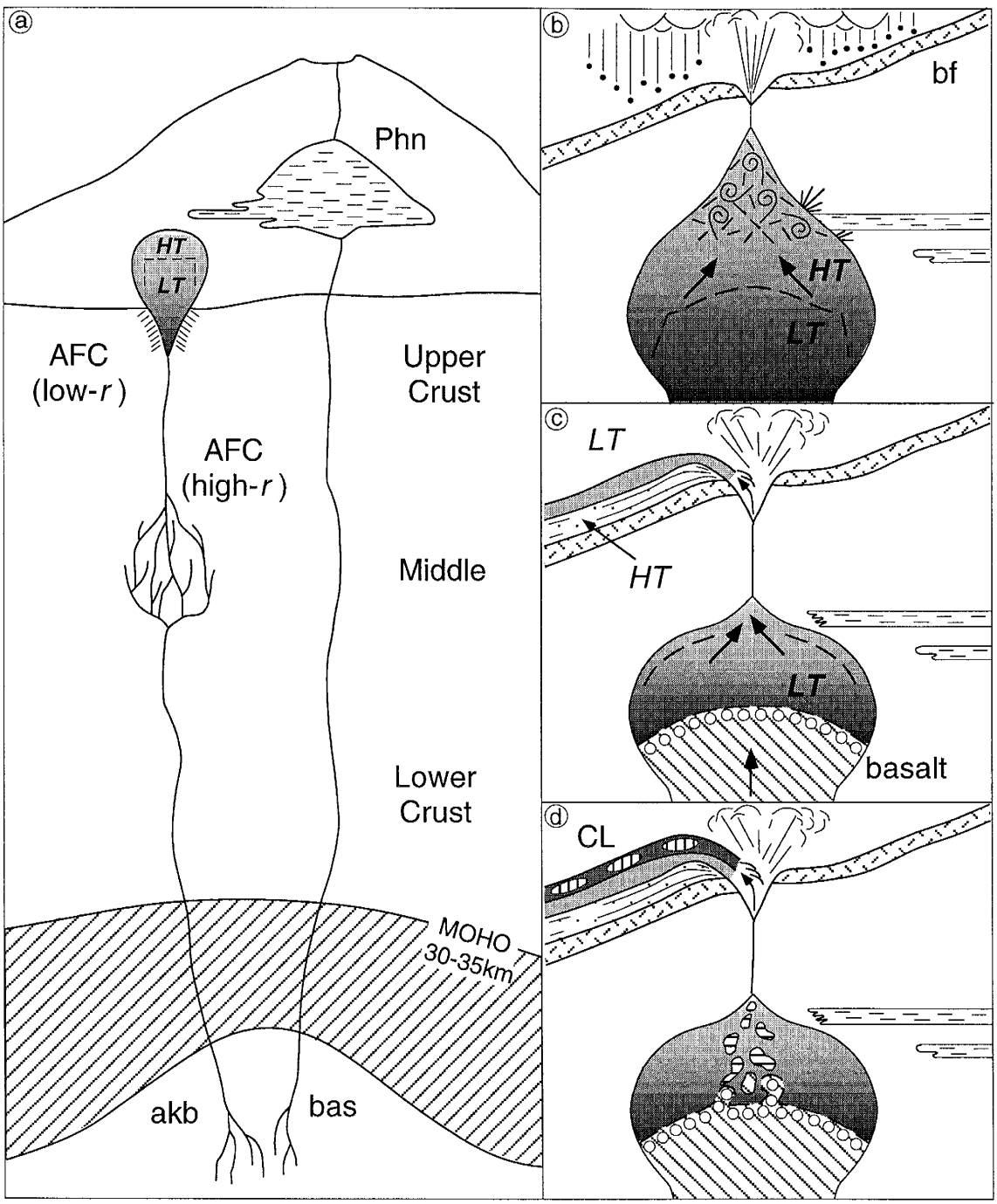
a
Phn
HT
LT
AFC
(low-r)
AFC
(high-r)
Upper
Crust
Middle
Lower
Crust
MOHO
30-35km
akb
bas
b
bf
HT
LT
c
LT
HT
LT
basalt
d
CL

active volcanism (LeMasurier & Kawachi, 1990; Blankenship *et al.*, 1993) and by analogy with the western Ross Sea (Berg *et al.*, 1989; Della Vedova *et al.*, 1992; Kyle *et al.*, 1992). We consider it reasonable to suggest that high temperature conditions existed 5 million years ago within un-exhumed calc-alkaline granitoids beneath Mt. Sidley, facilitating high rates of assimilation by mantle partial melts (Fig. 25a).

The emplacement of AFC-derived trachytic compositions within an upper crustal reservoir allowed for the chemical stratification of magma. In Fig. 25, we illustrate *LT*-trachyte magma passing upward into *HT*-trachyte magma, implying strong roofward enrichment in Rb, Th, Nb, Ta, Hf, Y, Zr and REE (volatiles?) and depletion in Al, Ba and Sr. We speculate that differentiation at this stage was dominated by crystal fractionation of alkali feldspar, probably, in concert with very low rates of assimilation (e.g., Fig. 20b). The melting of wallrock by boundary layer liquids may have occurred during early stages of emplacement when temperatures at the margins were high (McBirney *et al.*, 1985). Fractionated and dilute (H_2O-rich) boundary layer fluids may then rise to the top of the magma reservoir by positive compositional buoyancy (Tait *et al.*, 1989), traversing a sidewall cumulate zone via melt-filled channels (Trial & Spera, 1990).

The eruption of the compositionally zoned system was initiated by explosive interaction between cupula liquids (*HT*-trachyte) and a separate body of phonolitic magma (Fig. 25b). The intrusion of slightly less dense trachytic magma (2·25 g/cm^3) into phonolite (> 2·26 g/cm^3) caused vigorous convection and magma mixing. The geochemical heterogeneity of the black pyroclastic fall deposit suggests that the mixing of magmas occurred shortly before eruption. Injection of trachyte magma into the overlying

chamber and the subsequent heating and vesiculation of the resident magma increased fluid pressure sufficiently to fracture the confining chamber walls and drive magmas explosively to the surface. Strongly welded textures towards the top of the black fall deposit may reflect higher accumulation rates near the vent; a consequence of lower eruption column height as the gas content in the magma and its rate of discharge decreased. Such a scenario may explain the physical passage of the black fall unit up into the basal lavas of the *HT*-trachyte suite. For a shallow magma system, the transition from pyroclastic to lava-forming eruptions is dependent on the magma discharge rate and chamber-conduit pressures (Jaupart & Allègre, 1991; Woods & Koyaguchi, 1994). The large overpressure induced by magma mixing was relieved by the high eruption rate of the black fall magmas. As the pressure in the system decreased and mixing abated, lower discharge rates were driven by volatile exsolution in reservoir magmas, erupting the upper portion of the chamber as lavas (Fig. 25c)

At some stage the chamber was replenished by basaltic magma which pooled beneath trachyte magma at the base of the system (Fig. 25c). Initially, mixing of the two magmas was inhibited due to their strong density contrast (see Koyaguchi & Blake, 1991). On the basis of field observations and fluid dynamical concepts, magma mixing in a stratified system may occur if the lower mafic layer becomes vesiculated, which effectively decreases its density until it is equal with the overlying magma (Eichelberger, 1980; Huppert *et al.*, 1982, 1984; Thomas *et al.*, 1993). This may occur when hot volatile-rich mafic magma is cooled rapidly against lower temperature reservoir magma, crystallizing and becoming saturated with respect to volatile components. Eichelberger (1980)

proposed that the physical mixing of mafic magma with an overlying silicic reservoir could occur in plumes rising from a vesiculated interfacial region. Huppert *et al.* (1982) suggested, in contrast, that density changes in the whole lower layer may cause mixing by convective overturn. In laboratory experiments, Thomas *et al.* (1993) demonstrated that gas bubbles moving through a high viscosity liquid will accumulate below a lower viscosity less-dense liquid and form a layer of gravitational instability, giving rise to bubble plumes which buoyantly ascend and mix with overlying fluids. Hence, agreeing with Eichelberger's original model. In Fig. 25d, we adopt the plume theory of mixing for comingled lavas of the *LT*-trachyte suite in order to best explain: 1) the coarse mixture of small (typically ≤ 10 cm) vesiculated mafic enclaves in trachyte; 2) the lack of hybrid lithologies (homogeneous mixtures) and; 3) the occurrence of individual small volume comingled units, which argues against a single eruption triggered by convective overturn (e.g., Sparks *et al.*, 1977; Wolff, 1985; Araña *et al.*, 1994).

CONCLUSIONS

The detailed study of Mt. Sidley permits the dynamic reconstruction of its volcanic history and magma genesis and offers an insight into the genetic relations of phonolitic and trachytic magma series within an intraplate continental setting. Previous petrological studies of alkaline volcanoes, in which phonolites and trachytes are closely associated, have appealed to either complex open system processes to explain their evolution from a common parent (e.g., Barbieri *et al.*, 1988; Turbeville, 1993) or their evolution along separate magma lineages from fundamentally different parental compositions (e.g., Price &

Chappell, 1975; Downes, 1984; Price *et al.*, 1985). At Mt. Sidley, the spatial and temporal distinction between phonolites and trachytes and their strongly divergent geochemistry has been explained by evolution along separate magma trends. Furthermore, each series appears to have originated from a distinct basaltic parent (i.e. basanite → phonolite; alkali basalt → trachyte).

Major changes in the composition of erupted magmas at each stage of activity can be related to variations in the degree of partial melting in the upper mantle. Our model suggests that strongly silica-undersaturated basanitic magmas were derived by low (≤ 2%) degrees of partial melting of a mantle peridotite, whereas more silica-saturated alkali basalts required higher (5–10%) degrees of melting of the same source. Hence, the transition from phonolite series compositions of stage-I to the trachytes of stage-II (*HT*- and *LT*-trachyte suites) must ultimately reflect an increase in the degree of partial melting of the source. The *N*-trachytes, which were erupted at the beginning of stage-III, are overlain by DPM tephras (both modeled as derivatives of alkali basalt) and then by SFM and other intermediate compositions (modeled as derivatives of basanite) at the southern end of Mt. Sidley. The stage-III succession is interpreted as being transitional between higher and lower degrees of partial melting that was culminated with the eruption of xenolith-bearing basanite during stage-IV.

The variation in the degree of partial melting (low → high → low) during the 1·5 Ma life-span of Mt. Sidley is coincident with a southward migration of its activity. The rate and style of migration is emulated on a larger scale by the Executive Committee Range, where the southward displacement of activity corresponds with major changes in

the composition of erupted magmas between centers (Panter *et al.*, 1994). Volcanic migration in Marie Byrd Land cannot be explained as traces of individual mantle hot spots; as the Antarctic Plate is stationary (Lawver *et al.*, 1991) and the trends of other linear volcanic chains (Ames and Flood Ranges), which also show progressive younging towards the outer edge of the province (LeMasurier & Rex, 1989), are at 90° to each other. Therefore, the gross surficial expression of volcanism must reflect a horizontal relocation of sub-lithospheric zones of decompressive melting towards the outer edge of the province. The partial melting cycle at Mt. Sidley is thus interpreted to reflect the passing influence of a mantle upwelling beneath that portion of the lithosphere. Taking into account the HIMU OIB-like geochemical signature of basaltic samples, volcanism must have tapped a source largely affected by mantle plume activity.

The whole-rock and mineral compositions of Mt. Sidley magmas elucidate a complex differentiation history within the continental crust. Theoretical modeling of geochemical variations reveal that, while crystal/liquid fractionation processes within shallow reservoirs was dominant during phonolite production, AFC played an important role in trachyte genesis and lead to the production of silica-oversaturated compositions. We consider this to be a partial function of the rate of ascent through the crust, inferring that alkali basaltic melts (parental to trachyte) rose more slowly than basanitic melts (parental to phonolite). The physical mixing of magmas appears to be a persistent process throughout Mt. Sidley's activity and in some instances (e.g., black fall magmas) could have been facilitated by southward propagating tensional fractures.

REFERENCES

Adams, C. J., 1987. Geochronology of granite terranes in the Ford Ranges, Marie Byrd Land, West Antarctica. *New Zealand J. Geol. Geophy.* **29**, 51-72.

Allégre, C. J., Treuil, M., Minster, J. F., Minster, B., & Albaréde, F., 1977. Systematic use of trace elements in igneous process, Part I: fractional crystallization processes in volcanic suites. *Contri. Miner. Petrol.* **60**, 57-75.

Anderson, A. T., 1968. Oxidation of the LaBlache Lake titaniferous magnetite deposit, Quebec. *J. Geol.* **76**, 528-47.

Aoki, K., & Kushiro, I., 1968. Some clinopyroxenes from ultramafic inclusions in Dreiser Weiher, Eifel. *Contr. Miner. Petrol.* **18**, 326-37.

Araña, V., Martí, J., Aparicio, A., García-Cacho, L., & García-García, R., 1994. Magma mixing in alkaline magmas: An example from Tenerife, Canary Islands. *Lithos* **32**, 1-19.

Arth, J. G., 1976. Behavior of tarce elements during magmatic processes-summary of theoretical models and their applications. *J. Res. U.S. Geol. Survey* **4**, 41-7.

Baker, B. H., & McBirney, A. R., 1985. Liquid fractionation. Part III: geochemistry of zoned magmas and the compositional effects of liquid fractionation. *Jour. Volc. Geotherm. Res.* **24**, 55-81.

Baker, B. H., Goles, G. G., Leeman, W. P., & Lindstrom, M. M., 1977. Geochemistry and petrogenesis of a basalt-benmoreite-trachyte suite from the southern part of the Gregory rift, Kenya. *Contr. Miner. Petrol.* **64**, 303-32.

Barbieri, M., Peccerillo, A., Poli, G., & Tolomeo, L., 1988. Major, trace element and Sr isotopic composition of lavas from Vico volcano (central Italy) and their evolution in an open system. *Contr. Miner. Petrol.* **99**, 485-97.

Bardintzeff, J., Demange, J., & Gachon, A., 1986. Petrology of the volcanic bedrock of Mururoa Atoll (Tuamotu Archipelago, French Polynesia). *J. Volcanol. Geotherm. Res.* **28**, 55-83.

Berg, J. H., Moscati, R. J., & Herz, D. L., 1989. A petrologic geotherm from a continental rift in Antarctica. *Earth Planet. Sci. Lett.* **93**, 98-108.

Bence, A. E., & Albee, A. L., 1968. Empirical correction factors for the electron microanalysis of silicates and oxides. *J. Geol.* 76, 382-403.

Blankenship, D. D., Bell, R. E., Hodge, S. M., Brozena, J. M., Behrendt, J. C., & Finn, C. A., 1993. Active volcanism beneath the west Antarctic ice sheet and implications for ice-sheet stability. *Nature* **361**, 526-9.

Bottinga, Y., Weill, D., & Richet, P., 1982. Density calculations for silicate liquids I: revised method for aluminosilicate compositions. *Geochim. Cosmochim. Acta* **46**, 909-19.

Boudette, E. L. & Ford, A. B., 1966. Physical properties of anorthoclase from Antarctica. *Am. Mineral.* **51**, 1374-87.

Bowen N. L., 1937. Recent high temperature research on silicates and its significance in igneous petrology. *Amer. J. Sci.* **33**, 1-21.

Bromwich, D. H., 1990. Estimates of Antarctic precipitation. *Nature* **343**, 627-9.

Brown, W. L., 1993. Fractional crystallization and zoning in igneous feldspars: ideal water-buffered liquid fractionation lines and feldspar zoning paths. *Contrib. Mineral. Petrol.* **113**, 115-25.

Bryan, W. B., Finger, L. W., & Chayes, F., 1969. Estimating proportions in petrographic mixing equations by least-squares approximation. *Science* **163**, 926-7.

Cann, J. R., 1982. Rayleigh fractionation with continuous removal of liquid. *Earth Planet. Sci. Lett.* **60**, 114-6.

Caroff, M., Maury, R. C., Leterrier, J., Joron, J. L., Cotten, J., & Guille, G., 1993. Trace element behavior in the alkali basalt-comenditic trachyte series from Mururoa Atoll, French Polynesia. *Lithos* **30**, 1-22.

Cameron, M., & Papike, J. J., 1981. Structural and chemical variations in pyroxenes. *Am. Miner.* **66**, 1-50.

Carmichael, I. S. E., 1967. The iron-titanium oxides of salic volcanic rocks and their associated ferromagnesian silicates. *Contr. Miner. Petrol.* **14**, 36-64.

Cawthorn, G. R., Curran, E. B., & Arculus, R. J., 1973. A petrogenetic model for the origin of the calc-alkaline suite of Grenada, Lesser Antilles. *J. Petrology* **14**, 327-37.

Cerling, T. H., Brown, F. H., & Bowman, J. R., 1985. Low-temperature alteration of volcanic glass: hydration, Na, K, ^{18}O and Ar mobility. *Chem. Geology* **52**, 281-93.

Chapman, D. S., 1986. Thermal gradients in the continental crust. In: Dawson, J. B., Carswell, D. A., Hall, J., & Wedepohl, K. H. (eds.) *The Nature of the Lower Continental Crust*, Geol. Soc. Spec. Pub. 24, 63-70.

Chauvel, C., & Jahn B.-M., 1984. Nd-Sr isotope and REE geochemistry of alkali basalts from the Massif Central, France. *Geochim. Cosmochim. Acta* **48**, 93-110.

Coombs, D. S., & Wilkinson, J. F. G., 1969. Lineages and fractionation trends in undersaturated volcanic rocks from the East Otago Volcanic Province (New Zealand) and related rocks. *J. Petrology* **10**, 440-501.

Coombs, D. S., Cas, R. A., Kawachi, Y., Landis, C. A., McDonough, W. F., & Reay, A., 1986. Cenozoic volcanism in north, east and central Otago. In: Smith, I. E. M. (ed.) *Late Cenozoic Volcanism in New Zealand*, The Royal Society of New Zealand, Bulletin 23, 278-312.

Cox, K. G., & Bell., 1972. A crystal fractionation model for the basaltic rocks of the New Georgia Group, British Solomon Islands. *Contrib. Mineral. Petrol.* **37**, 1-13.

Cox, K. G., Bell, J. D., & Pankhurst, R. J., 1979. *The Interpretation of Igneous Rocks.* Allen & Unwin, London, 450 pp.

Cox, K. G., & Mitchell, C., 1988. Importance of crystal settling in the differentiation of Deccan Trap basaltic magmas. *Nature* **333**, 447-9.

Cox, K. G., Charnley, N., Gill, R. C. O., & Parish, K. A., 1993. Alkali basalts from Shuqra, Yemen: magmas generated in the crust-mantle transition zone? In: Prishard, H. M., Alabaster, T., Harris, N. B., & Neary, C. R. (eds.) *Magmatic Processes and Plate Tectonics*, Geol. Soc. Spec. Pub. 76, 443-53.

Craig, H., 1961. Standard for reporting concentrations of deuterium and oxygen-18 in natural waters. *Science* **133**, 1833-34.

Davidson, J. P., & Wilson, I. R., 1989. Evolution of an alkali basalt-trachyte suite from Jebel Marra volcano, Sudan, through assimilation and fractional crystallization. *Earth Planet. Sci. Lett.* **95**, 141-60.

Deer, W. A., Howie, R. A., & Zussman, J., 1966. *An Introduction to the Rock-Forming Minerals.* London: Longmans, 528 pp.

Della Vedova, B., Pellis, G., Lawver, L. A., & Brancolini, G., 1992. Heat flow and tectionics of the western Ross Sea. In: Yoshida, Y., Kaminuma, K., & Shiraishi, K. (eds.) *Recent Progress in Antarctic Earth Science*. Terra Scientific, Tokyo, 627-37.

DePaolo, D. J., 1981. Trace element and isotopic effects of combined wallrock assimilation and fractional crystallization. *Earth Planet. Sci. Lett.* **53**, 189-202.

Dobosi, G., 1989. Clinopyroxene zoning patterns in the young alkali basalts of Hungary and their petrogenetic significance. *Contr. Miner. Petrol.* **101**, 112-21.

Dobosi, G., & Fodor, R. V., 1992. Magma fractionation, replenishment, and mixing as inferred from green-core clinopyroxenes in Pliocene basanite, southern Slovakia. *Lithos* **28**, 133-50.

Downes, H., 1984. Sr and Nd isotope geochemistry of coexisting alkaline magma series, Cantal, Massif Central, France. *Earth Planet. Sci. Lett.* **69**, 321-34.

Downes, H., 1987. Tertiary and Quaternary volcanism in the Massif Central, France. In: Fitton, J. G., & Upton, B. G. L. (eds.) *Alkaline Igneous Rocks*, Geol. Soc. Spec. Pub. 30, Blackwell Scientific, Oxford, 517-30.

Downes, H., 1989. Magma mixing in undersaturated alkaline volcanics, Cantal, Massif central, France. *Miner. Mag.* **53**, 43-53.

Eggler, D. H., 1978. The effect of CO_2 upon partial melting of peridotite in the system Na_2O–CaO–Al_2O_3–MgO–SiO_2–CO_2 to 35 kb, with an analysis of melting in a peridotite-H_2O–CO_2 system. *Am. J. Sci.* **278**, 305-43.

Eichelberger, J. C., 1980. Vesiculation of mafic magma during replenishment of silicic magma reservoirs. *Nature* **288**, 446-50.

Ernst, W. G., 1962. Synthesis, stability relations, and occurrence of riebeckite and riebeckite-arfvedsonite solid solutions. *J. Geol.* **70**, 689-736.

Esser, R., Kyle, P. R., McIntosh, W. C., 1995. Revison of the eruptive history of Mount Erebus volcano, Ross Island: application of high precision $^{40}Ar/^{39}Ar$ dating. *Abst.* VII International Symposium on Antarctic Earth Sciences, Siena, Italy, 122.

Feng, X., & Savin, S. M., 1993. Oxygen isotope studies of zeolites-stilbite, analcime, heulandite, and clinoptilolite: II. Kinetics and mechanisms of isotopic exchange between zeolites and water vapor. *Geochim. Cosmochim. Acta* **57**, 4219-38.

Fitton, J. G., 1987. The Cameroon line, west Africa: a comparison between oceanic and continental alkaline volcanism. In: Fitton, J. G., & Upton, B. G. L. (eds.) *Alkaline Igneous Rocks*, Geol. Soc. Spec. Pub. 30, Blackwell Scientific, Oxford, 273-91.

Foland, K. A., Landoll, J. D., Henderson, C. M. B., & Jiangfeng, C., 1993. Formation of cogenetic quartz and nepheline syenites. *Geochim. Cosmochim. Acta* **57**, 697-704.

Freundt, A., & Schmincke, H-U., 1995. Petrogenesis of rhyolite-trachyte-basalt composite ignimbrite P1, Gran Canaria, Canary Islands. *J. Geophy. Res.* **100**, 455-74.

Frey, F. A., Green, D. H., & Roy, S. D., 1978. Integrated models of basalt petrogenesis: a study of quartz tholeiites to olivine melilites from south eastern Australia utilizing geochemical and experimental petrological data. *J. Petrology* **19**, 463-513.

Frey, F. A., & Roden, M. F., 1987. The mantle source for the Hawaiian Islands: Constraints from the lavas and ultramafic inclusions. In: Menzies, M. A., & Hawkesworth, C. J. (eds.) *Mantle Metasomatism*. London: Academic Press, 423-63.

Fudali, R. F., 1963. Experimental studies bearing on the origin of pseudoleucite and associated problems of alkalic rock systems. *Geol. Soc. Amer. Bull.* **74**, 1101-1126.

Gamble, J. A., 1979. Some relationships between coexisting granitic and basaltic magmas and the genesis of hybrid rocks in the Tertiary central complex of Slieve Gullion, northeast Ireland. *J. Volcanol. Geotherm. Res.* **5**, 297-316.

Gourgaud, A., 1991. Comagmatic enclaves in lavas from the Mont-Dore composite volcano, Massif Central, France. In: Didier, J., & Barbarin, B. (eds.) *Enclaves and Granite Petrology*, Developments in Petrology 13, Elsevier, Amsterdam, 221-33.

Gibb, F. G., 1972. The zoned clinopyroxenes of the Shiant Isles sill, Scotland. *J. Petrology* **14**, 203-30.

Green, D. H., 1971. Composition of basaltic magmas as indicators of conditions of origin: application to oceanic volcanism. *Phil. Trans. R. Soc. Lond.* **268A**, 707-25.

Green, D. H., 1973. Conditions of melting of basanite magma from garnet peridotite. *Earth Planet. Sci. Lett.* **17**, 456-65.

Gupta, A. K., Onuma, K., & Yagi, K., 1973. Effect of silica concentration on the diopsidic pyroxenes in the system diopside-$CaTiAl_2O_6SiO_2$. *Contr. Miner. Petrol.* **41**, 333-44.

Haase, K. M., & Devey, C. W., 1994. The petrology and geochemistry of Vesteris Seamount, Greenland Basin-an intraplate alkaline volcano of non-plume origin. *J. Petrology* **35**, 295-328.

Hallett, R. B., & Kyle, P. R., 1993. XRF and INAA determinations of major and trace elements in Geological Survey of Japan igneous and sedimentary rock standards. *Geostandards Newsletter* **17**, 127-33

Hallett, R. B., 1994. Volcanic geology, paleomagnetism, geochronology and geochemistry of the Rio Puerco Necks, west-central New Mexico. Unpublished Ph.D. thesis, New Mexico Institute of Mining and Technology, Socorro, New Mexico, U.S.A., 340 pp.

Halliday, A. N., Dickin, A. P., Fallick, A. E., & Fitton, J. G., 1988. Mantle dynamics: A Nd, Sr, Pb and O isotopic study of the Cameroon line volcanic chain. *J. Petrology* **29**, 181-211.

Hamilton, D. L., & MacKenzie W. S., 1965. Phase equilibrium studies in the system $NaAlSiO_4$-$KAlSiO_4$-SiO_2-H_2O. *Mineral. Mag.* **34**, 214-31.

Hart, S. R., Blusztajn, J. S., & Kyle, P. R., 1994. The geochemistry of McMurdo Group volcanic rocks, Antarctica. ICOG8, Berkeley, CA., U.S. Geological Survey Circular 1107, 130.

Hart, S. R., & Kyle, P. R., 1994. The geochemistry of McMurdo Group volcanic rocks. *Antarctic J. U.S.*

Hernandez, J. E. G., Nortario Del Pino, J. S., Martin G. M. M., Reguera, F. H., & Losada, J. A. R., 1993. Zeolites in pyroclastic deposits in southeastern Tenerife (Canary Islands). *Clays and Clay Minerals* **41**, 521-6.

Hildreth, W., 1979. The Bishop Tuff: evidence for the origin of compositional zonation in silicic magma chambers. *Geol. Soc. Amer., Spec. Pap.* **180**, 43-75.

Hildreth, W., 1981. Gradients in silicic magma chambers: implications for lithospheric magmatism. *J. Geophy. Res.* **86**, 10153-92.

Hoernle, K., & Schmincke, H-U., 1993. The role of partial melting in the 15-Ma geochemical evolution of Gran Canaria: a blob model for the Canary hotspot. *J. Petrology* **34**, 599-626.

Hole, M. J., & LeMasurier, W. E., 1994. Tectonic controls on the geochemical composition of Cenozoic mafic alkaline volcanic rocks from West Antarctica. *Contrib. Mineral. Petrol.* **117**, 187-202.

Höller, H., Wirsching, U., & Fakhuri, M., 1974. Experimente zur zeolithbildung durch hydrothermale umwandlung. *Contrib. Mineral. Petrol.* **46**, 49-60.

Huppert, H. E., Sparks, R. S. J., & Turner, J. S., 1982. Effects of volatiles on mixing in calc-alkaline magma systems. *Nature* **297**, 554-7.

Huppert, H. E., Sparks, R. S. J., & Turner, J. S., 1984. Some effects of viscosity on the dynamics of replenished magma chamber. *J. Geophys. Res.* **89**, 6857-77.

Jacobs, J. W., Korotev, R. L., Blanchard, D. P., & Haskins, L. A., 1977. A well tested procedure for instrumental neutron activation analysis of silicate rocks and minerals. *J. Radioanal. Nucl. Chem.* **40**, 98-114.

James, D. E., 1981. The combined use of oxygen and radiogenic isotopes as indications of crustal contamination. *Ann. Rev. Earth Planet. Sci.* **9**, 311-44.

Jaupart, C., & Allègre, C. J., 1991. Gas content, eruption rate and instabilities of eruption regime in silicic volcanoes. *Earth Planet. Sci. Lett.* **102**, 413-29.

Jezek, P. A., & Noble, D., 1978. Natural hydration and ion exchange of obsidian: an electron microprobe study. *Am. Mineral.* **63**, 266-73.

Johnson, K. T. M., Dick, H. J. B., & Shimizu, N., 1990. Melting in the Oceanic upper mantle: an ion microprobe study of diopsides in abyssal peridotites. *J. Geophy. Res.* **95**, 2661-78.

Juster, T. C., Grove, T. L., & Perfit, M. R., 1989. Experimental constraints on the generation of FeTi basalts, andesites and rhyodacites at the Galapagos spreading center, 85°W and 95°W. *J. Geophy. Res.* **94**, 9251-74.

Karlsson, H. R., & Clayton, R. N., 1990. Oxygen and hydrogen isotope geochemistry of zeolites. *Geochim. Cosmochim. Acta* **54**, 1369-86.

Kay, R. W., & Gast, P. W., 1973. The rare earth content and origin of alkali-rich basalts. *J. Geol.* **81**, 653-82.

Kyle, P. R., 1981. Mineralogy and geochemistry of a basanite to phonolite sequence at Hut Point Peninsula, Antarctica, based on core from Dry Valley Drilling Project drillholes 1, 2, and 3. *J. Petrology* **22**, 451-500.

Kyle, P. R., 1986. Mineral chemistry of Late Cenozoic McMurdo Volcanic Group rocks from The Pleiades, northern Victoria Land. In: Stump, E. (ed.) *Geological Investigations in Northern Victoria Land, Antarctic Research Series, Vol. 46.* Washington, DC: Am. Geophys. Union, 305-37.

Kyle, P. R., & Rankin, P. C., 1976. Rare earth element geochemistry of Late Cenozoic alkaline lavas of the McMurdo Volcanic Group, Antarctica. *Geochim. Cosmochim. Acta* **40**, 1497-1507.

Kyle, P. R., Dibble, R. R., Giggenbach, W. F., & Keys, J., 1982. Volcanic activity associated with the anorthoclase phonolite lava lake, Mt. Erebus, Antarctica. In: Craddock, C. (ed.) *Antarctic Geosciences.* Madison: University of Wisconsin Press, 735-45.

Kyle, P. R., Moore, J. A., & Thirlwall, M. F., 1992. Petrologic evolution of anorthoclase phonolite lavas at Mount Erebus, Ross Island, Antarctica. *J. Petrology* **33**, 849-75.

Kyle, P. R., Pankhurst, R., Mukasa, S., Panter, K., Smellie, J., & McIntosh, W., 1994. Sr, Nd and Pb isotopic variations in the Marie Byrd Plume, West Antarctica. ICOG8, Berkeley, CA., U.S. Geological Survey Circular 1107, 184.

Koyaguchi, T., & Blake, S., 1991. Origin of mafic enclaves: constraints on the magma mixing model from fluid dynamic experiments. In: Didier, J., & Barbarin, B. (eds.) *Enclaves and Granite Petrology*, Developments in Petrology 13, Elsevier, Amsterdam, 415-29.

Köhler, T. P., & Brey, G. P., 1990. Calcium exchange between olivine and clinopyroxene calibrated as a geothermobarometer for natural peridotites from 2 to 60 kb with applications. *Geochim. Cosmochim. Acta* **54**, 2375-88.

Laird, M. G., 1991. Lower-mid-Palaeozoic sedimentation and tectonic patterns on the paleo-Pacific margin of Antarctica. In: Thompson, M. R. A., Crame, J. A., & Thomson, J. W. (eds.) *Geological Evolution of Antarctica.* Cambridge University Press, 177-85.

Langmuir, C. H., Vocke, R. D., Hanson, G. N., & Hart, S. R., 1978. A general mixing equation with applications to Icelandic basalts. *Earth Planet. Sci. Lett.* **37**, 380-92.

Larsen, L. M., 1976. Clinopyroxene and coexisting mafic minerals from the alkaline Ilímaussaq intrusion, south Greenland. *J. Petrology* **17**, 258-90.

Larsen, L. M., 1979. Distribution of REE and other trace elements between phenocyrsts and peralkaline undersaturated magmas, exemplified by rocks from the Gardar igneous province, south Greeland. *Lithos* **12**, 303-15.

Larsen, L. M., & Sørensen, H., 1987. The Ilímaussaq intrusion-progressive crystallization and formation of layering in an agpaitic magma. In: Fitton, J. G., & Upton, B. G. L. (eds.) *Alkaline Igneous Rocks*, Geol. Soc. Spec. Pub. 30, 473-88.

Lawver, L. A., Royer, J. Y., Sandwell, D. T., & Scotese, C. R., 1991. Evolution of the Antarctic continental margin. In: Thompson, M. R. A., Crame, J. A., & thomson, J. W. (eds.) *Geological Evolution of Antarctica*, Cambridge University Press, 533-9.

Leake, B. E., 1978. Nomenclature of amphiboles. *Am. Miner.* **63**, 1023-52.

Leat, P. T., Macdonald, R., & Smith, R. L., 1984. Geochemical evolution of the Menengai caldera volcano, Kenya. *J. Geophy. Res.* **89**, 8571-92.

Le Bas, M. J., Maitre, R. W., Streckeisen, A., & Zanettin, B., 1986. A chemical classification of volcanic rocks based on the total alkali-silica diagram. *J. Petrology* **27**, 745-50.

Lemarchand, F., Villemant, B., & Calas, G., 1987. Treace element distribution coefficients in alkaline series. *Geochim. Cosmochim. Acta* **51**, 1071-81.

LeMasurier, W. E., 1990. Mount Waesche. In: LeMasurier W. E., & Thomson, J. (eds.) *Volcanoes of the Antarctic Plate and Southern Oceans.* Antarctic Research Series **48**, Am. Geophys. Union, Washington D. C., 208-11.

LeMasurier, W. E., & Rex, D. C., 1989. Evolution of linear volcanic ranges in Marie Byrd Land, west Antarctica. *J. Geophys. Res.* **94**, 7223-36.

LeMasurier, W. E., & Thomson, J. W., 1990. *Volcanoes of the Antarctic Plate and Southern Oceans.* Antarctic Research Series **48**, Am. Geophys. Union, Washington D.C., 487 pp.

LeMasurier, W. E., Kawachi, Y., & Rex, D. C., 1990. Crary Mountains. In: LeMasurier W., & Thomson, J. (eds.) *Volcanoes of the Antarctic Plate and Southern Oceans. Antarctic Research Series,* **48**, Am. Geophys. Union, Washington D. C., 180-4.

LeMasurier, W. E., & Kawachi, Y., 1990. Mount Berlin. In: LeMasurier W. E., & Thomson, J. (eds.) *Volcanoes of the Antarctic Plate and Southern Oceans.* Antarctic Research Series **48**, Am. Geophys. Union, Washington D. C., 229-33.

LeMasurier, W. E., Harwood, D. M., & Rex, D. C., 1994. Geology of Mount Murphy volcano: an 8-m.y. history of interaction between a rift volcano and the West Antarctic ice sheet. *Geo. Soc. Amer. Bull.* **106**, 265-80.

Lindsley, D. H., & Spencer, K. J., 1982. Fe-Ti oxide geothermometry: reducing analyses of coexisting Ti-magnetite (Mt) and Ilmenite (Ilm). EOS (*Trans. Am. Geophys. Union*) **63**, 471.

Lindstrom, D. J., & Korotev, R. L., 1982. TEABAGS: computer programs for instrumental neutron activation analysis. *J. Radioanal. Nucl. Chem.* **70**, 439-58.

Long, P. E., 1978. Experimental determination of partition coefficients for Rb, Sr, and Ba between alkali feldspar and silicate liquid. *Geochim. Cosmochim. Acta* **42**, 833-46.

Luyendyk, B. P., Richard, S. M., Smith, C. H., & Kimbrough, D. L., 1992. Geological and geophysical exploration in the northern Ford Ranges, Marie Byrd Land, west Antarctica. In: Yoshida, Y., Kaminuma, K., & Shiraishi, K. (eds.) *Recent Progress in Antarctic Earth Science*. Terra Scientific, Tokyo, 279-88.

Macdonald, R., Navarro, J. M., Upton, B. G. J., & Davies, G. R., 1994. Strong compositional zonation in peralkaline magma: Menengai, Kenya Rift Valley. *J. Volcanol. Geotherm. Res.* **60**, 301-25.

Macdonald, R., Davies, G. R., Upton, B. G. J., Dunkley, P. N., Smith, M., & Leat, P. T., 1995. Petrogenesis of Silali volcano, Gregory Rift, Kenya. *J. Geol. Soc. Lond.* **152**, 703-20.

Mahood, G. A., & Stimac, J. A., 1990. Trace-element partitioning in pantellerites and trachytes. *Geochim. Cosmochim. Acta* **54**, 2257-76.

McBirney, A. R., Baker, B. H., & Nilson, R. H., 1985. Liquid fractionation. Part I: basic principles and experimental simulations. *J. Volcanol. Geotherm. Res.* **24**, 1-24.

McIntosh, W. C., & Wilch, T. I., 1995. Late Pleistocene (223-125 ka) plinian eruptions in Marie Byrd Land: potential time horizons in west Antarctic ice cores. *Abst.* VII International Symposium on Antarctic Earth Sciences, Siena, Italy, 261.

Michael, P. J., 1988. Partition coefficients for rare earth elements in mafic minerals of high silica rhyolites: the importance of accessory mineral inclusions. *Geochim. Cosmochim. Acta* **52**, 275-82.

Mogessie, A., Tessadri, R., & Veltman, C. B., 1990. EMP-AMPH-A hypercard program to determine the name of an amphibole from electron microprobe analysis according to the International ineralogical Association scheme. *Computers and Geosciences* **16**, 309-30.

Morimoto, N., Fabries, J., Ferguson, A. K., Ginzburg, I. V., Ross, M., Seifert, F. A., Zussman, J., Aoki, K., & Gottardi, G., 1988. Nomenclature of Pyroxenes. *Miner. & Petrol.* **39**, 55-76.

Moriwaki, K., Yoshida, Y., & Harwood, D. M., 1992. Cenozoic glacial history of Antarctica-a correlative synthesis-. In: Yoshida, Y., Kaminuma, K., & Shiraishi, K. (eds.) *Recent Progress in Antarctic Earth Science*, Terra Scientific Publishing, Tokyo, 773-80.

Morse, S. A., 1980. Basalts and phase diagrams. Springer-Verlag, New York, 493 pp.

Mukasa, S., McCabe, R., & Gill, J., 1987. Pb-isotopic compositions of volcanic rocks in the West and East Philippine island arcs: presence of the Dupal isotopic anomaly. *Earth Planet. Sci. Lett.* **84**, 153-64.

Mukasa, S. B., Shervais, J. W., Wilshire, H. G., & Nielson, J., 1991. Intrinsic isotopic heterogeneities exhibited by the Lherz alpine peridotite massif, French Pyrenees. *J. Petrology* (**Special Lherzolites Issue**), 117-34.

Nash, W. P., & Wilkinson, J. F. G., 1970. Shonkin Sag Laccolith, Montana. *Contr. Miner. Petrol.* 25, 241-69.

Nicolas, A., 1986. A melt extraction model based on structural studies in mantle peridotites. *J. Petrology* **27**, 999-1022.

Nono, A., Deruelle, B., Demaiffe, D., & Kambou, R., 1994. Tchabal Nganha volcano in Adamawa (Cameroon): petrology of a continental alkaline lava series. *J. Volcanol. Geotherm. Res.* **60**, 147-78.

Onuma, K., Akasaka, M., & Yagi, K., 1981. The bearing of the system $CaMgSi_2O_6$-$CaAl_2SiO_6$-$CaFeAlSiO_6$ on fassaitic pyroxene. *Lithos* **14**, 173-82.

Palais, J. M., Kyle, P. R., McIntosh, W. C., & Seward, D., 1988. Magmatic and phreatomagmatic volcanic activity at Mt. Takahe, west Antarctica, based on tephra layers in the Byrd ice core and field observations at Mt. Takahe. *J. Volcanol. Geotherm. Res.* **35**, 295-317.

Papike, J. J., Cameron, K. L., & Baldwin, K., 1974. Amphiboles and pyroxenes. Characterization of other than quadrilateral components and estimates of ferric iron from microprobe data. *Geol. Soc. Am. Abstr. Programs* **6**, 1053-4.

Panter, K. S., McIntosh, W. C., & Smellie, J. L., 1994. Volcanic history of Mount Sidley, a major alkaline volcano in Marie Byrd Land, Antarctica. *Bull. Volcanol.* **56**, 361-76.

Price, R. C., & Chappell, B. W., 1975. Fractional crystallization and the petrology of Dunedin Volcano. *Contri. Miner. Petrol.* **53**, 157-82.

Price, R. C., Johnson, R. W., Gray, C. M., & Frey, F. A., 1985. Geochemistry of phonolites and trachytes from the summit region of Mt. Kenya. *Contrib. Mineral. Petrol.* **89**, 394-409.

Reiners, P. W., Nelson, B. K., & Ghiorso, M. S., 1995. Assimilation of felsic crust by basaltic magam: thermal limits and extents of crustal contamination of mantle-derived magmas. *Geology* **23**, 563-6.

Robinson, P., Spear, F. S., Schumacher, J. C., Laird, J., Klein, C., Evans, B. W., & Doolan, B. L., 1982. Phase relations of metamorphic amphiboles: natural occurrence and theroy. In: Veblen, D. R., & Ribbe, P. H. (eds.) *Amphiboles: Petrology and Experimental Phase Relations. Miner. Soc. Am. Rev. Miner., Vol 9B*, 1-22.

Roeder, P. L., & Emslie, R. F., 1970. Olivine - liquid equilibrium. *Contrib. Mineral. Petrol.* **29**, 275-89.

Ryan, M. P., 1987. Neutral buoyancy and the mechanical evolution of magmatic systems. In: Mysen, B. O. (ed.) *Magmatic Processes: Physicochemical Principles.* The Geochemical Society, Special Pub. 1, 259-87.

Shaw, A., Downes, H., & Thirlwall, M. F., 1993. The quartz-diorites of Limousin: elemental and isotopic evidence for Devono-Carboniferous subduction in the Hercynian belt of the French Massif Central. *Chem. Geol.* **107**, 1-18.

Shaw, D. M., 1970. Trace element fractionation during anatexis. *Geochim. Cosmochim. Acta* **50**, 711-24.

Simkin, T., & Smith, J. V., 1970. Minor-element distribution in olivine. *Jour. Geol.* **78**, 304-25.

Smellie, J. L., McIntosh, W. C., Gamble, J. A., & Panter, K. S., 1990. Preliminary stratigraphy of volcanoes in the Executive Committee Range, central Marie Byrd Land. *Antarctic Sci.* **2**, 353-4.

Smellie, J. L., Panter, K. S., McIntosh, W. C., & Kyle, P. R., 1991. Geochemical evolution of volcanoes in the Executive Committee Range, central Marie Byrd Land, west Antarctica. In: *Abstracts. Sixth International Symposium on Antarctic Earth Sciences,* National Institute of Polar Research, Saitama, Japan, 536.

Smellie, J. L., McIntosh, W. C., Gamble, J. A., Panter, K. S., & Dunbar, N. W., 1993. Preliminary lithofacies assessment and $^{40}Ar/^{39}Ar$ ages of Cenozoic volcanic sequences in eastern Marie Byrd Land. *Antarctic Sci.* **5**, 105-6.

Smith, C. H., 1992. Metapelites and migmatites at the granulite facies transition, Fosdick Metamorphic Complex, Marie Byrd Land, west Antarctica. In: Yoshida, Y., Kaminuma, K., & Shiraishi, K. (eds.) *Recent Progress in Antarctic Earth Science.* Terra Scientific, Tokyo, 295-301.

Sparks, R. S. J., Sigurdsson, H., & Wilson, L., 1977. Magma mixing: a mechanism for triggering acid explosive eruptions. *Nature* **267**, 315-8.

Sparks, R. S. J., Huppert, H. E., & Turner, J. S., 1984. The fluid dynamics of evolving magma chambers. *Phil. Trans. R. Soc. Lond.* **310**, 511-34.

Sparks, R. S. J., Huppert, H. E., Koyaguchi, T., & Hallworth, M. A., 1993. Origin of modal and rhythmic igneous layering by sedimentation in a convecting magma chamber. *Nature* **361**, 246-9.

Spear, F. S., & Kimball, K. L., 1984. RECAMP- A Fortran IV program for estimating Fe^{3+} contents in amphiboles. *Computers and Geosciences* **10**, 317-25.

Spera, F. J., 1984. Carbon dioxide in petrogenesis III: role of volatiles in the ascent of alkaline magma with special reference to xenolith-bearing mafic lavas. *Contrib. Mineral. Petrol.* **88**, 217-32.

Stephenson, D., & Upton, B. G. J., 1982. Ferromagnesian silicates in a differentiating alkaline complex: Kûngnât Fjeld, south Greenland. *Miner. Mag.* **46,** 283-300.

Stimac, J. A., & Pearce, T. H., 1992. Textural evidence of mafic-felsic magma interaction in dacite lavas, Clear Lake, California. *Am. Miner.* **77**, 795-809.

Stromer, J. C., 1973. Calcium zoning in olivine and its relationship to silica activity and pressure. *Geochim. Cosmochim. Acta* **37**, 1815-21.

Stormer, J. C., 1983. The effects of recalculation on estimates of temperature and oxygen fugacity from analyses of multicomponent iron-titanium oxides. *Am. Miner.* **68**, 586-94.

Stout, J. H., 1972. Phase petrology and mineral chemistry of coexisting amphiboles from Telemark, Norway. *J. Petrology* **13**, 99-145.

Sun, S., & McDonough, W. F., 1989. Chemical and isotopic systematics of oceanic basalts: implications for mantle composition and processes. In: Saunders, A. D., & Norry, M. J. (eds.) *Magmatism in the Ocean Basins*, Geol. Soc. Spec. Pub. 42, 313-45.

Tait, S. R., Wörner, G., van den Bogaard, P., & Schmincke, H-U., 1989. Cumulate nodules as evidence for convective fractionation in a phonolite magma chamber. *J. Volcanol. Geotherm. Res.* **37**, 21-37.

Thirlwall, M. F., Smith, T. E., Graham, A. M., Theodorou, N., Hollings, P., Davidson, J.P., & Arculus, R. J., 1994. High field strength element anomalies in arc lavas: source or process? *J. Petrology* **35**, 819-38.

Thomas, N., Tait, S., & Koyaguchi, T., 1993. Mixing of stratified liquids by the motion of gas bubbles: application to magma mixing. *Earth Planet. Sci. Lett.* **115**, 161-75.

Thompson, R. N., Morrison, M. A., Hendry, G. L., & Parks, S. J., 1984. An assessment of the relative roles of crust and mantle in magma genesis: an elemental approach. *Phil. Trans. R. Soc. Lond.* **A310**, 549-90.

Treuil, M., & Joron, J. M., 1975. Utilisation des éléments hygromagmatophiles pour la simplification de la modèlisation quantitative des processus magmatiques, exemples de l'Afar et de la dorsade médioatlantique. *Soc. Ital. Mineral. Petrol.* **31**, 125-74.

Trial, A. F., & Spera, F. J., 1990. Mechanisms for the generation of compositional heterogeneities in magma chambers. *Geol. Soc. Am. Bull.* **102**, 353-67.

Tschernich, R. W., 1992. *Zeolites of the world.* Geoscience Press, Phoenix, 563 pp.

Turbeville, B. N., 1993. Petrology and petrogenesis of the Latera Caldera, central Italy. *J. Petrology* **34**, 77-123.

Tuttle, O. F., & Bowen, N. L., 1958. origin of granite in the light of experimental studies in the system $NaAlSi_3O_8$-$KAlSi_3O_8$-SiO_2-H_2O. *Mem. Geol. Soc Am.* **74**, 153 pp.

Ulmer, P., 1989. The dependence of the Fe^{2+}-Mg cation-partitioning between olivine and basaltic liquid on pressure, temperature and composition. An experimental study to 30 kbars. *Contrib. Mineral. Petrol.* **101**, 261-73.

Velde, B., & Kurshiro, I., 1978. Structure of sodium alumino-silica melts quenched at high pressure; infrared and aluminium K-radiation data. *Earth Planet. Sci. Lett.* **40**, 137-40.

Villemant, B., 1988. Trace element evolution in the Phlegrean Fields (central Italy): fractional crystallization and selective enrichment. *Contrib. Mineral. Petrol.* **98**, 169-83.

Villemant, B., Jaffrezic, H., Jordon, J. L., & Treuil, M., 1981. Distribution coefficients of major and trace elements; fractional crystallization in the alkali basalt series of Chaîne des Puys (Massif Central, France). *Geochim. Cosmochim. Acta* **45**, 1997-2016.

Wager, L. R., & Brown, G. M., 1968. *Layered Igneous Rocks.* Oliver & Boyd, Edinburgh.

Wass, S. Y., 1979. Multiple origins of clinopyroxenes in alkali basaltic rocks. *Lithos* **12**, 115-32.

Watson, B. E., 1977. Partitioning of manganese between forsterite and silicate liquid. *Geochim. Cosmochim. Acta* **41**, 1363-74.

Weaver, B. L., 1991. Trace element evidence for the origin of ocean-island basalts. *Geology* **19**, 23-6.

Weaver, S. D., Bradshaw, J. D., & Adams, C. J., 1991. Granitoids of the Ford Ranges, Marie Byrd Land, Antarctica. In: Thompson, M. R. A., Crame, J. A., & Thomson, J. W. (eds.) *Geological Evolution of Antarctica.* Cambridge University Press, 345-51.

Weaver, S. D., Adams, C. J., Pankhurst, R. J., & Gibson, I. L., 1992. Granites of Edward VII Peninsula, Marie Byrd Land: anorogenic magmatism related to Antarctic-New Zealand rifting. *Trans. R. Soc. Edinburgh* **83**, 281-90.

Weaver, S. D., Storey, B. C., Pankhurst, R. J., Mukasa, S. B., DiVenere, V. J., & Bradshaw, J. D., 1994. Antarctica-New Zealand rifting and Marie Byrd Land lithospheric magmatism linked to ridge subduction and mantle plume activity. *Geology* **22**, 811-4.

Wolff, J. A., 1984. Variation in Nb/Ta during differentiation of phonolitic magma, Tenerife, Canary Islands. *Geochim. Cosmochim. Acta* **48**, 1345-8.

Wolff, J. A., 1985. Zonation, mixing and eruption of silica-undersaturated alkaline magma: a case study from Tenerife, Canary Islands. *Geol. Mag.* **122**, 641-7.

Wolff, J. A., 1990. Gradients in physical parameters in zoned felsic magma bodies: implications for evolution and eruptive withdrawal. *J. Volcanol. Geotherm. Res.* **43**, 37-55.

Wolff, J. A., & Toney, J. B., 1993. Trapped liquid from a nepheline syenite: a re-evaluation of Na-, Zr-, F-rich interstitial glass in a xenolith from Tenerife, Canary Islands. *Lithos* **29**, 285-93.

Wood, D. A., Tarney, J., & Weaver, B. L., 1981. Trace element variations in Atlantic Ocean basalts and Proterozoic dykes from northwest Scotland: their bearing upon the nature and geochemical evolution of the upper mantle. *Tectonophysics* **75**, 91-112.

Woods, A. W., & Koyaguchi, T., 1994. Transitions between explosive and effusive eruptions of silicic magmas. *Nature* **370**, 641-4.

Wörner, G., Beusen J. M., Duchateau, N., Gijbels, R., & Schmincke, H. U., 1983. Trace element abundances and mineral/melt distribution coefficients in phonolites from the Laacher See Volcano (Germany). *Contrib. Mineral. Petrol.* **84**, 152-73.

Wörner, G., & Schmincke, H.-U., 1984. Mineralogical and chemical zonation of the Laacher See tephra sequence (East Eifel, FRG). *J. Petrology* **25**, 805-35.

Wright, J. B., 1963. A note on possible differentiation trends in Tertiary to Recent lavas of Kenya. *Geol. Mag.* **100**, 164-80.

Wyllie, P. J., 1979. Magmas and volatile components. *Am. Miner.* **64**, 469-500.

Wysoczanski, R. J., 1993. Lithospheric xenoliths from the Marie Byrd Land volcanic province, west Antarctica. Unpublished Ph.D. thesis, Victoria University of Wellington, New Zealand, 475 pp.

Zindler, A., & Hart, S., 1986. Chemical geodynamics. *Ann. Rev. Earth Planet. Sci.* **14**, 493-571.

Appendix C1: Sample Information

Table C1.1: Sample list for Mt. Sidley and Mt. Waesche rocks.

sample	rock	group	stage	location	age	TS	PS	O	Nd	Sr	Pb
Mt. Sidley											
				S W							
MB22.1	trac	*LT*	II	77°05'35" 126°11'15"							
MB23.2	trac	*N*	III	77°05'50" 126°08'30"							
MB23.6	trac	*N*	III	77°05'50" 126°08'30"							
MB23.7	trac	*N*	III	77°05'50" 126°08'30"							
MB24.1	trac	CL-host	II	77°05'50" 126°10'40"							
MB24.3	trac	CL-host	II	77°05'50" 126°10'40"							
MB25.7	trac	CL-host	II	77°05'50" 126°11'15"							
MB25.10	trac	CL-host	II	77°05'50" 126°11'15"							
MB25.11	trac	CL-host	II	77°05'50" 126°11'15"							
MB27.5	bas	Pc	IV	77°05'00" 126°10'25"				X	X	X	X
MB28.1	bas	Pc	IV	77°06'30" 126°14'45"							
MB29.4	trac	*LT*	II	77°04'30" 126°14'30"	4.53			$X_{,An}$	X	$X_{,An}$	
MB29.9	trac	*HT*	II	77°04'30" 126°14'30"							
MB30.3	trac	CL-host	II	77°04'20" 126°10'15"							
MB30.6	trac	CL-host	II	77°04'20" 126°10'15"				X			
MB30.7	trac-ben	CL-encl	II	77°04'20" 126°10'15"							
MB31.1	mug	SFM	III	77°07'50" 126°08'10"							
MB32.4	trac	*N*	III	77°07'00" 126°03'45"							
MB32.8	trac	*N*	III	77°07'00" 126°03'45"							
MB32.11	mug	DPM	III	77°07'00" 126°03'45"				X	X	X	X
MB33.2	trac	*LT*	II	77°04'30" 126°10'35"							
MB33.3	trac	*HT*	II	77°04'30" 126°10'35"	4.58			$X_{,An}$	X		
MB33.8	trac	*HT*	II	77°04'30" 126°10'35"				X	X		
MB33.11	trac	bf	II	77°04'30" 126°10'35"						X	
MB33.12	ben	Sv	I	77°04'30" 126°10'35"							
MB33.14	phn	Sv	I	77°04'30" 126°10'35"							
MB34.4	phn	Sv	I	77°03'15" 126°22'45"							
MB35.1	trac	bf	II	77°04'25" 126°18'05"							
MB35.2	phn	Sv	I	77°04'25" 126°18'05"				X	X	X	
MB35.4	trac	*HT*	II	77°04'25" 126°18'05"							
MB35.5	phn	bf	II	77°04'25" 126°18'05"	4.45			$X_{,An}$		$X_{,An}$	
MB35.6	phn	bf	II	77°04'25" 126°18'05"							
MB36.2	trac	CL-encl	II	77°06'30" 126°07'15"							
MB37.1	trac	*LT*	II	77°07'00" 126°08'30"							
MB38.3	trac	bf	II	77°03'15" 126°13'15"					X	X	
MB38.6	trac	*HT*	II	77°03'15" 126°13'15"							
MB39.2	trac	*HT*	II	77°02'45" 126°11'45"							
MB39.3	phn	Sv	I	77°02'45" 126°11'45"							
MB39.4	phn	Sv	I	77°02'45" 126°11'45"							
MB39.5	phn	Sv	I	77°02'45" 126°11'45"							
MB39.6	trac	CL-host	II	77°02'45" 126°11'45"							
MB39.7	trac-ben	CL-encl	II	77°02'45" 126°11'45"							
MB41.1	phn	Sv	I	77°04'40" 126°10'45"							
MB41.5	trac	*HT*	II	77°04'40" 126°10'45"							
MB41.11	trac	*HT*	II	77°04'40" 126°10'45"							

Table C1.1: continued											
sample	rock	group	stage	location	age	TS	PS	O	Nd	Sr	Pb
Mt. Sidley											
MB42.3	tphn	Sv	I	77°03'45" 126°11'10"	5.08			$X_{,An}$	X	$X_{,An}$	
MB42.4	trac	*HT*	II	77°03'45" 126°11'10"							
K054 (51)	trac	*N*	III	77°05'50" 126°08'30"	4.37	X		$X_{,An}$			
K055	trac	*LT*	II	77°05'50" 126°08'30"	4.60	X		X	X	X	
K056	trac	*N*	III	77°05'50" 126°08'30"		X					
K057	trac	*N*	III	77°05'50" 126°08'30"				X			
K059	trac	*N*	III	77°05'50" 126°08'30"				X			
K061	trac	*N*	III	77°05'50" 126°08'30"							
K062	trac	*N*	III	77°05'50" 126°08'30"							
K063	trac	CL	II	77°06'30" 126°07'15"		X	X				
K063A	trac	CL-host	II	77°06'30" 126°07'15"				X	X	X	
K063B	ben	CL-encl	II	77°06'30" 126°07'15"				X	X	X	
K064	trac	CL-host	II	77°06'40" 126°07'00"		X					
K066	trac	*LT*	II	77°05'35" 126°11'15"		X	X	X	X	X	
K068	tphn	Bv	I	77°04'30" 126°04'35"	5.69	X		X			
K069	phn	Wv	I	77°04'30" 126°04'35"		X					
K073	tphn	Bv	I	77°04'30" 126°03'30"		X					
K076	phn	Wv	I	77°04'30" 126°03'30"							
K077	phn	Wv	I	77°04'30" 126°03'30"		X					
K082	trac	*N*	III	77°04'45" 126°10'35"							
K086 (85)	mug	DPM	III	77°07'00" 126°03'45"	4.31						
K087	mug	DPM	III	77°07'00" 126°03'45"							
K090	trac	*N*	III	77°07'00" 126°03'45"							
K091	trac	*N*	III	77°07'00" 126°03'45"		X					
K093	mug	SFM	III	77°07'50" 126°08'10"		X	X				
K094	trac	*LT*	II	77°08'45" 126°03'45"		X					
K095	bas	Pc	IV	77°08'30" 126°04'40"		X					
K096	trac	*LT*	II	77°08'40" 126°03'15"		X					
K097	ben		IV	77°08'50" 126°00'00"		X		X	X	X	
K099	mug	SFM	III	77°07'00" 125°57'15"		X		X		X	
K100	trac	*LT*	II	77°07'20" 126°02'15"		X	X	X			
K104	trac	*LT*	II	77°06'30" 125°52'30"		X					
K105	trac	*LT*	II	77°05'00" 125°55'30"	4.55	X		$X_{,An}$		X	
K106	phn	Wv	I	77°05'00" 125°55'30"	5.36	X					
K108	tphn	Bv	I	77°05'00" 125°55'30"	5.53	X	X	X	X	X	
K109	bas	Pc	IV	77°04'15" 125°56'15"		X					
K110	phn	Wv	I	77°05'40" 125°54'30"		X		X			
K114	tphn-phn	Bv	I	77°03'15" 126°01'45"		X	X				
K115	phn	Sv	I	77°03'15" 126°01'45"		X	X	X		X	
K120	phn	Sv	I	77°03'45" 126°03'45"		X	X				
K121	phn	Bv	I	77°03'45" 126°03'45"		X					
K122	phn	Bv	I	77°03'45" 126°03'45"		X	X	X		X	
K123	trac	*LT*	II	77°05'50" 126°10'40"		X					
K126	mug	SFM	III	77°05'35" 125°48'45"							
K127	phn	Sv	I	77°04'30" 125°48'45"							
K128	phn	Sv	I	77°03'00" 125°52'30"							

Table C1.1: continued											
sample	rock	group	stage	location	age	TS	PS	O	Nd	Sr	Pb
Mt. Sidley											
K129	phn	Sv	I	77°02'30" 125°50'00"		X					
K131	tphn	Bv	I	77°02'00" 125°52'15"		X					
K132	phn	Sv	I	77°01'15" 125°46'45"		X					
K133	bas	Pc	IV	77°04'05" 125°46'15"							
K134	ben		IV	77°08'50" 125°58'15"				X		X	
K137	trac	*N*	III	77°04'30" 126°02'15"	4.25	X		$X_{,An}$		$X_{,An}$	
K140	trac	*HT*	II	77°03'40" 126°01'45"		X					
K141	phn	Sv	I	77°03'15" 126°00'45"		X	X				
K144	phn	Sv	I	77°02'45" 125°59'15"		X	X	X	X	X	
K145	bas	Pc	IV	77°04'15" 126°00'45"		X					
K149	phn	Sv	I	77°02'15" 126°01'30"	4.81	X	X				
K159	phn	Wv	I	77°02'00" 126°01'45"		X		X			
K165	phn	Sv	I	77°01'30" 126°01'45"		X		X			
K166	ben	Wv	I	77°02'00" 126°04'30"		X	X	X			
K167	phn	Wv	I	77°02'00" 126°01'45"		X					
K168	bas	Pc	IV	77°03'30" 126°04'30"	4.18	X	X	X	X	X	
Mt. Waesche											
MB4.1	akb			77°15'15" 126°51'45"						X	
MB4.4	phntph			77°15'15" 126°51'45"							
MB5.1	akb			77°13'30" 126°49'30"							
MB5.3	akb			77°13'30" 126°49'30"							
MB6.1	trac			77°13'15" 126°51'45"							
MB7.3	rhy			77°04'45" 126°38'30"					X		
MB8.1	rhy			77°06'00" 126°34'15"							
MB9.1	phn			77°12'30" 126°53'45"							
MB10.1	akb			77°12'45" 126°53'50"						X	
MB10.2	tphn			77°12'45" 126°53'50"							
MB10.5	phntph			77°12'45" 126°53'50"							
MB11.2	tphn			77°13'45" 126°56'30"					X	X	
MB14.1	tphn			77°14'00" 126°52'15"					X	X	
MB15.1	trac			77°13'30" 126°52'00"						X	
MB16.1	akb			77°13'15" 126°50'15"					X		X
MB21.1	mug			77°12'15" 126°49'45"							
MB21.2	haw			77°12'15" 126°49'45"					X	X	
MB45.1	phntph			77°11'15" 126°53'45"							
MB45.2	haw			77°11'15" 126°53'45"							
MB45.5	phn			77°11'15" 126°53'45"							
MB45.7	trac			77°11'15" 126°53'45"							
K01	phntph			77°16'30" 126°49'45"		X			X	X	
K04	akb			77°13'00" 126°49'15"							
K05	trac			77°12'45" 126°52'00"	0.48						
K06	bas			77°10'15" 126°52'30"						X	
K08	akb			77°10'30" 126°52'30"							
K09	haw			77°10'45" 126°52'00"							

Table C1.1: continued											
sample	rock	group	stage	location	age	TS	PS	O	Nd	Sr	Pb
Mt. Waesche											
K13	haw			77°10'00" 126°52'30"							
K16	trac			77°10'00" 126°52'15"							
K18	phn			77°09'30" 126°51'15"						X	
K19	akb			77°09'45" 126°49'30"					X	X	
K20	haw			77°10'15" 126°53'15"					X	X	
K22	phntph			77°10'30" 126°54'45"							
K26	haw			77°12'45" 126°56'00"							
K27	tphn			77°12'30" 126°57'15"							
K28	phntph			77°12'30" 126°56'45"							
K29	bas			77°12'50" 126°59'15"							
K30	mug			77°13'15" 126°58'30"						X	
K31	haw			77°15'45" 127°02'30"							
K32	rhy			77°16'00" 127°02'00"	1.60	X					
K34	phntph			77°12'30" 127°00'45"							
K35	tphn			77°12'45" 127°00'45"					X	X	
K36	tphn			77°12'45" 127°01'30"							
K39	phntph			77°13'05" 127°01'15"							
K41	trac			77°11'30" 126°57'45"						X	
K44	phntph			77°11'45" 126°57'30"		X			X	X	
K45	phntph			77°11'15" 126°57'45"							
K175	rhy			77°04'45" 126°55'45"	1.98	X					
K178	rhy			77°05'30" 127°00'00"	1.08	X					
Analyses: $^{40}Ar/^{39}Ar$ age; TS = thin section; PS = probe section; O, Nd, Sr and Pb isotopes.											
$X_{,An}$ = whole-rock and anorthoclase separate from the same sample.											
Rocks: trac = trachyte; ben = benmoreite; mug = mugearite; phn = phonolite; tphn = tephriphonolite; bas = basanite; akb = alkali basalt; phntph = phonotephrite; rhy = rhyolite; haw = hawaiite;											
"Group" abbreviations please refer to text, Pc = parasitic cone.											

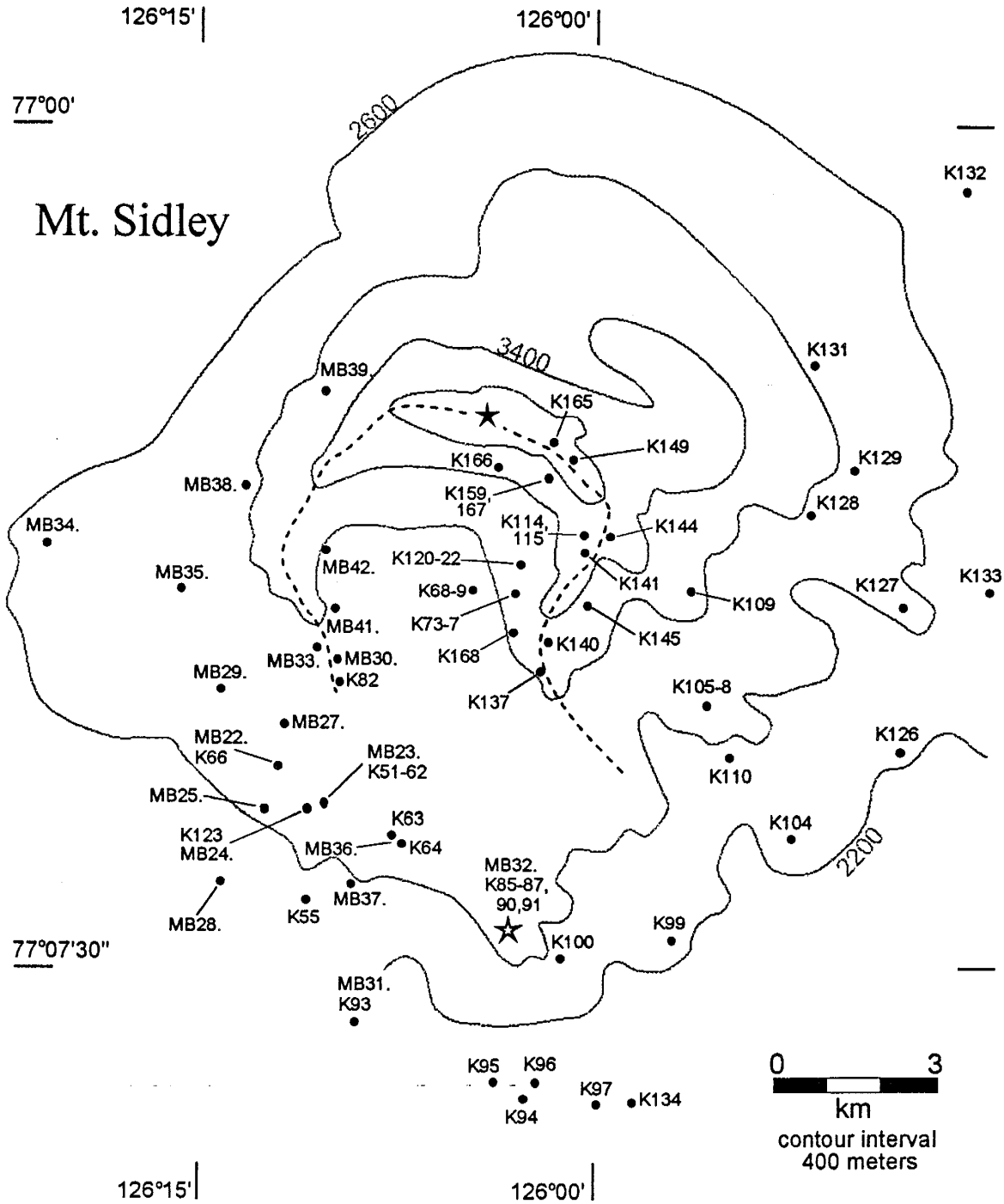

Figure C1.1. Sample location map for Mt. Sidley. MB numbers refer to geological stations, not individual sample sites. The solid star represents the summit at 4181m, and the open star is Doumani Peak (2675m). Dashed line marks the caldera rim of the Weiss Amphitheater.

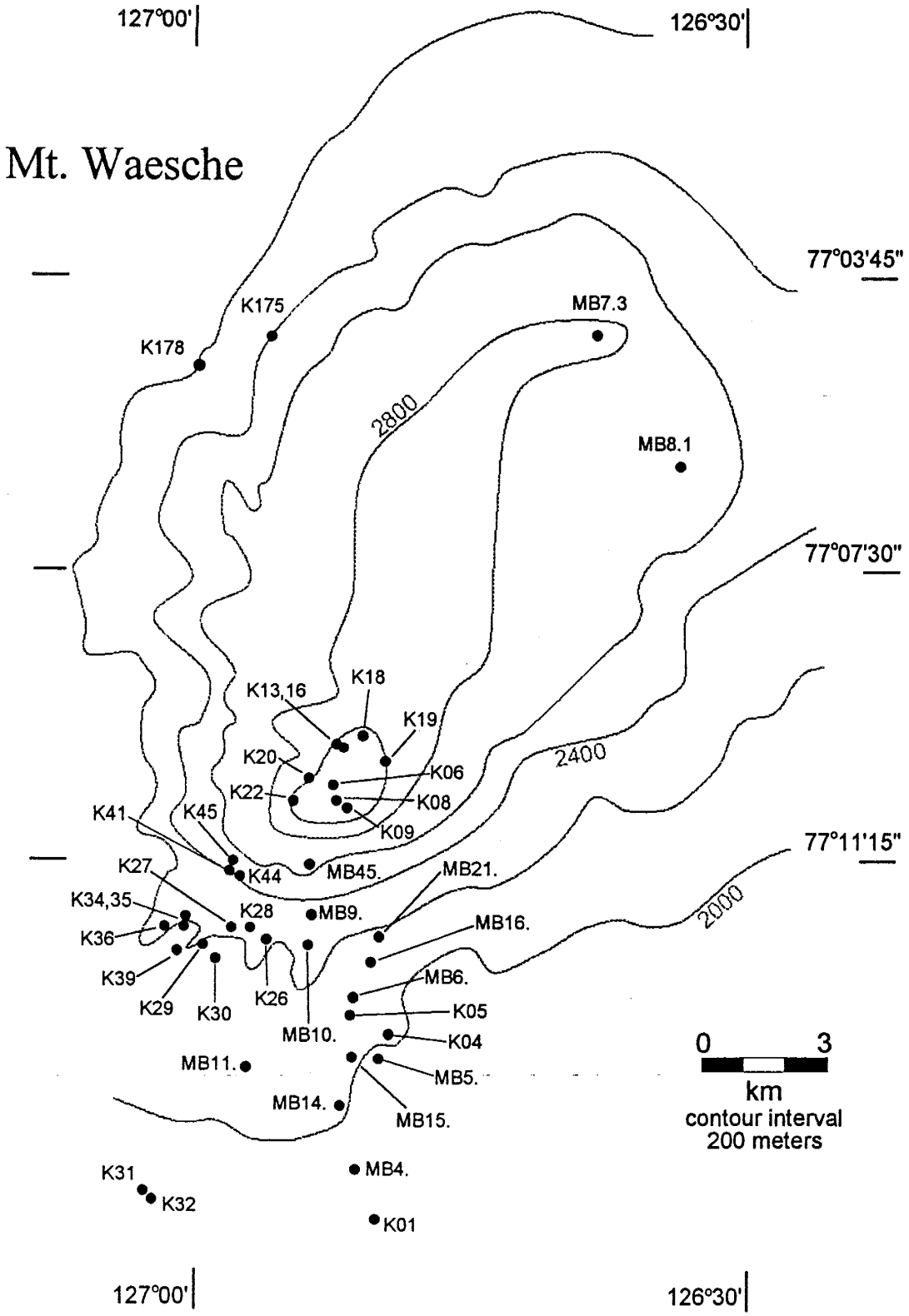

Figure C1.2. Sample location map for Mt. Waesche.

Appendix C2: $^{40}Ar/^{39}Ar$ age determination for Mt. Sidley volcanic rocks

Table C2.1: $^{40}Ar/^{39}Ar$ age spectra data

temp (°C)	$^{40}Ar/^{39}Ar$	$^{37}Ar/^{39}Ar$	$^{36}Ar/^{39}Ar$	^{39}Ar (%)	$^{40}Ar^{*}$(%)	^{39}Ar (mol)	K/Ca	age (Ma) ± 1σ
MB33.3	anorthoclase	J = .001849	wt = 0.1490 g	RD84	Reston			
825	1.837	8.72E-03	1.64E-03	8.8	73.7	9.50E-14	59.6	4.51 ± 0.06
900	1.422	8.62E-03	2.0E-4	7.5	95.9	8.10E-14	60.3	4.54 ± 0.08
975	1.388	8.65E-03	4.0E-5	10.1	99.2	1.08E-13	60.1	4.59 ± 0.06
1050	1.390	9.19E-03	4.0E-5	14.7	99.1	1.58E-13	56.6	4.59 ± 0.04
1125	1.400	9.66E-03	7.0E-5	23.2	98.5	2.50E-13	53.8	4.59 ± 0.03
1175	1.379	8.96E-03	9.0E-5	26.7	98.1	2.87E-13	58.0	4.51 ± 0.02
1250	1.405	8.72E-03	2.0E-5	7.7	99.5	8.30E-14	59.6	4.66 ± 0.07
1400	1.456	1.53E-02	9.0E-5	1.3	98.1	1.40E-14	34.0	4.76 ± 0.36
total gas								**4.57**
plateau	825-1125			64.3				**4.58 ± 0.02**
K168	basanite	J = .001823	wt = 0.3502 g	RD84	Reston			
625	1.837	0.794	1.51E-03	12.9	75.8	7.40E-14	0.7	4.57 ± 0.10
750	2.270	0.708	3.41E-03	29.9	55.5	1.72E-13	0.7	4.14 ± 0.05
850	1.600	0.824	1.07E-03	23.6	80.2	1.36E-13	0.6	4.21 ± 0.05
950	1.859	1.178	1.53E-03	8.3	75.7	4.80E-14	0.4	4.62 ± 0.14
1050	2.305	2.412	2.62E-03	6.5	66.4	3.80E-14	0.2	5.03 ± 0.30
1150	1.860	8.095	2.35E-03	18.7	62.7	1.08E-13	0.1	3.83 ± 0.15
total gas								**4.25**
plateau	750-850			53.5				**4.18 ± 0.04**
K85	anorthoclase	J = 0.001845	wt= 0.0827 g	RD84	Reston			
825	1.335	0.446	***	2.6	100.0	1.2E-14	1.2	4.50 ± 0.47
900	1.304	0.467	***	9.0	100.0	4.1E-14	1.1	4.39 ± 0.15
975	1.297	0.441	4.0E-05	16.7	99.2	7.7E-14	1.2	4.28 ± 0.10
1050	1.348	0.306	2.2E-04	16.5	95.3	7.6E-14	1.7	4.27± 0.07
1150	1.292	0.155	***	19.1	100.0	8.8E-14	3.4	4.30 ± 0.05
1250	1.361	0.086	2.6E-04	17.6	94.3	8.1E-14	6.0	4.27 ± 0.06
1375	1.569	0.135	9.3E-04	6.1	82.4	2.8E-14	3.9	4.30 ± 0.13
1650	1.533	0.151	7.0E-04	12.4	86.5	5.7E-14	3.4	4.41 ± 0.07
total gas								**4.31**
plateau	825-1650			100.0				**4.31 ± 0.03**
MB29.4	anorthoclase	J = 0.001849	wt = 0.1494 g	RD84	Reston			
825	1.836	2.706E-02	1.52E-03	10.3	75.5	1.19E-13	19.2	4.62 ± 0.03
975	1.411	2.340E-02	1.10E-04	11.7	97.9	1.36E-13	22.2	4.59 ± 0.04
1050	1.444	2.257E-02	2.10E-04	8.1	95.6	9.50E-14	23.0	4.60 ± 0.04
1125	1.529	2.071E-02	5.90E-04	10.5	88.6	1.22E-13	25.1	4.51 ± 0.05
1175	1.474	2.189E-02	4.10E-04	28.4	91.8	3.30E-13	23.8	4.51 ± 0.02
1275	1.500	2.092E-02	4.60E-04	23.4	91.0	2.72E-13	24.9	4.55 ± 0.03
1350	1.578	2.097E-02	7.20E-04	3.0	86.5	3.40E-14	24.8	4.55 ± 0.19
1525	1.760	2.114E-02	1.38E-03	4.6	76.8	5.40E-14	24.6	4.50 ± 0.11
total gas								**4.55**
plateau	1050-1525			78.0				**4.53 ± 0.02**

Table C2.1: $^{40}Ar/^{39}Ar$ age spectra data

temp (°C)	$^{40}Ar/^{39}Ar$	$^{37}Ar/^{39}Ar$	$^{36}Ar/^{39}Ar$	^{39}Ar (%)	$^{40}Ar^{*}$(%)	^{39}Ar (mol)	K/Ca	age (Ma) ± 1σ
MB35.5	anorthoclase J = 0.003396	wt = 0.3580 g		RD79	Reston			
925	1.870	3.001E-02	4.03E-03	2.1	36.3	2.60E-13	17.3	4.15 ± 0.10
1000	0.875	2.914E-02	5.10E-04	7.8	82.6	9.79E-13	17.8	4.42 ± 0.03
1060	0.774	2.830E-02	1.60E-04	12.0	94.0	1.50E-12	18.4	4.45 ± 0.02
1110	0.778	2.739E-02	1.70E-04	12.2	93.6	1.53E-12	19.0	4.46 ± 0.02
1160	0.775	2.694E-02	1.70E-04	11.2	93.6	1.40E-12	19.3	4.44 ± 0.01
1245	0.765	2.676E-02	1.20E-04	19.3	95.5	2.41E-12	19.4	4.47 ± 0.01
1350	0.776	2.707E-02	1.30E-04	26.2	94.9	3.28E-12	19.2	4.51 ± 0.01
1525	0.842	2.828E-02	3.50E-04	9.3	87.9	1.17E-12	18.4	4.53 ± 0.02
total gas								**4.47**
plateau	1000-1245			62.5				**4.45 ± 0.01**
MB42.3	anorthoclase J = 0.001853	wt = 0.2015 g		RD84	Reston			
800	1.595	0.581	5.40E-4	34.9	90.0	1.94E-13	0.9	4.79 ± 0.04
1025	1.526	0.573	3.00E-5	27.5	99.3	1.53E-13	0.9	5.06 ± 0.08
1075	1.497	0.568	***	8.9	100.0	5.00E-14	0.9	5.07 ± 0.27
1125	1.520	0.561	4.00E-5	3.7	99.2	2.10E-14	0.9	5.03 ± 0.67
1180	1.458	0.555	***	5.3	100.0	3.00E-14	0.9	5.28 ± 0.54
1250	1.458	0.568	***	13.5	100.0	7.50E-14	0.9	5.17 ± 0.26
1350	1.541	0.578	***	2.1	100.0	1.20E-14	0.9	6.41 ± 1.93
1525	1.603	0.558	***	3.9	100.0	2.20E-14	0.9	5.91 ± 1.39
total gas								**5.06**
plateau	1025-1525			65.1				**5.08 ± 0.07**
K105	anorthoclase J = 0.001196	wt = 0.0989 g			Denver			
625	5.021	0.197	8.871E-03	2.6	46.8	4.22E-14	2.6	5.07 ± 1.13
750	4.577	6.207E-02	8.448E-03	10.6	45.2	1.69E-13	8.4	4.47 ± 0.09
1025	2.248	5.074E-02	4.616E-04	25.4	93.3	4.05E-13	10.2	4.54 ± 0.07
1125	2.258	5.382E-02	4.475E-04	23.3	93.6	3.72E-13	9.7	4.50 ± 0.10
1250	2.430	5.552E-02	1.009E-03	32.3	87.3	5.15E-13	9.4	4.59 ± 0.05
1450	4.473	0.195	7.427E-03	5.8	50.6	9.22E-14	2.7	4.89 ± 0.39
total gas								**4.57**
plateau	750-1250			91.6				**4.55 ± 0.04**
K106	anorthoclase J = 0.001198	wt = 0.0823 g			Denver			
625	5.150	0.206	8.601E-03	4.3	50.1	7.23E-14	2.5	5.58 ± 0.50
750	8.400	6.173E-02	1.751E-03	29.3	29.7	4.88E-13	8.4	5.38 ± 0.02
900	2.716	5.882E-02	8.172E-04	36.6	90.6	6.09E-13	8.8	5.33 ± 0.04
1025	2.691	6.788E-02	8.236E-04	19.7	91.0	3.28E-13	7.7	5.30 ± 0.05
1125	2.915	7.690E-02	1.193E-03	6.3	87.4	1.04E-13	6.8	5.51 ± 0.39
1250	6.160	9.217E-02	1.176E-02	2.3	43.3	3.89E-14	5.6	5.76 ± 0.98
1450	14.797	0.532	4.329E-02	1.5	13.7	2.45E-14	1.0	4.38 ± 0.89
total gas								**5.36**
plateau	750-1025			85.6				**5.36 ± 0.02**

Table C2.1: $^{40}Ar/^{39}Ar$ age spectra data

temp (°C)	$^{40}Ar/^{39}Ar$	$^{37}Ar/^{39}Ar$	$^{36}Ar/^{39}Ar$	^{39}Ar (%)	$^{40}Ar^{*}$(%)	^{39}Ar (mol)	K/Ca	age (Ma) ± 1σ
K108	anorthoclase J = 0.001184		wt = 0.1001 g		Denver			
600	8.794	0.833	2.394E-02	2.8	20.8	2.27E-14	0.6	3.91 ± 0.55
675	4.991	0.529	8.269E-03	14.4	51.3	1.16E-13	1.0	5.46 ± 0.08
750	4.962	0.529	8.052E-03	21.9	52.2	1.75E-13	1.0	5.54 ± 0.11
925	3.092	0.529	1.142E-03	27.4	86.3	2.20E-13	1.0	5.71 ± 0.13
1025	3.079	0.633	1.449E-03	12.5	85.5	1.00E-13	0.8	5.47 ± 0.21
1100	3.410	0.806	3.003E-03	4.3	74.5	3.45E-14	0.6	5.43 ± 1.11
1250	4.898	0.667	7.023E-03	10.3	56.8	8.27E-14	0.8	5.94 ± 0.69
1450	5.273	4.348	1.066E-02	6.3	39.2	5.07E-14	0.1	4.41 ± 0.32
total gas								**5.49**
plateau	675-1100			80.5				**5.53 ± 0.07**
K137	anorthoclase J = 0.001208		wt = 0.1038 g		Denver			
625	8.668	0.316	2.489E-02	0.7	15.9	1.42E-14	1.4	3.00 ± 1.33
750	6.154	9.099E-02	1.547E-02	4.0	25.6	8.46E-14	5.7	3.43 ± 0.32
900	2.216	**	9.386E-04	15.8	87.0	3.33E-13	**	4.21 ± 0.04
1025	2.133	2.437E-02	5.884E-04	30.3	91.3	6.36E-13	21.3	4.26 ± 0.05
1125	2.059	1.938E-02	3.080E-04	25.7	95.2	5.38E-13	26.8	4.28 ± 0.06
1250	2.271	4.558E-02	8.999E-04	19.8	87.7	4.16E-13	11.4	4.35 ± 0.08
1450	3.691	0.446	5.510E-03	3.8	55.8	7.92E-14	1.2	4.49 ± 0.19
total gas								**4.24**
plateau	900-1250			91.6				**4.25 ± 0.03**
K149	anorthoclase J = 0.001217		wt = 0.1001 g		Denver			
625	2.891	0.546	2.385E-03	14.2	75.2	1.48E-13	1.0	4.78 ± 0.17
750	4.449	0.465	7.931E-03	21.4	47.2	2.22E-13	1.1	4.61 ± 0.13
925	2.473	0.444	9.296E-04	34.3	88.5	3.57E-13	1.2	4.82 ± 0.03
1100	2.504	0.457	1.353E-03	14.7	84.5	1.53E-13	1.1	4.66 ± 0.21
1250	3.342	0.498	3.805E-03	10.0	55.5	1.04E-13	1.0	4.81 ± 0.34
1450	3.968	1.818	7.477E-03	5.3	44.0	5.55E-14	0.3	3.84 ± 0.30
total gas								**4.69**
plateau	625-1250			94.7				**4.81 ± 0.03**
K51	anorthoclase J = 0.001204		wt = 0.0982 g		Denver			
750	5.494	4.281E-02	1.164E-02	7.9	37.7	1.46E-13	12.2	4.50 ± 0.10
1025	2.109	1.753E-02	2.995E-04	48.6	95.5	9.02E-13	29.7	4.39 ± 0.03
1125	2.101	**	3.912E-04	25.7	94.3	4.78E-13	*	4.31 ± 0.06
1175	2.164	**	4.782E-04	11.7	92.8	2.16E-13	*	4.37 ± 0.16
1250	7.566	**	1.934E-02	3.7	25.0	6.88E-14	*	4.11 ± 0.28
1450	6.245	3.777E-04	1.574E-02	2.4	24.4	4.49E-14	*	3.32 ± 0.49
total gas								**4.34**
plateau	1025-1175			86.0				**4.37 ± 0.03**

Table C2.1: $^{40}Ar/^{39}Ar$ age spectra data

temp (°C)	$^{40}Ar/^{39}Ar$	$^{37}Ar/^{39}Ar$	$^{36}Ar/^{39}Ar$	^{39}Ar (%)	$^{40}Ar^{*}$(%)	^{39}Ar (mol)	K/Ca	age (Ma) ± 1σ
K55	anorthoclase J = 0.00119		wt = 0.1006 g		Denver			
750	4.888	1.709E-03	9.220E-03	10.8	44.2	1.95E-13	6.8	4.63 ± 0.12
925	2.441	1.523E-03	1.013E-03	22.0	87.6	3.95E-13	5.8	4.58 ± 0.11
1000	2.362	1.554E-03	9.167E-04	7.4	88.4	1.34E-13	7.4	4.47 ± 0.14
1075	2.330	1.940E-03	1.164E-03	4.8	85.2	8.56E-14	5.8	4.25 ± 0.87
1150	2.243	1.671E-03	4.217E-04	14.5	94.3	2.62E-13	6.8	4.53 ± 0.19
1250	3.175	9.952E-04	3.432E-03	36.0	67.9	6.48E-13	11.5	4.62 ± 0.05
1450	7.699	1.600E-03	1.987E-02	4.3	23.7	7.79E-14	7.2	3.90 ± 0.19
total gas								**4.54**
plateau	925-1250			84.8				**4.60 ± 0.05**
K68	anorthoclase J = 0.001209		wt = 0.1060 g		Denver			
750	4.398	0.490	5.997E-03	42.4	59.7	3.77E-13	1.1	5.73 ± 0.06
875	4.099	0.478	5.138E-03	20.9	62.5	1.86E-13	1.1	5.59 ± 0.11
1050	2.898	0.463	1.094E-03	19.2	88.7	1.71E-13	1.1	5.61 ± 0.13
1150	3.097	0.481	2.637E-03	3.5	75.0	3.15E-14	1.1	5.08 ± 0.84
1250	8.708	0.526	1.997E-02	7.6	32.1	6.76E-14	1.0	6.10 ± 0.30
1450	7.327	0.209	1.891E-02	6.4	23.9	5.71E-14	2.5	3.82 ± 0.23
total gas								**5.56**
plateau	750-1050			82.5				**5.69 ± 0.06**

Explanation: Each data set is preceded by sample number, mineral-rock, irradiation parameter (J), sample weight, irradiation batch number (for Reston samples) and USGS laboratory. Columns in data sets give temperature of incremental heating steps, ratios of Ar isotopes (^{40}Ar = initial and radiogenic, ^{39}Ar = potassium-derived, ^{37}Ar = calcium derived, ^{36}Ar = initial), % of total ^{39}Ar in heating steps, radiogenic yield of ^{40}Ar, moles of potassium derived ^{39}Ar, K/Ca ratio calculated from $^{37}Ar/^{39}Ar$ ratio, sample age, and 1σ error. Lines following each data step show total gas K/Ca and age, and plateau temperature range, ^{39}Ar percent, age, and error (method of Fleck *et al.*, 1977).

Correction factors for interfering reactions: $^{40}Ar/^{39}Ar_K = 0.0057 \pm 1.0$; $^{39}Ar/^{37}Ar_{Ca} = 0.0006730 \pm 0.0000037$; $^{36}Ar/^{37}Ar_{Ca} = 0.000264 \pm 0.000002$.

*** ^{36}Ar below detection limit; ** ^{37}Ar below detection limit; * ^{37}Ar too much decay for accurate K/Ca determination.

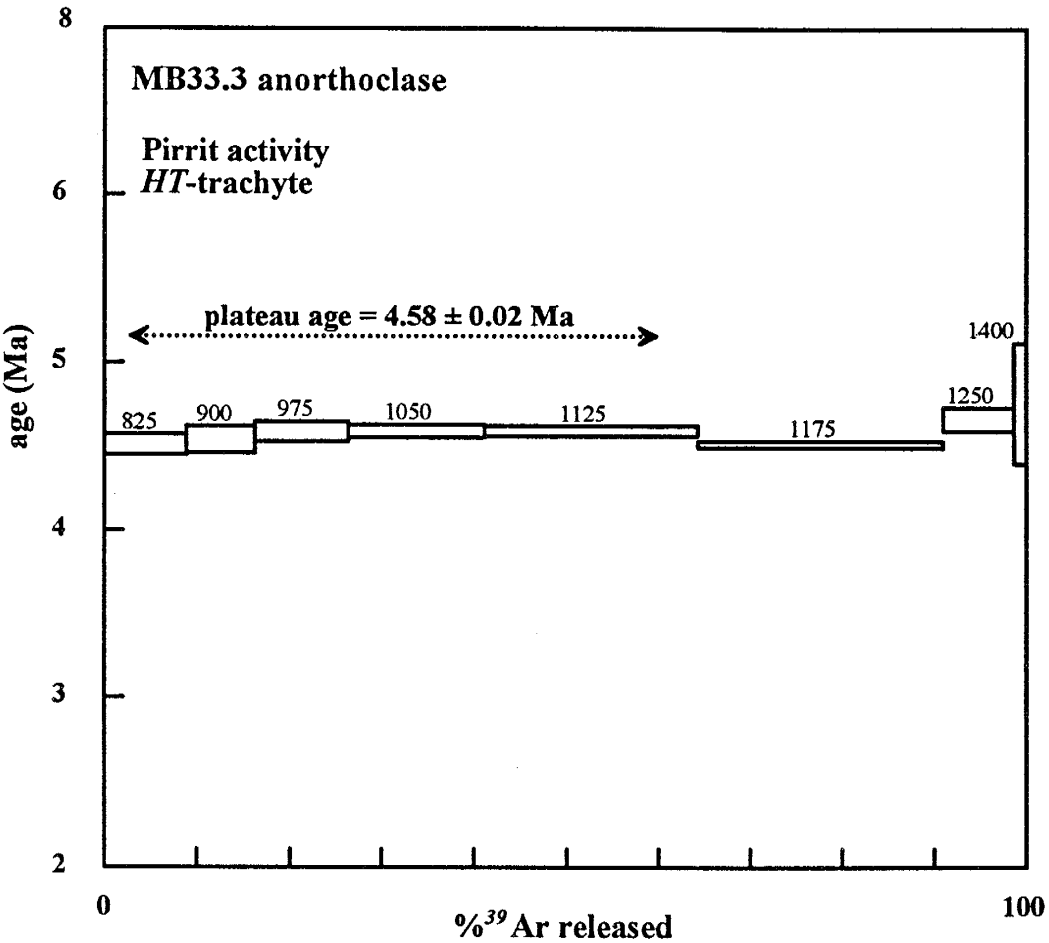

Figure C2.1. $^{40}Ar/^{39}Ar$ age spectra for sample MB33.3.

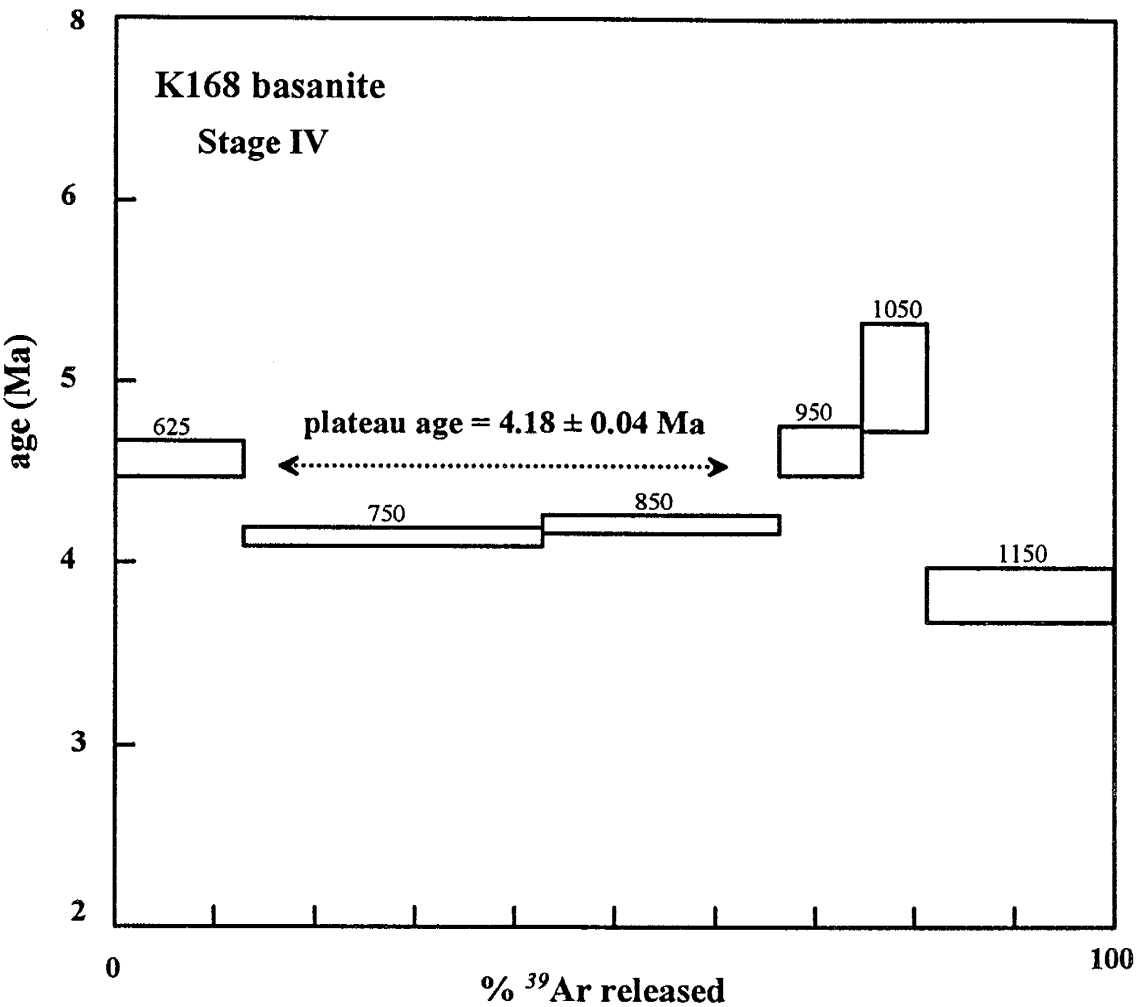

Figure C2.2. $^{40}Ar/^{39}Ar$ age spectra for sample K168.

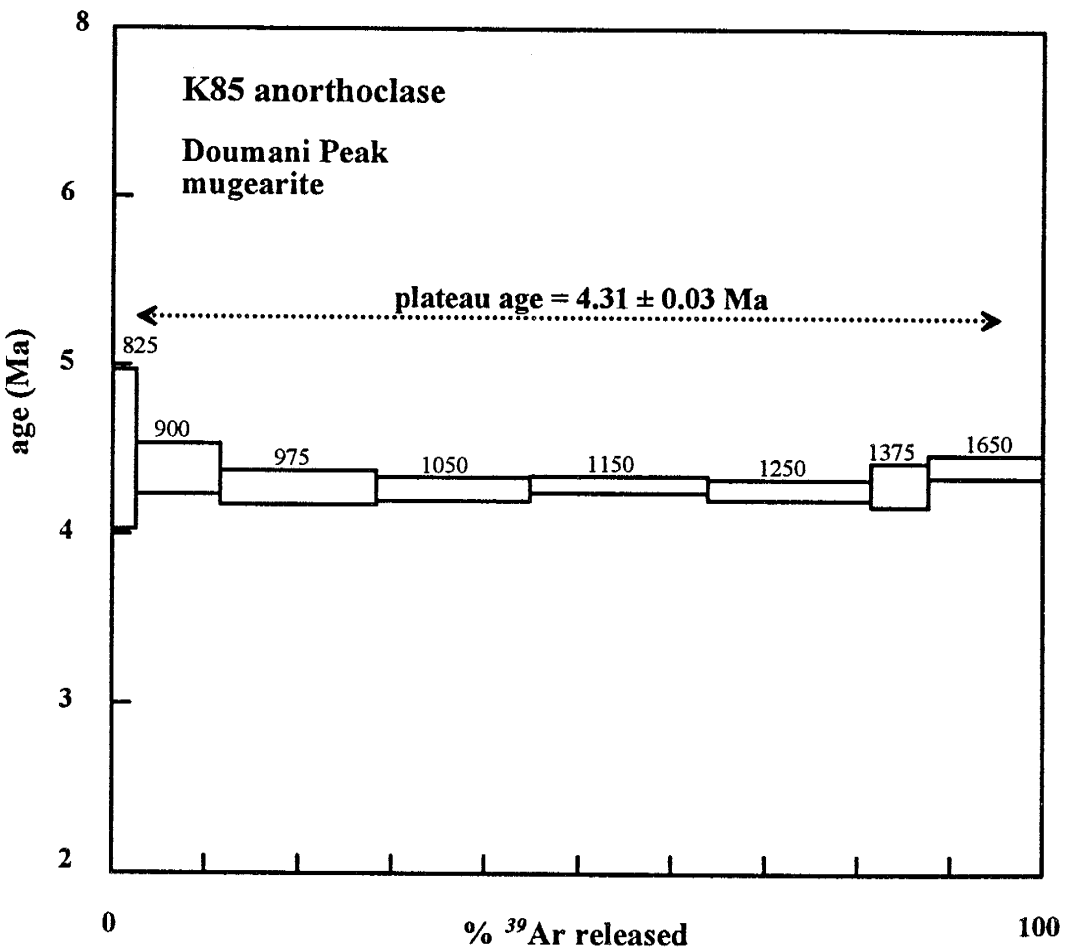

Figure C2.3. $^{40}Ar/^{39}Ar$ age spectra for sample K85.

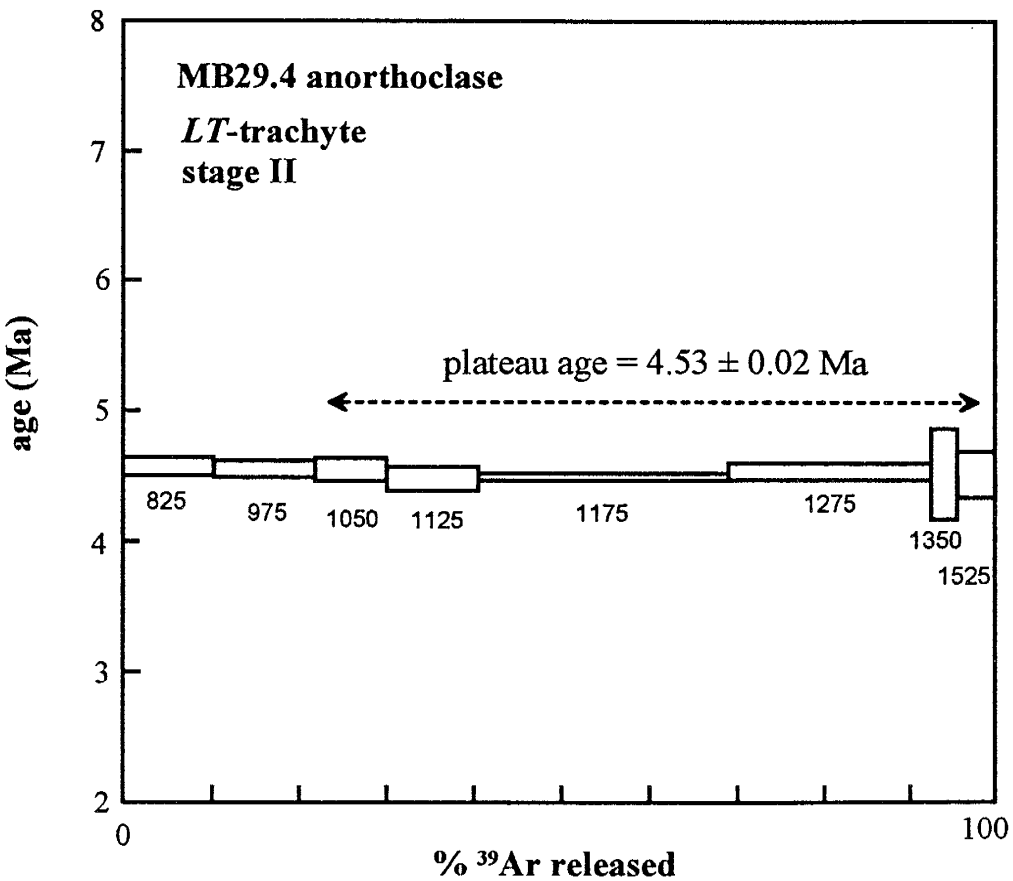

Figure C2.4. $^{40}Ar/^{39}Ar$ age spectra for sample MB29.4.

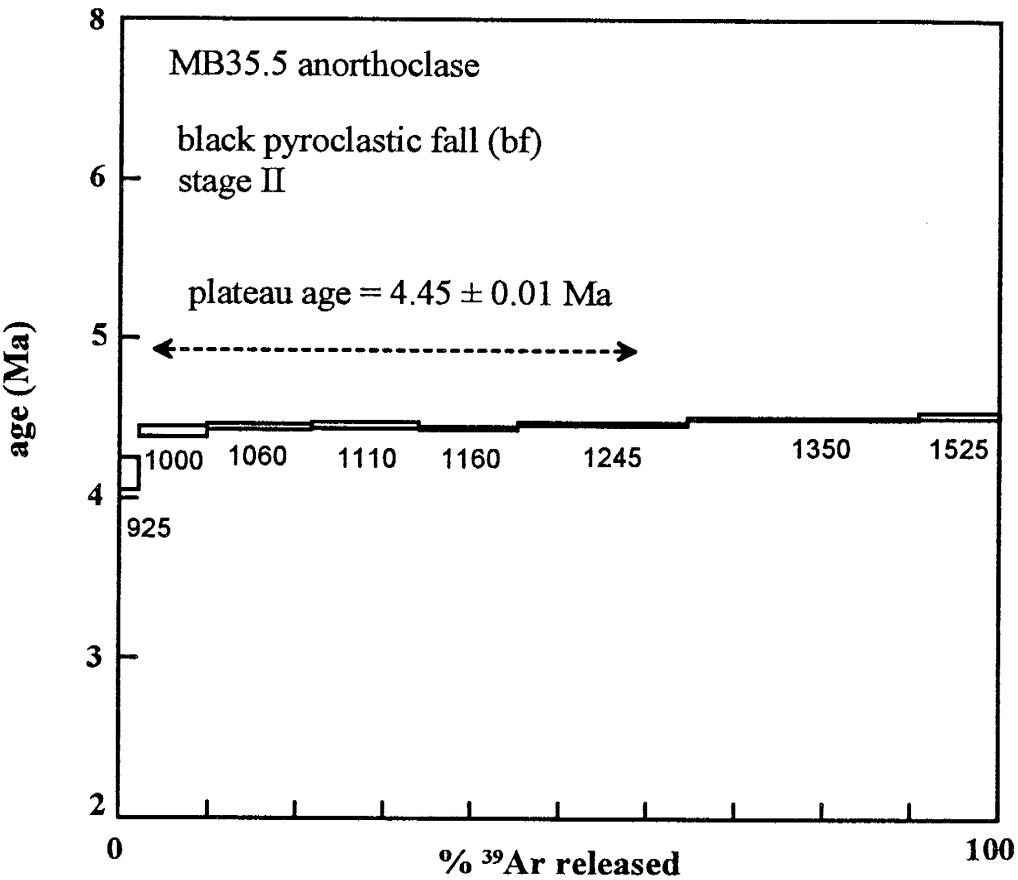

Figure C2.5. $^{40}Ar/^{39}Ar$ age spectra for sample MB35.5.

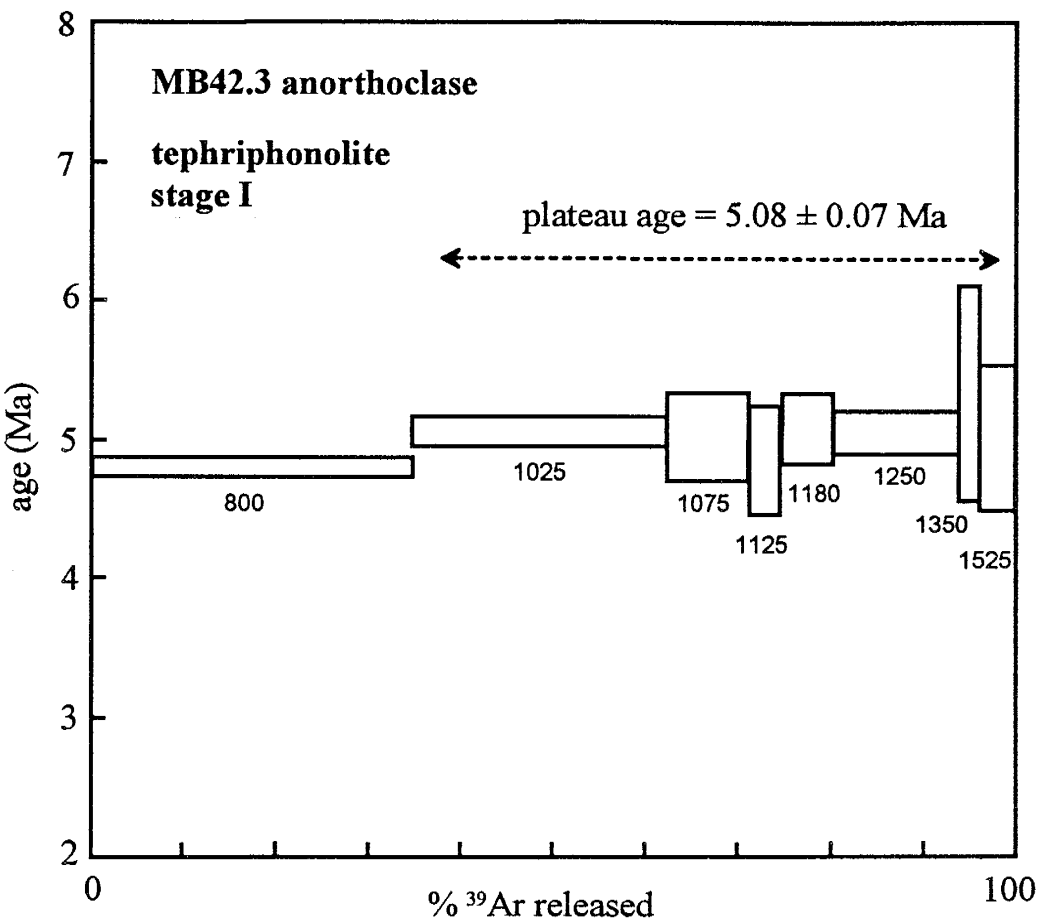

Figure C2.6. $^{40}Ar/^{39}Ar$ age spectra for sample MB42.3.

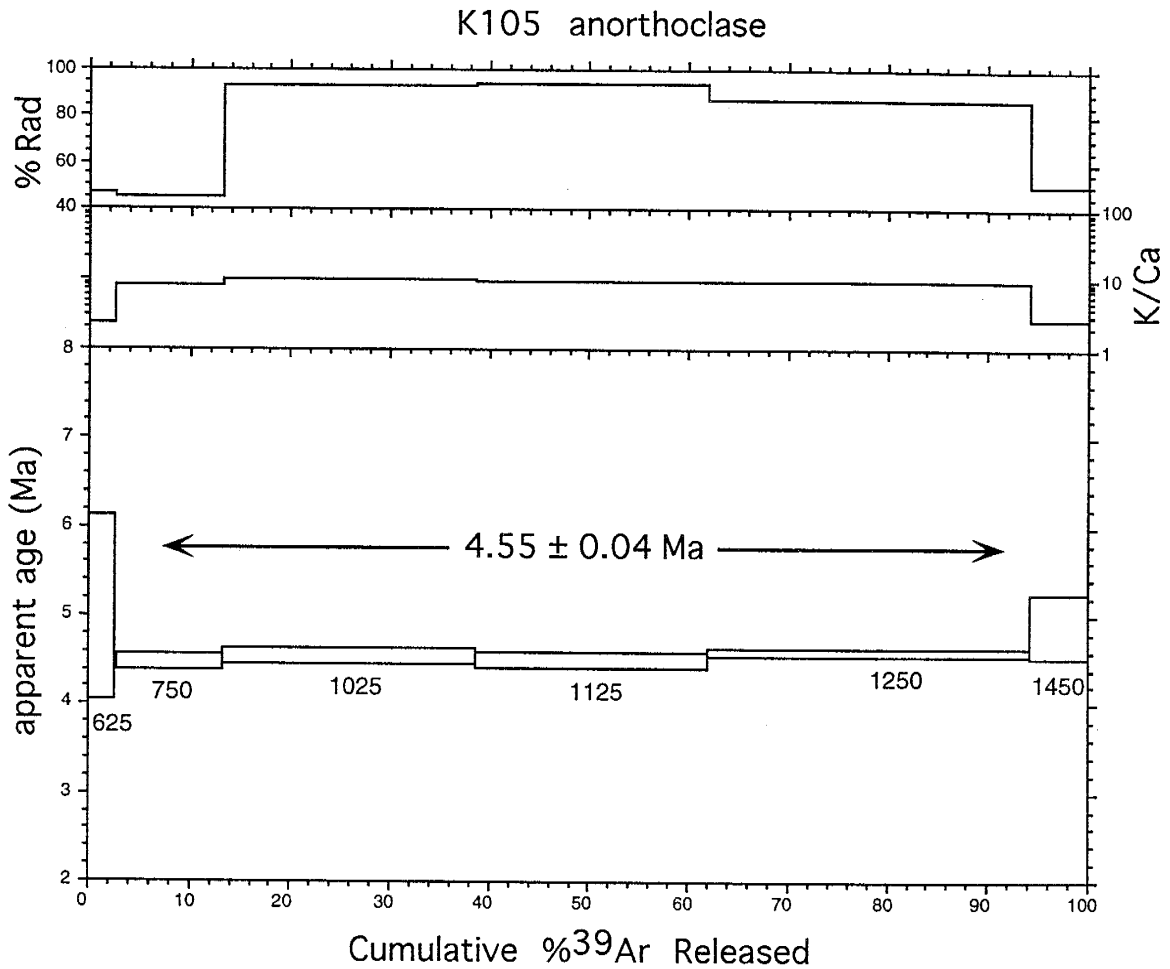

Figure C2.7. $^{40}Ar/^{39}Ar$ age spectra for sample K105.

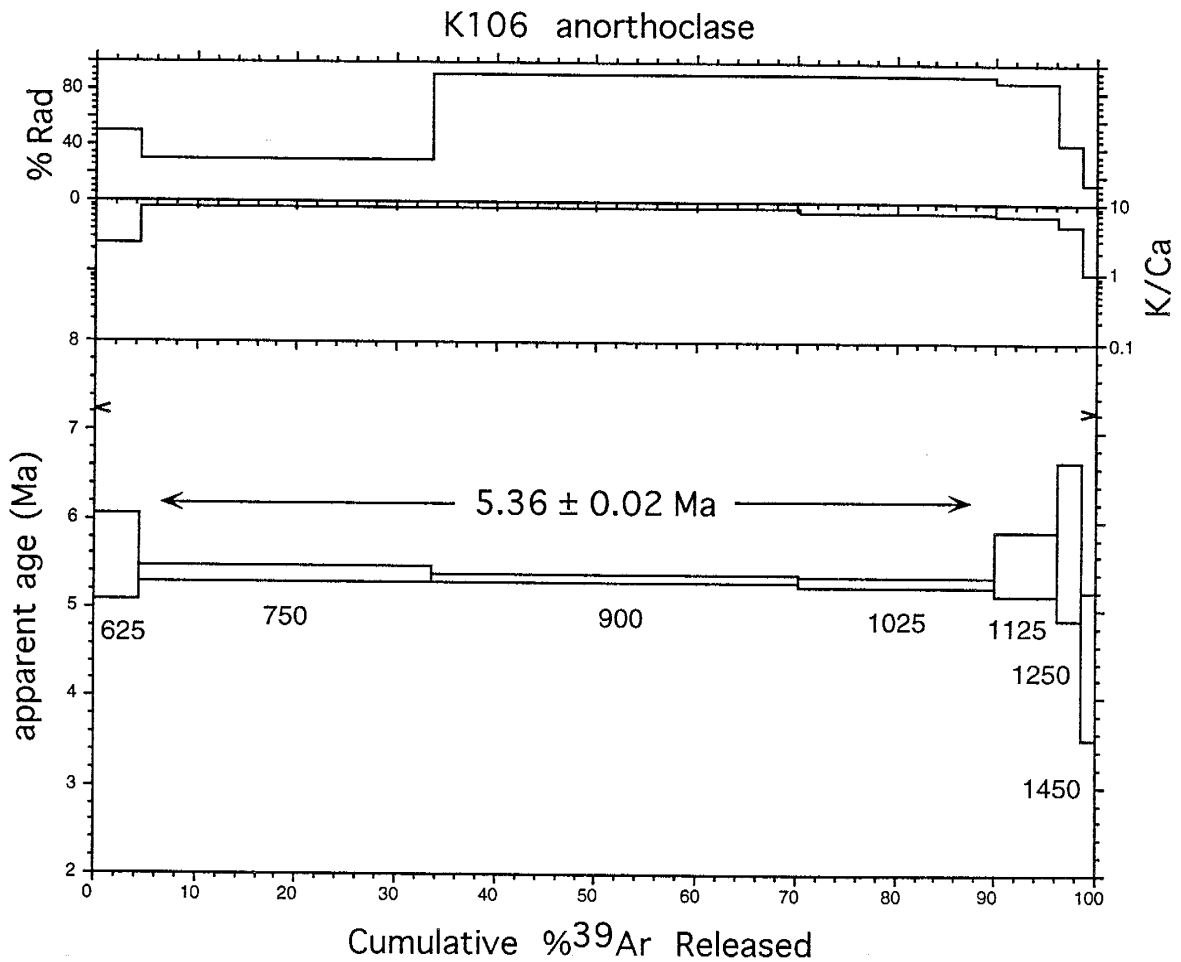

Figure C2.8. $^{40}Ar/^{39}Ar$ age spectra for sample K106.

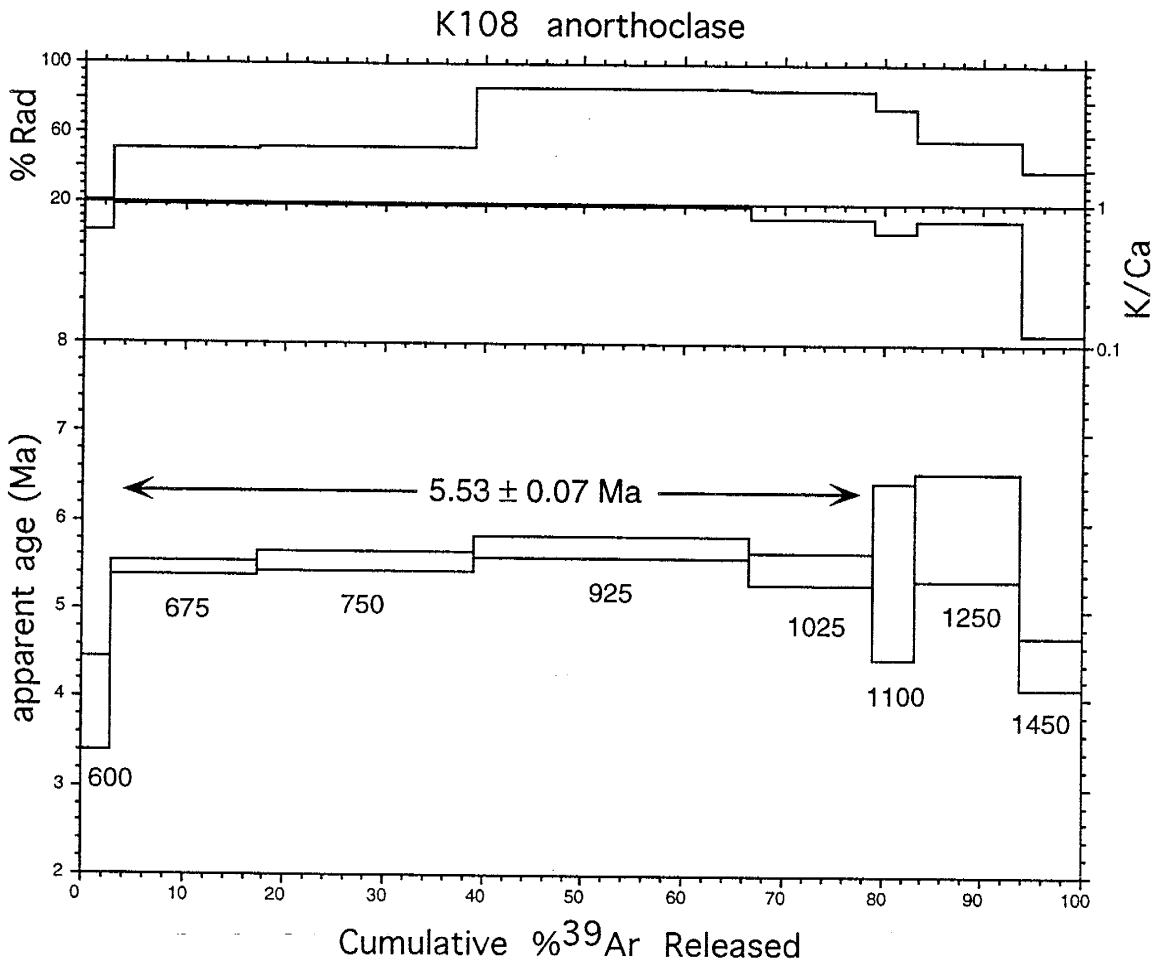

Figure C2.9. $^{40}Ar/^{39}Ar$ age spectra for sample K108.

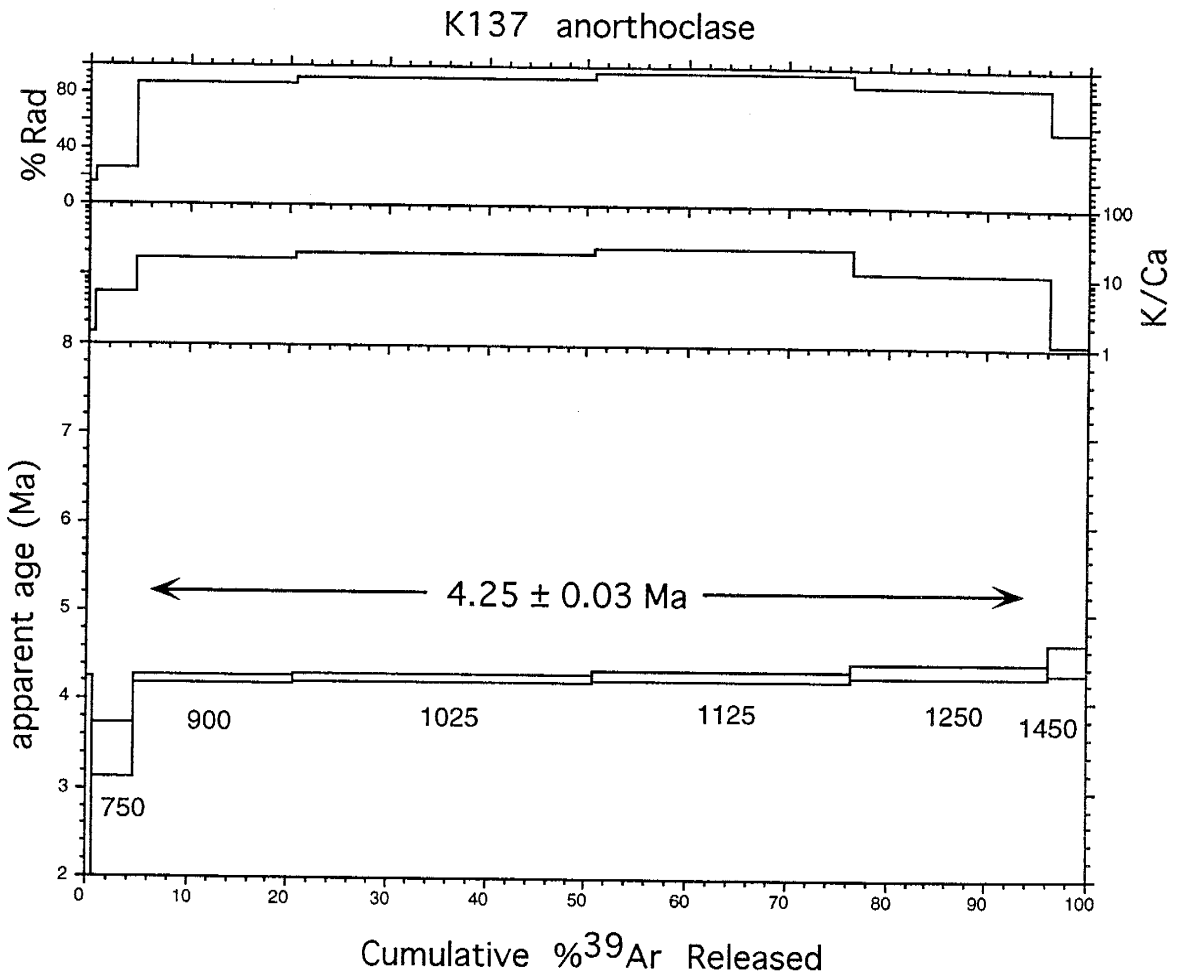

Figure C2.10. $^{40}Ar/^{39}Ar$ age spectra for sample K137.

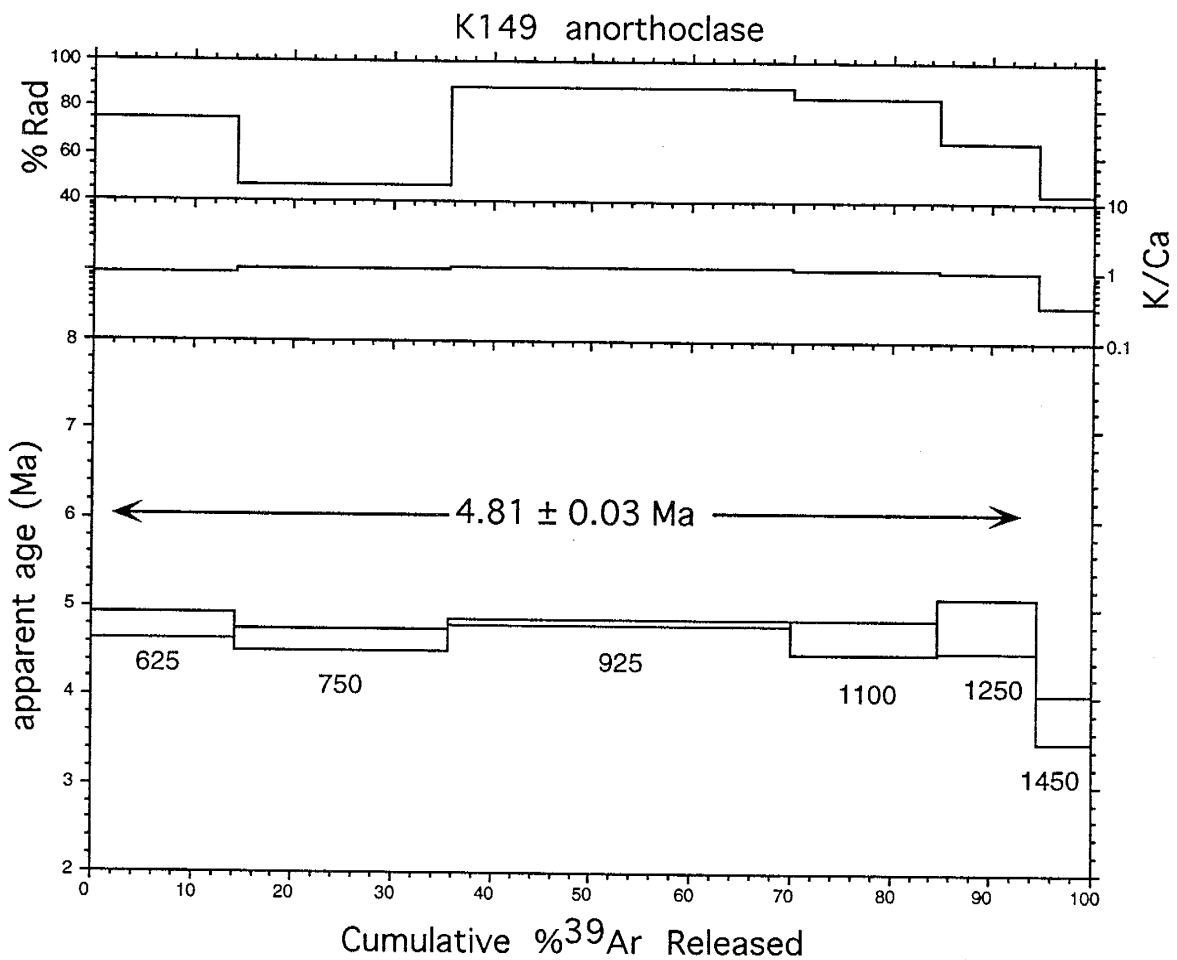

Figure C2.11. $^{40}Ar/^{39}Ar$ age spectra for sample K149.

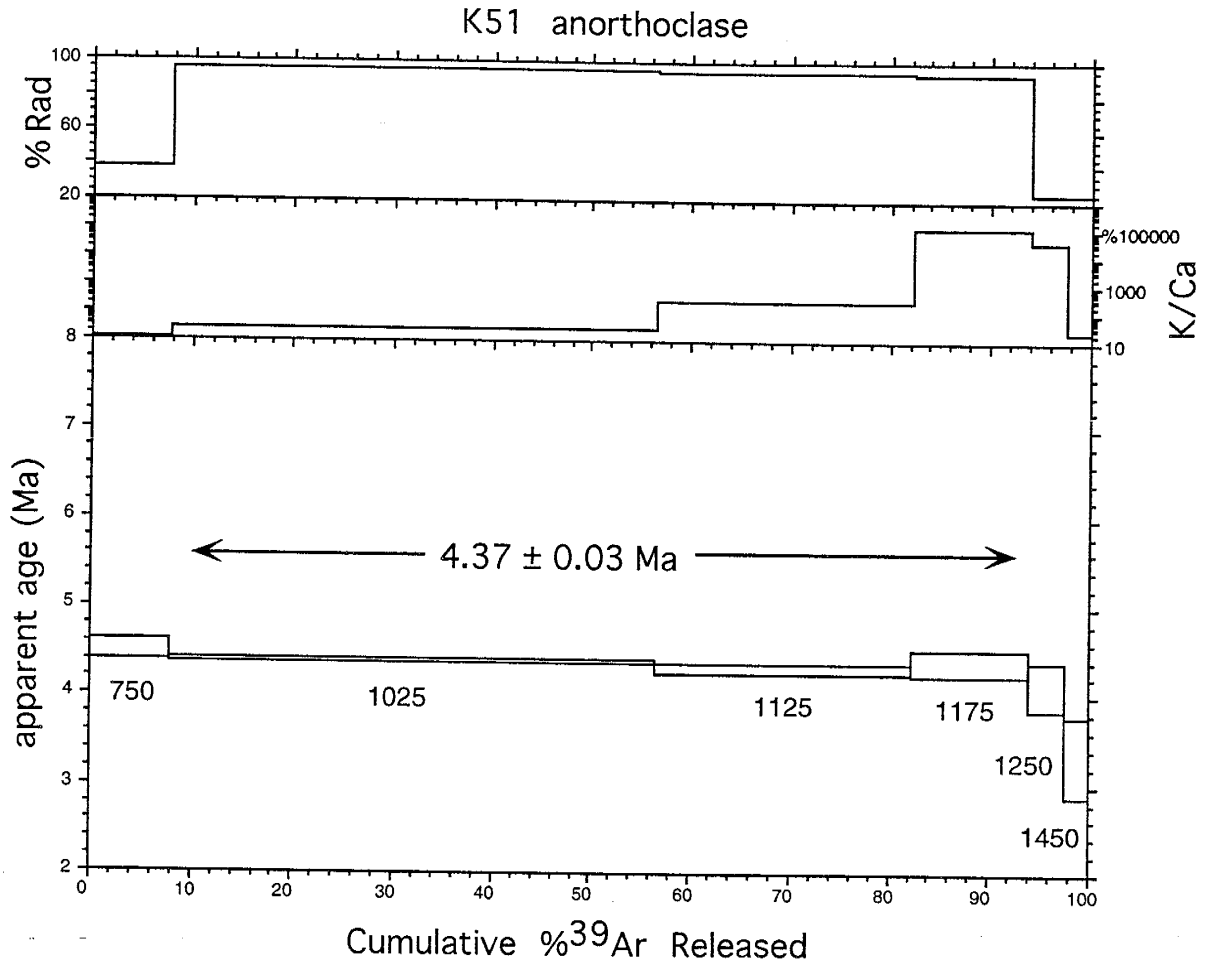

Figure C2.12. $^{40}Ar/^{39}Ar$ age spectra for sample K51.

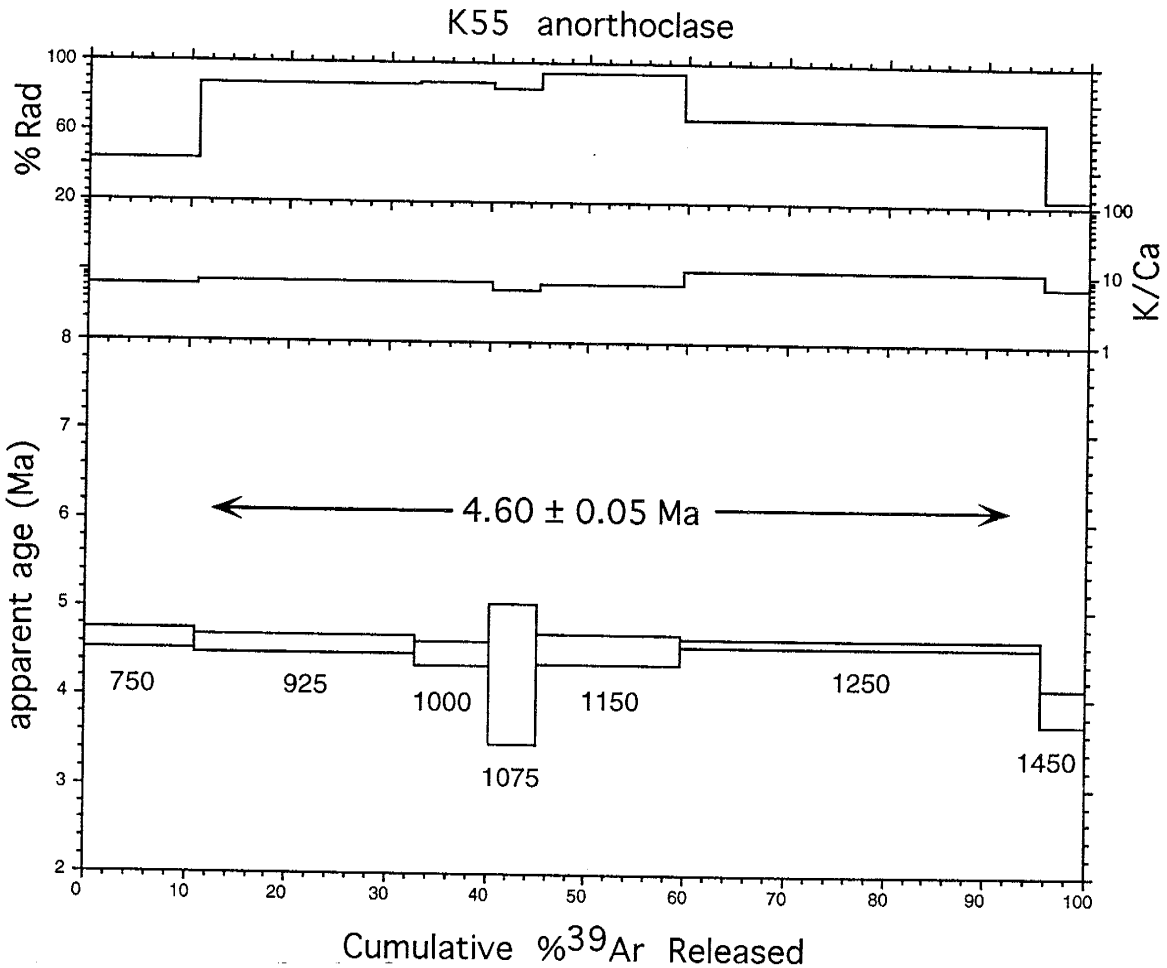

Figure C2.13. $^{40}Ar/^{39}Ar$ age spectra for sample K55.

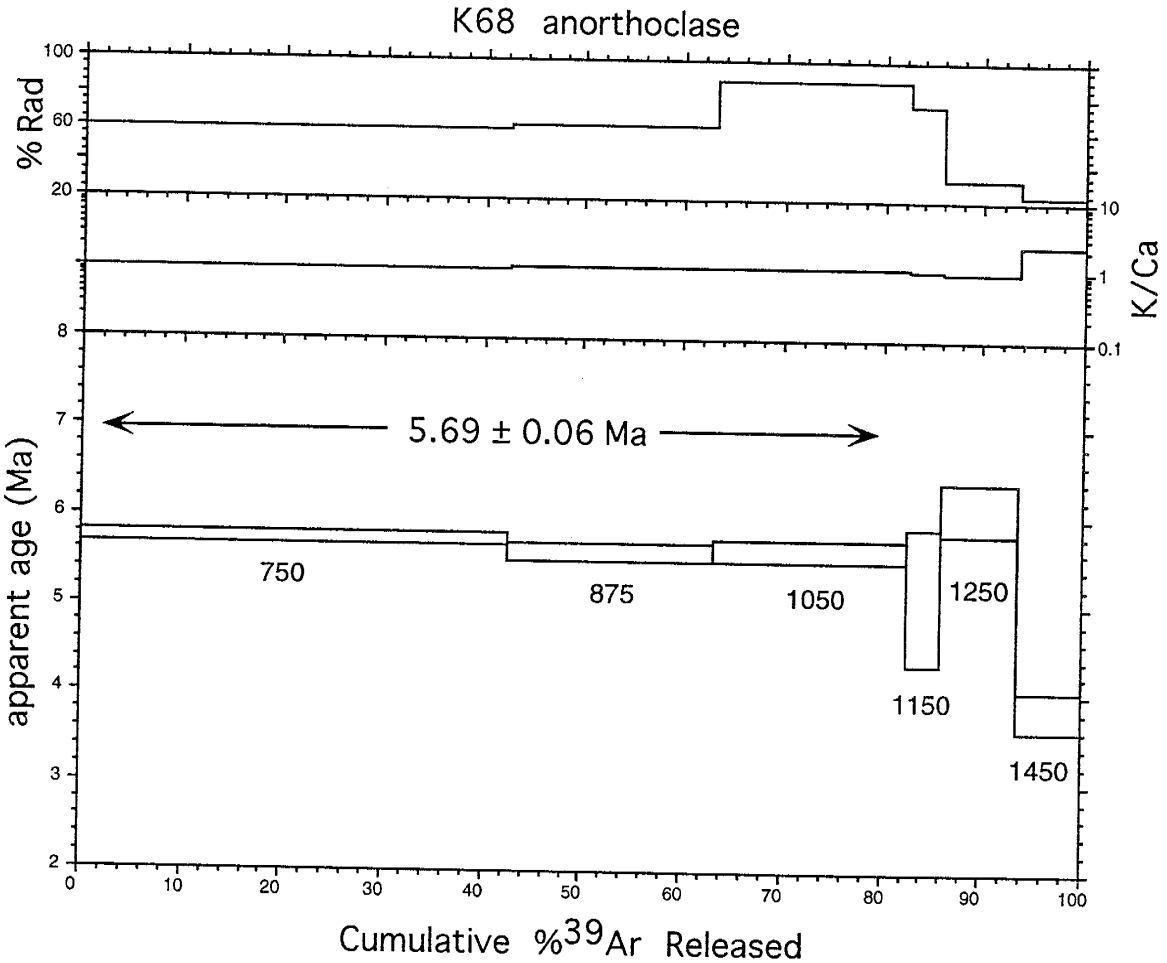

Figure C2.14. $^{40}Ar/^{39}Ar$ age spectra for sample K68.

Appendix C3: Electron Microprobe Mineral Analyses

Table C3.1: Olivine

sample	JG025	JG025	JG025	JG025	JG025	JG025	JG025	K63	K63	K63	K63
type	CL-encl. core-	CL-encl. rim	CL-encl. core	CL-encl. core	CL-encl. core	CL-encl. core	CL-encl. core	CL-host core	CL-encl. core-	CL-encl. rim	CL-encl. core-
	wt.% oxide										
SiO_2	40.02	40.26	39.73	39.79	41.76	40.95	41.77	33.10	39.50	32.78	39.87
FeO*	13.52	14.88	16.97	16.43	15.45	16.34	13.37	52.04	14.45	52.41	14.86
MnO	0.28	0.24	0.29	0.37	0.23	0.34	0.16	1.84	0.21	1.96	0.28
MgO	46.13	43.86	42.93	43.29	44.14	42.69	46.15	13.95	46.03	12.86	46.13
CaO	0.26	0.29	0.33	0.37	0.27	0.35	0.28	0.29	0.25	0.37	0.24
sum	100.21	99.53	100.25	100.25	101.85	100.67	101.73	101.22	100.44	100.38	101.38
	formula based on 4 oxygens										
Si	0.997	1.014	1.004	1.004	1.027	1.025	1.019	1.000	0.987	1.004	0.988
Fe^{2+}	0.282	0.313	0.359	0.347	0.318	0.342	0.273	1.315	0.302	1.342	0.308
Mn	0.006	0.005	0.006	0.008	0.005	0.007	0.003	0.047	0.004	0.051	0.006
Mg	1.712	1.646	1.617	1.628	1.617	1.592	1.678	0.628	1.714	0.587	1.704
Ca	0.007	0.008	0.009	0.010	0.007	0.009	0.007	0.009	0.007	0.012	0.006
total	3.004	2.986	2.995	2.997	2.974	2.975	2.980	2.999	3.014	2.996	3.012
mg-number	86	84	82	82	84	82	86	32	85	30	85

sample	K63	K63	K63	K63	K63	K63	K63	K63	K63	K63	K63
type	CL-encl. rim	CL-encl. core-	CL-encl. rim	CL-host core	CL-host core	CL-host core	CL-host core-	CL-host rim	CL-encl. core	CL-encl. core	CL-encl. core
	wt.% oxide										
SiO_2	34.55	39.54	33.88	30.65	30.01	29.76	30.09	30.11	39.20	31.00	30.10
FeO*	43.72	14.62	49.88	59.65	67.43	67.40	67.53	66.51	16.61	63.17	62.01
MnO	1.62	-	1.95	2.17	2.90	2.76	2.78	2.93	0.20	2.40	2.32
MgO	21.03	46.16	15.78	6.10	0.92	0.49	0.68	0.39	44.62	4.44	4.70
CaO	0.35	0.31	0.25	0.63	0.41	0.36	0.27	0.26	0.31	0.60	0.69
sum	101.27	100.63	101.74	99.20	101.67	100.77	101.35	100.20	100.94	101.61	99.82
	formula based on 4 oxygens										
Si	0.996	0.986	1.004	0.998	0.995	0.997	1.000	1.011	0.984	0.999	0.989
Fe^{2+}	1.054	0.305	1.237	1.625	1.869	1.889	1.878	1.867	0.349	1.703	1.704
Mn	0.040	-	0.049	0.060	0.081	0.078	0.078	0.083	0.004	0.066	0.065
Mg	0.904	1.715	0.697	0.296	0.045	0.024	0.034	0.020	1.670	0.213	0.230
Ca	0.011	0.008	0.008	0.022	0.015	0.013	0.010	0.009	0.008	0.021	0.024
total	3.005	3.014	2.995	3.001	3.005	3.001	3.000	2.990	3.015	3.002	3.012
mg-number	46	85	36	15	2	1	2	1	83	11	12

Table C3.1: Olivine

sample	K63	K63	K63	K66	K66	K66	K93	K93	K93	K93	K93
type	CL-encl.	CL-encl.	CL-encl.	trac	trac	trac	mug	mug	mug	mug	mug
	core	core	core	core	core	core	core-	rim	core	core	core
	wt.% oxide										
SiO_2	31.06	32.51	30.62	30.36	32.53	29.78	33.89	33.79	33.83	34.13	32.96
FeO*	60.45	49.96	58.74	64.50	59.42	64.33	46.33	46.35	45.78	46.15	53.15
MnO	2.58	1.69	2.54	5.14	3.06	3.92	0.95	1.16	0.94	0.93	1.74
MgO	4.74	14.82	4.74	0.81	1.34	0.39	18.97	18.68	19.23	19.25	12.01
CaO	0.71	0.28	0.56	0.22	2.40	0.46	0.39	0.27	0.33	0.41	0.76
sum	99.54	99.26	97.20	101.03	98.75	98.88	100.53	100.25	100.11	100.87	100.62
	formula based on 4 oxygens										
Si	1.013	0.996	1.019	1.008	1.067	1.012	0.997	0.998	0.997	0.998	1.010
Fe^{2+}	1.648	1.280	1.635	1.791	1.630	1.828	1.139	1.145	1.128	1.129	1.362
Mn	0.071	0.044	0.072	0.145	0.085	0.113	0.024	0.029	0.023	0.023	0.045
Mg	0.230	0.676	0.235	0.040	0.066	0.020	0.831	0.822	0.844	0.839	0.548
Ca	0.025	0.009	0.020	0.008	0.084	0.017	0.012	0.009	0.010	0.013	0.025
total	2.987	3.005	2.981	2.992	2.932	2.990	3.003	3.003	3.002	3.002	2.990
mg-number	12	35	13	2	4	1	42	42	43	43	29

sample	K108	K108	K108	K108	K108	K108	K108	K108	K115	K115	K115
type	tphn	tphn	tphn	tphn	tphn	tphn	tphn	tphn	phn	phn	phn
	core	core	core	core	core-	core-	rim	core	core	core	core
	wt.% oxide										
SiO_2	33.07	32.98	33.10	33.17	33.08	33.29	32.99	33.16	32.43	32.64	32.77
FeO*	47.70	47.14	47.99	47.77	48.12	48.04	47.12	46.80	51.61	51.14	48.87
MnO	1.89	1.91	2.07	1.93	2.01	2.06	1.10	1.97	1.67	2.11	2.18
MgO	15.72	16.15	16.85	16.53	16.53	16.66	15.29	16.06	13.10	13.57	15.52
CaO	0.64	0.62	0.69	0.56	0.67	0.69	0.63	0.63	0.68	0.61	0.60
sum	99.02	98.80	100.70	99.96	100.41	100.74	97.13	98.62	99.49	100.07	99.94
	formula based on 4 oxygens										
Si	1.004	1.001	0.989	0.996	0.991	0.993	1.017	1.007	1.000	0.999	0.993
Fe^{2+}	1.211	1.197	1.199	1.200	1.206	1.199	1.215	1.188	1.331	1.309	1.238
Mn	0.049	0.049	0.052	0.049	0.051	0.052	0.029	0.051	0.044	0.055	0.056
Mg	0.711	0.731	0.750	0.740	0.738	0.741	0.702	0.727	0.602	0.619	0.701
Ca	0.021	0.020	0.022	0.018	0.022	0.022	0.021	0.020	0.022	0.020	0.019
total	2.996	2.998	3.012	3.003	3.008	3.007	2.984	2.993	2.999	3.002	3.007
mg-number	37	38	38	38	38	38	37	38	31	32	36

Table C3.1: Olivine

sample	K115	K120	K120	K120	K120	K120	K122	K122	K122	K141	K144
type	phn	phn	phn	phn	phn	phn	phn	phn	phn	phn	phn
	core	rim	core	core	core	rim	core	rim	core	core	rim
	wt.% oxide										
SiO_2	32.58	32.98	32.81	33.08	33.31	32.53	33.20	33.01	33.39	30.86	33.17
FeO*	50.80	48.55	49.37	48.83	49.52	49.13	50.27	50.28	49.97	60.66	49.90
MnO	2.13	1.91	2.09	1.89	2.04	2.09	2.20	2.35	2.44	3.86	2.23
MgO	13.76	15.71	15.24	15.37	15.44	15.21	14.82	14.73	15.33	3.66	15.39
CaO	0.74	0.55	0.54	0.60	0.57	1.33	0.72	0.70	0.73	1.00	0.63
sum	100.01	99.70	100.05	99.77	100.88	100.29	101.21	101.07	101.86	100.04	101.32
	formula based on 4 oxygens										
Si	0.997	0.998	0.994	1.001	0.999	0.986	0.997	0.995	0.995	1.010	0.993
Fe^{2+}	1.300	1.229	1.251	1.236	1.242	1.245	1.263	1.267	1.245	1.660	1.250
Mn	0.055	0.049	0.054	0.048	0.052	0.054	0.056	0.060	0.062	0.107	0.057
Mg	0.627	0.708	0.688	0.693	0.690	0.687	0.663	0.661	0.681	0.178	0.687
Ca	0.024	0.018	0.018	0.019	0.018	0.043	0.023	0.023	0.023	0.035	0.020
total	3.003	3.002	3.005	2.997	3.001	3.015	3.002	3.006	3.006	2.990	3.007
mg-number	33	37	35	36	36	36	34	34	35	10	35

sample	K144	K144	K144	K144	K144	K144	K144	K149	K149	K149	K149
type	phn	phn	phn	phn	phn	phn	phn	phn	phn	phn	phn
	-core-	rim	core-	rim	rim	core	core	core-	rim	core-	rim
	wt.% oxide										
SiO_2	33.68	33.50	33.02	32.56	33.16	33.36	33.41	33.55	33.86	33.55	33.49
FeO*	49.67	49.26	50.79	49.80	51.76	50.37	48.76	49.68	48.48	49.12	48.72
MnO	2.18	2.10	2.39	2.20	2.35	2.24	2.05	1.86	1.88	1.89	1.94
MgO	15.63	15.43	13.65	14.23	13.91	14.70	15.95	15.94	16.48	16.01	16.35
CaO	0.58	0.61	0.65	0.73	0.68	0.75	0.64	0.61	0.72	0.66	0.67
sum	101.74	100.90	100.50	99.52	101.86	101.42	100.81	101.64	101.42	101.23	101.17
	formula based on 4 oxygens										
Si	1.000	1.003	1.004	0.997	0.997	1.000	0.999	0.997	1.002	0.999	0.996
Fe^{2+}	1.234	1.233	1.291	1.275	1.301	1.263	1.219	1.234	1.200	1.223	1.212
Mn	0.055	0.053	0.062	0.057	0.060	0.057	0.052	0.047	0.047	0.048	0.049
Mg	0.692	0.688	0.618	0.649	0.623	0.657	0.711	0.706	0.727	0.710	0.725
Ca	0.018	0.020	0.021	0.024	0.022	0.024	0.021	0.019	0.023	0.021	0.021
total	2.999	2.997	2.996	3.002	3.003	3.001	3.002	3.003	2.999	3.001	3.003
mg-number	36	36	32	34	32	34	37	36	38	37	37

Table C3.1: Olivine

sample	K149	K149	K149	K168	K168	K168	K168	K168	K168	K168	K168
type	phn	phn	phn	bas	bas	bas	bas	bas	bas	bas	bas
	core	core	core	core	core	core	core	core-	rim	core-	rim
	wt.% oxide										
SiO_2	33.55	33.33	33.61	35.84	35.90	36.73	36.17	37.86	37.60	34.59	35.41
FeO*	48.29	47.85	46.11	40.51	39.31	40.07	39.63	23.90	21.44	41.24	38.86
MnO	1.87	1.84	2.02	0.78	0.89	0.82	0.73	0.28	0.32	0.79	0.75
MgO	16.04	16.28	15.83	24.39	24.31	24.03	24.21	38.15	38.30	22.52	24.60
CaO	0.70	0.82	0.77	0.16	0.11	0.15	0.21	0.13	0.11	0.18	0.29
sum	100.45	100.12	98.34	101.68	100.52	101.80	100.95	100.32	97.77	99.32	99.91
	formula based on 4 oxygens										
Si	1.004	1.000	1.019	1.004	1.013	1.023	1.016	0.990	0.999	1.002	1.005
Fe^{2+}	1.208	1.200	1.169	0.949	0.928	0.933	0.931	0.523	0.476	0.999	0.922
Mn	0.047	0.047	0.052	0.019	0.021	0.019	0.017	0.006	0.007	0.019	0.018
Mg	0.715	0.728	0.715	1.019	1.022	0.997	1.013	1.487	1.516	0.972	1.041
Ca	0.022	0.026	0.025	0.005	0.003	0.004	0.006	0.004	0.003	0.006	0.009
total	2.996	3.001	2.980	2.996	2.987	2.976	2.983	3.010	3.001	2.998	2.995
mg-number	37	38	38	52	52	52	52	74	76	49	53

sample	K168	K168	K168	K168	K168
type	bas	bas	bas	bas	bas
	rim	gm	gm	core	core
	wt.% oxide				
SiO_2	34.51	38.94	39.45	38.57	38.26
FeO*	41.23	20.77	21.68	23.34	23.23
MnO	0.90	0.21	0.25	0.31	0.31
MgO	22.52	39.12	39.66	38.44	38.27
CaO	0.24	0.16	0.15	0.15	0.14
sum	99.40	99.20	101.19	100.81	100.21
	formula based on 4 oxygens				
Si	1.000	1.012	1.008	0.999	0.998
Fe^{2+}	0.999	0.451	0.463	0.506	0.507
Mn	0.022	0.005	0.005	0.007	0.007
Mg	0.972	1.515	1.511	1.484	1.487
Ca	0.007	0.004	0.004	0.004	0.004
total	3.000	2.987	2.991	3.000	3.003
mg-number	49	77	77	75	75

abbreviations: bas = basanite; mug = mugearite; tphn = tephriphonolite; phn = phonolite; trac = trachyte
commingled lavas (CL) consist of mafic enclaves (encl.) and trachytic host (host).

* Total Fe as FeO

mg-number = atomic % ($Mg/Mg + Fe^{2+}$)

Appendix C3: Electron Microprobe Mineral Analyses

Table C3.2: Clinopyroxene

Sample	JG025	JG025	JG025	JG025	JG025	JG025	JG025	JG025	JG025	JG025	JG025
rock	CL-encl.	CL-host	CL-host	CL-host	CL-encl.	CL-encl.	CL-encl.	CL-encl.	CL-encl.	CL-encl.	CL-encl.
position	core	core-	rim-a	rim-b	core-	rim	core	core	core	core	rim
	wt. % oxide										
SiO_2	53.74	48.07	48.28	49.24	47.11	47.29	48.08	49.67	46.08	47.06	49.82
TiO_2	0.25	0.45	0.33	0.35	2.09	2.29	2.13	1.53	2.28	2.38	0.57
Al_2O_3	0.61	0.38	0.33	0.40	7.55	7.79	6.82	4.90	7.66	7.60	0.89
FeO*	2.84	28.06	28.09	24.62	6.04	5.67	5.41	4.99	5.63	5.42	21.61
MnO	0.14	0.84	0.97	0.92	0.26	0.17	0.12	-	0.22	0.20	0.77
MgO	16.59	0.86	0.57	3.48	13.33	13.24	14.50	15.15	13.15	13.38	4.88
CaO	24.06	20.20	19.83	20.08	21.68	22.28	22.37	22.49	22.28	21.88	20.93
Na_2O	0.26	0.54	0.83	0.64	0.42	0.48	0.44	0.46	0.40	0.47	0.50
sum	98.49	99.40	99.23	99.73	98.48	99.21	99.87	99.19	97.70	98.39	99.97
Fe_2O_3	0.12	1.08	1.48	1.38	1.73	1.76	2.96	2.41	2.85	1.41	0.16
FeO	2.73	27.09	26.75	23.38	4.48	4.08	2.75	2.82	3.07	4.15	21.47
total	98.50	99.51	99.37	99.87	98.65	99.38	100.17	99.43	97.99	98.53	99.99
	formula based on 6 oxygens										
Si	1.988	1.982	1.992	1.984	1.765	1.758	1.768	1.834	1.739	1.762	1.979
Ti	0.007	0.014	0.010	0.011	0.059	0.064	0.059	0.042	0.065	0.067	0.017
Al	0.026	0.018	0.016	0.019	0.333	0.341	0.295	0.213	0.341	0.336	0.042
Fe^{3+}	0.003	0.033	0.046	0.042	0.049	0.049	0.082	0.067	0.081	0.040	0.005
Fe^{2+}	0.084	0.934	0.923	0.788	0.140	0.127	0.085	0.087	0.097	0.130	0.713
Mn	0.004	0.029	0.034	0.031	0.008	0.005	0.004	-	0.007	0.006	0.026
Mg	0.915	0.053	0.035	0.209	0.744	0.734	0.795	0.833	0.740	0.747	0.289
Ca	0.954	0.893	0.877	0.867	0.871	0.887	0.882	0.890	0.901	0.878	0.891
Na	0.019	0.043	0.067	0.050	0.030	0.034	0.031	0.033	0.030	0.034	0.039
sum	4.000	3.999	4.000	4.001	3.999	3.999	4.001	3.999	4.001	4.000	4.001
mg-number	92	5	4	21	84	85	90	91	88	85	29

Sample	JG025	K55	K55	K55	K55	K55	K55	K63	K63	K63	K63
rock	CL-host	trac	trac	trac	trac	trac	trac	CL-encl.	CL-encl.	CL-host	CL-host
position	core	core	core	core	core	core	core	core-	rim	core	core
	wt. % oxide										
SiO_2	48.48	50.44	50.83	50.13	49.79	50.01	50.24	43.85	50.23	48.52	48.37
TiO_2	1.01	0.66	0.51	0.54	0.63	0.41	0.46	3.81	0.48	0.36	0.36
Al_2O_3	0.40	1.37	1.28	1.27	1.30	0.59	0.92	9.04	0.74	0.33	0.20
FeO*	28.87	17.69	17.69	18.09	17.42	21.59	20.11	9.15	22.27	28.52	29.11
MnO	0.91	0.62	0.77	0.79	0.61	1.02	0.80	0.00	0.86	0.59	1.10
MgO	0.76	8.11	8.40	7.71	7.57	5.81	6.46	11.36	5.47	-	1.85
CaO	17.42	20.57	21.09	20.32	20.21	19.52	20.08	21.14	20.05	19.81	18.39
Na_2O	2.25	0.40	0.51	0.56	0.62	0.79	0.53	0.77	0.80	0.80	1.13
sum	100.10	99.86	101.08	99.41	98.15	99.74	99.60	99.12	100.90	98.93	100.51
Fe_2O_3	4.42	0.08	1.76	0.93	0.22	1.65	0.14	4.66	1.99	0.82	2.51
FeO	24.90	17.62	16.10	17.26	17.23	20.11	19.98	4.96	20.48	27.78	26.86
total	100.55	99.87	101.25	99.51	98.18	99.91	99.61	99.59	101.10	99.01	100.77
	formula based on 6 oxygens										
Si	1.969	1.963	1.950	1.962	1.971	1.980	1.983	1.653	1.970	2.010	1.969
Ti	0.031	0.019	0.015	0.016	0.019	0.012	0.014	0.108	0.014	0.011	0.011
Al	0.019	0.063	0.058	0.059	0.061	0.028	0.043	0.402	0.034	0.016	0.010
Fe^{3+}	0.135	0.002	0.051	0.027	0.006	0.049	0.004	0.132	0.059	0.026	0.077
Fe^{2+}	0.846	0.573	0.517	0.565	0.570	0.666	0.660	0.156	0.672	0.962	0.914
Mn	0.031	0.020	0.025	0.026	0.020	0.034	0.027	0.000	0.029	0.021	0.038
Mg	0.046	0.470	0.480	0.450	0.447	0.343	0.380	0.638	0.320	-	0.112
Ca	0.758	0.858	0.867	0.852	0.857	0.828	0.849	0.854	0.842	0.879	0.802
Na	0.177	0.030	0.038	0.043	0.048	0.061	0.041	0.056	0.061	0.064	0.089
sum	4.012	3.998	4.001	4.000	3.999	4.001	4.001	3.999	4.001	3.989	4.022
mg-number	5	45	48	44	44	34	37	80	32	-	11

Table C3.2: Clinopyroxene

Sample	K63	K63	K63	K63	K63	K63	K63	K63	K63	K66	K66
rock	CL-encl.	CL-encl.	CL-encl.	CL-encl.	CL-encl.	CL-host	CL-host	CL-host	CL-host	trac	trac
position	core	core-	inter-	rim	core	core	core	core	core	core-	rim
	wt. % oxide										
SiO_2	50.67	46.30	50.76	50.49	49.83	48.85	49.02	48.41	47.99	48.82	49.29
TiO_2	0.67	2.93	0.83	0.33	0.59	0.42	0.27	0.40	0.29	0.59	0.53
Al_2O_3	1.58	7.56	2.37	0.40	0.88	0.41	0.33	0.39	0.31	0.81	0.90
FeO*	15.51	9.05	18.53	23.33	22.42	29.48	29.00	29.17	30.32	22.83	22.84
MnO	0.68	0.22	0.65	0.86	0.77	1.06	0.98	1.09	1.01	0.85	0.86
MgO	9.86	12.18	6.76	4.99	5.07	0.67	0.54	0.57	0.41	4.66	4.33
CaO	19.62	21.41	19.80	20.39	21.06	19.74	19.51	19.06	19.84	20.92	20.69
Na_2O	1.18	0.58	1.13	0.68	0.41	0.72	0.80	0.83	0.92	0.34	0.44
sum	99.77	100.23	100.83	101.47	101.03	101.35	100.45	99.92	101.09	99.82	99.88
Fe_2O_3	3.54	3.45	0.45	1.72	1.12	1.66	1.00	1.46	2.28	0.97	0.63
FeO	12.32	5.95	18.13	21.78	21.41	27.99	28.10	27.86	28.27	21.96	22.28
total	100.12	100.58	100.88	101.64	101.14	101.52	100.55	100.07	101.32	99.92	99.95
	formula based on 6 oxygens										
Si	1.938	1.725	1.958	1.980	1.961	1.979	2.001	1.989	1.962	1.955	1.971
Ti	0.019	0.082	0.024	0.010	0.017	0.013	0.008	0.012	0.009	0.018	0.016
Al	0.071	0.332	0.108	0.018	0.041	0.020	0.016	0.019	0.015	0.038	0.042
Fe^{3+}	0.102	0.097	0.013	0.051	0.033	0.051	0.031	0.045	0.070	0.029	0.019
Fe^{2+}	0.394	0.185	0.585	0.714	0.705	0.948	0.959	0.957	0.966	0.736	0.745
Mn	0.022	0.007	0.021	0.029	0.026	0.036	0.034	0.038	0.035	0.029	0.029
Mg	0.562	0.676	0.389	0.292	0.297	0.040	0.033	0.035	0.025	0.278	0.258
Ca	0.804	0.854	0.818	0.857	0.888	0.857	0.853	0.839	0.869	0.898	0.886
Na	0.088	0.042	0.085	0.052	0.031	0.057	0.063	0.066	0.073	0.026	0.034
sum	4.000	4.000	4.001	4.003	3.999	4.001	3.998	4.000	4.024	4.007	4.000
mg-number	59	79	40	29	30	4	3	4	3	27	26

Sample	K66	K66	K66	K66	K93	K93	K100	K100	K100	K100	K115
rock	trac	trac	trac	trac	mug	mug	trac	trac	trac	trac	phn
position	core	core	core	core	core-	rim	core-	rim	core	core	core
	wt. % oxide										
SiO_2	49.45	49.74	48.59	48.79	49.06	49.17	49.10	49.19	49.46	48.52	50.32
TiO_2	0.54	0.52	0.46	0.48	0.52	0.48	0.49	0.62	0.44	0.41	0.67
Al_2O_3	0.91	0.85	0.43	0.61	0.46	0.49	0.70	0.94	0.78	0.70	1.87
FeO*	23.26	23.35	26.93	26.96	27.06	26.18	24.42	23.41	25.07	24.98	13.20
MnO	0.93	0.93	1.00	0.98	0.68	0.81	0.93	0.91	1.13	1.20	0.50
MgO	4.61	4.39	1.83	1.81	2.48	2.80	3.40	4.15	3.73	3.13	10.10
CaO	20.94	21.19	20.25	20.36	20.74	20.63	20.79	20.69	20.04	19.74	21.83
Na_2O	0.42	0.47	0.55	0.46	0.62	0.56	0.44	0.50	0.80	0.68	0.75
sum	101.06	101.44	100.04	100.45	101.62	101.12	100.27	100.41	101.45	99.36	99.24
Fe_2O_3	1.43	1.50	1.17	0.70	1.28	1.25	1.05	1.31	2.40	2.03	2.65
FeO	21.97	22.00	25.88	26.33	25.91	25.05	23.47	22.23	22.91	23.15	10.82
total	101.20	101.59	100.16	100.52	101.75	101.24	100.37	100.54	101.69	99.56	99.51
	formula based on 6 oxygens										
Si	1.954	1.959	1.978	1.978	1.963	1.969	1.970	1.959	1.958	1.966	1.928
Ti	0.016	0.015	0.014	0.015	0.016	0.014	0.015	0.019	0.013	0.012	0.019
Al	0.042	0.039	0.021	0.029	0.022	0.023	0.033	0.044	0.036	0.033	0.084
Fe^{3+}	0.042	0.045	0.036	0.021	0.039	0.038	0.032	0.039	0.072	0.062	0.076
Fe^{2+}	0.726	0.725	0.881	0.893	0.867	0.839	0.788	0.740	0.758	0.785	0.347
Mn	0.031	0.031	0.034	0.034	0.023	0.027	0.032	0.031	0.038	0.041	0.016
Mg	0.272	0.258	0.111	0.109	0.148	0.167	0.203	0.246	0.220	0.189	0.577
Ca	0.887	0.894	0.883	0.885	0.889	0.885	0.894	0.883	0.850	0.857	0.896
Na	0.032	0.036	0.043	0.036	0.048	0.043	0.034	0.039	0.061	0.053	0.056
sum	4.002	4.002	4.001	4.000	4.015	4.005	4.001	4.000	4.006	3.998	3.999
mg-number	27	26	11	11	15	17	20	25	22	19	62

Table C3.2: Clinopyroxene

Sample	K115	K115	K115	K120	K120	K120	K122	K122	K122	K122	K122
rock	phn	phn	phn	phn	phn	phn	phn	phn	phn	phn	phn
position	core	core-	rim	core	core	core	core-	rim	core	core	core
	wt. % oxide										
SiO_2	50.64	50.45	50.66	50.66	50.97	51.19	50.38	50.30	51.62	51.42	51.00
TiO_2	0.68	0.76	0.53	0.93	0.80	0.74	0.93	1.15	0.91	0.88	0.79
Al_2O_3	2.16	1.98	1.58	2.47	2.21	2.04	1.86	2.27	1.55	1.56	1.85
FeO*	12.42	12.96	13.45	12.83	12.15	12.80	12.93	12.56	13.45	12.85	13.06
MnO	0.51	0.61	0.51	0.54	0.53	0.57	0.70	0.68	0.63	0.65	0.64
MgO	10.61	9.82	9.86	10.60	10.68	10.54	10.56	10.52	10.50	10.45	10.09
CaO	21.92	21.94	22.11	21.64	21.99	21.47	20.90	20.87	21.85	21.88	21.98
Na_2O	0.88	0.68	0.75	0.92	0.82	0.87	0.91	0.98	0.78	0.71	0.84
sum	99.82	99.20	99.45	100.59	100.15	100.22	99.17	99.33	101.29	100.40	100.25
Fe_2O_3	3.16	1.48	2.55	3.16	2.26	2.03	2.64	2.33	2.08	1.31	2.28
FeO	9.57	11.63	11.16	9.98	10.12	10.97	10.55	10.46	11.58	11.67	11.01
total	100.13	99.35	99.71	100.90	100.38	100.42	99.43	99.56	101.50	100.53	100.48
	formula based on 6 oxygens										
Si	1.920	1.937	1.940	1.908	1.926	1.936	1.927	1.919	1.939	1.947	1.934
Ti	0.019	0.022	0.015	0.026	0.023	0.021	0.027	0.033	0.026	0.025	0.023
Al	0.097	0.090	0.071	0.110	0.098	0.091	0.084	0.102	0.069	0.070	0.083
Fe^{3+}	0.090	0.043	0.073	0.090	0.064	0.058	0.076	0.067	0.059	0.037	0.065
Fe^{2+}	0.304	0.373	0.357	0.314	0.320	0.347	0.338	0.334	0.364	0.370	0.349
Mn	0.016	0.020	0.017	0.017	0.017	0.018	0.023	0.022	0.020	0.021	0.021
Mg	0.599	0.562	0.563	0.595	0.601	0.594	0.602	0.598	0.588	0.590	0.570
Ca	0.890	0.903	0.907	0.873	0.890	0.870	0.857	0.853	0.879	0.888	0.893
Na	0.065	0.051	0.056	0.067	0.060	0.064	0.067	0.072	0.057	0.052	0.062
sum	4.000	4.001	3.999	4.000	3.999	3.999	4.001	4.000	4.001	4.000	4.000
mg-number	66	60	61	65	65	63	64	64	62	61	62

Sample	K122	K122	K122	K144	K144	K144	K144	K144	K144	K144	K144
rock	phn	phn	phn	phn	phn	phn	phn	phn	phn	phn	phn
position	core	core	core	core-	rim	core-	rim	core-	rim	core-	rim
	wt. % oxide										
SiO_2	50.88	51.40	49.01	50.57	51.06	50.11	50.71	50.87	49.24	51.47	51.63
TiO_2	0.79	0.88	1.10	1.04	0.67	0.84	0.73	0.71	0.75	0.47	0.66
Al_2O_3	1.58	1.64	2.19	2.66	1.93	2.59	2.10	1.90	1.92	1.59	1.83
FeO*	12.41	13.22	13.62	13.92	13.19	13.92	13.24	13.45	13.17	14.33	12.76
MnO	0.52	0.62	0.61	0.53	0.64	0.63	0.47	0.40	0.54	0.59	0.56
MgO	10.56	10.19	9.85	9.90	9.81	9.62	9.88	10.08	9.55	9.60	10.11
CaO	21.48	21.35	20.96	21.93	22.10	21.83	21.89	22.20	22.11	21.65	22.42
Na_2O	0.73	0.85	0.90	0.96	0.72	0.81	0.81	0.76	0.79	0.95	0.75
sum	98.95	100.15	98.24	101.51	100.12	100.35	99.83	100.37	98.07	100.65	100.72
Fe_2O_3	1.24	1.17	3.55	3.61	1.46	3.06	2.04	2.58	3.53	2.46	1.35
FeO	11.30	12.17	10.42	10.68	11.87	11.17	11.41	11.13	10.00	12.12	11.54
total	99.08	100.27	98.59	101.88	100.26	100.66	100.04	100.63	98.43	100.90	100.85
	formula based on 6 oxygens										
Si	1.951	1.953	1.900	1.896	1.943	1.904	1.933	1.928	1.912	1.951	1.949
Ti	0.023	0.025	0.032	0.029	0.019	0.024	0.021	0.020	0.022	0.013	0.019
Al	0.071	0.073	0.100	0.118	0.087	0.116	0.094	0.085	0.088	0.071	0.081
Fe^{3+}	0.036	0.033	0.104	0.102	0.042	0.087	0.058	0.074	0.103	0.070	0.038
Fe^{2+}	0.362	0.387	0.338	0.335	0.378	0.355	0.364	0.353	0.325	0.384	0.364
Mn	0.017	0.020	0.020	0.017	0.021	0.020	0.015	0.013	0.018	0.019	0.018
Mg	0.603	0.577	0.569	0.553	0.556	0.545	0.561	0.569	0.553	0.542	0.569
Ca	0.882	0.869	0.870	0.881	0.901	0.889	0.894	0.902	0.920	0.879	0.907
Na	0.054	0.063	0.068	0.070	0.053	0.060	0.060	0.056	0.059	0.070	0.055
sum	3.999	4.000	4.001	4.001	4.000	4.000	4.000	4.000	4.000	3.999	4.000
mg-number	62	60	63	62	60	61	61	62	63	59	61

Table C3.2: Clinopyroxene

Sample	K144	K144	K144	K144	K144	K144	K144	K166	K166	K166	K166
rock	phn	phn	phn	phn	phn	phn	phn	ben	ben	ben	ben
position	core-	rim-a	rim-b	rim-c	rim-d	core-	rim	core-	inter-	rim	core
	wt. % oxide										
SiO_2	51.15	50.95	51.48	51.53	50.76	50.81	50.43	51.13	50.79	49.72	51.52
TiO_2	0.53	0.77	0.61	0.61	0.81	0.83	0.80	0.55	0.81	0.60	0.70
Al_2O_3	1.55	2.19	1.67	1.55	2.16	2.19	2.04	1.15	1.97	1.01	1.73
FeO*	14.07	13.50	13.27	12.86	13.51	13.55	13.58	15.27	14.10	21.78	14.09
MnO	0.64	0.51	0.52	0.54	0.60	0.46	0.56	0.46	0.54	0.73	0.50
MgO	9.19	9.80	10.13	10.21	9.82	9.51	9.91	8.95	9.51	4.45	10.68
CaO	21.65	22.49	22.65	22.22	22.19	22.13	22.27	22.22	21.24	19.44	19.80
Na_2O	0.84	0.71	0.72	0.66	0.85	0.72	0.70	0.67	0.83	1.74	0.75
sum	99.62	100.92	101.05	100.18	100.70	100.20	100.29	100.40	99.79	99.47	99.77
Fe_2O_3	1.21	2.19	2.34	1.07	2.85	1.28	2.85	1.81	1.33	3.82	0.27
FeO	12.98	11.53	11.17	11.89	10.94	12.40	11.01	13.64	12.90	18.35	13.85
total	99.74	101.14	101.29	100.28	100.98	100.33	100.57	100.58	99.92	99.86	99.80
	formula based on 6 oxygens										
Si	1.963	1.924	1.939	1.957	1.919	1.935	1.916	1.957	1.944	1.969	1.965
Ti	0.015	0.022	0.017	0.017	0.023	0.024	0.023	0.016	0.023	0.018	0.020
Al	0.070	0.098	0.074	0.069	0.096	0.098	0.091	0.052	0.089	0.047	0.078
Fe^{3+}	0.035	0.062	0.066	0.031	0.081	0.037	0.082	0.052	0.038	0.114	0.008
Fe^{2+}	0.417	0.364	0.352	0.378	0.346	0.395	0.350	0.437	0.413	0.607	0.442
Mn	0.021	0.016	0.017	0.017	0.019	0.015	0.018	0.015	0.018	0.024	0.016
Mg	0.526	0.552	0.569	0.578	0.553	0.540	0.561	0.511	0.542	0.263	0.607
Ca	0.890	0.910	0.914	0.904	0.899	0.903	0.907	0.911	0.871	0.825	0.809
Na	0.063	0.052	0.053	0.049	0.062	0.053	0.052	0.050	0.062	0.134	0.055
sum	4.000	4.000	4.001	4.000	3.998	4.000	4.000	4.001	4.000	4.001	4.000
mg-number	56	60	62	60	62	58	62	54	57	30	58

Sample	K166	K166	K166	K168	K168	K168	K168	K168	K168	K168
rock	ben	ben	ben	bas	bas	bas	bas	bas	bas	bas
position	core	core	core	core	grm	core	core-xn	core-xn	core-xn	core-xn
	wt. % oxide									
SiO_2	50.71	49.86	49.87	54.15	43.55	54.55	50.69	51.43	50.09	48.67
TiO_2	0.58	0.84	0.91	0.30	4.21	0.29	1.01	1.01	0.58	1.27
Al_2O_3	1.47	1.11	0.76	0.67	8.66	0.74	3.88	3.89	3.21	4.33
FeO*	14.79	20.92	23.31	2.73	8.00	2.64	9.85	9.81	9.85	9.71
MnO	0.36	0.69	0.70	0.16	0.25	0.19	0.22	0.25	0.46	0.35
MgO	9.32	4.84	3.13	17.16	11.04	17.28	13.14	13.09	13.32	12.69
CaO	21.67	20.67	17.93	24.25	21.34	24.49	21.40	21.05	20.40	20.77
Na_2O	0.87	1.51	2.98	0.26	0.56	0.75	0.85	0.73	0.77	0.62
sum	99.77	100.44	99.59	99.68	97.61	100.93	101.04	101.26	98.68	98.41
Fe_2O_3	2.67	3.73	6.60	0.81	2.23	2.10	3.70	1.49	3.72	3.14
FeO	12.39	17.57	17.37	2.00	5.99	0.75	6.52	8.47	6.51	6.88
total	100.04	100.82	100.25	99.76	97.83	101.14	101.41	101.41	99.06	98.72
	formula based on 6 oxygens									
Si	1.944	1.952	1.971	1.975	1.671	1.961	1.867	1.889	1.886	1.845
Ti	0.017	0.025	0.027	0.008	0.122	0.008	0.028	0.028	0.016	0.036
Al	0.066	0.051	0.035	0.029	0.392	0.031	0.168	0.168	0.143	0.194
Fe^{3+}	0.077	0.110	0.196	0.022	0.064	0.068	0.103	0.041	0.105	0.090
Fe^{2+}	0.397	0.575	0.574	0.061	0.192	0.011	0.201	0.260	0.205	0.218
Mn	0.012	0.023	0.023	0.005	0.008	0.006	0.007	0.008	0.015	0.011
Mg	0.532	0.282	0.184	0.933	0.631	0.926	0.721	0.717	0.748	0.717
Ca	0.890	0.867	0.759	0.948	0.877	0.943	0.845	0.829	0.823	0.844
Na	0.065	0.115	0.228	0.018	0.042	0.052	0.061	0.052	0.056	0.046
sum	4.000	4.000	3.997	3.999	3.999	4.006	4.001	3.992	3.997	4.001
mg-number	57	33	24	94	77	99	78	73	78	77

* Total Fe as FeO; Fe_2O_3 and FeO partitioned using the charge balance equation of Papike *et al*. (1974).

abbreviations: gm = groundmass; xn = xenocryst; ben = benmoreite; other rock names as in Table C3.1.

Appendix C3: Electron Microprobe Mineral Analyses

Table C3.3: Feldspars

Sample	JG025	JG025	JG025	JG025	JG025	JG025	JG025	JG025	JG025	JG025	JG025
rock	CL-encl.	CL-host	CL-host	CL-host	CL-host	CL-encl.	CL-encl.	CL-encl.	CL-encl.	CL-encl.	CL-encl.
position	core	core-	rim-a	rim-b	rim-c	gm	core-	inter-a	inter-b	rim-a	rim-b
	wt.% oxide										
SiO_2	66.78	66.62	70.95	67.35	67.39	60.94	64.88	65.16	65.81	65.36	66.58
TiO_2	0.09	-	-	-	-	-	-	-	-	-	-
Al_2O_3	19.86	18.30	19.13	18.36	18.24	24.87	19.67	19.78	20.08	19.46	19.50
FeO*	0.25	0.41	0.25	0.37	0.76	0.54	0.14	0.13	0.20	0.26	0.28
CaO	1.07	0.14	0.16	0.22	0.19	6.78	1.04	0.89	0.96	0.86	0.95
Na_2O	6.24	7.76	6.28	7.72	7.92	6.67	6.40	6.18	8.00	6.73	6.61
K_2O	6.78	5.82	5.22	5.77	5.89	0.67	6.71	6.95	5.13	6.34	6.71
sum	101.07	99.05	101.99	99.79	100.39	100.47	98.84	99.09	100.18	99.01	100.63
	formula based on 8 oxygens										
Si	2.959	3.005	3.058	3.012	3.007	2.701	2.945	2.949	2.935	2.956	2.966
Ti	0.003	-	-	-	-	-	-	-	-	-	-
Al	1.038	0.973	0.972	0.968	0.959	1.300	1.053	1.055	1.056	1.038	1.024
Fe^{2+}	0.009	0.016	0.009	0.014	0.028	0.020	0.005	0.005	0.008	0.010	0.010
Ca	0.051	0.007	0.008	0.010	0.009	0.322	0.050	0.043	0.046	0.042	0.046
Na	0.536	0.679	0.525	0.670	0.685	0.573	0.563	0.542	0.692	0.591	0.571
K	0.383	0.335	0.287	0.329	0.335	0.038	0.388	0.401	0.292	0.366	0.381
total	4.979	5.015	4.859	5.003	5.023	4.954	5.004	4.995	5.029	5.003	4.998
An %	5.26	0.69	0.98	0.99	0.87	34.51	5.00	4.36	4.47	4.20	4.61
Ab %	55.26	66.50	64.02	66.40	66.57	61.41	56.24	54.97	67.18	59.16	57.21
Or %	39.48	32.81	35.00	32.61	32.56	4.07	38.76	40.67	28.35	36.64	38.18

Sample	JG025	JG025	K55	K55	K55	K55	K55	K55	K55	K55	K55
rock	CL-encl.	CL-encl.	trac	trac	trac	trac	trac	trac	trac	trac	trac
position	core	core	core-	inter-a	inter-b	rim-a	rim-b	rim-c	core	core	core
	wt.% oxide										
SiO_2	66.11	65.78	61.25	62.56	62.37	62.13	63.45	63.04	64.01	65.79	64.86
TiO_2	-	-	0.11	0.10	0.09	-	0.05	0.09	0.10	-	0.10
Al_2O_3	19.73	19.74	22.79	21.74	21.50	21.30	21.53	21.08	20.09	18.61	18.94
FeO*	0.22	0.30	0.77	0.16	0.10	0.24	0.21	0.17	0.28	0.52	0.33
CaO	0.98	0.95	4.58	3.09	3.10	2.99	2.79	2.46	1.90	0.41	0.66
Na_2O	6.47	6.46	9.62	9.19	9.21	9.94	9.15	9.86	8.36	7.26	7.33
K_2O	6.95	6.67	1.23	2.53	2.74	3.06	2.65	3.13	3.81	6.37	5.97
sum	100.46	99.90	100.35	99.37	99.11	99.66	99.83	99.83	98.55	98.96	98.19
	formula based on 8 oxygens										
Si	2.954	2.952	2.743	2.817	2.819	2.809	2.839	2.836	2.901	2.983	2.961
Ti	-	-	0.004	0.003	0.003	-	0.002	0.003	0.003	-	0.003
Al	1.039	1.044	1.203	1.154	1.146	1.135	1.136	1.118	1.074	0.995	1.019
Fe^{2+}	0.008	0.011	0.029	0.006	0.004	0.009	0.008	0.006	0.011	0.020	0.013
Ca	0.047	0.046	0.220	0.149	0.150	0.145	0.134	0.119	0.092	0.020	0.032
Na	0.560	0.562	0.835	0.802	0.807	0.871	0.794	0.860	0.735	0.638	0.649
K	0.396	0.382	0.070	0.145	0.158	0.177	0.151	0.180	0.220	0.369	0.348
total	5.004	4.997	5.104	5.076	5.087	5.146	5.064	5.122	5.036	5.025	5.025
An %	4.69	4.65	19.56	13.59	13.45	12.15	12.42	10.27	8.79	1.95	3.11
Ab %	55.83	56.77	74.22	73.18	72.38	73.01	73.59	74.20	70.20	62.12	63.07
Or %	39.48	38.59	6.22	13.23	14.17	14.84	13.99	15.53	21.01	35.93	33.82

Table C3.3: Feldspars

Sample	K55	K55	K55	K55	K55	K55	K063	K063	K063	K063	K063
rock	trac	trac	trac	trac	trac	trac	CL-host	CL-encl.	CL-encl.	CL-encl.	CL-encl.
position	core	core	core	core	core	gm	core	core	core-	rim	core
	wt.% oxide										
SiO_2	64.09	64.14	63.76	63.73	64.22	65.25	67.76	66.67	66.67	66.92	65.61
TiO_2	0.10	-	0.06	-	-	0.05	-	-	-	-	-
Al_2O_3	18.63	20.41	20.73	21.30	21.02	19.39	18.90	19.50	19.70	19.50	19.95
FeO*	1.50	0.21	0.37	0.28	0.24	0.58	0.27	0.17	-	0.18	-
CaO	1.27	2.18	2.26	2.67	2.58	0.84	0.19	0.74	0.80	0.83	1.28
Na_2O	7.91	7.94	7.57	8.02	7.75	7.62	7.29	7.62	6.79	7.22	6.48
K_2O	4.59	3.51	4.11	3.50	3.63	4.65	5.97	5.28	6.50	5.70	6.39
sum	98.09	98.39	98.86	99.50	99.44	98.38	100.38	99.98	100.46	100.35	99.71
	formula based on 8 oxygens										
Si	2.938	2.902	2.882	2.861	2.880	2.956	3.007	2.971	2.967	2.974	2.945
Ti	0.003	-	0.002	-	-	0.002	-	-	-	-	-
Al	1.007	1.089	1.105	1.127	1.111	1.036	0.989	1.024	1.034	1.022	1.056
Fe^{2+}	0.058	0.008	0.014	0.011	0.009	0.022	0.010	0.006	-	0.007	-
Ca	0.062	0.106	0.109	0.128	0.124	0.041	0.009	0.035	0.038	0.040	0.062
Na	0.703	0.697	0.664	0.698	0.674	0.669	0.627	0.658	0.586	0.622	0.564
K	0.269	0.203	0.237	0.200	0.208	0.269	0.338	0.300	0.369	0.323	0.366
total	5.040	5.005	5.013	5.025	5.006	4.995	4.981	4.996	4.994	4.988	4.992
An %	6.00	10.54	10.79	12.48	12.33	4.19	0.92	3.52	3.83	4.06	6.25
Ab %	67.99	69.28	65.74	68.03	67.00	68.34	64.37	66.26	59.01	63.15	56.85
Or %	26.02	20.18	23.47	19.49	20.68	27.48	34.70	30.21	37.16	32.79	36.90

Sample	K063	K063	K063	K063	K063	K063	K063	K063	K063	K063	K063
rock	CL-encl.	CL-encl.	CL-encl.	CL-encl.	CL-encl.	CL-encl.	CL-encl.	CL-host	CL-host	CL-host	CL-host
position	core-	inter-a	inter-b	rim-a	rim-b	rim-c	rim-d	core	core-	rim-a	rim-b
	wt.% oxide										
SiO_2	65.93	66.10	65.52	65.78	64.19	66.04	66.22	67.37	66.66	67.87	67.64
TiO_2	-	-	-	-	-	-	-	-	-	-	-
Al_2O_3	20.12	19.99	20.28	19.27	19.55	20.05	19.80	18.87	18.44	18.94	18.98
FeO*	-	0.19	0.17	0.28	0.08	0.14	0.14	0.21	0.59	0.24	0.20
CaO	1.61	1.29	1.61	1.40	1.66	1.34	1.13	0.22	0.19	0.17	0.20
Na_2O	6.87	6.61	7.02	7.25	6.35	6.58	6.56	7.18	7.24	7.55	7.23
K_2O	5.89	6.51	5.20	5.74	5.95	6.16	6.67	5.93	5.96	6.24	6.09
sum	100.42	100.69	99.80	99.72	97.78	100.31	100.52	99.78	99.08	101.01	100.34
	formula based on 8 oxygens										
Si	2.937	2.943	2.930	2.955	2.939	2.945	2.953	3.006	3.005	3.001	3.004
Ti	-	-	-	-	-	-	-	-	-	-	-
Al	1.057	1.049	1.069	1.021	1.055	1.054	1.041	0.993	0.980	0.987	0.994
Fe^{2+}	-	0.007	0.006	0.011	0.003	0.005	0.005	0.008	0.022	0.009	0.007
Ca	0.077	0.062	0.077	0.067	0.081	0.064	0.054	0.011	0.009	0.008	0.010
Na	0.593	0.571	0.609	0.632	0.564	0.569	0.567	0.621	0.633	0.647	0.623
K	0.335	0.370	0.297	0.329	0.348	0.351	0.380	0.338	0.343	0.352	0.345
total	4.999	5.002	4.988	5.015	4.990	4.988	5.000	4.977	4.992	5.004	4.983
An %	7.66	6.18	7.83	6.52	8.16	6.50	5.39	1.13	0.91	0.79	1.02
Ab %	59.00	56.93	61.95	61.48	56.80	57.83	56.64	64.02	64.26	64.25	63.70
Or %	33.33	36.89	30.21	32.00	35.05	35.67	37.96	34.85	34.82	34.96	35.28

Table C3.3: Feldspars

Sample	K063	K063	K063	K063	K066	K066	K066	K066	K066	K066	K066
rock	CL-host	CL-host	CL-encl.	CL-host	trac	trac	trac	trac	trac	trac	trac
position	rim-c	rim-d	core	core	core	core-	inter	rim-a	rim-b	core-	inter
	wt.% oxide										
SiO_2	66.01	67.87	68.56	68.35	66.57	66.47	66.30	65.74	65.88	62.66	65.51
TiO_2	-	-	-	-	-	-	-	-	-	-	-
Al_2O_3	18.71	18.64	18.65	17.33	18.92	18.82	19.01	19.43	19.12	21.98	20.02
FeO*	0.28	0.36	0.92	2.20	0.19	0.17	0.16	0.19	-	0.17	0.20
CaO	0.12	0.15	0.34	-	0.40	0.42	0.71	0.63	0.69	3.56	1.45
Na_2O	7.23	7.09	5.98	6.42	6.86	6.81	6.53	7.55	6.70	7.35	7.07
K_2O	6.31	6.33	5.46	7.31	6.44	6.72	6.52	5.53	5.80	2.67	4.71
sum	98.66	100.44	99.91	101.61	99.38	99.41	99.23	99.07	98.19	98.39	98.96
	formula based on 8 oxygens										
Si	2.992	3.015	3.038	3.037	2.993	2.992	2.986	2.963	2.986	2.832	2.944
Ti	-	-	-	-	-	-	-	-	-	-	-
Al	1.000	0.976	0.974	0.908	1.003	0.999	1.010	1.032	1.022	1.171	1.061
Fe^{2+}	0.011	0.013	0.034	0.082	0.007	0.006	0.006	0.007	-	0.006	0.008
Ca	0.006	0.007	0.016	-	0.019	0.020	0.034	0.030	0.034	0.172	0.070
Na	0.635	0.611	0.514	0.553	0.598	0.594	0.570	0.660	0.589	0.644	0.616
K	0.365	0.359	0.309	0.414	0.369	0.386	0.375	0.318	0.335	0.154	0.270
total	5.009	4.981	4.885	4.994	4.989	4.997	4.981	5.010	4.966	4.979	4.969
An %	0.60	0.72	1.91	-	1.93	2.00	3.47	2.98	3.55	17.73	7.32
Ab %	63.12	62.54	61.26	57.19	60.65	59.40	58.22	65.48	61.48	66.39	64.44
Or %	36.28	36.75	36.83	42.81	37.42	38.60	38.30	31.55	34.97	15.88	28.24

Sample	K066	K066	K066	K093	K093	K093	K093	K100	K100	K100	K100
rock	trac	trac	trac	mug	mug	mug	mug	trac	trac	trac	trac
position	rim-a	rim-b	rim-c	core	core	core	rim	core-	inter	rim-a	rim-b
	wt.% oxide										
SiO_2	66.10	64.46	66.31	56.19	56.26	56.15	55.51	63.61	65.12	64.54	66.86
TiO_2	-	-	-	-	-	-	-	-	-	-	-
Al_2O_3	19.41	21.01	19.10	27.13	27.16	26.52	26.36	20.26	20.46	20.47	18.81
FeO*	-	0.21	-	0.30	-	0.35	0.26	0.22	0.25	0.20	0.49
CaO	0.63	2.59	0.84	9.51	9.81	8.91	9.46	2.01	1.83	1.88	0.42
Na_2O	7.01	7.53	7.27	5.82	6.15	6.30	5.71	7.07	7.29	7.34	7.18
K_2O	6.44	3.09	5.93	0.35	0.30	0.40	0.41	5.61	4.50	4.18	6.51
sum	99.59	98.89	99.45	99.30	99.68	98.63	97.71	98.78	99.45	98.61	100.27
	formula based on 8 oxygens										
Si	2.969	2.892	2.978	2.545	2.540	2.561	2.555	2.894	2.918	2.913	2.989
Ti	-	-	-	-	-	-	-	-	-	-	-
Al	1.028	1.111	1.011	1.448	1.445	1.426	1.431	1.087	1.081	1.089	0.991
Fe^{2+}	-	0.008	-	0.011	-	0.013	0.010	0.008	0.009	0.008	0.018
Ca	0.030	0.125	0.040	0.461	0.475	0.435	0.467	0.098	0.088	0.091	0.020
Na	0.611	0.655	0.633	0.511	0.538	0.557	0.510	0.624	0.633	0.642	0.622
K	0.369	0.177	0.340	0.020	0.017	0.023	0.024	0.326	0.257	0.241	0.371
total	5.007	4.968	5.002	4.996	5.015	5.015	4.997	5.037	4.986	4.984	5.011
An %	2.97	13.06	3.95	46.47	46.12	42.86	46.65	9.35	9.00	9.34	1.97
Ab %	60.50	68.44	62.49	51.51	52.23	54.88	50.95	59.54	64.72	65.91	61.40
Or %	36.53	18.50	33.56	2.02	1.65	2.27	2.40	31.11	26.28	24.74	36.62

Table C3.3: Feldspars

Sample	K108	K108	K108	K108	K108	K108	K108	K108	K108	K114	K114
rock	tphn	tphn	tphn	tphn	tphn	tphn	tphn	tphn	tphn	tphn-phn	tphn-phn
position	core	core	core	core-	inter	rim-a	rim-b	core	core	core	core-
	wt.% oxide										
SiO_2	65.50	63.85	63.01	63.56	63.36	63.80	63.60	64.18	66.68	65.97	62.61
TiO_2	0.20	0.12	-	-	0.11	0.14	-	0.11	-	-	-
Al_2O_3	19.76	21.52	21.08	20.79	21.12	21.36	21.05	21.43	22.00	18.91	22.16
FeO*	0.80	0.21	0.21	0.17	0.26	0.25	0.21	0.24	0.25	0.18	0.19
CaO	1.17	3.13	2.69	3.00	2.93	2.88	2.83	2.90	2.90	0.43	3.91
Na_2O	7.69	7.92	8.01	7.84	8.07	7.93	8.18	8.09	8.03	6.22	7.00
K_2O	4.49	2.41	2.68	2.60	2.55	2.46	2.52	2.61	2.52	7.47	2.45
sum	99.61	99.16	97.68	97.96	98.40	98.82	98.39	99.56	102.38	99.18	98.32
	formula based on 8 oxygens										
Si	2.936	2.859	2.867	2.881	2.863	2.865	2.872	2.865	2.884	2.985	2.828
Ti	0.007	0.004	-	-	0.004	0.005	-	0.004	-	-	-
Al	1.044	1.136	1.131	1.111	1.125	1.131	1.121	1.128	1.122	1.009	1.180
Fe^{2+}	0.030	0.008	0.008	0.006	0.010	0.009	0.008	0.009	0.009	0.007	0.007
Ca	0.056	0.150	0.131	0.146	0.142	0.139	0.137	0.139	0.134	0.021	0.189
Na	0.668	0.688	0.707	0.689	0.707	0.691	0.716	0.700	0.673	0.546	0.613
K	0.257	0.138	0.156	0.150	0.147	0.141	0.145	0.149	0.139	0.431	0.141
total	4.998	4.983	5.000	4.983	4.998	4.981	4.999	4.994	4.961	4.999	4.958
An %	5.71	15.37	13.18	14.82	14.26	14.32	13.73	14.07	14.16	2.10	20.04
Ab %	68.09	70.49	71.13	69.95	70.98	71.16	71.74	70.85	71.14	54.71	65.01
Or %	26.20	14.14	15.69	15.23	14.76	14.52	14.53	15.08	14.69	43.19	14.95

Sample	K114	K114	K114	K114	K114	K114	K115	K115	K115	K115	K115
rock	tphn-phn	tphn-phn	tphn-phn	tphn-phn	tphn-phn	tphn-phn	phn	phn	phn	phn	phn
position	rim	core	core	core	core	core	core-	rim	core	core-	rim-a
	wt.% oxide										
SiO_2	62.92	62.82	61.36	62.65	65.84	61.67	63.08	64.24	62.69	63.90	62.80
TiO_2	-	-	-	-	-	-	-	-	-	-	-
Al_2O_3	22.12	22.22	23.18	22.34	19.21	22.69	21.70	21.06	22.26	20.72	21.86
FeO*	0.17	0.19	0.21	0.23	0.18	0.32	0.15	0.19	0.24	0.18	0.21
CaO	3.60	3.94	4.99	4.01	0.37	3.81	3.09	2.54	3.74	2.41	3.39
Na_2O	7.83	7.37	7.26	7.59	6.24	8.28	7.72	7.97	7.94	7.64	7.85
K_2O	2.92	2.62	1.69	2.70	7.65	1.39	2.87	3.44	2.28	3.69	2.74
sum	99.56	99.16	98.69	99.52	99.49	98.16	98.61	99.44	99.15	98.54	98.85
	formula based on 8 oxygens										
Si	2.818	2.821	2.768	2.810	2.974	2.792	2.846	2.879	2.816	2.889	2.832
Ti	-	-	-	-	-	-	-	-	-	-	-
Al	1.168	1.176	1.233	1.181	1.023	1.211	1.154	1.113	1.179	1.104	1.162
Fe^{2+}	0.006	0.007	0.008	0.009	0.007	0.012	0.006	0.007	0.009	0.007	0.008
Ca	0.173	0.190	0.241	0.193	0.018	0.185	0.149	0.122	0.180	0.117	0.164
Na	0.680	0.642	0.635	0.660	0.546	0.727	0.675	0.692	0.692	0.670	0.686
K	0.167	0.150	0.097	0.155	0.441	0.080	0.165	0.197	0.131	0.213	0.158
total	5.012	4.986	4.982	5.008	5.009	5.007	4.995	5.010	5.007	5.000	5.010
An %	16.96	19.35	24.77	19.15	1.79	18.65	15.07	12.07	17.95	11.70	16.27
Ab %	66.67	65.38	65.26	65.48	54.33	73.29	68.25	68.45	68.99	67.00	68.06
Or %	16.37	15.27	9.97	15.38	43.88	8.06	16.68	19.49	13.06	21.30	15.67

Table C3.3: Feldspars

Sample	K115	K120	K120	K120	K120	K120	K120	K120	K120	K120	K122
rock	phn	phn	phn	phn	phn	phn	phn	phn	phn	phn	phn-c1
position	rim-b	core-	inter	rim	core-	rim	core-	rim	core	rim	core
	wt.% oxide										
SiO_2	63.62	63.94	63.71	62.44	63.77	62.77	63.18	63.49	63.37	63.53	63.81
TiO_2	-	-	-	-	-	-	-	-	-	-	-
Al_2O_3	20.85	21.53	21.83	22.18	21.73	21.55	21.84	22.20	21.17	21.72	21.07
FeO*	0.17	-	0.13	0.15	-	0.18	0.17	-	-	-	0.18
CaO	2.63	3.15	3.17	3.89	3.28	3.15	3.28	3.49	2.98	3.26	2.48
Na_2O	7.51	7.77	7.76	7.58	7.82	7.72	7.70	7.89	7.60	7.48	8.16
K_2O	3.46	2.94	2.87	2.08	2.88	2.76	2.68	2.58	3.24	2.90	2.87
sum	98.24	99.33	99.47	98.32	99.48	98.13	98.85	99.65	98.36	98.89	98.57
	formula based on 8 oxygens										
Si	2.883	2.862	2.849	2.821	2.852	2.846	2.843	2.833	2.867	2.854	2.877
Ti	-	-	-	-	-	-	-	-	-	-	-
Al	1.114	1.136	1.151	1.181	1.146	1.152	1.158	1.168	1.129	1.150	1.120
Fe^{2+}	0.006	-	0.005	0.006	-	0.007	0.006	-	-	-	0.007
Ca	0.128	0.151	0.152	0.188	0.157	0.153	0.158	0.167	0.144	0.157	0.120
Na	0.660	0.674	0.673	0.664	0.678	0.679	0.672	0.683	0.667	0.652	0.713
K	0.200	0.168	0.164	0.120	0.164	0.160	0.154	0.147	0.187	0.166	0.165
total	4.991	4.991	4.994	4.980	4.997	4.997	4.991	4.998	4.994	4.979	5.002
An %	12.96	15.21	15.37	19.34	15.72	15.42	16.06	16.75	14.43	16.10	12.02
Ab %	66.80	67.88	68.05	68.31	67.87	68.45	68.29	68.51	66.83	66.87	71.44
Or %	20.24	16.92	16.58	12.35	16.42	16.13	15.65	14.74	18.74	17.03	16.53

Sample	K122	K122	K122	K122	K122	K122	K122	K122	K122	K122	K122
rock	phn-c1	phn-c1	phn-c1	phn-c1	phn-c1	phn-c1	phn-c1	phn-c1	phn-c2	phn-c2	phn-c2
position	inter	core	core	core	rim	rim	inter	core	rim	rim	inter
	wt.% oxide										
SiO_2	64.11	64.12	63.70	64.28	64.90	64.90	63.03	63.26	64.56	63.97	64.38
TiO_2	-	-	-	-	-	-	-	-	-	-	-
Al_2O_3	21.09	20.96	21.61	20.71	20.62	20.86	21.22	21.23	21.18	21.56	21.12
FeO*	0.17	0.21	0.17	0.25	0.21	-	0.23	0.24	0.13	0.14	0.18
CaO	2.66	2.39	2.88	2.30	1.90	2.35	2.79	2.76	2.60	3.06	2.74
Na_2O	8.00	8.07	8.30	8.06	8.04	7.98	7.82	7.99	8.26	8.13	8.09
K_2O	2.69	3.00	2.61	3.22	3.46	3.01	2.64	2.67	2.82	2.52	2.95
sum	98.72	98.75	99.27	98.82	99.13	99.10	97.73	98.15	99.55	99.38	99.46
	formula based on 8 oxygens										
Si	2.882	2.885	2.854	2.893	2.909	2.903	2.864	2.865	2.881	2.860	2.879
Ti	-	-	-	-	-	-	-	-	-	-	-
Al	1.118	1.112	1.141	1.099	1.090	1.100	1.137	1.133	1.114	1.136	1.113
Fe^{2+}	0.006	0.008	0.006	0.009	0.008	-	0.009	0.009	0.005	0.005	0.007
Ca	0.128	0.115	0.138	0.111	0.091	0.113	0.136	0.134	0.124	0.147	0.131
Na	0.697	0.704	0.721	0.703	0.699	0.692	0.689	0.702	0.715	0.705	0.701
K	0.154	0.172	0.149	0.185	0.198	0.172	0.153	0.154	0.161	0.144	0.168
total	4.985	4.996	5.009	5.000	4.995	4.980	4.988	4.997	5.000	4.997	4.999
An %	13.07	11.60	13.69	11.11	9.21	11.57	13.91	13.54	12.40	14.76	13.10
Ab %	71.20	71.04	71.53	70.37	70.75	70.83	70.45	70.91	71.50	70.78	70.10
Or %	15.73	17.36	14.78	18.52	20.04	17.60	15.64	15.56	16.10	14.46	16.80

Table C3.3: Feldspars

Sample	K122	K122	K122	K122	K122	K122	K122	K122	K122	K122	K122
rock	phn-c2	phn-c2	phn-c2	phn-c2	phn-c2	phn-c2	phn-c2	phn-c2	phn-c2	phn-c2	phn-c2
position	inter	core	core	rim	rim	rim	inter	core	core	core	inter
	wt.% oxide										
SiO_2	63.80	64.68	64.18	64.43	64.29	64.14	64.55	64.92	64.85	63.95	63.70
TiO_2	-	-	-	-	-	-	-	-	-	-	-
Al_2O_3	21.76	21.15	21.41	21.20	21.04	21.27	20.94	21.09	21.25	21.60	21.45
FeO*	0.22	0.22	0.24	0.38	0.23	0.17	0.21	0.25	0.22	0.18	0.17
CaO	3.14	2.80	2.87	2.78	2.43	2.72	2.45	2.50	2.61	3.08	2.96
Na_2O	8.07	7.96	7.95	7.96	8.16	8.10	7.87	8.03	8.04	7.97	8.09
K_2O	2.45	2.81	2.75	2.89	2.93	2.85	2.91	2.85	2.85	2.53	2.60
sum	99.44	99.62	99.40	99.64	99.08	99.25	98.93	99.64	99.82	99.31	98.97
	formula based on 8 oxygens										
Si	2.851	2.883	2.869	2.876	2.884	2.873	2.894	2.891	2.884	2.860	2.861
Ti	-	-	-	-	-	-	-	-	-	-	-
Al	1.146	1.112	1.128	1.116	1.113	1.123	1.107	1.107	1.114	1.139	1.136
Fe^{2+}	0.008	0.008	0.009	0.014	0.009	0.006	0.008	0.009	0.008	0.007	0.006
Ca	0.150	0.134	0.137	0.133	0.117	0.131	0.118	0.119	0.124	0.148	0.142
Na	0.699	0.688	0.689	0.689	0.710	0.703	0.684	0.693	0.693	0.691	0.704
K	0.140	0.160	0.157	0.165	0.168	0.163	0.167	0.162	0.162	0.144	0.149
total	4.994	4.985	4.989	4.993	5.001	4.999	4.978	4.981	4.985	4.989	4.998
An %	15.17	13.65	13.94	13.48	11.76	13.14	12.18	12.22	12.67	15.06	14.27
Ab %	70.68	70.06	70.09	69.81	71.36	70.51	70.59	71.15	70.79	70.30	70.75
Or %	14.16	16.29	15.97	16.72	16.88	16.35	17.23	16.63	16.55	14.65	14.97

Sample	K122	K122	K122	K122	K141	K141	K141	K141	K141	K141	K141
rock	phn-c2	phn-c2	phn-c2	phn-c2	phn	phn	phn	phn	phn	phn	phn
position	rim	rim	core	core	core	core	core-	rim-a	rim-b	core	core
	wt.% oxide										
SiO_2	64.37	64.50	64.51	64.07	64.20	65.47	64.91	64.90	65.22	63.71	64.18
TiO_2	-	-	-	-	-	-	-	-	-	-	-
Al_2O_3	21.03	21.33	21.43	20.73	21.45	20.80	20.88	20.75	20.62	21.83	21.59
FeO*	0.21	0.15	0.25	0.22	0.20	-	0.17	0.18	-	0.15	0.22
CaO	2.58	2.85	2.93	2.50	3.09	2.02	2.14	2.02	2.07	3.13	3.12
Na_2O	7.73	7.97	8.04	7.90	7.41	7.50	7.46	7.19	7.11	7.80	7.80
K_2O	2.83	2.66	2.66	2.88	3.11	4.25	4.20	4.41	4.27	2.89	2.88
sum	98.75	99.46	99.82	98.30	99.46	100.04	99.76	99.45	99.29	99.51	99.79
	formula based on 8 oxygens										
Si	2.890	2.877	2.871	2.893	2.870	2.912	2.900	2.907	2.919	2.849	2.861
Ti	-	-	-	-	-	-	-	-	-	-	-
Al	1.113	1.122	1.124	1.104	1.130	1.091	1.100	1.096	1.088	1.151	1.135
Fe^{2+}	0.008	0.006	0.009	0.008	0.007	-	0.006	0.007	-	0.006	0.008
Ca	0.124	0.136	0.140	0.121	0.148	0.096	0.102	0.097	0.099	0.150	0.149
Na	0.673	0.689	0.694	0.692	0.642	0.647	0.646	0.624	0.617	0.676	0.674
K	0.162	0.151	0.151	0.166	0.177	0.241	0.239	0.252	0.244	0.165	0.164
total	4.970	4.981	4.989	4.984	4.974	4.987	4.993	4.983	4.967	4.997	4.991
An %	12.93	13.93	14.21	12.36	15.31	9.76	10.33	9.97	10.31	15.14	15.10
Ab %	70.18	70.59	70.46	70.68	66.39	65.75	65.45	64.13	64.27	68.21	68.29
Or %	16.89	15.47	15.33	16.96	18.30	24.49	24.21	25.90	25.42	16.65	16.62

Table C3.3: Feldspars

Sample	K141	K141	K141	K144	K144	K144	K144	K144	K144	K144	K144
rock	phn	phn	phn	phn	phn	phn	phn	phn	phn	phn	phn
position	core	core	core	core	core-	rim-a	rim-b	rim-c	rim-d	core	core-
	wt.% oxide										
SiO_2	64.21	64.41	64.21	63.26	63.32	62.59	63.28	63.25	65.32	63.03	64.05
TiO_2	-	-	-	-	-	-	-	-	-	-	-
Al_2O_3	21.98	21.44	21.77	22.11	22.18	22.72	21.99	22.07	20.69	21.25	21.62
FeO*	0.18	0.17	-	0.21	0.23	0.26	0.19	0.13	-	0.17	-
CaO	3.48	3.13	3.32	3.80	3.68	4.25	3.50	3.47	2.12	2.93	3.17
Na_2O	7.48	7.89	7.83	7.57	7.72	7.73	7.66	7.58	7.53	7.65	7.67
K_2O	2.79	2.85	2.68	2.50	2.56	1.96	2.73	2.58	3.86	3.04	2.99
sum	100.12	99.89	99.81	99.45	99.69	99.51	99.35	99.08	99.52	98.07	99.50
	formula based on 8 oxygens										
Si	2.851	2.867	2.857	2.830	2.828	2.799	2.836	2.837	2.915	2.861	2.861
Ti	-	-	-	-	-	-	-	-	-	-	-
Al	1.150	1.125	1.142	1.166	1.168	1.198	1.162	1.167	1.089	1.137	1.139
Fe^{2+}	0.007	0.006	-	0.008	0.009	0.010	0.007	0.005	-	0.006	-
Ca	0.166	0.149	0.158	0.182	0.176	0.204	0.168	0.167	0.101	0.142	0.152
Na	0.644	0.681	0.676	0.657	0.669	0.670	0.666	0.659	0.652	0.673	0.664
K	0.158	0.162	0.152	0.143	0.146	0.112	0.156	0.148	0.220	0.176	0.170
total	4.976	4.990	4.985	4.986	4.996	4.993	4.995	4.983	4.977	4.995	4.986
An %	17.15	15.02	16.02	18.53	17.76	20.69	16.97	17.15	10.38	14.33	15.42
Ab %	66.53	68.65	68.56	66.90	67.51	67.95	67.27	67.66	67.01	67.91	67.34
Or %	16.32	16.33	15.42	14.56	14.73	11.36	15.76	15.20	22.61	17.76	17.24

Sample	K144	K144	K144	K149	K149	K149	K149	K149	K149	K149	K149
rock	phn	phn	phn	phn	phn	phn	phn	phn	phn	phn	phn
position	rim	core	core	core	core-	rim-a	rim-b	rim-c	rim-d	core	core
	wt.% oxide										
SiO_2	63.94	64.43	62.83	63.54	63.53	63.76	63.00	63.84	62.53	64.51	63.30
TiO_2	-	-	-	-	-	-	-	-	-	-	-
Al_2O_3	22.02	21.26	23.39	21.47	22.18	21.79	21.81	21.82	22.28	22.43	21.05
FeO*	0.13	-	0.19	0.16	0.17	-	0.15	0.17	0.17	0.24	0.14
CaO	3.53	2.84	4.93	2.94	3.51	3.35	3.31	3.03	4.18	3.78	3.28
Na_2O	7.68	7.44	7.90	7.23	7.78	7.30	7.38	7.24	7.25	7.33	7.17
K_2O	2.67	3.40	1.73	3.73	3.13	3.59	3.42	3.51	2.85	3.15	3.50
sum	99.97	99.37	100.97	99.07	100.30	99.79	99.07	99.61	99.26	101.44	98.44
	formula based on 8 oxygens										
Si	2.844	2.881	2.774	2.860	2.828	2.849	2.838	2.855	2.811	2.835	2.867
Ti	-	-	-	-	-	-	-	-	-	-	-
Al	1.155	1.121	1.217	1.139	1.164	1.148	1.158	1.150	1.181	1.162	1.124
Fe^{2+}	0.005	-	0.007	0.006	0.006	-	0.006	0.006	0.006	0.009	0.005
Ca	0.168	0.136	0.233	0.142	0.167	0.160	0.160	0.145	0.201	0.178	0.159
Na	0.662	0.645	0.676	0.631	0.671	0.633	0.645	0.628	0.632	0.625	0.630
K	0.152	0.194	0.097	0.214	0.178	0.205	0.197	0.200	0.164	0.177	0.202
total	4.986	4.977	5.004	4.992	5.014	4.995	5.004	4.984	4.995	4.986	4.987
An %	17.11	13.95	23.16	14.39	16.44	16.03	15.97	14.90	20.16	18.16	16.04
Ab %	67.41	66.15	67.20	63.93	66.04	63.43	64.37	64.54	63.39	63.78	63.57
Or %	15.48	19.90	9.64	21.68	17.52	20.54	19.66	20.55	16.45	18.06	20.38

Table C3.3: Feldspars

Sample	K166	K166	K166	K166	K166	K166	K168	K168	K168	K168	K168
rock	ben	ben	ben	ben	ben	ben	bas	bas	bas	bas	bas
position	core-	rim	core	core-	inter	rim	gm	core	core	core	core
	wt.% oxide										
SiO_2	65.03	64.55	64.64	64.95	65.90	66.78	53.89	53.63	53.68	54.62	53.10
TiO_2	-	-	-	-	-	-	0.16	0.11	-	0.08	0.09
Al_2O_3	20.42	19.88	20.58	20.73	20.02	18.52	27.64	27.95	27.87	29.04	29.73
FeO*	0.18	0.19	0.17	-	0.19	0.13	0.63	0.13	0.22	0.22	0.20
CaO	1.90	1.58	2.14	1.80	1.38	0.15	9.76	10.83	10.70	11.14	11.23
Na_2O	7.52	7.39	7.47	7.60	7.28	5.64	5.45	5.35	5.38	6.39	6.45
K_2O	4.33	4.64	3.74	4.23	5.24	8.31	0.43	0.16	0.21	0.26	0.26
sum	99.38	98.23	98.74	99.31	100.01	99.53	97.96	98.16	98.06	101.75	101.06
	formula based on 8 oxygens										
Si	2.916	2.930	2.909	2.910	2.941	3.012	2.486	2.468	2.473	2.438	2.393
Ti	-	-	-	-	-	-	0.006	0.004	-	0.003	0.003
Al	1.079	1.064	1.092	1.095	1.053	0.985	1.503	1.516	1.514	1.528	1.579
Fe^{2+}	0.007	0.007	0.006	-	0.007	0.005	0.024	0.005	0.008	0.008	0.008
Ca	0.091	0.077	0.103	0.086	0.066	0.007	0.482	0.534	0.528	0.533	0.542
Na	0.654	0.650	0.652	0.660	0.630	0.493	0.487	0.477	0.481	0.553	0.564
K	0.248	0.269	0.215	0.242	0.298	0.478	0.025	0.009	0.012	0.015	0.015
total	4.995	4.997	4.977	4.993	4.995	4.980	5.013	5.013	5.016	5.078	5.104
An %	9.16	7.73	10.62	8.70	6.64	0.72	48.49	52.35	51.71	48.41	48.35
Ab %	65.86	65.26	67.22	66.80	63.38	50.41	48.99	46.76	47.11	50.23	50.31
Or %	24.97	27.01	22.16	24.49	29.98	48.88	2.52	0.88	1.18	1.36	1.34

Sample	K168	K168	K168	K168	K168	K168	K168
rock	bas	bas	bas	bas	bas	bas	bas
position	core	core-	rim	core	core	core	core
	wt.% oxide						
SiO_2	52.28	52.83	53.81	53.79	49.75	54.60	53.58
TiO_2	0.17	0.09	0.09	0.10	1.31	-	0.11
Al_2O_3	30.19	29.06	29.37	29.73	28.13	29.42	28.30
FeO*	0.53	0.27	0.16	0.16	3.54	0.18	0.15
CaO	12.23	11.23	11.05	11.20	10.21	11.15	10.55
Na_2O	5.56	6.39	6.25	6.06	6.13	6.22	5.36
K_2O	0.35	0.25	0.23	0.20	0.36	0.31	0.18
sum	101.31	100.12	100.96	101.24	99.43	101.88	98.23
	formula based on 8 oxygens						
Si	2.358	2.404	2.419	2.412	2.324	2.433	2.462
Ti	0.006	0.003	0.003	0.003	0.046	-	0.004
Al	1.605	1.559	1.556	1.571	1.549	1.545	1.533
Fe^{2+}	0.020	0.010	0.006	0.006	0.138	0.007	0.006
Ca	0.591	0.548	0.532	0.538	0.511	0.532	0.519
Na	0.486	0.564	0.544	0.527	0.555	0.537	0.478
K	0.020	0.015	0.013	0.011	0.021	0.018	0.011
total	5.086	5.103	5.073	5.068	5.144	5.072	5.013
An %	53.87	48.62	48.85	50.00	47.01	48.94	51.49
Ab %	44.30	50.04	49.95	48.98	51.06	49.40	47.42
Or %	1.82	1.33	1.19	1.02	1.93	1.66	1.09

* Total Fe as FeO.

Abbreviations as in previous tables.

Analyses of sample K122 traverse two large (> 4cm) anorthoclase phenocrysts (c1 & c2).

Dashes mean not determined or not detected.

Appendix C3: Electron Microprobe Mineral Analyses

Table C3.4: Spinel

Sample	K63	K63	K93	K108	K108	K114	K115	K115	K115	K120
rock	CL-host	CL-encl.	mug	tphn	tphn	tphn-phn	phn	phn	phn	phn
position	core	core	core	core	core	core	core	core	core	core
	wt.% oxide									
SiO_2	0.18	0.19	0.16	-	0.14	-	0.13	0.12	-	0.18
TiO_2	20.10	23.68	26.61	26.37	26.35	24.60	22.89	22.51	23.16	24.84
Al_2O_3	0.15	1.13	1.67	1.61	1.72	1.98	2.03	2.14	2.01	2.01
FeO*	75.32	71.42	66.79	67.32	67.76	68.36	69.81	69.90	69.94	67.37
MnO	0.88	1.18	0.72	1.12	1.09	0.96	1.29	1.21	1.30	1.31
MgO	-	0.58	1.54	1.38	1.77	1.15	1.43	1.67	1.42	1.62
CaO	0.09	-	-	-	-	-	-	-	-	-
sum	96.72	98.18	97.49	97.80	98.83	97.05	97.58	97.55	97.83	97.33
Fe_2O_3	29.38	22.08	15.44	16.56	17.10	19.07	22.79	23.58	22.76	18.56
FeO	48.89	51.55	52.90	52.42	52.37	51.20	49.30	48.68	49.46	50.67
total	99.67	100.39	99.04	99.46	100.54	98.96	99.86	99.91	100.11	99.19
	formula based on 4 oxygens									
Si	0.007	0.007	0.006	-	0.005	-	0.005	0.004	-	0.007
Ti	0.572	0.660	0.742	0.734	0.723	0.689	0.635	0.623	0.641	0.691
Al	0.007	0.049	0.073	0.070	0.074	0.087	0.088	0.093	0.087	0.088
Fe^{3+}	0.836	0.616	0.431	0.461	0.470	0.535	0.633	0.653	0.630	0.517
Fe^{2+}	1.547	1.598	1.640	1.623	1.598	1.595	1.521	1.498	1.523	1.567
Mn	0.028	0.037	0.023	0.035	0.034	0.030	0.040	0.038	0.041	0.041
Mg	-	0.032	0.085	0.076	0.096	0.064	0.079	0.092	0.078	0.089
Ca	0.003	-	-	-	-	-	-	-	-	-
total	3.000	2.999	3.000	2.999	3.000	3.000	3.001	3.001	3.000	3.000
Usp %	57	68	77	75	74	71	65	64	65	71

Sample	K120	K120	K122	K122	K144	K144	K144	K144	K144	K144
rock	phn	phn	phn	phn	phn	phn	phn	phn	phn	phn
position	core	core	core	core	core	core	core	core	core	core
	wt.% oxide									
SiO_2	0.17	-	0.24	0.19	-	0.17	-	0.21	0.17	0.12
TiO_2	25.17	24.81	24.83	25.11	22.38	22.10	23.15	21.35	23.96	23.11
Al_2O_3	2.12	2.35	1.92	1.59	2.17	2.12	2.10	1.67	2.06	2.05
FeO*	67.19	68.58	68.81	69.22	70.35	71.19	69.16	66.95	69.97	68.85
MnO	1.06	1.63	1.32	1.34	1.22	1.37	1.33	1.24	1.20	1.17
MgO	1.58	1.63	1.53	1.37	1.43	1.56	1.55	1.32	1.35	1.37
CaO	0.22	-	-	-	-	0.07	-	3.44	-	1.07
sum	97.51	99.00	98.65	98.82	97.55	98.58	97.29	96.18	98.71	97.74
Fe_2O_3	17.92	19.90	19.48	19.48	23.97	25.05	22.34	25.85	21.22	22.64
FeO	51.07	50.67	51.28	51.69	48.78	48.65	49.06	43.69	50.87	48.48
total	99.31	100.99	100.60	100.77	99.95	101.09	99.53	98.77	100.83	100.01
	formula based on 4 oxygens									
Si	0.006	-	0.009	0.007	-	0.006	-	0.008	0.006	0.004
Ti	0.699	0.678	0.682	0.691	0.620	0.605	0.644	0.595	0.658	0.638
Al	0.092	0.101	0.083	0.069	0.094	0.091	0.092	0.073	0.089	0.089
Fe^{3+}	0.498	0.544	0.536	0.536	0.665	0.686	0.621	0.721	0.583	0.626
Fe^{2+}	1.576	1.539	1.567	1.581	1.504	1.482	1.517	1.355	1.554	1.489
Mn	0.033	0.050	0.041	0.042	0.038	0.042	0.042	0.039	0.037	0.036
Mg	0.087	0.088	0.083	0.075	0.079	0.085	0.085	0.073	0.073	0.075
Ca	0.009	-	-	-	-	0.003	-	0.137	-	0.042
total	3.000	3.000	3.001	3.001	3.000	3.000	3.001	3.001	3.000	2.999
Usp %	73	70	71	71	64	62	66	58	68	65

Table C3.4: Spinel

Sample	K149	K149	K168	K168	K168	K168
rock	phn	phn	bas	bas	bas	bas
position	core	core	core	core	core	core
	wt.% oxide					
SiO_2	0.52	-	0.15	0.15	0.10	0.12
TiO_2	24.59	24.89	0.85	0.79	1.04	0.91
Al_2O_3	2.58	1.89	57.88	58.54	57.80	58.26
FeO*	68.43	69.52	22.14	22.43	22.66	21.90
MnO	1.03	1.03	0.23	0.39	0.21	0.18
MgO	1.82	1.91	16.66	16.86	16.63	17.04
CaO	-	-	-	-	-	-
sum	98.97	99.24	97.90	99.15	98.44	98.41
Fe_2O_3	18.85	20.65	6.94	7.28	7.17	7.01
FeO	51.47	50.94	15.89	15.88	16.21	15.59
total	100.86	101.31	98.59	99.88	99.16	99.11
	formula based on 4 oxygens					
Si	0.019	-	0.004	0.004	0.003	0.003
Ti	0.670	0.678	0.017	0.016	0.021	0.018
Al	0.110	0.081	1.819	1.817	1.810	1.818
Fe^{3+}	0.514	0.563	0.139	0.144	0.143	0.140
Fe^{2+}	1.558	1.543	0.354	0.350	0.360	0.345
Mn	0.032	0.032	0.005	0.009	0.005	0.004
Mg	0.098	0.103	0.662	0.661	0.658	0.672
Ca	-	-	-	-	-	-
total	3.001	3.000	3.000	3.000	3.000	3.000
Usp %	71	69	2	2	2	2

* Total Fe as FeO.

Cation proportions of Fe^{2+} and Fe^{3+} estimated using the procedures of Stromer (1983).

Percent ulvospinel (Usp) calculated using the model of Carmicaheal (1976).

Dashes mean not detected or not determined.

Appendix C3: Electron Microprobe Mineral Analyses

Table C3.5: Amphibole

Sample	K063	K063	K063	K063	K063	K063	K063	K063	K063	K100
rock	CL-host	CL-host	CL-host	CL-host	CL-host	CL-host	CL-host	CL-host	CL-host	trac
	wt. % oxide									
SiO_2	50.20	49.98	48.67	49.10	50.75	49.27	49.49	49.02	49.64	49.22	52.01
Al_2O_3	0.23	0.23	0.60	0.62	0.25	0.43	0.60	0.65	0.44	0.67	0.11
TiO_2	0.01	0.18	2.99	3.91	0.47	2.52	3.46	3.27	2.94	2.73	-
MgO	0.30	0.54	1.31	1.34	0.96	0.60	1.36	1.78	1.17	1.72	0.17
FeO*	35.31	34.86	33.72	31.64	33.11	33.14	31.55	31.55	32.39	31.81	31.17
MnO	1.40	1.19	0.92	0.95	1.17	0.88	0.74	0.80	0.86	0.78	1.18
CaO	1.07	1.92	3.97	3.73	2.96	3.35	4.23	4.02	3.81	4.43	2.85
Na_2O	8.07	6.25	6.33	6.70	6.94	6.52	6.35	6.27	6.32	6.02	10.77
K_2O	1.04	1.35	1.25	1.33	1.30	1.34	1.30	1.26	1.39	1.22	0.01
sum	97.63	96.50	99.76	99.32	97.91	98.05	99.08	98.62	98.96	98.60	98.27
FeO	28.55	26.85									
Fe_2O_3	7.51	8.91									
total	98.38	97.39									
Sum of recalculated cations partitioned into Z- and Y-sites set to 13.			Recalculation is nonstoichiometric. All Ca partitioned into the A-site.								
Si	7.993	7.987	Si	7.719	7.747	8.135	7.913	7.807	7.775	7.866	7.812	8.248
Al (IV)	0.007	0.013	Al	0.112	0.115	0.047	0.081	0.112	0.122	0.082	0.125	0.021
sum Z	8.000	8.000	Ti	0.357	0.464	0.057	0.304	0.410	0.390	0.350	0.326	-
			Mg	0.310	0.315	0.229	0.144	0.320	0.421	0.276	0.407	0.040
Al (VI)	0.037	0.030	Fe^{2+}	4.473	4.175	4.439	4.451	4.162	4.185	4.293	4.222	4.134
Ti	0.001	0.022	Mn	0.124	0.127	0.159	0.120	0.099	0.107	0.115	0.105	0.159
Mg	0.071	0.129	Ca	0.675	0.631	0.508	0.576	0.715	0.683	0.647	0.753	0.484
Fe^{3+}	0.900	1.071	Na	1.947	2.050	2.157	2.030	1.942	1.928	1.942	1.853	3.312
Fe^{2+}	3.802	3.587	K	0.253	0.268	0.266	0.275	0.262	0.255	0.281	0.247	0.002
Mn	0.189	0.161	total	15.970	15.892	15.997	15.894	15.829	15.866	15.852	15.850	16.400
sum Y	5.000	5.000									
Ca (M_4)	0.183	0.329									
Na (M_4)	1.817	1.671									
Na (A)	0.674	0.265									
K (A)	0.211	0.275									
sum X	2.885	2.540									
X+Y+Z	15.885	15.540									

* Total Fe as FeO.

Amphibole structural formulae based on 23 oxygens and 2 OH groups and follows the procedure of Spear & Kimball (1984).

Appendix C4: Major and Trace Element Analyses

Table C4.1: Mt. Sidley

sample	MB22.1	MB23.2	MB23.6	MB23.7	MB24.1	MB24.3	MB25.7	MB25.10	MB25.11	MB27.5	MB28.1	MB29.4	MB29.9	MB30.3	MB30.6	MB30.7	MB31.1	MB32.4
rock type	trac	trac	trac	trac	trac	trac	trac	trac	trac	bas	bas	trac	trac	trac	trac	trac/ben	mug	trac
group	*LT*	*N*	*N*	*N*	CL-host	CL-host	CL-host	CL-host	CL-host	stage IV	stage IV	*LT*	*HT*	CL-host	CL-host	CL-encl	SFM	*N*
SiO_2	63.84	62.98	62.77	62.76	64.50	65.17	64.53	65.63	65.81	44.71	45.32	64.01	61.22	68.41	64.03	59.56	51.15	62.51
TiO_2	0.39	0.21	0.22	0.21	0.40	0.38	0.36	0.34	0.37	3.15	3.23	0.32	0.49	0.25	0.57	0.97	1.56	0.32
Al_2O_3	16.77	15.07	15.30	15.33	15.90	15.91	15.48	15.73	15.94	15.68	15.98	15.80	16.84	14.46	15.87	16.59	16.60	15.63
Fe_2O_3	5.69	5.39	5.32	5.26	5.28	5.13	4.96	4.98	5.17	13.65	13.54	5.49	6.08	4.49	6.41	8.15	13.89	5.98
MnO	0.16	0.13	0.13	0.13	0.14	0.14	0.13	0.13	0.14	0.18	0.18	0.15	0.17	0.11	0.16	0.20	0.25	0.16
MgO	-	-	-	-	0.01	-	-	-	-	7.44	6.42	-	0.18	-	0.16	0.60	2.34	-
CaO	1.73	0.78	0.89	0.84	1.55	1.40	1.86	1.26	1.32	9.11	8.36	1.57	1.88	0.58	2.05	3.25	5.19	1.05
Na_2O	6.24	6.83	7.01	7.13	6.14	6.09	6.10	6.19	6.22	4.65	5.05	6.28	6.56	6.65	6.03	5.99	5.81	7.22
K_2O	5.29	4.94	5.08	5.04	5.48	5.36	5.46	5.45	5.54	1.43	1.74	5.42	5.61	5.01	4.84	4.19	2.24	5.01
P_2O_5	0.13	0.09	0.09	0.09	0.13	0.11	0.11	0.10	0.12	0.76	0.82	0.10	0.15	0.09	0.22	0.36	1.20	0.11
LOI	0	3.98	3.67	3.56	0.52	0.39	1.42	0.04	0	0	0	0.84	0.76	0.13	0.02	0.31	0	2.06
Total	100.24	100.40	100.48	100.35	100.05	100.08	100.41	99.85	100.63	100.76	100.64	99.98	99.94	100.18	100.36	100.17	100.23	100.05
mg-number	-	-	-	-	< 1	-	-	-	-	52	48	-	6	-	5	13	25	-
Sc	2.1	0.2	0.4	0.3	2.8	2.5	2.0	1.9	2.2	20.6	17.7	1.0	3.3	0.3	4.7	9.2	6.4	1.1
V	-	8	-	1	-	-	4	2	6	191	199	-	5	-	-	14	11	-
Cr	-	-	-	-	-	-	4	-	-	68	65	-	-	-	-	-	-	-
Ni	4	7	6	5	7	2	6	7	4	111	58	6	6	7	4	6	11	5
Cu	12	21	18	14	12	12	9	10	13	93	69	11	16	11	15	22	46	12
Zn	91	216	194	193	87	106	89	100	99	85	90	120	105	142	99	97	89	149
Ga	29	43	40	40	32	30	34	34	32	19	21	32	35	38	29	28	25	35
Rb	131	304	272	275	163	165	183	194	186	32	42	171	338	289	164	106	56	203
Sr	88	1	2	2	20	13	14	10	15	877	941	6	30	-	101	10	738	6
Y	48	125	10	110	49	51	58	58	55	25	25	57	83	47	53	39	40	76
Zr	499	1600	1399	1417	556	567	623	674	631	241	287	645	1531	1169	585	355	419	1052
Nb	86	265	232	235	93	97	105	111	105	59	76	114	243	186	95	64	95	179
As	4.3	7.8	6.3	6.3	2.1	-	1.1	3.2	2.9	1.2	-	2.1	8.9	4.2	1.4	2.0	3.8	4.7
Sb	0.2	0.4	0.3	0.4	0.2	0.1	0.1	0.2	0.2	-	0.1	0.2	0.6	0.2	-	0.1	0.1	0.3
Cs	3.74	11.76	10.38	10.35	5.36	5.56	6.18	7.69	12.18	0.42	0.56	8.75	6.57	3.00	2.46	3.32	0.46	5.49
Ba	763	-	-	50	199	152	123	95	131	419	567	75	84	46	637	1312	608	29
La	69.10	182.20	161.00	158.80	74.45	77.50	91.10	88.60	86.30	42.90	51.50	85.30	142.35	153.20	82.30	57.15	82.30	117.80
Ce	129.4	368.0	308.0	306.0	143.8	151.8	167.7	172.3	167.6	84.6	100.0	162.6	260.7	279.8	160.3	114.3	155.0	225.2
Nd	54.7	118.0	109.0	110.0	50.0	54.0	61.0	63.0	68.0	36.0	39.5	60.0	97.0	121.0	59.0	43.0	54.0	96.0
Sm	10.54	24.26	20.56	21.04	11.03	11.50	12.32	12.76	12.75	7.88	8.81	12.77	15.70	20.48	12.12	9.28	12.00	15.58
Eu	2.32	0.45	0.46	0.43	1.15	1.02	0.91	0.81	0.93	2.57	2.70	1.05	1.30	0.65	2.06	3.45	3.38	0.63
Tb	1.49	3.56	3.09	3.05	1.51	1.55	1.60	1.73	1.59	0.93	1.00	1.72	2.27	2.95	1.70	1.28	1.36	2.20
Yb	4.45	11.62	10.25	10.70	4.64	5.06	5.35	5.73	5.63	1.71	1.69	5.88	9.00	8.93	5.06	3.39	3.65	7.87
Lu	0.69	1.57	1.50	1.56	0.76	0.77	0.78	0.86	0.84	0.25	0.26	0.86	1.36	1.33	0.78	0.54	0.54	1.15
Hf	10.80	35.05	30.55	30.60	12.73	13.24	14.79	15.10	14.42	5.83	6.71	14.45	31.70	26.65	13.59	7.99	9.17	22.50
Ta	5.55	17.35	15.60	15.50	6.17	6.44	7.38	7.55	7.15	3.87	2.70	7.38	16.45	12.95	6.81	4.28	6.28	11.80
Pb	10	42	34	35	16	7	6	23	22	8	5	15	32	42	13	18	7	19
Th	14.6	43.4	35.9	35.6	17.1	18.6	20.5	20.8	20.1	5.0	6.0	18.3	60.4	37.1	18.5	10.3	8.3	27.3
U	3.7	11.7	10.7	11.2	4.7	5.5	5.9	6.9	5.7	1.5	1.6	6.2	15.8	9.7	4.1	2.2	1.6	7.3

Table C4.1: Mt. Sidley

sample	MB32.8	MB32.11	MB33.2	MB33.3	MB33.8	MB33.11	MB33.12	MB33.14	MB34.4	MB35.1	MB35.2	MB35.4	MB35.5	MB35.6	MB36.2	MB37.1	MB38.3	MB38.6
rock type	trac	mug	trac	trac	trac	trac	ben	phn	phn	trac	phn	trac	phn	phn	trac	trac	trac	trac
group	*N*	DPM	*LT*	*HT*	*HT*	bf	Sv	Sv	Sv	bf	Sv	*HT*	bf	bf	CL-encl	*LT*	bf	*HT*
SiO_2	62.78	50.62	63.17	68.30	67.57	59.73	56.71	56.27	55.62	61.98	57.02	65.55	56.71	56.35	62.42	62.50	59.38	67.72
TiO_2	0.21	1.75	0.65	0.26	0.21	0.75	1.24	0.59	0.49	0.27	0.25	0.23	0.19	0.20	0.52	0.40	0.77	0.19
Al_2O_3	17.02	16.71	15.50	13.17	13.58	17.62	18.22	18.79	20.44	15.77	19.17	14.86	19.49	19.31	16.30	17.64	17.32	13.61
Fe_2O_3	5.42	10.24	6.77	5.84	5.92	7.36	8.00	7.35	6.42	7.02	7.17	4.69	7.15	7.05	6.08	5.36	7.20	5.85
MnO	0.15	0.17	0.19	0.15	0.16	0.19	0.18	0.22	0.20	0.20	0.25	0.12	0.25	0.24	0.15	0.15	0.19	0.16
MgO	-	4.48	0.34	-	-	0.46	1.17	0.37	0.35	0.13	0.04	-	-	-	0.38	0.09	0.34	-
CaO	0.86	7.11	2.31	0.70	0.80	2.28	4.27	3.02	1.63	1.30	1.43	0.90	1.20	1.18	1.88	2.03	1.96	0.83
Na_2O	7.25	4.79	5.68	6.07	5.98	5.19	5.51	6.34	9.03	7.45	9.06	6.57	9.41	10.53	6.51	6.75	6.75	6.20
K_2O	5.14	2.13	4.64	4.98	4.91	5.71	3.97	5.71	5.62	5.13	5.19	5.11	5.39	5.31	5.28	4.96	5.68	4.91
P_2O_5	0.10	0.47	0.24	0.08	0.09	0.21	0.48	0.22	0.20	0.11	0.15	0.09	0.12	0.13	0.15	0.15	0.21	0.09
LOI	1.12	1.13	0.68	0.21	0.32	0.95	0.44	0.42	0.43	0.41	0.41	1.98	0.24	0	0.81	0.11	0.32	0.67
Total	100.05	99.60	100.17	99.76	99.54	100.45	100.19	99.30	100.43	99.77	100.14	100.10	100.15	100.30	100.48	100.14	100.12	100.23
mg-number	-	46	9	-	-	11	22	9	10	4	1	-	-	-	11	3	9	-
Sc	0.8	16.7	5.5	0.4	0.3	4.9	6.7	2.9	2.0	1.0	1.1	0.4	0.8	0.8	5.5	2.6	5.2	0.3
V	6	113	2	1	13	-	12	-	3	3	-	1	-	-	10	2	-	9
Cr	-	60	-	-	-	-	-	-	-	-	-	-	-	-	8	1	-	-
Ni	6	40	6	9	10	7	6	7	4	8	6	7	7	6	10	7	6	10
Cu	17	48	16	14	22	26	39	17	16	17	15	12	14	16	12	14	15	20
Zn	159	86	127	212	271	133	113	132	124	213	185	183	186	183	94	101	133	275
Ga	40	23	31	46	48	33	30	31	36	41	44	40	44	45	26	34	36	49
Rb	260	40	165	593	672	395	303	225	206	350	249	442	275	273	124	229	284	663
Sr	1	492	133	-	-	76	373	28	67	8	49	-	1	2	38	192	43	-
Y	101	30	63	190	210	93	81	79	74	123	107	122	109	110	36	67	84	214
Zr	1446	268	680	2260	2291	1981	1525	1171	1714	1850	1869	1444	2018	2015	385	1000	1619	2244
Nb	240	58	114	405	516	355	285	282	322	309	341	296	369	369	66	157	281	500
As	10.5	2.0	3.3	-	13.3	5.0	9.7	2.9	4.5	9.4	8.9	12.8	8.7	10.3	0.7	9.2	4.9	60.0
Sb	0.4	0.1	0.2	0.6	1.1	0.5	0.5	0.4	0.5	0.6	0.5	0.5	0.6	0.5	0.1	0.4	0.4	1.2
Cs	7.01	0.50	7.93	10.69	34.10	18.45	18.62	4.27	4.05	8.40	4.99	18.12	6.27	5.78	1.82	7.74	6.17	36.50
Ba	-	500	823	-	-	450	479	202	172	-	105	-	-	-	294	461	301	-
La	152.90	42.50	87.00	270.80	331.00	181.85	155.95	134.20	123.20	199.50	172.65	186.80	176.80	173.00	55.90	108.80	135.75	328.00
Ce	295.1	82.8	169.8	494.0	600.0	344.0	293.0	262.0	225.4	367.0	312.0	360.0	325.0	321.0	106.8	206.7	245.8	607.0
Nd	101.0	32.5	70.0	181.0	175.0	106.0	94.0	81.0	66.0	134.0	105.0	116.0	112.0	102.0	41.0	66.0	84.0	194.0
Sm	18.64	7.23	12.50	34.20	32.75	18.81	16.55	14.96	13.04	24.50	19.41	21.90	19.88	19.62	8.73	13.54	15.26	37.50
Eu	0.24	2.26	2.36	0.49	0.67	2.32	2.67	1.95	1.65	1.09	1.77	0.44	1.27	1.21	1.37	1.95	1.95	0.65
Tb	2.73	0.94	1.74	5.30	5.64	2.72	2.24	2.20	1.92	3.46	2.95	3.26	2.91	2.84	1.17	1.88	2.28	5.62
Yb	10.48	2.65	5.80	18.50	20.50	11.12	8.58	8.50	8.77	11.95	11.26	12.00	11.90	11.97	3.61	7.02	9.51	20.50
Lu	1.54	0.39	0.80	2.53	2.83	1.62	1.26	1.27	1.28	1.78	1.59	1.70	1.76	1.75	0.54	1.02	1.34	2.91
Hf	31.00	5.85	15.37	52.50	57.15	41.20	32.15	27.30	32.40	39.00	36.95	3.42	40.45	39.40	8.78	21.10	32.45	55.10
Ta	16.20	3.51	7.84	27.30	34.80	23.90	19.45	18.73	20.60	20.80	21.75	19.30	24.20	23.70	4.37	10.97	18.55	34.40
Pb	30	4	23	29	95	42	30	17	16	48	27	57	26	26	8	20	12	260
Th	37.1	5.9	21.4	86.8	110.4	100.3	87.2	39.6	40.6	53.8	42.8	67.8	47.7	46.6	10.2	32.4	49.2	106.2
U	10.5	7.1	5.3	23.7	33.4	10.7	15.6	0.6	11.7	10.9	12.7	19.9	14.5	14.3	2.9	9.2	13.0	30.5

Table C4.1: Mt. Sidley

sample	MB39.2	MB39.3	MB39.4	MB39.5	MB39.6	MB39.7	MB41.1	MB41.5	MB41.11	MB42.3	MB42.4	K054	K055	K056	K057	K059	K061	K062
rock type	trac	phn	phn	phn	trac	trac/ben	phn	trac	trac	tphn	trac	trac	trac	trac	trac	trac	trac	trac
group	*HT*	Sv	Sv	Sv	CL-host	CL-encl	Sv	*HT*	*HT*	Sv	*HT*	*N*	*LT*	*N*	*N*	*N*	*N*	*N*
SiO_2	63.26	57.10	57.78	57.07	65.37	59.14	55.48	60.58	62.03	55.97	67.39	63.43	61.94	63.49	63.12	63.22	63.29	64.02
TiO_2	0.33	0.57	0.62	0.55	0.27	0.88	0.56	0.78	0.42	0.69	0.22	0.21	0.47	0.22	0.24	0.24	0.23	0.21
Al_2O_3	15.62	19.80	19.13	19.69	15.72	17.38	20.26	17.27	17.13	19.65	13.76	15.33	17.87	15.54	15.77	15.67	15.78	15.76
Fe_2O_3	6.10	6.30	6.21	6.70	5.37	7.20	5.27	7.19	5.91	6.75	5.93	5.87	5.51	5.58	5.44	5.55	5.45	5.44
MnO	0.18	0.20	0.18	0.21	0.15	0.17	0.15	0.10	0.16	0.20	0.16	0.14	0.16	0.14	0.13	0.14	0.14	0.14
MgO	-	0.39	0.44	0.37	-	0.84	0.61	0.23	-	0.59	-	-	0.29	-	0.02	0.02	0.01	-
CaO	1.36	2.30	2.82	2.07	0.98	3.18	2.86	1.64	1.35	2.51	0.88	0.57	2.04	0.95	0.84	0.97	1.13	0.63
Na_2O	7.54	8.28	7.70	8.23	7.03	6.25	7.79	5.50	6.95	6.65	6.26	7.47	6.81	7.29	6.85	6.92	7.12	8.12
K_2O	5.19	5.10	4.85	5.45	5.17	4.25	4.74	5.80	5.69	4.93	5.01	4.89	4.82	5.11	5.31	5.26	5.30	4.98
P_2O_5	0.10	0.26	0.23	0.24	0.09	0.35	0.25	0.22	0.12	0.32	0.09	0.04	0.11	0.05	0.05	0.05	0.05	0.05
LOI	0.31	0	0.46	0	0.27	0.40	2.06	0.82	0.16	2.17	0.22	1.56	0.08	1.86	1.78	1.85	1.38	0.69
Total	99.99	100.30	100.42	100.58	100.42	100.04	99.93	100.13	99.92	100.43	99.92	99.51	100.10	100.23	99.55	99.89	99.88	100.04
mg-number	-	11	12	10	-	19	16	6	-	15	-	-	9	-	< 1	< 1	< 1	-
Sc	1.5	2.5	3.1	2.5	0.7	6.2	2.1	5.3	2.6	2.7	0.4	0.2	3.2	0.2	0.6	0.5	0.4	-
V	-	-	1	3	-	21	3	2	-	1	1	11	1	4	2	4	1	3
Cr	-	-	-	-	-	-	-	-	-	-	-	-	-	-	-	-	-	-
Ni	6	5	6	6	7	8	6	4	7	4	10	2	4	5	4	3	3	3
Cu	11	17	17	19	10	27	16	22	13	20	22	14	13	12	11	10	11	14
Zn	170	120	122	129	131	108	87	123	106	116	282	212	90	211	182	189	184	195
Ga	42	35	37	35	40	29	31	30	39	42	47	43	31	41	40	40	35	39
Rb	443	203	247	223	265	107	200	359	380	203	595	292	214	304	260	270	266	285
Sr	1	210	214	131	2	268	350	85	4	264	-	-	220	1	5	5	3	-
Y	130	71	79	78	84	63	62	80	93	66	221	121	64	124	103	107	104	115
Zr	2219	1324	1634	1487	1113	419	1390	1412	1746	1138	2439	1545	923	1605	1307	1373	1342	1486
Nb	395	262	287	292	181	78	236	247	278	252	541	262	146	263	216	227	220	245
As	11.8	1.3	6.9	4.6	6.6	3.5	-	9.3	10.6	4.1	12.7	6.4	7.7	7.2	5.5	6.1	6.8	-
Sb	0.8	0.4	0.6	0.4	0.4	0.1	0.5	0.6	0.7	0.5	1.2	0.4	0.3	0.2	0.4	0.4	0.4	-
Cs	19.74	5.04	8.26	5.92	8.90	17.62	4.03	13.78	9.04	8.94	3.78	10.75	4.18	12.14	9.78	10.14	10.09	-
Ba	-	536	393	409	-	1085	461	507	-	571	-	-	566	-	-	49	-	-
La	201.30	119.30	128.15	130.20	131.30	75.90	99.55	135.80	161.00	118.65	336.00	178.90	109.40	186.70	152.20	157.80	157.40	-
Ce	368.0	217.0	242.7	242.6	244.9	118.1	179.4	251.2	300.5	238.5	635.0	339.0	199.1	365.0	291.5	299.9	300.4	-
Nd	119.0	65.0	79.0	83.0	75.5	53.0	61.0	67.0	97.0	71.0	217.0	121.0	66.0	122.0	99.0	106.0	104.0	-
Sm	23.00	12.80	14.06	14.40	16.70	11.16	10.65	15.05	17.42	13.06	37.70	23.50	13.65	24.20	19.90	20.60	20.60	-
Eu	0.74	2.63	2.08	2.39	0.51	3.25	2.48	2.18	1.12	2.76	0.68	0.45	2.20	0.48	0.53	0.60	0.49	-
Tb	3.34	1.90	2.13	2.09	2.40	1.71	1.66	2.15	2.46	1.83	5.84	3.38	1.91	3.53	2.93	3.00	3.04	-
Yb	14.09	8.01	9.18	9.09	8.17	4.53	7.26	8.30	10.24	6.80	21.70	11.60	6.84	11.84	9.86	10.52	10.19	-
Lu	2.02	1.13	1.34	1.33	1.25	0.63	1.06	1.31	1.52	1.00	2.92	1.66	1.02	1.74	1.46	1.48	1.49	-
Hf	46.00	25.10	31.60	28.70	23.50	9.10	27.00	29.30	36.60	22.50	57.40	33.40	19.70	34.60	28.30	29.80	29.50	-
Ta	25.80	16.80	18.80	18.90	12.33	5.21	15.55	16.30	19.15	15.88	35.10	17.70	10.30	17.60	14.60	15.40	15.10	-
Pb	38	10	20	15	13	40	8	27	34	10	108	42	25	42	31	35	36	37
Th	77.6	34.8	49.5	40.0	32.1	12.3	34.0	62.4	71.1	35.4	110.3	40.3	28.2	42.3	33.1	34.6	34.3	-
U	24.8	10.4	14.1	11.4	10.4	4.8	4.4	4.0	14.5	2.0	13.0	12.2	8.6	12.3	9.9	10.2	11.1	-

Table C4.1: Mt. Sidley

sample	K063	K063A	K063B	K064	K066	K068	K069	K073	K076	K077	K082	K086	K087	K090	K091	K093	K094	K095
rock type	trac	trac	ben	trac	trac	tphn	phn	tphn	phn	phn	trac	mug	mug	trac	trac	mug	trac	bas
group	CL	CL-host	CL-encl	CL-host	*LT*	Bv	Wv	Bv	Wv	Wv	*N*	DPM	DPM	*N*	*N*	SFM	*LT*	stage IV
SiO_2	65.27	65.88	57.22	66.03	63.04	55.52	55.81	55.69	56.29	55.97	62.81	52.54	52.95	60.43	63.13	51.31	64.79	47.73
TiO_2	0.41	0.38	1.12	0.37	0.39	0.90	0.39	0.73	0.46	0.51	0.27	1.61	1.60	0.18	0.33	1.57	0.33	2.48
Al_2O_3	15.10	14.88	15.84	15.22	16.84	17.80	18.81	19.46	19.09	19.34	16.37	17.57	17.65	16.43	16.19	16.92	16.13	17.36
Fe_2O_3	5.52	5.46	7.86	5.49	5.73	7.98	7.51	6.31	6.75	7.46	5.50	9.50	9.56	5.14	6.08	13.70	5.37	12.53
MnO	0.13	0.12	0.12	0.13	0.16	0.24	0.24	0.16	0.21	0.23	0.15	0.17	0.17	0.13	0.16	0.24	0.14	0.19
MgO	0.42	0.35	3.31	0.26	0.13	0.75	0.24	0.72	0.33	0.39	0.03	3.81	3.74	-	0.06	2.49	0.02	5.18
CaO	1.19	1.20	4.43	0.99	1.67	2.90	1.07	3.42	1.51	2.02	1.45	6.40	6.34	0.82	1.04	5.22	1.03	7.30
Na_2O	6.41	6.48	5.61	6.57	6.74	7.10	6.76	6.59	9.47	6.18	6.88	5.17	5.23	8.01	7.56	5.94	6.60	5.16
K_2O	5.17	5.08	4.03	5.23	5.30	4.25	5.87	4.69	5.61	5.99	5.50	2.56	2.62	5.23	5.25	2.27	5.52	1.63
P_2O_5	0.06	0.01	0.13	0.07	0.08	0.33	0.09	0.26	0.06	0.09	0.05	0.38	0.40	-	0.06	1.13	0.05	0.61
LOI	0	0	0.05	0.13	0.07	1.78	3.22	2.44	0	1.78	1.34	0.47	0.19	3.51	0.54	0	0	0
Total	99.68	99.84	99.72	100.49	100.15	99.55	100.01	100.47	99.78	99.96	100.35	100.18	100.45	99.88	100.40	100.79	99.98	100.17
mg-number	13	11	45	9	4	16	6	18	9	9	1	44	44	-	2	26	< 1	45
Sc	2.7	2.5	12.7	2.3	2.1	3.9	2.2	3.3	2.1	2.0	0.7	13.8	13.9	0.6	1.4	6.5	2.1	15.0
V	7	3	78	14	-	-	-	2	4	5	-	99	84	-	4	11	8	143
Cr	9	15	93	3	-	-	-	-	4	-	-	52	49	1	-	-	-	-
Ni	10	8	48	6	3	5	4	3	4	6	3	34	35	4	4	11	5	31
Cu	14	9	57	15	10	15	10	19	11	11	9	39	38	13	12	39	13	47
Zn	134	130	107	142	88	141	192	51	170	184	143	91	91	160	140	91	114	81
Ga	34	34	24	34	29	32	45	32	40	43	33	23	21	37	34	24	33	20
Rb	238	244	96	235	135	117	244	135	244	237	199	54	58	257	194	56	201	44
Sr	24	23	176	17	84	284	29	319	14	21	1	433	430	2	7	734	1	715
Y	82	82	40	80	46	-	76	62	102	105	75	31	34	104	72	40	62	30
Zr	1002	963	308	1009	475	1005	1124	999	1840	2076	935	291	313	1374	947	433	744	307
Nb	155	154	59	152	82	194	346	211	346	363	160	61	63	234	160	93	121	71
As	3.6	1.7	3.1	4.7	1.8	2.1	4.0	-	7.6	2.7	3.7	1.5	-	7.2	4.9	-	-	-
Sb	0.2	0.2	0.1	0.3	0.1	0.1	0.4	0.2	0.6	0.3	0.2	-	-	0.4	0.2	0.1	0.2	-
Cs	6.36	5.84	4.15	4.42	4.09	0.99	3.29	1.70	4.70	4.09	5.95	0.98	1.11	7.20	10.34	0.52	8.57	0.55
Ba	73	-	264	-	700	666	72	604	44	67	-	761	714	-	-	662	37	404
La	120.20	122.50	48.20	119.70	66.40	106.70	157.90	97.40	145.30	164.40	112.60	46.40	49.30	151.70	110.80	80.60	96.50	52.50
Ce	230.6	235.6	94.6	230.7	129.3	223.6	302.0	190.3	271.0	320.0	214.1	89.3	95.3	288.4	209.3	153.9	185.7	99.2
Nd	83.0	77.5	40.0	78.0	46.0	79.0	100.0	59.0	80.2	94.0	75.0	30.0	35.0	98.0	70.0	62.0	65.0	39.0
Sm	16.94	16.81	8.16	16.64	10.20	14.75	19.60	12.19	16.84	19.10	15.70	7.70	7.90	18.94	14.24	11.42	13.20	7.80
Eu	0.66	0.58	1.51	0.65	2.19	4.17	2.10	3.34	1.62	1.89	0.67	2.63	2.67	0.21	0.75	3.31	0.48	2.39
Tb	2.36	2.39	1.12	2.32	1.39	2.11	2.49	1.83	2.65	2.90	2.18	1.05	1.06	2.60	2.04	1.31	1.85	1.00
Yb	7.86	8.01	3.41	7.71	4.55	6.51	6.12	6.37	11.01	11.47	7.28	2.56	2.97	10.87	6.99	3.39	6.22	2.47
Lu	1.15	1.18	0.51	1.05	0.68	0.94	0.86	0.94	1.54	1.70	1.07	0.40	0.44	1.50	1.08	0.52	0.93	0.34
Hf	22.30	23.30	7.36	21.80	10.60	21.40	36.60	22.20	38.90	42.00	20.30	6.30	6.80	32.90	20.30	9.20	16.60	6.70
Ta	10.30	11.05	4.36	10.50	5.80	12.50	22.30	13.50	22.50	22.60	10.90	4.30	4.50	16.30	10.70	6.30	8.20	5.20
Pb	28	32	30	28	13	7	20	6	28	27	22	3	6	33	20	7	21	6
Th	28.0	29.5	8.1	27.4	13.6	14.6	12.8	21.7	42.9	45.4	23.2	6.5	7.1	38.0	24.7	8.9	21.2	7.5
U	9.4	8.7	4.2	6.7	4.1	1.4	0.5	3.2	11.2	3.6	6.3	2.3	2.2	11.7	7.2	2.9	5.7	2.2

Table C4.1: Mt. Sidley

sample	K096	K097	K099	K100	K104	K105	K106	K108	K109	K110	K114	K115	K120	K121	K122	K123	K126	K127
rock type	trac	ben	mug	trac	trac	trac	phn	tphn	bas	phn	tphn-phn	phn	phn	phn	phn	trac	mug	phn
group	*LT*	stage IV	SFM	*LT*	*LT*	*LT*	Wv	Bv	stage IV	Wv	Bv	Sv	Sv	Bv	Bv	*LT*	SFM	Sv
SiO_2	62.25	55.75	51.38	62.49	62.13	61.57	57.12	55.90	44.67	56.50	56.03	56.06	56.60	56.40	57.13	63.93	51.60	56.28
TiO_2	0.44	0.95	1.54	0.42	0.49	0.43	0.39	1.26	3.03	0.39	0.77	0.59	0.51	0.83	0.78	0.45	1.75	0.55
Al_2O_3	16.73	17.41	16.91	16.59	16.80	16.31	18.91	16.62	15.03	18.79	19.52	19.74	19.97	17.98	18.30	16.31	16.68	19.07
Fe_2O_3	6.48	11.20	14.08	6.45	6.18	6.04	7.61	10.07	13.30	7.58	6.49	6.72	5.23	7.87	7.43	5.57	13.95	6.87
MnO	0.18	0.25	0.25	0.19	0.17	0.17	0.25	0.31	0.17	0.25	0.18	0.20	0.16	0.25	0.23	0.15	0.26	0.21
MgO	0.15	1.13	2.30	0.15	0.25	0.23	0.29	1.03	8.35	0.34	0.72	0.61	0.56	0.77	0.66	0.20	2.36	0.40
CaO	1.81	3.71	5.17	1.75	1.51	1.38	1.50	2.87	9.33	1.63	2.71	2.05	2.27	2.37	2.42	1.39	5.32	1.58
Na_2O	6.57	6.54	6.21	6.60	6.71	7.88	8.40	7.86	4.42	8.79	7.57	8.61	8.45	7.33	7.53	6.25	5.81	9.60
K_2O	5.32	2.92	2.25	5.41	5.58	5.31	5.77	4.12	1.45	5.60	4.46	5.27	4.64	4.66	4.60	5.65	1.98	5.29
P_2O_5	0.08	0.58	1.27	0.08	0.08	0.07	0.10	0.46	0.58	0.10	0.27	0.19	0.17	0.28	0.30	0.08	0.92	0.09
LOI	0.07	0	0	0.09	0.09	0.62	0.13	0	0	0.06	1.52	0	1.45	1.67	0.95	0.24	0	0
Total	100.08	100.44	101.36	100.22	99.99	100.01	100.47	100.50	100.33	100.03	100.24	100.04	100.01	100.41	100.33	100.22	100.63	99.94
mg-number	4	17	24	4	7	7	7	17	55	8	18	15	18	16	15	7	25	10
Sc	2.7	6.1	5.5	2.4	3.2	2.5	1.8	6.4	21.8	1.9	3.3	2.6	2.1	3.3	3.2	3.4	6.1	2.3
V	1	9	4	5	2	8	2	6	193	-	-	4	2	-	-	4	15	7
Cr	-	-	-	-	-	2	-	-	145	-	-	-	-	-	-	-	-	6
Ni	4	6	9	2	5	1	5	5	136	6	4	3	4	4	3	4	10	4
Cu	12	25	42	12	14	12	10	16	80	11	16	17	10	14	13	9	24	10
Zn	91	88	97	103	128	107	205	169	87	195	103	114	94	140	126	84	99	155
Ga	28	26	20	31	33	33	45	36	22	45	31	30	28	34	31	28	24	36
Rb	117	87	56	126	268	302	268	105	35	258	140	219	150	150	111	161	45	245
Sr	83	562	756	68	43	40	12	210	752	21	322	169	318	266	313	27	809	43
Y	44	41	41	42	81	94	118	82	25	115	58	70	56	66	55	52	41	94
Zr	421	584	443	456	1218	1410	2172	995	254	2131	962	1482	1125	1064	815	538	361	1583
Nb	78	117	97	86	192	225	375	199	60	362	214	266	205	209	188	92	78	310
As	-	2.1	1.3	3.1	-	-	4.7	3.3	1.0	-	-	5.4	-	1.5	4.6	3.2	1.2	6.9
Sb	0.1	0.2	0.1	0.1	0.2	0.4	0.5	0.2	-	0.5	0.2	0.4	0.3	0.1	0.2	0.2	0.1	0.5
Cs	2.38	0.91	0.44	1.67	5.85	11.48	4.55	1.06	0.58	4.15	1.94	6.29	2.72	1.49	1.06	5.50	0.42	6.18
Ba	847	891	645	708	306	246	-	717	344	-	663	352	659	669	732	262	660	235
La	62.50	101.10	83.00	68.30	127.80	155.50	167.30	112.60	40.70	171.20	98.90	116.50	94.80	110.40	103.50	77.30	67.60	145.90
Ce	119.4	187.1	160.9	122.4	240.2	293.5	310.0	214.6	82.8	307.0	201.7	210.8	171.7	225.1	244.0	144.0	133.3	264.8
Nd	46.0	67.0	60.0	51.0	80.0	90.0	98.0	83.0	32.0	107.0	60.0	67.0	58.0	66.0	70.0	54.0	48.6	79.0
Sm	9.65	11.31	12.00	10.28	16.02	18.60	19.80	16.80	7.60	20.20	12.56	12.70	10.60	14.95	13.74	11.07	11.13	15.33
Eu	2.43	3.11	3.51	2.19	1.57	1.53	2.00	4.79	2.43	1.96	3.36	2.34	2.90	4.18	4.22	1.31	3.62	2.08
Tb	1.34	1.28	1.33	1.32	2.33	2.70	2.99	2.37	0.96	2.97	1.77	1.84	1.50	1.99	1.85	1.51	1.39	2.37
Yb	4.11	3.80	3.48	4.23	8.72	10.35	12.61	7.82	1.84	12.47	6.30	7.93	6.32	7.03	5.24	4.95	3.11	9.90
Lu	0.64	0.54	0.50	0.65	1.30	1.53	1.79	1.12	0.28	1.87	0.94	1.17	0.96	1.07	0.81	0.72	0.45	1.40
Hf	9.40	12.81	9.50	10.70	26.00	31.60	42.00	20.60	6.00	42.00	21.50	27.90	21.50	21.40	18.70	12.00	8.37	32.90
Ta	5.30	8.15	6.50	5.90	13.50	16.40	23.50	12.80	4.30	23.30	13.70	17.40	13.20	13.50	12.60	6.40	5.73	20.20
Pb	10	15	9	10	27	35	27	7	7	30	5	18	6	4	3	9	14	29
Th	11.5	12.9	8.7	10.8	35.9	48.4	43.0	17.8	5.1	43.1	21.0	41.0	27.0	15.3	11.7	16.5	7.4	42.8
U	3.0	3.5	1.7	2.5	10.8	14.4	12.4	4.5	1.5	13.4	1.7	10.2	6.8	0.9	0.7	4.9	2.2	12.5

Table C4.1: Mt. Sidley

sample	K128	K129	K131	K132	K133	K134	K137	K140	K141	K144	K145	K149	K159	K165	K166	K167	K168
rock type	phn	phn	tphn	phn	bas	ben	trac	trac	phn	phn	bas	phn	phn	phn	ben	phn	bas
group	Sv	Sv	Bv	Sv	stage IV	stage IV	*N*	*HT*	Sv	Sv	stage IV	Sv	Wv	Sv	Wv	Wv	stage IV
SiO_2	56.37	56.76	56.20	56.31	45.88	56.07	64.96	61.74	56.10	56.12	45.15	56.12	56.42	55.90	55.17	56.28	45.00
TiO_2	0.55	0.78	0.83	0.30	3.05	0.73	0.33	0.42	0.56	0.61	3.02	0.65	0.30	0.62	0.96	0.33	3.21
Al_2O_3	19.19	18.32	19.75	19.76	16.11	17.76	14.94	17.01	19.13	19.75	15.74	19.71	19.22	19.72	17.62	19.22	15.81
Fe_2O_3	6.81	7.87	6.47	6.38	13.65	10.49	6.08	5.97	7.21	6.78	13.43	6.42	6.86	6.84	8.67	6.71	13.97
MnO	0.21	0.24	0.17	0.21	0.21	0.24	0.14	0.16	0.23	0.20	0.17	0.20	0.23	0.20	0.23	0.23	0.18
MgO	0.39	0.76	0.91	0.24	5.84	0.92	0.02	0.25	0.42	0.63	7.45	0.67	0.20	0.64	1.23	0.19	7.11
CaO	1.57	2.18	3.14	1.16	7.95	3.26	0.98	1.19	1.62	2.11	8.99	2.72	1.43	2.33	3.44	1.32	9.00
Na_2O	9.52	7.99	8.30	9.51	5.40	6.96	7.19	6.83	8.53	8.77	4.66	8.42	8.55	7.53	5.71	8.86	4.50
K_2O	5.35	4.94	4.13	5.69	1.96	2.99	5.03	5.69	5.87	5.19	1.62	4.83	5.06	4.01	4.76	5.40	1.59
P_2O_5	0.09	0.31	0.31	0.08	0.86	0.51	-	0.08	0.14	0.21	0.61	0.24	0.08	0.20	0.35	0.08	0.68
LOI	0	0	0	0.18	0	0	0.23	0.27	0.13	0	0	0	1.42	2.40	1.74	0.93	0.00
Total	100.05	100.15	100.21	99.82	100.91	99.93	99.90	99.61	99.94	100.37	100.84	99.98	99.77	100.39	99.88	99.55	101.05
mg-number	10	16	22	7	46	15	< 1	8	10	16	52	17	5	16	22	5	50
Sc	2.3	3.7	3.5	1.4	17.3	3.9	1.1	2.7	3.1	2.7	21.5	2.7	1.4	2.7	5.3	1.6	20.8
V	1	50	2	1	137	1	1	-	9	-	188	-	5	9	3	92	168
Cr	5	-	-	-	43	3	6	-	-	-	78	-	-	-	-	-	90
Ni	5	4	4	5	54	7	4	4	5	4	141	5	4	4	4	4	116
Cu	12	17	17	9	49	23	10	11	17	17	108	16	9	14	16	12	86
Zn	154	155	98	168	92	90	163	123	133	110	87	126	177	114	109	167	90
Ga	37	39	33	44	20	28	33	35	35	31	21	31	39	31	29	38	21
Rb	248	160	141	256	55	85	225	364	229	227	32	205	236	158	176	247	36
Sr	41	150	371	16	950	557	5	8	32	165	817	272	28	150	199	10	877
Y	95	51	63	107	34	45	85	106	78	68	25	73	91	68	79	92	28
Zr	1588	1398	1147	1962	334	606	897	1617	1414	1478	250	1330	1953	1422	1258	1650	257
Nb	310	264	211	343	96	116	157	270	281	263	59	259	329	258	215	300	62
As	7.5	6.3	3.1	5.7	1.0	-	3.3	5.6	5.4	6.9	0.5	5.5	-	5.3	-	3.9	-
Sb	0.5	0.3	0.3	0.6	-	0.1	0.2	0.7	0.4	0.5	0.6	0.4	0.2	0.5	0.1	0.2	-
Cs	6.26	2.19	1.83	4.65	0.59	0.87	8.10	5.94	5.51	6.46	0.42	5.58	4.53	7.53	5.84	4.16	0.42
Ba	211	570	618	-	666	878	-	159	250	350	440	519	76	324	583	62	415
La	148.70	126.70	94.50	162.50	68.80	101.70	125.30	167.60	130.10	117.70	42.30	119.40	170.70	111.80	131.70	155.50	45.10
Ce	265.6	233.8	176.9	300.1	134.0	175.7	232.4	285.0	235.0	211.5	81.7	217.4	302.0	224.0	238.9	282.9	86.8
Nd	94.0	94.0	62.0	97.0	51.0	68.0	90.0	92.0	73.0	64.0	32.0	71.0	89.0	60.0	82.0	88.0	35.9
Sm	16.20	16.12	11.99	17.80	11.27	11.95	17.56	18.22	14.70	12.60	7.60	13.50	17.90	12.15	15.33	16.50	7.89
Eu	2.03	3.80	3.55	1.78	3.20	3.07	0.63	1.13	2.15	2.41	2.47	2.73	2.16	2.03	3.41	1.95	2.60
Tb	2.29	2.33	1.71	2.74	1.24	1.32	2.34	2.68	2.04	1.85	0.90	1.92	2.52	1.68	2.15	2.42	0.97
Yb	10.07	8.90	6.61	11.70	2.63	4.32	8.04	10.68	8.84	8.02	1.88	8.03	10.24	8.01	8.02	9.58	2.04
Lu	1.44	1.29	0.96	1.74	0.33	0.62	1.10	1.53	1.26	1.14	0.24	1.17	1.50	1.12	1.19	1.39	0.25
Hf	34.80	27.85	22.40	39.30	8.12	13.79	21.90	34.20	28.30	27.90	5.90	25.20	36.70	27.00	24.90	33.80	6.17
Ta	20.80	16.80	13.60	22.20	6.57	8.62	10.90	18.40	18.60	17.20	4.20	16.90	21.80	17.10	15.00	21.00	4.34
Pb	30	11	8	25	11	16	33	41	20	20	8	12	29	16	20	6	11
Th	43.8	27.1	22.9	44.9	7.9	13.1	26.9	66.0	38.6	41.0	5.4	35.7	41.1	42.4	31.6	30.2	5.3
U	13.3	6.7	6.3	12.6	2.5	4.0	8.4	7.8	5.6	12.0	1.4	10.3	2.5	7.2	3.2	1.8	1.7

Major elements in wt.%, trace elements in ppm. LOI, loss on ignition; *mg*-number = atomic % Mg/(Mg + Fe^{2+}), where Fe^{2+} is calculated using FeO = 0.9*Fe_2O_3.
Abbreviations for rock types are the same as in previous tables. Sample group refers to subdivisions based on relative stratigraphic position and compositional differences (see text).

Appendix C4: Major and Trace Element Analyses

Table C4.2: Mt. Waesche

sample	MB4.1	MB4.4	MB5.1	MB5.3	MB6.1	MB7.3	MB8.1	MB9.1	MB10.1	MB10.2	MB10.5	MB11.2	MB14.1	MB15.1	MB16.1	MB21.1	MB21.2	MB45.1
rock type	akb	phntph	akb	akb	trac	rhy	rhy	phn	akb	tphn	phntph	tphn	tphn	trac	akb	mug	haw	phntph
SiO_2	45.62	52.27	45.62	45.50	59.62	72.23	73.88	56.35	46.04	56.02	50.24	55.97	59.16	59.71	47.38	50.39	50.05	50.65
TiO_2	2.03	1.57	2.53	2.44	0.59	0.17	0.27	0.56	2.20	1.03	1.93	1.02	0.51	0.60	1.65	1.77	1.66	1.90
Al_2O_3	16.54	17.68	17.27	17.15	17.80	9.87	10.03	19.46	17.82	17.24	17.66	17.38	16.55	17.84	15.71	18.42	18.27	17.73
Fe_2O_3	12.38	11.12	12.48	12.51	7.44	4.95	5.21	6.26	11.89	8.89	11.58	8.87	8.89	7.53	12.77	10.55	11.04	11.60
MnO	0.18	0.26	0.16	0.17	0.23	0.08	0.10	0.17	0.17	0.23	0.25	0.23	0.27	0.23	0.18	0.18	0.18	0.24
MgO	7.63	1.79	5.53	5.98	0.32	-	-	0.83	7.15	1.44	2.56	1.35	0.06	0.29	8.38	3.01	3.59	2.49
CaO	10.92	5.66	11.49	11.64	2.29	0.23	0.29	2.43	11.01	3.68	6.96	3.54	1.52	2.27	10.32	8.53	9.38	6.76
Na_2O	3.31	6.95	3.72	3.55	8.02	5.94	4.93	8.97	3.52	7.69	6.48	7.90	8.49	7.88	3.27	5.35	4.88	6.52
K_2O	0.58	2.29	0.67	0.65	3.68	4.18	4.64	4.63	0.68	3.65	2.03	3.71	4.60	3.61	0.72	1.53	1.29	2.07
P_2O_5	0.48	0.60	0.43	0.42	0.21	0.08	0.09	0.19	0.48	0.37	0.73	0.37	0.16	0.19	0.35	0.53	0.47	0.72
LOI	0.40	0	0.10	0	0.20	2.40	0.30	0.50	0	0	0	0	0.10	0.10	0	0	0	0
Total	100.07	100.19	100.00	100.01	100.40	100.13	99.74	100.35	100.96	100.24	100.42	100.34	100.31	100.25	100.73	100.26	100.81	100.68
mg-number	55	24	47	49	8	-	-	21	54	24	30	23	1	7	57	36	39	30
Sc	26.0	7.0	28.0	28.0	2.0	-	-	4.0	26.0	7.0	10.0	6.0	1.0	2.0	29.0	16.0	21.0	10.0
V	223	5	249	227	-	3	-	19	192	29	38	22	-	1	193	88	141	50
Cr	158	-	76	93	-	-	-	1	154	-	-	-	-	-	324	10	29	-
Ni	80	7	49	58	8	9	8	12	103	15	11	12	8	5	148	20	24	8
Cu	73	32	78	82	18	11	8	21	83	30	45	26	18	15	86	59	67	43
Zn	84	119	85	77	131	429	317	108	74	127	103	126	183	129	90	88	87	108
Ga	23	24	21	21	30	41	37	33	20	32	26	29	37	31	20	23	22	24
Rb	11	52	14	13	87	546	329	128	12	89	46	90	114	80	16	31	26	46
Sr	494	581	524	514	211	-	9	115	552	207	611	201	11	221	311	513	489	588
Y	22	46	22	23	65	279	216	61	24	62	43	62	92	63	25	34	31	43
Zr	135	366	147	142	700	2820	1978	818	143	660	328	674	1031	673	154	269	232	335
Nb	27	104	30	27	128	331	247	165	31	129	95	132	189	124	29	59	48	97
As	0.4	1.7	-	0.6	5.6	12.5	4.1	4.0	0.7	3.1	-	2.4	4.9	3.8	-	1.1	1.6	1.5
Sb	-	-	-	-	0.2	0.6	0.3	0.1	-	0.2	0.1	0.2	0.2	-	-	-	-	-
Cs	0.20	0.60	0.20	0.30	1.90	24.30	7.60	2.10	0.10	1.30	0.60	1.20	1.40	1.70	0.50	0.40	0.40	0.50
Ba	199	774	173	173	990	-	67	263	208	642	672	668	304	1023	169	457	409	662
La	20.20	71.30	21.70	21.20	82.90	205.30	239.00	87.00	23.40	84.20	64.10	85.80	109.00	81.50	19.50	43.00	36.00	66.60
Ce	44.8	139.5	46.5	45.5	158.4	443.0	460.0	166.3	48.8	166.5	128.3	166.0	212.0	161.3	42.0	87.5	73.7	130.9
Nd	21.0	57.0	21.0	18.0	68.0	176.0	173.0	58.0	20.0	63.0	50.0	57.0	75.0	63.0	21.0	32.0	27.0	52.0
Sm	5.03	11.01	5.34	5.24	12.61	41.10	36.70	10.64	5.63	13.22	10.74	13.30	17.05	12.43	4.90	7.46	7.40	10.37
Eu	1.81	3.68	1.87	1.78	3.49	2.15	2.34	1.36	1.96	2.79	3.39	2.82	2.70	3.54	1.57	2.69	2.38	3.38
Tb	0.73	1.55	0.81	0.81	1.84	7.24	6.10	1.47	0.79	1.90	1.40	1.90	2.61	1.83	0.80	1.09	1.00	1.44
Yb	1.78	4.03	1.96	1.85	6.22	23.40	19.80	6.34	1.95	5.92	3.72	5.80	8.96	6.10	2.16	2.96	2.73	3.81
Lu	0.26	0.63	0.28	0.27	0.91	3.24	2.79	0.92	0.26	0.86	0.56	0.85	1.31	0.88	0.30	0.39	0.40	0.56
Hf	3.60	8.30	3.96	3.66	15.08	65.70	49.40	17.06	3.83	14.05	7.51	14.29	22.15	14.72	3.66	6.17	5.43	7.73
Ta	1.58	6.50	0.98	1.78	8.05	22.90	16.80	10.65	1.92	8.47	3.48	8.34	11.87	8.01	1.69	3.64	1.88	6.11
Pb	4	1	4	4	4	128	80	8	4	7	7	9	10	4	4	6	4	4
Th	1.7	7.6	2.2	1.9	12.0	76.4	50.8	16.5	1.8	11.5	6.7	11.9	16.0	11.3	2.3	4.5	3.8	7.1
U	0.5	2.2	0.8	0.5	3.6	23.1	11.4	4.4	0.7	2.6	1.8	2.8	4.3	3.1	0.7	1.2	1.3	1.5

Table C4.2: Mt. Waesche

sample	MB45.2	MB45.5	MB45.7	K01	K04	K05	K06	K08	K09	K13	K16	K18	K19	K20	K22	K26	K27	K28
type	haw	phn	trac	phntph	akb	trac	bas	akb	haw	haw	trac	phn	akb	haw	phntph	haw	tphn	phntph
SiO_2	47.38	58.64	60.41	51.59	45.68	59.60	46.19	46.87	48.18	45.77	58.99	55.30	45.84	47.16	50.25	48.73	52.70	50.70
TiO_2	2.30	0.54	0.43	1.66	2.44	0.62	2.72	1.90	2.14	2.61	0.25	0.65	2.55	2.29	2.31	2.28	1.68	2.03
Al_2O_3	18.35	16.41	16.23	17.41	16.97	17.89	16.99	16.38	17.63	18.58	17.71	19.32	15.03	18.27	17.05	17.45	17.75	17.10
Fe_2O_3	12.29	8.99	9.03	11.47	12.55	7.62	12.95	12.68	11.37	11.58	7.22	6.74	12.87	12.06	11.39	12.03	10.31	11.50
MnO	0.21	0.27	0.28	0.27	0.17	0.23	0.22	0.18	0.18	0.16	0.20	0.19	0.19	0.21	0.21	0.21	0.23	0.23
MgO	3.78	0.10	0.01	2.00	6.05	0.50	3.91	7.54	4.00	4.95	0.23	1.28	9.26	3.83	2.62	3.71	2.12	2.70
CaO	9.70	1.49	1.81	5.79	11.63	2.27	9.50	10.69	9.75	10.69	1.07	2.73	9.68	9.81	6.55	8.55	5.38	6.45
Na_2O	4.90	8.59	7.79	7.06	3.62	8.28	5.13	3.33	4.96	4.34	7.59	9.26	3.55	4.88	6.61	5.64	7.46	6.86
K_2O	1.42	4.53	3.83	2.25	0.65	3.70	1.44	0.57	1.18	1.21	5.00	4.38	1.17	1.37	2.60	1.51	2.43	2.07
P_2O_5	0.71	0.16	0.15	0.56	0.35	0.16	0.82	0.33	0.47	0.56	0.06	0.19	0.59	0.62	0.74	0.62	0.59	0.75
LOI	0	0.40	0.30	0	0	0	0	0	0.50	0	1.40	0.10	0	0	0	0	0	0
Total	101.04	100.12	100.27	100.06	100.11	100.87	99.87	100.47	100.36	100.45	99.72	100.14	100.73	100.50	100.33	100.73	100.65	100.39
mg-number	38	2	< 1	26	49	12	37	54	41	46	6	27	59	39	31	38	29	32
Sc	17.0	2.0	1.0	8.0	28.0	2.0	18.0	27.0	20.0	20.0	-	4.0	25.0	16.0	11.0	17.0	9.0	11.0
V	145	-	-	2	241	1	120	181	175	182	4	29	202	150	58	112	7	51
Cr	-	-	-	-	95	-	-	214	18	6	-	8	412	-	-	1	-	-
Ni	20	8	7	5	63	4	17	119	24	28	6	10	180	19	11	22	4	6
Cu	59	19	16	32	82	15	60	89	49	59	11	24	84	56	89	54	32	40
Zn	92	173	151	11	81	131	59	76	74	84	174	114	91	90	103	98	112	110
Ga	22	36	32	22	20	31	21	18	19	22	39	33	19	19	25	23	27	22
Rb	32	107	86	51	14	89	31	12	25	27	170	173	25	32	72	31	53	45
Sr	673	25	71	589	509	207	672	384	459	743	8	173	581	675	436	520	412	460
Y	33	88	69	47	23	65	38	26	30	26	102	65	27	33	51	40	53	51
Zr	225	978	689	364	146	713	243	132	204	242	1405	936	253	226	453	304	481	418
Nb	66	181	133	102	28	130	67	25	42	51	223	144	52	65	105	64	102	89
As	0.7	4.7	1.3	1.5	0.8	4.9	1.6	1.0	1.3	-	8.4	3.0	-	1.3	2.5	0.8	2.3	1.7
Sb	-	0.2	0.1	0.1	-	0.2	-	-	0.1	-	-	0.3	-	-	0.1	0.1	0.1	-
Cs	0.30	1.40	1.50	0.60	0.20	2.00	0.40	0.30	0.30	0.30	2.70	2.20	0.50	0.30	2.60	0.40	0.70	0.70
Ba	392	343	1254	703	158	945	401	116	412	342	35	207	250	403	550	378	607	607
La	48.70	105.00	88.80	70.00	20.90	84.30	51.00	19.50	33.10	36.40	131.20	103.70	39.00	47.70	66.90	47.50	69.90	64.10
Ce	97.5	210.3	177.1	135.5	45.4	160.9	103.4	42.6	67.9	72.5	250.6	181.1	80.9	93.6	134.6	99.1	139.1	129.7
Nd	35.0	74.0	62.0	53.0	19.0	64.0	47.0	16.0	23.0	27.0	96.0	54.0	34.0	39.0	57.0	42.0	53.0	52.0
Sm	8.91	16.40	13.98	11.37	5.14	12.70	9.90	4.89	6.93	7.04	17.53	10.23	7.29	8.46	12.15	9.57	11.83	11.69
Eu	2.80	2.81	3.79	3.64	1.87	3.45	3.15	1.70	2.31	2.27	1.94	1.29	2.30	2.77	3.30	2.98	3.45	3.53
Tb	1.16	2.60	2.09	1.51	0.77	1.88	1.28	0.83	0.95	0.89	2.51	1.58	0.94	1.13	1.68	1.29	1.61	1.61
Yb	2.91	8.55	6.69	4.23	1.63	6.29	3.09	2.07	2.38	2.14	10.52	6.83	2.05	2.81	4.43	3.47	4.79	4.32
Lu	0.46	1.26	0.97	0.59	0.24	0.89	0.43	0.30	0.36	0.26	1.48	0.96	0.28	0.40	0.62	0.55	0.69	0.62
Hf	5.53	21.10	15.00	8.07	3.99	15.45	5.80	3.45	4.91	5.61	29.05	18.57	5.91	5.30	9.86	7.10	10.49	9.20
Ta	2.48	11.43	8.35	6.54	2.02	8.37	4.52	1.67	3.01	3.65	14.85	11.44	3.48	4.30	6.95	4.37	6.68	6.02
Pb	7	9	6	4	7	5	8	2	4	9	13	12	7	6	8	8	6	6
Th	4.6	15.9	12.1	7.5	2.0	11.9	4.8	2.1	3.5	4.4	22.1	30.7	4.1	4.8	10.1	4.5	7.5	6.6
U	1.0	4.5	3.7	2.1	0.4	3.4	1.2	0.5	0.9	1.3	9.7	3.8	1.1	1.3	2.7	1.2	1.8	1.1

Table C4.2: Mt. Waesche

sample	K29	K30	K31	K34	K35	K36	K39	K41	K44	K45	K175	K178
type	bas	mug	haw	phntph	tphn	tphn	phntph	trac	phntph	phntph	rhy	rhy
SiO_2	45.33	49.59	46.12	48.76	53.76	52.20	49.06	60.10	50.18	51.00	75.92	75.25
TiO_2	3.24	2.07	2.58	2.13	1.29	1.78	2.12	0.42	1.86	1.82	0.12	0.19
Al_2O_3	15.46	17.14	16.56	18.18	18.18	17.47	18.03	16.23	17.50	17.65	11.78	11.07
Fe_2O_3	14.29	11.44	12.62	11.88	10.02	10.79	11.88	9.04	11.59	11.34	2.29	3.33
MnO	0.23	0.20	0.18	0.23	0.25	0.23	0.23	0.27	0.24	0.25	0.03	0.05
MgO	4.64	3.79	7.17	3.18	1.65	2.19	3.11	0.16	2.85	2.44	-	-
CaO	10.02	8.25	9.92	8.45	4.87	5.62	8.05	1.78	6.64	6.39	0.05	0.08
Na_2O	4.76	5.44	4.05	5.68	7.51	7.27	5.85	8.02	6.36	6.69	4.86	4.84
K_2O	0.98	1.81	1.05	1.66	2.62	2.35	1.73	3.85	2.03	2.13	4.53	4.79
P_2O_5	1.24	0.46	0.55	0.65	0.45	0.62	0.67	0.09	0.63	0.63	0.02	0.04
LOI	0	0	0	0	0	0	0	0.10	0	0	0.10	0.20
Total	100.19	100.19	100.80	100.80	100.60	100.52	100.73	100.06	99.88	100.34	99.70	99.84
mg-number	39	40	53	35	25	29	34	3	33	30	-	-
Sc	21.0	18.0	24.0	13.0	6.0	9.0	12.0	1.0	9.0	9.0	-	-
V	152	145	211	84	-	1	73	-	44	21	9	-
Cr	-	8	170	-	-	-	-	-	-	-	9	4
Ni	20	25	99	13	6	6	12	6	10	8	1	3
Cu	57	65	73	48	28	33	46	15	40	40	2	5
Zn	104	89	86	97	111	117	98	139	108	108	145	165
Ga	22	20	21	22	24	25	24	33	21	23	33	27
Rb	18	41	19	37	61	50	39	88	46	49	321	313
Sr	576	469	573	654	485	426	640	72	581	570	1	1
Y	41	35	27	39	46	52	40	69	44	46	113	99
Zr	203	284	222	278	420	470	287	683	337	353	776	1070
Nb	45	62	42	79	116	102	82	133	96	99	107	111
As	0.7	1.3	1.3	1.1	2.9	1.4	2.4	2.8	1.0	1.5	3.2	5.2
Sb	-	-	-	0.1	0.1	0.1	-	0.1	-	-	0.2	0.2
Cs	0.20	0.80	0.20	0.40	0.60	0.70	0.40	1.60	0.40	0.50	14.40	11.70
Ba	291	546	224	501	805	600	540	1327	640	709	79	83
La	45.00	45.10	32.10	56.30	74.80	70.50	58.60	88.40	66.10	68.10	70.80	110.30
Ce	97.0	90.3	67.5	110.5	145.3	142.5	115.7	168.0	130.1	134.0	133.1	228.1
Nd	46.0	33.0	25.0	40.0	55.0	58.0	49.0	69.0	58.0	54.0	81.0	96.0
Sm	11.51	8.28	6.99	9.60	10.73	11.91	9.80	14.05	10.70	10.97	19.43	19.88
Eu	3.81	2.53	2.24	3.10	3.25	3.51	3.16	3.72	3.40	3.47	0.24	0.58
Tb	1.53	1.10	0.98	1.26	1.48	1.68	1.33	2.02	1.41	1.48	3.17	2.83
Yb	3.03	2.95	2.22	3.37	4.48	4.78	3.53	6.62	3.87	3.89	9.38	9.37
Lu	0.40	0.44	0.31	0.51	0.65	0.68	0.50	0.93	0.54	0.58	1.16	1.23
Hf	5.00	6.54	5.24	6.49	9.17	10.19	6.54	15.02	7.58	7.97	24.50	27.00
Ta	3.29	4.14	2.80	5.07	7.81	6.84	5.38	8.57	6.51	6.55	8.83	8.92
Pb	7	8	9	6	4	6	5	-	6	7	33	53
Th	3.2	5.7	2.8	5.6	8.9	7.4	6.0	11.6	6.9	7.3	33.0	38.7
U	1.3	1.8	1.2	1.4	2.2	2.1	1.8	3.2	2.1	2.0	12.2	10.8

Abbreviations for rock type include, akb = alkali basalt; haw = hawaiite; phntph = phonotephrite; rhy = rhyolite; all others are defined in previous tables.

Appendix C5: Isotopic Analyses

Table C5.1: Mt. Waesche

sample	rock type	age[a]	Sm[b]	Nd[b]	$^{147}Sm/^{144}Nd$	$^{143}Nd/^{144}Nd_m$	$^{143}Nd/^{144}Nd_i$	1σ	εNd	Rb[c]	Sr	$^{87}Rb/^{86}Sr$	$^{87}Sr/^{86}Sr_m$	$^{87}Sr/^{86}Sr_i$	1σ
K01	phonotephrite	0.1	11.18	59.48	0.113689	0.512886	0.512885	8	4.8	51	589	0.2504	0.702697	0.702697	7
K06	basanite	0.1	–	–	–	–	–	–	–	31	672	0.1334	0.702671	0.702671	7
K18	phonolite	0.5	–	–	–	–	–	–	–	173	173	2.8917	0.702750	0.702729	7
K19	alkali basalt	0.5	7.33	37.49	0.118148	0.512877	0.512876	9	4.6	25	581	0.1244	0.702732	0.702731	6
K20	hawaiite	0.1	8.40	43.41	0.116974	0.512887	0.512886	8	4.8	32	675	0.1371	0.702706	0.702706	7
K30	mugearite	0.1	–	–	–	–	–	–	–	41	469	0.2528	0.702715	0.702715	8
K35	tephriphonolite	0.5	10.56	57.53	0.111021	0.512888	0.512887	9	4.8	61	485	0.3637	0.702687	0.702685	7
K41	trachyte	0.5	–	–	–	–	–	–	–	88	72	3.5343	0.702828	0.702803	7
K44	phonotephrite	0.5	10.46	55.56	0.113875	0.512874	0.512873	9	4.6	46	581	0.2289	0.702695	0.702694	7
MB4.1	alkali basalt	0.1	–	–	–	–	–	–	–	11	494	0.0644	0.702681	0.702681	7
MB7.3	rhyolite	1.6	42.74	191.71	0.134783	0.512750	0.512749	4	2.2	–	–	–	–	–	–
MB10.1	alkali basalt	0.5	–	–	–	–	–	–	–	12	552	0.0629	0.702665	0.702665	7
MB.11.2	tephriphonolite	0.5	13.05	68.61	0.114965	0.512890	0.512890	9	4.9	90	201	1.2948	0.702728	0.702719	7
MB14.1	tephriphonolite	0.5	15.64	80.10	0.118074	0.512867	0.512867	4	4.4	114	11	29.9690	0.703071	0.702858	10
MB15.1	trachyte	0.5	–	–	–	–	–	–	–	80	221	1.0468	0.702760	0.702753	7
MB16.1	alkali basalt	0.5	5.09	22.22	0.138460	0.512882	0.512882	4	4.7	16	311	0.1488	0.702724	0.702723	7
MB21.2	hawaiite	0.5	7.00	34.33	0.123211	0.512874	0.512873	10	4.6	26	489	0.1537	0.702667	0.702666	7

[a] in millions of years (Ma), interpolated from known K-Ar ages (LeMasurier & Thomson, 1990) and unpublished WAVE $^{40}Ar/^{39}Ar$ age data.
[b] Sm and Nd concentrations (ppm) determined by isotope dilution.
[c] Rb and Sr concentrations (ppm) determined by XRF.

Appendix C5: Isotopic Analyses

Table C5.2: Lead isotope analyses from Mt. Sidley and Mt. Waesche.

sample	$^{206}Pb/^{204}Pb$	1σ	$^{207}Pb/^{204}Pb$	1σ	$^{208}Pb/^{204}Pb$	1σ
Mt. Sidley						
MB27.5	19.524	± 5	15.651	± 4	39.099	± 10
MB32.11	19.534	± 1	15.669	± 1	39.174	± 3
Mt. Waesche						
MB16.1	19.758	± 4	15.683	± 3	39.415	± 8

$1\sigma = 1 \times 10^{-3}$.

Appendix C5: Isotopic Analyses

Table C5.3: Oxygen isotopic analyses for Mt. Sidley volcanic rocks.

sample	rock	type	LOI (wt%)	$\delta^{18}O$ (‰)	sample mg	O_2 factor	µmoles O_2	pressure CO_2	µmoles CO_2	% Yield
MB27.5	basanite	lava	0	5.17	23.0	13.76	316.5	1.536	278.3	87.9
MB29.4	trachyte	w.tephra	0.84	5.76	16.1	14.50	233.5	1.356	244.8	104.8
MB29.4an	Akf	pheno		8.44	16.0	14.37	229.9	1.175	211.1	91.8
MB30.6	trachyte	lava	0.02	5.89	12.1	14.66	177.4	1.098	196.8	110.9
MB32.11	mugearite	tephra	1.13	1.78	20.3	13.85	281.2	1.462	264.5	94.1
MB33.3	trachyte	lava	0.21	5.44	16.4	14.73	241.6	1.416	255.9	105.9
MB33.3an	Akf	pheno		6.60	20.2	14.37	290.3	1.763	320.5	110.4
MB33.8	trachyte	lava	0.32	5.07	20.5	14.67	300.7	1.764	320.7	106.7
MB35.2	phonolite	lava	0.41	5.16	13.2	14.20	187.4	1.067	191.0	101.9
MB35.5	phonolite	w.tephra	0.24	5.30	25.3	14.19	359.0	2.027	369.6	103.0
MB35.5an	Akf	pheno		6.48	16.6	14.37	238.5	1.379	249.1	104.4
MB42.3	tephriphon	lava	2.17	2.42	14.1	14.09	198.7	0.916	162.9	82.0
MB42.3an	Akf	pheno		6.06	20.7	14.37	297.5	1.742	316.6	106.4
K54	trachyte	pumice	1.56	−0.97	13.3	14.76	196.3	1.056	189.0	96.3
K54an	Akf	pheno		6.04	21.0	14.37	301.8	1.810	329.2	109.1
K55	trachyte	lava	0.08	5.76	13.8	14.57	201.1	1.168	209.8	104.3
K57	trachyte	pumice	1.78	−0.46	13.6	14.30	194.5	1.065	190.7	98.1
K59	trachyte	pumice	1.85	−1.18	13.3	14.32	190.5	1.038	185.6	97.4
K63A	trachyte	lava	0	5.41	26.6	14.67	390.2	2.205	402.7	103.2
K63B	benmoreite	lava	0.05	5.75	21.9	14.24	311.9	1.611	306.0	98.1
K66	trachyte	lava	0.07	7.61	16.9	14.57	246.2	1.333	240.5	97.7
K68	tephriphon	lava	1.78	2.14	17.7	13.95	246.9	1.404	253.7	102.8
K97	benmoreite	lava	0	5.67	16.3	14.28	232.8	1.352	244.0	104.8
K99	mugearite	lava	0	6.15	16.5	14.16	233.6	1.044	186.7	79.9
K100	trachyte	lava	0.09	3.56	12.1	14.52	175.7	1.109	198.8	113.2
K105	trachyte	lava	0.62	4.07	13.2	14.36	189.6	1.074	192.3	101.4
K105an	Akf	pheno		5.04	15.0	14.37	215.6	1.307	235.7	109.3
K108	tephriphon	lava	0	3.06	11.6	14.19	164.6	0.800	141.4	85.9
K110	phonolite	lava	0.06	5.28	17.7	14.16	250.6	1.363	246.1	98.2
K115	phonolite	lava	0	6.15	15.4	14.22	219.0	NR	–	–
K122	phonolite	lava	0.95	3.76	13.2	14.21	187.6	1.083	194.0	103.4
K134	benmoreite	lava	0	6.20	14.7	14.25	209.5	1.108	198.7	94.8
K137	trachyte	w.tephra	0.23	5.29	15.9	14.57	231.7	1.567	284.0	122.6
K137an	Akf	pheno		7.81	17.7	14.37	254.4	1.421	256.9	101.0
K144	phonolite	lava	0	5.71	14.1	14.26	201.1	1.121	201.1	100.0
K159	phonolite	lava	1.42	0.91	11.1	14.04	155.8	0.931	165.7	106.4
K165	phonolite	lava	2.40	−1.44	12.4	14.08	174.6	0.814	144.0	82.5
K166	benmoreite	intrusive	1.74	1.32	15.4	13.96	215.0	1.198	215.4	100.2
K168	basanite	lava	0	5.68	14.9	13.79	205.5	0.722	126.9	61.8
NBS-28	quartz	standard		9.482	14.2	16.6	235.7	1.370	247.4	105.0
NBS-28	quartz	"		9.684	10.0	16.6	166.0	0.985	175.8	105.9
NBS-28	quartz	"		9.590	14.3	16.6	237.4	1.295	233.4	98.3

LOI = loss on ignition from whole-rock analyses; NR = no reading; Akf = alkali feldspar (anorthoclase); pheno = phenocryst; w.tephra = welded pyroclastic deposit. µmoles O_2 = sample wt. X (O_2 factor). O_2 factor is the total oxide weight in the whole-rock sample; µmoles CO_2 = (186 X CO_2 pressure) – 7.44; % Yield = µmolCO_2 / µmolO_2

Analysis of oxygen isotopes at New Mexico Tech followed the procedures outlined by Hallett (1994, and references therein). Hallett (1994) reported an analytical precision for whole-rock samples of ± 0.21‰ based on multiple analyses (n = 20) of an in-house basalt standard (Parido-1). Repeated analysis of quartz standard NBS-28 in the New Mexico Tech laboratory yield 1σ errors of ± 0.2‰ or less. Three runs of NBS-28 in this study give a 1σ of ± 0.1‰. The reported value for NBS-28 = 9.64‰.

This dissertation is accepted on behalf of the faculty of the Institute by the following committee:

Philip R. Kyle
Adviser

William C. McIntosh

Andrew Campbell

Chris E. Chapman

Date

I release this document to New Mexico Institute of Mining and Technology.

Kurt S Panter
Students Signature

Date